

**ASU**  
ARIZONA STATE UNIVERSITY

August 24, 2001

The Air Force Office of Scientific Research (AFOSR)  
AFOSR/NA (Attention: Thomas J. Beutner)  
801 North Randolph Street, Room 732  
Arlington VA 22203-1977

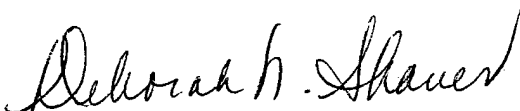
Subject: Final Technical Report

Reference: AFOSR Grant F49620-97-1-0520, "Control of Transition in Swept-Wing Boundary Layers using MEMS Devices as Distributed Roughness."

Arizona State University is pleased to provide an original and two copies of the final technical report for the referenced grant. This report covers the period 7/1/97- 12/31/00.

Your support of Dr. Saric's research is greatly appreciated. If you have questions or require any additional information, please contact me at (602) 965-1158.

Sincerely,



Deborah N. Shaver  
Lead Sponsored Projects Officer

Enclosures

xc: Dr. William S. Saric  
ASU XAA 0034/TE  
AFOSR/PKA (letter only)

**REPORT DOCUMENTATION PAGE**Form Approved  
OMB No. 0704-0188

Public reporting burden for this collection of information is estimated to average 1 hour per response, including the time for reviewing instructions, searching existing data sources, gathering and maintaining the data needed, and completing and reviewing this collection of information. Send comments regarding this burden estimate or any other aspect of this collection of information, including suggestions for reducing this burden to Department of Defense, Washington Headquarters Services, Directorate for Information Operations and Reports (0704-0188), 1215 Jefferson Davis Highway, Suite 1204, Arlington, VA 22202-4302. Respondents should be aware that notwithstanding any other provision of law, no person shall be subject to any penalty for failing to comply with a collection of information if it does not display a currently valid OMB control number. **PLEASE DO NOT RETURN YOUR FORM TO THE ABOVE ADDRESS.**

**1. REPORT DATE (DD-MM-YYYY)**

08/24/2001

**2. REPORT TYPE**

Final Technical Report

**3. DATES COVERED (From - To)**

07/01/1997 - 12/31/2000

**4. TITLE AND SUBTITLE**Control of Transition in Swept-Wing Boundary Layers using  
MEMS Devices as Distributed Roughness**5a. CONTRACT NUMBER****5b. GRANT NUMBER**

F49620-97-1-0520

**5c. PROGRAM ELEMENT NUMBER****6. AUTHOR(S)**

William S. Saric

**5d. PROJECT NUMBER****5e. TASK NUMBER****5f. WORK UNIT NUMBER****7. PERFORMING ORGANIZATION NAME(S) AND ADDRESS(ES)**Arizona Board of Regents for Arizona State University  
Office of Research & Sponsored  
Projects Administration  
Box 873503  
Tempe, AZ 85287-3503**8. PERFORMING ORGANIZATION REPORT  
NUMBER**

XAA0034F

**9. SPONSORING / MONITORING AGENCY NAME(S) AND ADDRESS(ES)**AFOSR  
801 North Randolph Street  
Room 732  
Arlington VA 22203-1977**10. SPONSOR/MONITOR'S ACRONYM(S)****11. SPONSOR/MONITOR'S REPORT  
NUMBER(S)****12. DISTRIBUTION / AVAILABILITY STATEMENT**

Approved for public release; distribution is unlimited

**13. SUPPLEMENTARY NOTES**

20010905 064

**14. ABSTRACT**

Active flow control using MEMS-based microactuators holds tremendous promise for achieving laminar flow control and drag reduction for a wide class of aircraft. In order to achieve effective control it is necessary to have a complete understanding of the fundamental instability processes that apply to a particular boundary layer and to develop a sensor and actuator system that is capable of providing an appropriate control input to that boundary layer. In the present work, crossflow-dominated swept-wing boundary layers are the primary interest. These boundary layers are known to undergo a highly nonlinear transition process that involves, in low-disturbance environments, stationary waves of longitudinal vorticity. These stationary waves have the potential to be controlled or suppressed by an appropriate surface roughness configurations that could be provided by MEMS-based actuators. The work performed here consists of a parallel experimental and hardware development efforts. The breakdown phase of the crossflow instability is investigated in the experiments in an effort to determine an appropriate control input. A MEMS-based roughness actuator system is developed to provide controlled roughness inputs. The results of the experimental phase conclusively demonstrate that the destabilization of a high-frequency secondary instability is responsible for breakdown. The MEMS development effort did not produce a useful control device because of certain shortcomings in the present state of MEMS fabrication quality control and overall system integration.

**15. SUBJECT TERMS**

transition control; MEMS; stability; secondary instabilities

**16. SECURITY CLASSIFICATION OF:**  
UNCLASSIFIED**a. REPORT**  
UNCLASSIFIED**b. ABSTRACT**  
UNCLASSIFIED**c. THIS PAGE**  
UNCLASSIFIED**17. LIMITATION  
OF ABSTRACT**

UNLIMITED

**18. NUMBER  
OF PAGES**

193

**19a. NAME OF RESPONSIBLE PERSON**  
William S. Saric**19b. TELEPHONE NUMBER (include area  
code)**  
(480) 965-2822

# Abstract

Active flow control using MEMS-based microactuators holds tremendous promise for achieving laminar flow control and drag reduction for a wide class of aircraft. In order to achieve effective control it is necessary to have a complete understanding of the fundamental instability processes that apply to a particular boundary layer and to develop a sensor and actuator system that is capable of providing an appropriate control input to that boundary layer. In the present work, crossflow-dominated swept-wing boundary layers are the primary interest. These boundary layers are known to undergo a highly nonlinear transition process that involves, in low-disturbance environments, stationary waves of longitudinal vorticity. These stationary waves have the potential to be controlled or suppressed by an appropriate surface roughness configurations that could be provided by MEMS-based actuators. The work performed here consists of a parallel experimental and hardware development efforts. The breakdown phase of the crossflow instability is investigated in the experiments in an effort to determine an appropriate control input. A MEMS-based roughness actuator system is developed to provide controlled roughness inputs. The results of the experimental phase conclusively demonstrate that the destabilization of a high-frequency secondary instability is responsible for breakdown. The MEMS development effort did not produce a useful control device because of certain shortcomings in the present state of MEMS fabrication quality control and overall system integration.

This work was supported by AFOSR grant F49620-97-1-0520 and was managed by Dr. Thomas Beutner.

# Contents

<b>1</b>	<b>Introduction</b>	<b>1</b>
1.1	Overview and motivation . . . . .	1
1.2	Introduction to crossflow transition . . . . .	2
1.2.1	Receptivity . . . . .	3
1.2.2	Primary instability . . . . .	5
1.2.3	Implications for $N$ -factor transition prediction . . . . .	6
1.3	Objectives and outline . . . . .	7
<b>2</b>	<b>Experimental Design, Facility, and Techniques</b>	<b>9</b>
2.1	General philosophy . . . . .	9
2.2	Swept-wing model . . . . .	10
2.3	MEMS roughness insert . . . . .	11
2.4	Wind tunnel, test section, and traverse . . . . .	14
2.5	Instrumentation . . . . .	17
2.5.1	General instrumentation . . . . .	17
2.5.2	Hotwire procedures . . . . .	17
2.6	Measurement techniques . . . . .	21
2.6.1	Coordinate systems . . . . .	21
2.6.2	Boundary-layer velocity profiles . . . . .	22
2.6.3	Spanwise-line and full-field scans . . . . .	24
2.6.4	Fluctuating-velocity spectra . . . . .	24
<b>3</b>	<b>Secondary Instability</b>	<b>26</b>
3.1	Literature review . . . . .	27
3.2	Experimental approach . . . . .	34
3.3	Results and discussion . . . . .	35
3.3.1	Baseline case . . . . .	35
3.3.2	Increased roughness amplitude case . . . . .	42
3.3.3	Decreased Reynolds number case . . . . .	44
3.3.4	Increased Reynolds number case . . . . .	45
3.3.5	Enhanced freestream fluctuation cases . . . . .	47
<b>4</b>	<b>Absolute Instability</b>	<b>49</b>
4.1	Foundation . . . . .	49
4.2	Literature review . . . . .	51
4.3	Experimental approach . . . . .	52
4.4	Results and discussion . . . . .	54
4.4.1	Baseline case . . . . .	54



4.4.2	Increased Reynolds number case . . . . .	57
4.4.3	Decreased Reynolds number case . . . . .	57
5	Conclusions	59
A	Figures	67

# List of Tables

2.1 Traverse Capabilities. . . . .	16
------------------------------------	----

# List of Figures

1	Swept-wing streamline and coordinate systems. . . . .	68
2	Crossflow boundary-layer profiles. . . . .	68
3	Airfoil shape and suction-side pressure distribution, $C_{p,2}$ , for the ASU(67)-0315 swept wing at $-3^\circ$ angle of attack. . . . .	69
4	ASU(67)-0315 features. . . . .	69
5	Modular leading-edge insert for the ASU(67)-0315. . . . .	70
6	Schematic cross section of the variable leading-edge roughness device. . . . .	70
7	Spanwise mean-flow hotwire scan at $x/c = 0.20$ , $Y = 1.0$ mm, $Re_c = 2.4 \times 10^6$ . . . . .	71
8	Spatial mean-flow spectrum of data from Figure 7. . . . .	71
9	Center-displacement height versus pressure difference, $\Delta p$ , across 3-mm-diameter roughness elements. Different line styles indicate different elements. . . . .	72
10	Activated 3-mm-diameter roughness shape of a 10- $\mu$ m-high element. . . . .	72
11	Activated 3-mm-diameter roughness shape of a 50- $\mu$ m-high element. . . . .	73
12	Schematic view of the Unsteady Wind Tunnel. All dimensions in meters. . . . .	74
13	Side view of the traverse frame. All dimensions in millimeters. . . . .	75
14	Front view of the traverse frame. All dimensions in millimeters. . . . .	75
15	Top view of the hotwire sting. All dimensions in millimeters. . . . .	76
16	Schematic of root and tip wall liners for a zero-lift configuration. . . . .	77
17	Upper and lower span suction-side $C_{p,3}$ distributions at $Re_c = 2.0 \times 10^6$ . . . . .	77
18	Upper and lower span suction-side $C_{p,3}$ distributions at $Re_c = 2.4 \times 10^6$ . . . . .	78
19	Upper and lower span suction-side $C_{p,3}$ distributions at $Re_c = 2.8 \times 10^6$ . . . . .	78
20	Polynomial and nonlinear temperature-compensation curves without interpolated data. . . . .	79
21	Nonlinear temperature-compensation curve with interpolated data. . . . .	79
22	Coordinate systems, $X, Y$ plane. . . . .	80
23	Mean-flow velocity profiles, $Re_c = 2.4 \times 10^6$ , [18 12] roughness, $x/c = 0.30$ , $z = 117$ – $128$ mm. . . . .	80
24	Mean-flow velocity contours, $Re_c = 2.4 \times 10^6$ , [18 12] roughness, $x/c = 0.30$ , contour lines at $U/U_{edge} = 0.10, 0.20, \dots, 0.90$ . . . . .	81
25	Fluctuating-velocity spectra, $Re_c = 2.4 \times 10^6$ , [18 12] roughness, $x/c = 0.30$ , $z = 119$ mm. . . . .	81
26	Fluctuating-velocity spectra, $Re_c = 2.4 \times 10^6$ , [18 12] roughness, $x/c = 0.30$ , $z = 122$ mm. . . . .	82
27	Fluctuating-velocity spectra, $Re_c = 2.4 \times 10^6$ , [18 12] roughness, $x/c = 0.30$ , $z = 125$ mm. . . . .	82
28	200-Hz velocity-fluctuation rms distribution, $Re_c = 2.4 \times 10^6$ , [18 12] roughness, $x/c = 0.30$ , 100–300-Hz bandpass. Lines are 10% contours of the maximum in this band. . . . .	83

29	Schematic of the crossflow vortex velocity components and hotwire arrangement parallel to the plane of the wing's surface. . . . .	83
30	Mean-flow velocity profiles, $Re_c = 2.4 \times 10^6$ , [18 12] roughness, $x/c = 0.35$ , $z = 103$ – $114$ mm. . . . .	84
31	Mean-flow velocity contours, $Re_c = 2.4 \times 10^6$ , [18 12] roughness, $x/c = 0.35$ , contour lines at $U/U_{edge} = 0.10, 0.20, \dots, 0.90$ . . . . .	84
32	Fluctuating-velocity spectra, $Re_c = 2.4 \times 10^6$ , [18 12] roughness, $x/c = 0.35$ , $z = 105$ mm. . . . .	85
33	Fluctuating-velocity spectra, $Re_c = 2.4 \times 10^6$ , [18 12] roughness, $x/c = 0.35$ , $z = 108$ mm. . . . .	85
34	Fluctuating-velocity spectra, $Re_c = 2.4 \times 10^6$ , [18 12] roughness, $x/c = 0.35$ , $z = 111$ mm. . . . .	86
35	200-Hz velocity-fluctuation rms distribution, $Re_c = 2.4 \times 10^6$ , [18 12] roughness, $x/c = 0.35$ , 100–300-Hz bandpass. Lines are 10% contours of the maximum in this band. . . . .	86
36	Mean-flow velocity profiles, $Re_c = 2.4 \times 10^6$ , [18 12] roughness, $x/c = 0.40$ , $z = 89$ – $100$ mm. . . . .	87
37	Mean-flow velocity contours, $Re_c = 2.4 \times 10^6$ , [18 12] roughness, $x/c = 0.40$ , contour lines at $U/U_{edge} = 0.10, 0.20, \dots, 0.90$ . . . . .	87
38	Fluctuating-velocity spectra, $Re_c = 2.4 \times 10^6$ , [18 12] roughness, $x/c = 0.40$ , $z = 91$ mm. . . . .	88
39	Fluctuating-velocity spectra, $Re_c = 2.4 \times 10^6$ , [18 12] roughness, $x/c = 0.40$ , $z = 94$ mm. . . . .	88
40	Fluctuating-velocity spectra, $Re_c = 2.4 \times 10^6$ , [18 12] roughness, $x/c = 0.40$ , $z = 97$ mm. . . . .	89
41	200-Hz velocity-fluctuation rms distribution, $Re_c = 2.4 \times 10^6$ , [18 12] roughness, $x/c = 0.40$ , 100–300-Hz bandpass. Lines are 10% contours of the maximum in this band. . . . .	89
42	3.0-kHz velocity-fluctuation rms distribution, $Re_c = 2.4 \times 10^6$ , [18 12] roughness, $x/c = 0.40$ , 2.9–3.1-Hz bandpass. Lines are 10% contours of the maximum in this band. . . . .	90
43	Mean-flow velocity profiles, $Re_c = 2.4 \times 10^6$ , [18 12] roughness, $x/c = 0.41$ , $z = 85$ – $96$ mm. . . . .	90
44	Mean-flow velocity contours, $Re_c = 2.4 \times 10^6$ , [18 12] roughness, $x/c = 0.41$ , contour lines at $U/U_{edge} = 0.10, 0.20, \dots, 0.90$ . . . . .	91
45	Fluctuating-velocity spectra, $Re_c = 2.4 \times 10^6$ , [18 12] roughness, $x/c = 0.41$ , $z = 87$ mm. . . . .	91
46	Fluctuating-velocity spectra, $Re_c = 2.4 \times 10^6$ , [18 12] roughness, $x/c = 0.41$ , $z = 90$ mm. . . . .	92
47	Fluctuating-velocity spectra, $Re_c = 2.4 \times 10^6$ , [18 12] roughness, $x/c = 0.41$ , $z = 93$ mm. . . . .	92
48	Mean-flow velocity profiles, $Re_c = 2.4 \times 10^6$ , [18 12] roughness, $x/c = 0.42$ , $z = 82$ – $93$ mm. . . . .	93
49	Mean-flow velocity contours, $Re_c = 2.4 \times 10^6$ , [18 12] roughness, $x/c = 0.42$ , contour lines at $U/U_{edge} = 0.10, 0.20, \dots, 0.90$ . . . . .	93
50	Fluctuating-velocity spectra, $Re_c = 2.4 \times 10^6$ , [18 12] roughness, $x/c = 0.42$ , $z = 84$ mm. . . . .	94

51	Fluctuating-velocity spectra, $Re_c = 2.4 \times 10^6$ , [18 12] roughness, $x/c = 0.42$ , $z = 87$ mm. . . . .	94
52	Fluctuating-velocity spectra, $Re_c = 2.4 \times 10^6$ , [18 12] roughness, $x/c = 0.42$ , $z = 90$ mm. . . . .	95
53	1.8-kHz velocity-fluctuation rms distribution, $Re_c = 2.4 \times 10^6$ , [18 12] roughness, $x/c = 0.42$ , 1.7–1.9-kHz bandpass. Lines are 10% contours of the maximum in this band. . . . .	95
54	3.0-kHz velocity-fluctuation rms distribution, $Re_c = 2.4 \times 10^6$ , [18 12] roughness, $x/c = 0.42$ , 2.9–3.1-kHz bandpass. Lines are 10% contours of the maximum in this band. . . . .	96
55	Mean-flow velocity profiles, $Re_c = 2.4 \times 10^6$ , [18 12] roughness, $x/c = 0.43$ , $z = 79$ –90 mm. . . . .	96
56	Mean-flow velocity contours, $Re_c = 2.4 \times 10^6$ , [18 12] roughness, $x/c = 0.43$ , contour lines at $U/U_{edge} = 0.10, 0.20, \dots, 0.90$ . . . . .	97
57	Fluctuating-velocity spectra, $Re_c = 2.4 \times 10^6$ , [18 12] roughness, $x/c = 0.43$ , $z = 81$ mm. . . . .	97
58	Fluctuating-velocity spectra, $Re_c = 2.4 \times 10^6$ , [18 12] roughness, $x/c = 0.43$ , $z = 84$ mm. . . . .	98
59	Fluctuating-velocity spectra, $Re_c = 2.4 \times 10^6$ , [18 12] roughness, $x/c = 0.43$ , $z = 87$ mm. . . . .	98
60	Mean-flow velocity profiles, $Re_c = 2.4 \times 10^6$ , [18 12] roughness, $x/c = 0.44$ , $z = 76$ –87 mm. . . . .	99
61	Mean-flow velocity contours, $Re_c = 2.4 \times 10^6$ , [18 12] roughness, $x/c = 0.44$ , contour lines at $U/U_{edge} = 0.10, 0.20, \dots, 0.90$ . . . . .	99
62	Fluctuating-velocity spectra, $Re_c = 2.4 \times 10^6$ , [18 12] roughness, $x/c = 0.44$ , $z = 78$ mm. . . . .	100
63	Fluctuating-velocity spectra, $Re_c = 2.4 \times 10^6$ , [18 12] roughness, $x/c = 0.44$ , $z = 81$ mm. . . . .	100
64	Fluctuating-velocity spectra, $Re_c = 2.4 \times 10^6$ , [18 12] roughness, $x/c = 0.44$ , $z = 84$ mm. . . . .	101
65	3.0-kHz velocity-fluctuation rms distribution, $Re_c = 2.4 \times 10^6$ , [18 12] roughness, $x/c = 0.44$ , 2.9–3.1-Hz bandpass. Lines are 10% contours of the maximum in this band. . . . .	101
66	6.1-kHz velocity-fluctuation rms distribution, $Re_c = 2.4 \times 10^6$ , [18 12] roughness, $x/c = 0.44$ , 6.0–6.2-Hz bandpass. Lines are 10% contours of the maximum in this band. . . . .	102
67	Mean-flow velocity profiles, $Re_c = 2.4 \times 10^6$ , [18 12] roughness, $x/c = 0.45$ , $z = 75$ –86 mm. . . . .	102
68	Mean-flow velocity contours, $Re_c = 2.4 \times 10^6$ , [18 12] roughness, $x/c = 0.45$ , contour lines at $U/U_{edge} = 0.10, 0.20, \dots, 0.90$ . . . . .	103
69	Fluctuating-velocity spectra, $Re_c = 2.4 \times 10^6$ , [18 12] roughness, $x/c = 0.45$ , $z = 76$ mm. . . . .	103
70	Fluctuating-velocity spectra, $Re_c = 2.4 \times 10^6$ , [18 12] roughness, $x/c = 0.45$ , $z = 79$ mm. . . . .	104
71	Fluctuating-velocity spectra, $Re_c = 2.4 \times 10^6$ , [18 12] roughness, $x/c = 0.45$ , $z = 82$ mm. . . . .	104

72	6.1-kHz velocity-fluctuation rms distribution, $Re_c = 2.4 \times 10^6$ , [18 12] roughness, $x/c = 0.45$ , 6.0–6.2-Hz bandpass. Lines are 10% contours of the maximum in this band. . . . .	105
73	Mean-flow velocity profiles, $Re_c = 2.4 \times 10^6$ , [18 12] roughness, $x/c = 0.46$ , $z = 71$ –82 mm. . . . .	105
74	Mean-flow velocity contours, $Re_c = 2.4 \times 10^6$ , [18 12] roughness, $x/c = 0.46$ , contour lines at $U/U_{\text{edge}} = 0.10, 0.20, \dots, 0.90$ . . . . .	106
75	Fluctuating-velocity spectra, $Re_c = 2.4 \times 10^6$ , [18 12] roughness, $x/c = 0.46$ , $z = 72$ mm. . . . .	106
76	Fluctuating-velocity spectra, $Re_c = 2.4 \times 10^6$ , [18 12] roughness, $x/c = 0.46$ , $z = 75$ mm. . . . .	107
77	Fluctuating-velocity spectra, $Re_c = 2.4 \times 10^6$ , [18 12] roughness, $x/c = 0.46$ , $z = 78$ mm. . . . .	107
78	Total velocity-fluctuation rms distribution, $Re_c = 2.4 \times 10^6$ , [18 12] roughness, $x/c = 0.46$ , 20 Hz–8.0-kHz bandpass. Lines are 10% contours of the maximum rms fluctuations. . . . .	108
79	Mean-flow velocity profiles, $Re_c = 2.4 \times 10^6$ , [18 12] roughness, $x/c = 0.47$ , $z = 68$ –79 mm. . . . .	108
80	Mean-flow velocity contours, $Re_c = 2.4 \times 10^6$ , [18 12] roughness, $x/c = 0.47$ , contour lines at $U/U_{\text{edge}} = 0.10, 0.20, \dots, 0.90$ . . . . .	109
81	Mean-flow velocity profiles, $Re_c = 2.4 \times 10^6$ , [18 12] roughness, $x/c = 0.48$ , $z = 64$ –75 mm. . . . .	109
82	Mean-flow velocity contours, $Re_c = 2.4 \times 10^6$ , [18 12] roughness, $x/c = 0.48$ , contour lines at $U/U_{\text{edge}} = 0.10, 0.20, \dots, 0.90$ . . . . .	110
83	Fluctuating-velocity spectra, $Re_c = 2.4 \times 10^6$ , [18 12] roughness, $x/c = 0.48$ , $z = 65$ mm. . . . .	110
84	Fluctuating-velocity spectra, $Re_c = 2.4 \times 10^6$ , [18 12] roughness, $x/c = 0.48$ , $z = 68$ mm. . . . .	111
85	Fluctuating-velocity spectra, $Re_c = 2.4 \times 10^6$ , [18 12] roughness, $x/c = 0.48$ , $z = 71$ mm. . . . .	111
86	Fluctuating-velocity spectra, $Re_c = 2.4 \times 10^6$ , [18 12] roughness, $x/c = 0.48$ , $z = 74$ mm. . . . .	112
87	Velocity-fluctuation rms growth, $Re_c = 2.4 \times 10^6$ , [18 12] roughness. . . . .	112
88	Mean-flow velocity contours, $Re_c = 2.4 \times 10^6$ , [54 12] roughness, $x/c = 0.25$ , contour lines at $U/U_{\text{edge}} = 0.10, 0.20, \dots, 0.90$ . . . . .	113
89	Fluctuating-velocity spectra, $Re_c = 2.4 \times 10^6$ , [54 12] roughness, $x/c = 0.25$ , $z = 118.6$ mm. . . . .	113
90	Fluctuating-velocity spectra, $Re_c = 2.4 \times 10^6$ , [54 12] roughness, $x/c = 0.25$ , $z = 122.2$ mm. . . . .	114
91	Fluctuating-velocity spectra, $Re_c = 2.4 \times 10^6$ , [54 12] roughness, $x/c = 0.25$ , $z = 125.8$ mm. . . . .	114
92	Mean-flow velocity contours, $Re_c = 2.4 \times 10^6$ , [54 12] roughness, $x/c = 0.30$ , contour lines at $U/U_{\text{edge}} = 0.10, 0.20, \dots, 0.90$ . . . . .	115
93	Fluctuating-velocity spectra, $Re_c = 2.4 \times 10^6$ , [54 12] roughness, $x/c = 0.30$ , $z = 107$ mm. . . . .	115
94	Fluctuating-velocity spectra, $Re_c = 2.4 \times 10^6$ , [54 12] roughness, $x/c = 0.30$ , $z = 110$ mm. . . . .	116

95	Fluctuating-velocity spectra, $Re_c = 2.4 \times 10^6$ , [54 12] roughness, $x/c = 0.30$ , $z = 113$ mm. . . . .	116
96	200-Hz velocity-fluctuation rms distribution, $Re_c = 2.4 \times 10^6$ , [54 12] roughness, $x/c = 0.30$ , 100–300-Hz bandpass. Lines are 10% contours of the maximum in this band. . . . .	117
97	Mean-flow velocity contours, $Re_c = 2.4 \times 10^6$ , [54 12] roughness, $x/c = 0.34$ , contour lines at $U/U_{edge} = 0.10, 0.20, \dots, 0.90$ . . . . .	117
98	Fluctuating-velocity spectra, $Re_c = 2.4 \times 10^6$ , [54 12] roughness, $x/c = 0.34$ , $z = 101$ mm. . . . .	118
99	Fluctuating-velocity spectra, $Re_c = 2.4 \times 10^6$ , [54 12] roughness, $x/c = 0.34$ , $z = 104$ mm. . . . .	118
100	Fluctuating-velocity spectra, $Re_c = 2.4 \times 10^6$ , [54 12] roughness, $x/c = 0.34$ , $z = 107$ mm. . . . .	119
101	200-Hz velocity-fluctuation rms distribution, $Re_c = 2.4 \times 10^6$ , [54 12] roughness, $x/c = 0.34$ , 100–300-Hz bandpass. Lines are 10% contours of the maximum in this band. . . . .	119
102	3.0-kHz velocity-fluctuation rms distribution, $Re_c = 2.4 \times 10^6$ , [54 12] roughness, $x/c = 0.34$ , 2.9–3.1-kHz bandpass. Lines are 10% contours of the maximum in this band. . . . .	120
103	Mean-flow velocity contours, $Re_c = 2.4 \times 10^6$ , [54 12] roughness, $x/c = 0.38$ , contour lines at $U/U_{edge} = 0.10, 0.20, \dots, 0.90$ . . . . .	120
104	Fluctuating-velocity spectra, $Re_c = 2.4 \times 10^6$ , [54 12] roughness, $x/c = 0.38$ , $z = 88$ mm. . . . .	121
105	Fluctuating-velocity spectra, $Re_c = 2.4 \times 10^6$ , [54 12] roughness, $x/c = 0.38$ , $z = 91$ mm. . . . .	121
106	Fluctuating-velocity spectra, $Re_c = 2.4 \times 10^6$ , [54 12] roughness, $x/c = 0.38$ , $z = 94$ mm. . . . .	122
107	200-Hz velocity-fluctuation rms distribution, $Re_c = 2.4 \times 10^6$ , [54 12] roughness, $x/c = 0.38$ , 100–300-Hz bandpass. Lines are 10% contours of the maximum in this band. . . . .	122
108	3.0-kHz velocity-fluctuation rms distribution, $Re_c = 2.4 \times 10^6$ , [54 12] roughness, $x/c = 0.38$ , 2.9–3.1-Hz bandpass. Lines are 10% contours of the maximum in this band. . . . .	123
109	6.1-kHz velocity-fluctuation rms distribution, $Re_c = 2.4 \times 10^6$ , [54 12] roughness, $x/c = 0.38$ , 6.0–6.2-kHz bandpass. Lines are 10% contours of the maximum in this band. . . . .	123
110	Mean-flow velocity contours, $Re_c = 2.4 \times 10^6$ , [54 12] roughness, $x/c = 0.39$ , contour lines at $U/U_{edge} = 0.10, 0.20, \dots, 0.90$ . . . . .	124
111	Fluctuating-velocity spectra, $Re_c = 2.4 \times 10^6$ , [54 12] roughness, $x/c = 0.39$ , $z = 86$ mm. . . . .	124
112	Fluctuating-velocity spectra, $Re_c = 2.4 \times 10^6$ , [54 12] roughness, $x/c = 0.39$ , $z = 89$ mm. . . . .	125
113	Fluctuating-velocity spectra, $Re_c = 2.4 \times 10^6$ , [54 12] roughness, $x/c = 0.39$ , $z = 92$ mm. . . . .	125
114	200-Hz velocity-fluctuation rms distribution, $Re_c = 2.4 \times 10^6$ , [54 12] roughness, $x/c = 0.39$ , 100–300-Hz bandpass. Lines are 10% contours of the maximum in this band. . . . .	126

115	3.0-kHz velocity-fluctuation rms distribution, $Re_c = 2.4 \times 10^6$ , [54 12] roughness, $x/c = 0.39$ , 2.9–3.1-kHz bandpass. Lines are 10% contours of the maximum in this band. . . . .	126
116	6.1-kHz velocity-fluctuation rms distribution, $Re_c = 2.4 \times 10^6$ , [54 12] roughness, $x/c = 0.39$ , 6.0–6.2-kHz bandpass. Lines are 10% contours of the maximum in this band. . . . .	127
117	Mean-flow velocity contours, $Re_c = 2.4 \times 10^6$ , [54 12] roughness, $x/c = 0.40$ , contour lines at $U/U_{edge} = 0.10, 0.20, \dots, 0.90$ . . . . .	127
118	Fluctuating-velocity spectra, $Re_c = 2.4 \times 10^6$ , [54 12] roughness, $x/c = 0.40$ , $z = 82$ mm. . . . .	128
119	Fluctuating-velocity spectra, $Re_c = 2.4 \times 10^6$ , [54 12] roughness, $x/c = 0.40$ , $z = 85$ mm. . . . .	128
120	Fluctuating-velocity spectra, $Re_c = 2.4 \times 10^6$ , [54 12] roughness, $x/c = 0.40$ , $z = 88$ mm. . . . .	129
121	Total velocity-fluctuation rms distribution, $Re_c = 2.4 \times 10^6$ , [54 12] roughness, $x/c = 0.40$ , 20 Hz–8.0-kHz bandpass. Lines are 10% contours of the maximum rms fluctuations. . . . .	129
122	Velocity-fluctuation rms growth, $Re_c = 2.4 \times 10^6$ , [54 12] roughness. . . . .	130
123	Mean-flow velocity contours, $Re_c = 2.0 \times 10^6$ , [54 12] roughness, $x/c = 0.40$ , contour lines at $U/U_{edge} = 0.10, 0.20, \dots, 0.90$ . . . . .	130
124	Fluctuating-velocity spectra, $Re_c = 2.0 \times 10^6$ , [54 12] roughness, $x/c = 0.40$ , $z = 136.4$ mm. . . . .	131
125	Fluctuating-velocity spectra, $Re_c = 2.0 \times 10^6$ , [54 12] roughness, $x/c = 0.40$ , $z = 138.8$ mm. . . . .	131
126	Fluctuating-velocity spectra, $Re_c = 2.0 \times 10^6$ , [54 12] roughness, $x/c = 0.40$ , $z = 141.2$ mm. . . . .	132
127	200-Hz velocity-fluctuation rms distribution, $Re_c = 2.0 \times 10^6$ , [54 12] roughness, $x/c = 0.40$ , 100–300-Hz bandpass. Lines are 10% contours of the maximum in this band. . . . .	132
128	Mean-flow velocity contours, $Re_c = 2.0 \times 10^6$ , [54 12] roughness, $x/c = 0.46$ , contour lines at $U/U_{edge} = 0.10, 0.20, \dots, 0.90$ . . . . .	133
129	Fluctuating-velocity spectra, $Re_c = 2.0 \times 10^6$ , [54 12] roughness, $x/c = 0.46$ , $z = 116.4$ mm. . . . .	133
130	Fluctuating-velocity spectra, $Re_c = 2.0 \times 10^6$ , [54 12] roughness, $x/c = 0.46$ , $z = 118.8$ mm. . . . .	134
131	Fluctuating-velocity spectra, $Re_c = 2.0 \times 10^6$ , [54 12] roughness, $x/c = 0.46$ , $z = 121.2$ mm. . . . .	134
132	200-Hz velocity-fluctuation rms distribution, $Re_c = 2.0 \times 10^6$ , [54 12] roughness, $x/c = 0.46$ , 100–300-Hz bandpass. Lines are 10% contours of the maximum in this band. . . . .	135
133	2.4-kHz velocity-fluctuation rms distribution, $Re_c = 2.0 \times 10^6$ , [54 12] roughness, $x/c = 0.46$ , 2.3–2.5-kHz bandpass. Lines are 10% contours of the maximum in this band. . . . .	135
134	Mean-flow velocity contours, $Re_c = 2.0 \times 10^6$ , [54 12] roughness, $x/c = 0.50$ , contour lines at $U/U_{edge} = 0.10, 0.20, \dots, 0.90$ . . . . .	136
135	Fluctuating-velocity spectra, $Re_c = 2.0 \times 10^6$ , [54 12] roughness, $x/c = 0.50$ , $z = 103.8$ mm. . . . .	136



136	Fluctuating-velocity spectra, $Re_c = 2.0 \times 10^6$ , [54 12] roughness, $x/c = 0.50$ , $z = 106.2$ mm. . . . .	137
137	Fluctuating-velocity spectra, $Re_c = 2.0 \times 10^6$ , [54 12] roughness, $x/c = 0.50$ , $z = 108.6$ mm. . . . .	137
138	200-Hz velocity-fluctuation rms distribution, $Re_c = 2.0 \times 10^6$ , [54 12] roughness, $x/c = 0.50$ , 100–300-Hz bandpass. Lines are 10% contours of the maximum in this band. . . . .	138
139	2.4-kHz velocity-fluctuation rms distribution, $Re_c = 2.0 \times 10^6$ , [54 12] roughness, $x/c = 0.50$ , 2.3–2.5-kHz bandpass. Lines are 10% contours of the maximum in this band. . . . .	138
140	4.9-kHz velocity-fluctuation rms distribution, $Re_c = 2.0 \times 10^6$ , [54 12] roughness, $x/c = 0.50$ , 4.8–5.0-kHz bandpass. Lines are 10% contours of the maximum in this band. . . . .	139
141	Mean-flow velocity contours, $Re_c = 2.0 \times 10^6$ , [54 12] roughness, $x/c = 0.55$ , contour lines at $U/U_{edge} = 0.10, 0.20, \dots, 0.90$ . . . . .	139
142	Fluctuating-velocity spectra, $Re_c = 2.0 \times 10^6$ , [54 12] roughness, $x/c = 0.55$ , $z = 85.6$ mm. . . . .	140
143	Fluctuating-velocity spectra, $Re_c = 2.0 \times 10^6$ , [54 12] roughness, $x/c = 0.55$ , $z = 88.0$ mm. . . . .	140
144	Fluctuating-velocity spectra, $Re_c = 2.0 \times 10^6$ , [54 12] roughness, $x/c = 0.55$ , $z = 90.4$ mm. . . . .	141
145	200-Hz velocity-fluctuation rms distribution, $Re_c = 2.0 \times 10^6$ , [54 12] roughness, $x/c = 0.55$ , 100–300-Hz bandpass. Lines are 10% contours of the maximum in this band. . . . .	141
146	2.4-kHz velocity-fluctuation rms distribution, $Re_c = 2.0 \times 10^6$ , [54 12] roughness, $x/c = 0.55$ , 2.3–2.5-kHz bandpass. Lines are 10% contours of the maximum in this band. . . . .	142
147	4.9-kHz velocity-fluctuation rms distribution, $Re_c = 2.0 \times 10^6$ , [54 12] roughness, $x/c = 0.55$ , 4.8–5.0-kHz bandpass. Lines are 10% contours of the maximum in this band. . . . .	142
148	7.5-kHz velocity-fluctuation rms distribution, $Re_c = 2.0 \times 10^6$ , [54 12] roughness, $x/c = 0.55$ , 7.4–7.6-kHz bandpass. Lines are 10% contours of the maximum in this band. . . . .	143
149	Mean-flow velocity contours, $Re_c = 2.0 \times 10^6$ , [54 12] roughness, $x/c = 0.57$ , contour lines at $U/U_{edge} = 0.10, 0.20, \dots, 0.90$ . . . . .	143
150	Fluctuating-velocity spectra, $Re_c = 2.0 \times 10^6$ , [54 12] roughness, $x/c = 0.57$ , $z = 77.8$ mm. . . . .	144
151	Fluctuating-velocity spectra, $Re_c = 2.0 \times 10^6$ , [54 12] roughness, $x/c = 0.57$ , $z = 80.2$ mm. . . . .	144
152	Fluctuating-velocity spectra, $Re_c = 2.0 \times 10^6$ , [54 12] roughness, $x/c = 0.57$ , $z = 82.6$ mm. . . . .	145
153	Total velocity-fluctuation rms distribution, $Re_c = 2.0 \times 10^6$ , [54 12] roughness, $x/c = 0.57$ , 20-Hz–12.0-kHz bandpass. Lines are 10% contours of the maximum rms fluctuations. . . . .	145
154	Velocity-fluctuation rms growth, $Re_c = 2.0 \times 10^6$ , [54 12] roughness. . . . .	146
155	Mean-flow velocity contours, $Re_c = 2.8 \times 10^6$ , [54 12] roughness, $x/c = 0.30$ , contour lines at $U/U_{edge} = 0.10, 0.20, \dots, 0.90$ . . . . .	146

156	Fluctuating-velocity spectra, $Re_c = 2.8 \times 10^6$ , [54 12] roughness, $x/c = 0.30$ , $z = 80.2$ mm. . . . .	147
157	Fluctuating-velocity spectra, $Re_c = 2.8 \times 10^6$ , [54 12] roughness, $x/c = 0.30$ , $z = 82.6$ mm. . . . .	147
158	Fluctuating-velocity spectra, $Re_c = 2.8 \times 10^6$ , [54 12] roughness, $x/c = 0.30$ , $z = 85.0$ mm. . . . .	148
159	Fluctuating-velocity spectra, $Re_c = 2.8 \times 10^6$ , [54 12] roughness, $x/c = 0.30$ , $z = 87.4$ mm. . . . .	148
160	300-Hz velocity-fluctuation rms distribution, $Re_c = 2.8 \times 10^6$ , [54 12] roughness, $x/c = 0.30$ , 200–400-Hz bandpass. Lines are 10% contours of the maximum in this band. . . . .	149
161	3.6-kHz velocity-fluctuation rms distribution, $Re_c = 2.8 \times 10^6$ , [54 12] roughness, $x/c = 0.30$ , 3.5–3.7-kHz bandpass. Lines are 10% contours of the maximum in this band. . . . .	149
162	Mean-flow velocity contours, $Re_c = 2.8 \times 10^6$ , [54 12] roughness, $x/c = 0.35$ , contour lines at $U/U_{edge} = 0.10, 0.20, \dots, 0.90$ . . . . .	150
163	Fluctuating-velocity spectra, $Re_c = 2.8 \times 10^6$ , [54 12] roughness, $x/c = 0.35$ , $z = 66$ mm. . . . .	150
164	Fluctuating-velocity spectra, $Re_c = 2.8 \times 10^6$ , [54 12] roughness, $x/c = 0.35$ , $z = 68$ mm. . . . .	151
165	Fluctuating-velocity spectra, $Re_c = 2.8 \times 10^6$ , [54 12] roughness, $x/c = 0.35$ , $z = 70$ mm. . . . .	151
166	Fluctuating-velocity spectra, $Re_c = 2.8 \times 10^6$ , [54 12] roughness, $x/c = 0.35$ , $z = 72$ mm. . . . .	152
167	300-Hz velocity-fluctuation rms distribution, $Re_c = 2.8 \times 10^6$ , [54 12] roughness, $x/c = 0.35$ , 200–400-Hz bandpass. Lines are 10% contours of the maximum in this band. . . . .	152
168	3.6-kHz velocity-fluctuation rms distribution, $Re_c = 2.8 \times 10^6$ , [54 12] roughness, $x/c = 0.35$ , 3.5–3.7-kHz bandpass. Lines are 10% contours of the maximum in this band. . . . .	153
169	6.5-kHz velocity-fluctuation rms distribution, $Re_c = 2.8 \times 10^6$ , [54 12] roughness, $x/c = 0.35$ , 6.4–6.6 kHz bandpass. Lines are 10% contours of the maximum in this band. . . . .	153
170	Mean-flow velocity contours, $Re_c = 2.8 \times 10^6$ , [54 12] roughness, $x/c = 0.37$ , contour lines at $U/U_{edge} = 0.10, 0.20, \dots, 0.90$ . . . . .	154
171	Fluctuating-velocity spectra, $Re_c = 2.8 \times 10^6$ , [54 12] roughness, $x/c = 0.37$ , $z = 61$ mm. . . . .	154
172	Fluctuating-velocity spectra, $Re_c = 2.8 \times 10^6$ , [54 12] roughness, $x/c = 0.37$ , $z = 63$ mm. . . . .	155
173	Fluctuating-velocity spectra, $Re_c = 2.8 \times 10^6$ , [54 12] roughness, $x/c = 0.37$ , $z = 65$ mm. . . . .	155
174	Fluctuating-velocity spectra, $Re_c = 2.8 \times 10^6$ , [54 12] roughness, $x/c = 0.37$ , $z = 67$ mm. . . . .	156
175	3.6-kHz velocity-fluctuation rms distribution, $Re_c = 2.8 \times 10^6$ , [54 12] roughness, $x/c = 0.37$ , 3.5 kHz–3.7-kHz bandpass. Lines are 10% contours of the maximum in this band. . . . .	156

176	6.5-kHz velocity-fluctuation rms distribution, $Re_c = 2.8 \times 10^6$ , [54 12] roughness, $x/c = 0.37$ , 6.4 kHz–6.6-kHz bandpass. Lines are 10% contours of the maximum in this band. . . . .	157
177	Mean-flow velocity contours, $Re_c = 2.8 \times 10^6$ , [54 12] roughness, $x/c = 0.38$ , contour lines at $U/U_{edge} = 0.10, 0.20, \dots, 0.90$ . . . . .	157
178	Fluctuating-velocity spectra, $Re_c = 2.8 \times 10^6$ , [54 12] roughness, $x/c = 0.385$ , $z = 58$ mm. . . . .	158
179	Fluctuating-velocity spectra, $Re_c = 2.8 \times 10^6$ , [54 12] roughness, $x/c = 0.385$ , $z = 60$ mm. . . . .	158
180	Fluctuating-velocity spectra, $Re_c = 2.8 \times 10^6$ , [54 12] roughness, $x/c = 0.385$ , $z = 62$ mm. . . . .	159
181	Fluctuating-velocity spectra, $Re_c = 2.8 \times 10^6$ , [54 12] roughness, $x/c = 0.385$ , $z = 64$ mm. . . . .	159
182	Total velocity-fluctuation rms distribution, $Re_c = 2.8 \times 10^6$ , [54 12] roughness, $x/c = 0.385$ , 20-Hz–12.0-kHz bandpass. Lines are 10% contours of the maximum rms fluctuations. . . . .	160
183	Velocity-fluctuation rms growth, $Re_c = 2.8 \times 10^6$ , [54 12] roughness. . . . .	160
184	Spanwise mean-flow hotwire scan with and without activated 12-mm-spaced artificial roughness, $Re_c = 2.4 \times 10^6$ , $x/c = 0.40$ , $Y = 1.5$ mm. . . . .	161
185	Power spectral density of the spanwise mean-flow hotwire scan with and without activated 12-mm-spaced artificial roughness, $Re_c = 2.4 \times 10^6$ , $x/c = 0.40$ , $Y = 1.5$ mm. . . . .	161
186	Spanwise mean-flow hotwire scan with and without activated 12-mm-spaced artificial roughness, $Re_c = 2.4 \times 10^6$ , $x/c = 0.43$ , $Y = 2.0$ mm. . . . .	162
187	Power spectral density of the spanwise mean-flow hotwire scan with and without activated 12-mm-spaced artificial roughness, $Re_c = 2.4 \times 10^6$ , $x/c = 0.43$ , $Y = 2.0$ mm. . . . .	162
188	Spanwise distribution of velocity-fluctuation power spectral density at 3.0 kHz with and without activated 12-mm-spaced artificial roughness, $Re_c = 2.4 \times 10^6$ , $x/c = 0.43$ , $Y = 2.0$ mm. . . . .	163
189	Fluctuating-velocity spectral density with and without activated 12-mm-spaced artificial roughness, $Re_c = 2.4 \times 10^6$ , $x/c = 0.43$ , $Y = 2.0$ mm, $z = 24$ mm. . . . .	163
190	Fluctuating-velocity spectral density with and without activated 12-mm-spaced artificial roughness, $Re_c = 2.4 \times 10^6$ , $x/c = 0.43$ , $Y = 2.0$ mm, $z = 31$ mm. . . . .	164
191	Fluctuating-velocity spectral density with and without activated 12-mm-spaced artificial roughness, $Re_c = 2.4 \times 10^6$ , $x/c = 0.43$ , $Y = 2.0$ mm, $z = 46$ mm. . . . .	164
192	Fluctuating-velocity spectral density with and without activated 12-mm-spaced artificial roughness, $Re_c = 2.4 \times 10^6$ , $x/c = 0.43$ , $Y = 2.0$ mm, $z = 66$ mm. . . . .	165
193	Fluctuating-velocity spectral density with and without activated 12-mm-spaced artificial roughness, $Re_c = 2.4 \times 10^6$ , $x/c = 0.43$ , $Y = 2.0$ mm, $z = 108$ mm. . . . .	165
194	Spanwise mean-flow hotwire scan with and without activated 12-mm-spaced artificial roughness, $Re_c = 2.4 \times 10^6$ , $x/c = 0.45$ , $Y = 2.0$ mm. . . . .	166

195	Power spectral density of the spanwise mean-flow hotwire scan with and without activated 12-mm-spaced artificial roughness, $Re_c = 2.4 \times 10^6$ , $x/c = 0.45$ , $Y = 2.0$ mm. . . . .	166
196	Spanwise distribution of velocity-fluctuation power spectral density at 3.0 kHz with and without activated 12-mm-spaced artificial roughness, $Re_c = 2.4 \times 10^6$ , $x/c = 0.45$ , $Y = 2.0$ mm. . . . .	167
197	Fluctuating-velocity spectral density with and without activated 12-mm-spaced artificial roughness, $Re_c = 2.4 \times 10^6$ , $x/c = 0.45$ , $Y = 2.0$ mm, $z = 60$ mm. . . . .	167
198	Fluctuating-velocity spectral density with and without activated 12-mm-spaced artificial roughness, $Re_c = 2.4 \times 10^6$ , $x/c = 0.45$ , $Y = 2.0$ mm, $z = 60$ mm. . . . .	168
199	Spanwise mean-flow hotwire scan with and without activated 12-mm-spaced artificial roughness, $Re_c = 2.8 \times 10^6$ , $x/c = 0.38$ , $Y = 1.2$ mm. . . . .	168
200	Power spectral density of the spanwise mean-flow hotwire scan with and without activated 12-mm-spaced artificial roughness, $Re_c = 2.8 \times 10^6$ , $x/c = 0.38$ , $Y = 1.2$ mm. . . . .	169
201	Spanwise distribution of velocity-fluctuation power spectral density at 4.0 kHz with and without activated 12-mm-spaced artificial roughness, $Re_c = 2.8 \times 10^6$ , $x/c = 0.38$ , $Y = 1.2$ mm. . . . .	169
202	Fluctuating-velocity spectral density with and without activated 12-mm-spaced artificial roughness, $Re_c = 2.8 \times 10^6$ , $x/c = 0.38$ , $Y = 1.2$ mm, $z = 23$ mm. . . . .	170
203	Fluctuating-velocity spectral density with and without activated 12-mm-spaced artificial roughness, $Re_c = 2.8 \times 10^6$ , $x/c = 0.38$ , $Y = 1.2$ mm, $z = 26$ mm. . . . .	170
204	Fluctuating-velocity spectral density with and without activated 12-mm-spaced artificial roughness, $Re_c = 2.8 \times 10^6$ , $x/c = 0.38$ , $Y = 1.2$ mm, $z = 84$ mm. . . . .	171
205	Spanwise mean-flow hotwire scan with and without activated 12-mm-spaced artificial roughness, $Re_c = 2.8 \times 10^6$ , $x/c = 0.40$ , $Y = 1.2$ mm. . . . .	171
206	Power spectral density of the spanwise mean-flow hotwire scan with and without activated 12-mm-spaced artificial roughness, $Re_c = 2.8 \times 10^6$ , $x/c = 0.40$ , $Y = 1.2$ mm. . . . .	172
207	Spanwise distribution of velocity-fluctuation power spectral density at 4.0 kHz with and without activated 12-mm-spaced artificial roughness, $Re_c = 2.8 \times 10^6$ , $x/c = 0.40$ , $Y = 1.2$ mm. . . . .	172
208	Spanwise mean-flow hotwire scan with and without activated 12-mm-spaced artificial roughness, $Re_c = 2.0 \times 10^6$ , $x/c = 0.58$ , $Y = 2.0$ mm. . . . .	173
209	Power spectral density of the spanwise mean-flow hotwire scan with and without activated 12-mm-spaced artificial roughness, $Re_c = 2.0 \times 10^6$ , $x/c = 0.58$ , $Y = 2.0$ mm. . . . .	173
210	Spanwise distribution of velocity-fluctuation power spectral density at 2.0 kHz with and without activated 12-mm-spaced artificial roughness, $Re_c = 2.0 \times 10^6$ , $x/c = 0.58$ , $Y = 2.0$ mm. . . . .	174
211	Fluctuating-velocity spectral density with and without activated 12-mm-spaced artificial roughness, $Re_c = 2.0 \times 10^6$ , $x/c = 0.58$ , $Y = 2.0$ mm, $z = 16$ mm. . . . .	174

212	Fluctuating-velocity spectral density with and without activated 12-mm-spaced artificial roughness, $Re_c = 2.0 \times 10^6$ , $x/c = 0.58$ , $Y = 2.0$ mm, $z = 53$ mm. . . . .	175
213	Fluctuating-velocity spectral density with and without activated 12-mm-spaced artificial roughness, $Re_c = 2.0 \times 10^6$ , $x/c = 0.58$ , $Y = 2.0$ mm, $z = 103$ mm. . . . .	175
214	Fluctuating-velocity spectral density with and without activated 12-mm-spaced artificial roughness, $Re_c = 2.0 \times 10^6$ , $x/c = 0.58$ , $Y = 2.0$ mm, $z = 107$ mm. . . . .	176
215	Spanwise distribution of velocity-fluctuation power spectral density at 3.0 kHz with and without activated 12-mm-spaced artificial roughness, $Re_c = 2.0 \times 10^6$ , $x/c = 0.58$ , $Y = 2.0$ mm. . . . .	176
216	Spanwise mean-flow hotwire scan with and without activated 12-mm-spaced artificial roughness, $Re_c = 2.0 \times 10^6$ , $x/c = 0.60$ , $Y = 2.0$ mm. . . . .	177
217	Power spectral density of the spanwise mean-flow hotwire scan with and without activated 12-mm-spaced artificial roughness, $Re_c = 2.0 \times 10^6$ , $x/c = 0.60$ , $Y = 2.0$ mm. . . . .	177
218	Spanwise distribution of velocity-fluctuation power spectral density at 2.0 kHz with and without activated 12-mm-spaced artificial roughness, $Re_c = 2.0 \times 10^6$ , $x/c = 0.60$ , $Y = 2.0$ mm. . . . .	178
219	Spanwise distribution of velocity-fluctuation power spectral density at 3.0 kHz with and without activated 12-mm-spaced artificial roughness, $Re_c = 2.0 \times 10^6$ , $x/c = 0.60$ , $Y = 2.0$ mm. . . . .	178

# Chapter 1

## Introduction

### 1.1 Overview and motivation

Boundary-layer transition control for swept wings is a goal that holds tremendous promise for more-efficient aircraft. Swept wings are ubiquitous among both commercial and military jet aircraft and thus represent one of the most important avenues of practical, industrially oriented transition research. Despite the importance of this class of flows and a significant research effort that spans 50 years, the ability to predict transition behavior for general swept-wing aircraft does not exist. Moreover, experience has shown that design choices that can reduce drag due to other influences actually *enhance* the instability mechanism present on swept wings. Thus, conventional approaches to drag reduction often fail for this configuration.

In order to avoid poor designs that could result from an incorrect approach to transition control, what is desired is the ability to predict transition behavior at the design stage, allowing a designer to fully understand the ramifications of various design choices. The result would be fewer design and testing iterations and more-efficient final vehicles. A more optimistic goal is the ability to use such a predictive transition model to suggest a practical transition-control strategy. One of the more promising methods of achieving this sort of control involves using a micro electrical mechanical systems (MEMS) based array of active roughness actuators on a wing's surface. As will be described below, particular roughness patterns on a swept wing play a tremendously important role in the early stages of swept-wing transition, and MEMS actuators offer the possibility of actively controlling this process on fine spatial and temporal scales. This offers the possibility of achieving the tremendous savings possible with laminar flow, estimated to be 25% of the overall vehicle drag if 80% of the wings remain laminar on subsonic commercial and military transport aircraft.

What is particularly promising about using MEMS-based microactuators for swept-wing laminar flow control is that fine control provided by the MEMS actuators will be amplified through the inherent boundary-layer instability to provide a control effect on a much larger scale. This means that the power requirement of the MEMS will likely be many orders of magnitude less than the power savings achieved through drag reduction. (In other boundary-layer control systems such as distributed suction, this is not always the case.) Moreover, the control-system requirements and the total number of actuators required may be quite modest relative to a system that seeks to control a turbulent boundary layer. Through a detailed understanding of the important instability features it may be possible to use a very small number of MEMS devices to achieve control over an entire wing by applying control precisely where it will have the maximum effect. This is in contrast to turbulent

boundary layers where the experience has been that although a MEMS element can reduce drag, it does so only in an area of the same order as the MEMS element itself. This implies that to achieve significant drag reduction of an already turbulent boundary layer, essentially all of a vehicle's skin would need to consist of MEMS actuators. This approach would clearly have enormous manufacturing and maintenance cost and also enormous power requirements, perhaps more than the power that could be saved through such an approach.

If practical control of an unstable laminar boundary layer is to be achieved using MEMS-based actuators, a significant question remains: What is the mechanism that triggers the final breakdown of the laminar flow? Until this stage of the process is understood, transition prediction based on a correct physical model will be impossible.

It is the intent of this work to provide a detailed experimental description of the mechanism or mechanisms that are responsible for the breakdown of laminar flow at the last stage of swept-wing boundary layer transition and, simultaneously, to design, construct, and implement a MEMS-based microactuator system that is capable of controlling the transition process on swept-wings. In the experimental phase, what will be of principal interest is the possibility that breakdown is caused either by a secondary instability or by an absolute instability that is present in the distorted velocity field resulting from the nonlinear primary instability. Both a secondary instability and an absolute instability have been shown to be present in rotating disk flow, the model problem for swept wings, and hence both are candidates for swept-wing breakdown mechanisms. The MEMS actuators will play a significant role in the experimental objectives because they will provide a critical experimental capability as variable roughness elements that will be needed to make this assessment.

## 1.2 Introduction to crossflow transition

The basic features of swept-wing boundary layers are as follows. In the inviscid region outside a swept-wing boundary layer, the combined influences of wing sweep and favorable pressure gradient produce curved streamlines at the boundary-layer edge. Inside the boundary layer the streamwise fluid velocity is reduced but the pressure gradient is unchanged. Thus, within the boundary layer, a balance between centripetal acceleration of the fluid elements and the external pressure gradient does not exist, and a secondary flow results. This secondary flow is directed perpendicular to the external streamline, toward the streamline's center of curvature, and it is therefore referred to as crossflow. Upstream of the pressure minimum, the crossflow is directed inboard (for standard swept-back configurations). Downstream of the pressure minimum, the crossflow is outboard. A schematic of a crossflow-producing streamline is shown in Figure 1. The associated streamwise, crossflow, and resolved boundary-layer velocity profiles are shown in Figure 2. Notice that the crossflow velocity is zero at the wall where the no-slip condition applies, and it approaches zero at the boundary-layer edge where pressure gradient and streamline curvature balance. Because of these boundary conditions, the crossflow velocity profile has an inflection point. It is well known that an inflection point in a boundary layer is a sufficient condition for an inviscid instability. This means that the transition behavior for swept wings is fundamentally different from that of unswept wings because the unswept configuration is subject to the viscous Tollmien-Schlichting (T-S) instability mechanism.

The fact that swept-wing boundary layers are subject to a different type of instability was first discovered by Gray (1952) during a flow-visualization flight test experiment. Soon thereafter, Gregory, Stuart & Walker (1955) produced their classic work that shows the same crossflow instability mechanism is also present for rotating disk boundary layers. In

both configurations, the instability is manifested as a series of vortices that are aligned to within a few degrees of the inviscid streamlines. Both traveling and stationary ( $f = 0$ ) modes are amplified, and according to linear theory the most amplified mode is a traveling mode. Despite this, in nearly all experiments that approach flight conditions (i.e., with low freestream turbulence levels), a stationary mode, not the most amplified traveling mode, is observed to dominate transition. There are two reasons for this. First, receptivity theory shows that in low-disturbance environments the initial amplitudes of stationary disturbances are much larger than those of traveling disturbances. Second, because the stationary vortices are nearly aligned with the inviscid streamlines, the same  $u', v'$  disturbance acts on a fluid element along its entire trajectory. The result is a strong integrated effect that results in significant mean-flow modification, despite the relatively low amplitude of the stationary disturbance. The fact that modification of the boundary layer occurs means that its stability is not well described by linear theory. Instead a nonlinear model is required to understand crossflow boundary-layer stability for nearly the entire boundary layer. It is the importance of nonlinearities that makes crossflow such a challenging problem.

A number of reviews of crossflow stability research are available. Summaries of recent experimental results are provided by Bippes (1999); Saric, Carrillo & Reibert (1998); and Reibert & Saric (1997). Other related reviews are provided by Arnal (1997), Reshotko (1997), Crouch (1997), Herbert (1997*a,b*), and Kachanov (1996). The historical work is surveyed by Reed & Saric (1989). In the remainder of this section, the previous results that are most important for the current work are discussed. The literature covered in this chapter only includes those works that involve receptivity and the primary crossflow instability. Chapters 3 and 4 include independent literature reviews for the secondary and absolute instabilities, respectively.

### 1.2.1 Receptivity

Receptivity describes the collection of phenomena by which disturbances enter a boundary layer and provide the initial condition for growing disturbances. Common sources of receptivity are freestream sound and turbulence, surface roughness, and surface geometry. What is common to these parameters is that they all provide some means for generating boundary-layer-scale features from globally scaled disturbances. Over the past decade the experimental and computational approaches to receptivity have been rather divergent. The experiments have consisted of parametric studies of how freestream turbulence and surface roughness affect the transition location, whereas theoretical studies have focused on the effectiveness of various features of periodic surface roughness and on freestream acoustic (not turbulent) fluctuations.

The effect of freestream turbulence was investigated by Deyhle & Bippes (1996), who performed transition measurements on a crossflow-dominated swept-plate model in a number of different wind-tunnel facilities with varying freestream turbulence levels. They found that for turbulence intensities above  $Tu = 0.0015$ , where  $Tu = \sqrt{\frac{1}{3}(u'^2 + v'^2 + w'^2)}/U_\infty$ , transition is dominated by traveling waves, but that for lower turbulence levels, stationary waves dominate. Surprisingly, for increased turbulence levels where traveling waves dominate but the turbulence intensity is not too high,  $0.0015 < Tu < 0.0020$ , transition is actually *delayed* relative to low-turbulence cases at the same Reynolds number. This behavior means that wind-tunnel transition results may have no bearing on flight results if the wind tunnel has a moderate or high turbulence level and traveling waves dominate transition.



The receptivity mechanism for the stationary vortices that are important for transition in low-disturbance environments is surface roughness. This was conclusively established by Müller & Bippes (1989), who translated a swept flat-plate model relative to the test section and found that the recurring stationary transition pattern translated with the model. Therefore the instability features had to be related to model roughness rather than to fixed features of the freestream flow generated by nonuniformities of the screens or other effects. Juillen & Arnal (1990) find that for isolated roughness elements the von Doenhoff & Braslow (1961) correlation that describes the limit for bypass transition is correct.

Roughness studies by Radeztsky, Reibert & Saric (1999) show that the characteristics of isolated 3-D roughness play a very important role in transition behavior. Roughness is most effective at generating crossflow disturbances at or just upstream of the neutral point,  $x/c = 0.02$  in Radeztsky *et al.*'s experiment. The roughness diameter must be greater than 10% of the most amplified stationary wavelength to be effective, and the transition location is quite sensitive to roughness height even for roughness Reynolds numbers as low as  $Re_k = 0.1$ . Natural surface-roughness amplitude can also play a significant role in transition location. Radeztsky *et al.* (1999) find that a decrease in surface-roughness amplitude from  $9.0\text{ }\mu\text{m}$  rms to  $0.5\text{ }\mu\text{m}$  rms delays transition from  $x/c = 0.40$  to  $0.61$  for  $Re_c = 2.7 \times 10^6$ . Another decrease to  $0.25\text{ }\mu\text{m}$  rms delays transition even further to  $x/c = 0.68$ . Radeztsky *et al.* (1999) also determine that transition behavior is insensitive to sound even at amplitudes as high as 95 dB.

A number of theoretical and computational approaches to swept-wing boundary-layer receptivity have been applied. Some of the more recent include an adjoint equation approach by Fedorov (1989), a PSE approach by Herbert & Lin (1993), and a DNS approach by Spalart (1993). Crouch (1994) and Choudhari (1994) both consider the receptivity of Falkner-Skan-Cooke (FSC) boundary layers as perturbations of a parallel boundary layer. The framework of their approaches allowed both the surface roughness and acoustic freestream disturbances to be considered as receptivity sources. Choudhari (1994) extends his work to consider acoustic-wave-angle effects and a variety of different roughness configurations including isolated roughness, roughness arrays and lattices, and distributed random roughness. Crouch (1994) emphasizes a framework equally applicable to T-S and crossflow disturbances. Both authors note that because traveling-wave receptivity scales with two small parameters, the freestream velocity-fluctuation amplitude and surface-roughness amplitude, whereas the stationary-wave receptivity scales with only one, the surface roughness, it can be expected that stationary waves will dominate for low-disturbance environments and that traveling waves will only appear for large freestream acoustic variations. The experiments of Radeztsky *et al.* (1999) confirm this expectation.

A more recent approach by Collis & Lele (1999) begins by solving the steady Navier-Stokes equations in the leading-edge region of a swept parabolic body and then using that solution as a basic state for a linearized steady disturbance system that includes surface roughness. Comparing the results of this approach to those obtained by Choudhari (1994) and Crouch (1994) shows that receptivity to surface roughness is enhanced by convex surface curvature and suppressed by nonparallelism. Neglecting nonparallelism causes the local approach to overpredict receptivity by as much as 77% for the most amplified stationary crossflow wavenumber. The error introduced by neglecting nonparallelism is most severe for wavelengths in the range most amplified by the crossflow instability and for roughness close to the first neutral point. The implication is that amplitude-based transition-prediction methods need to employ a receptivity model that includes nonparallelism because the cross-flow modes that dominate transition are most strongly affected by this influence.

What is not considered in any of the receptivity models is freestream turbulence. Sound has been considered, but it is known not to be important. However, the DLR Göttingen group has shown that turbulence can be very important above a certain threshold, but no models exist that predict this behavior.

### 1.2.2 Primary instability

The primary crossflow instability has been extensively studied in a number of experiments over the past decade. The key findings are those listed above: the instability modes are traveling and stationary vortices that are nearly aligned with the inviscid streamlines, stationary modes dominate in low-disturbance environments, and nonlinear effects appear early in the development of the boundary layer. The first experiment that demonstrated the importance of nonlinearities was that of Saric & Yeats (1985), which identified harmonics of the fundamental stationary mode on a swept flat plate with a pressure gradient. Further work using swept plates has been extensively carried out at DLR. These experiments verify that linear theory is correct for traveling-wave-dominated boundary layers (see Bippes, 1999, for a summary). In contrast, experiments at the Arizona State University Unsteady Wind Tunnel on a  $45^\circ$  swept wing by Reibert, Saric, Carrillo & Chapman (1996) and Saric, Carrillo & Reibert (1998) show that the stationary modes are not correctly described by linear theory. Using spanwise arrays of artificial roughness near the leading edge to perform modal-growth studies, Reibert *et al.* (1996) show that when the most amplified stationary mode is forced, amplitude saturation occurs well upstream of the transition location, where linear theory indicates that the stationary mode should still be strongly amplified. The amplitude at which the fundamental mode saturates depends only on Reynolds number and the mode's wavelength; it is independent of the initial amplitude. In addition to amplitude saturation, another nonlinear feature is the growth of harmonics. When 12-mm-spaced roughness arrays are applied, 12-mm, 6-mm, 4-mm, and 3-mm stationary waves are observed downstream. However, no subharmonics (e.g., 24- or 36-mm waves) are detected.

Using the information regarding the nonlinear behavior of the stationary waves, Saric *et al.* (1998) discovered that crossflow transition can actually be suppressed using subcritically spaced roughness arrays. The idea is that forcing a stationary mode with a wavelength shorter than the most amplified wave will produce only short wavelength modes, none in the longer, more amplified wavelength band. Because the deformation of the mean flow that results from the addition of the short-wavelength roughness changes the stability of the boundary layer, what results is a boundary layer with rather large amplitude spanwise periodicity of the input wavelength that is stable to the longer-wavelength stationary modes. The most amplified waves never appear and transition is suppressed. Saric *et al.* (1998) were able to delay transition well past the pressure minimum at  $x/c = 0.71$  on the  $45^\circ$  swept-wing model using 6- $\mu$ m-high, 8-mm-spaced roughness at  $Re_c = 2.4 \times 10^6$ , where the most amplified stationary wavelength is about 12 mm. The transition location was even downstream of where it occurs for a highly polished leading edge without artificial roughness. This result is quite exciting because it provides the possibility of completely passive crossflow transition control.

Many of the computational works include both primary stability calculations and secondary stability calculations that address the behavior of high-frequency fluctuations present in the saturated primary disturbance field. Papers that include both calculations are covered in two parts: the primary stability calculations are discussed here and the secondary stability calculations are discussed later in Section 3.1.

What has proven to be the most effective means of modeling the crossflow instability is an approach using nonlinear parabolized stability equations (NPSE). Nonlinear parabolized stability codes incorporate mean-flow modification produced by the stationary vortices and include surface curvature and nonparallel effects. Recently, both Malik, Li, Choudhari & Chang (1999) and Haynes & Reed (2000) have used the NPSE approach to produce excellent computational agreement with the experiments of Reibert *et al.* (1996) that demonstrate the nonlinear growth and saturation of stationary crossflow vortices. The computational results confirm that saturation amplitudes are independent of the initial crossflow amplitude if it is sufficiently high to cause saturation. The NPSE codes further demonstrate that the disturbance growth is sensitive to very weak surface curvature.

An alternative DNS approach to the late transition stages was undertaken by Wintergerste & Kleiser (1996). These computations are an FSC approximation of the DLR swept flat-plate experiment. The emphasis of these calculations was to examine the vortex structure with a more highly resolved grid than the earlier DNS crossflow calculations by Meyer & Kleiser (1989). The approach by Wintergerste & Kleiser (1996) is local, temporal stability with local parameters to match 80% chord:  $R = 826$ , sweep angle  $\phi_e = 46.9^\circ$ , and Hartree parameter  $\beta_H = 0.63$ . These calculations identified the weak vortex that rotates counter to the main stationary crossflow vortex predicted by Malik *et al.* (1994), and they demonstrated breakdown to turbulence soon after, but the results do not appear to produce the secondary instability described below.

### 1.2.3 Implications for $N$ -factor transition prediction

The strategy most often employed for transition prediction is known as the  $e^N$  method, proposed independently by van Ingen (1956) and Smith & Gamberoni (1956). This method consists of finding the envelope of the growth curves of all possible instability modes using linear stability theory. Transition is expected to occur at the first point for which the ratio of any single mode's amplitude to its initial amplitude exceeds a threshold value. The threshold for transition is determined experimentally and is expressed in exponential form, hence  $e^N$ . Typically,  $N \approx 9$  leads to transition, although the  $N$ -factor can vary widely depending on a number of factors. Using this approach, transition experiments are performed either in a wind tunnel or in flight to produce an  $N$ -factor for transition. This  $N$ -factor is then applied to similar configurations in the hope that the value will be accurate enough for design purposes. Typically, wind-tunnel tests at low Reynolds numbers are used to produce  $N$ -factors that are then applied to flight conditions.

Successful implementation of the  $e^N$  method relies on a number of assumptions. The first and most fundamental requirement is that the process by which transition occurs in the baseline experiment must be the same process as that occurring in practice. Second, the method assumes that there is a uniform distribution of initial disturbance amplitudes across all of the relevant instability modes and that the amplitudes in the experiment are equivalent to those in practice. The last assumption is that the growth of the instability modes is accurately described by linear stability theory throughout most of the transition region, although this is the weakest requirement because some degree of nonlinearity may be lumped into the particular  $N$ -factor. However, each of these assumptions is strongly violated in swept-wing transition.

Perhaps the most serious flaw is that the character of the transition process—whether it is dominated by stationary or traveling waves—depends on the magnitude of freestream disturbances. This means that while the transition mechanism in flight is always stationary

waves, in many wind tunnels, traveling waves dominate. So an  $N$ -factor produced under high-disturbance conditions is invalid for low-disturbance conditions. Next is the idea that there is a uniform distribution of initial disturbance amplitudes. This may be valid for traveling crossflow disturbances, but for stationary waves, this depends entirely on the surface of the wing. A laboratory model may be uniformly polished and free from any imperfections, but any wing in service has numerous flaws that produce crossflow waves, and the distribution of these is not known. And finally, the fact that nonlinearities become important very early in the development of the boundary layer and become so important as to cause amplitude saturation means that any method based on linear theory predictions cannot be successful.

### 1.3 Objectives and outline

The most recent series of primary instability experiments conducted by Reibert *et al.* (1996) and Saric *et al.* (1998), and the excellent computational agreement that has been achieved with these results using the NPSE computations of Malik *et al.* (1999) and Haynes & Reed (2000), show that the primary crossflow instability is well understood. What is clear is that the primary crossflow instability is not directly responsible for transition to turbulence. However, it appears that the nonlinear evolution of the primary instability and amplitude saturation result in a spanwise-periodic laminar state in which the primary crossflow modes have stabilized. Therefore, physically correct transition prediction cannot rest on the primary instability alone. In light of this, another transition mechanism is needed to understand why transition occurs where it does. The objective of this work is to determine experimentally what mechanism acts in the final stage of transition to trigger the breakdown to turbulence.

The mechanism responsible clearly acts on the highly distorted boundary layer. Thus understanding this instability represents quite a challenging problem both experimentally and computationally because this aspect of the flow requires that one use the flow that results from the primary instability process as a basic state. So the basic state is itself the result of a highly sensitive instability process that must be very well controlled. This means that all of the care required to perform the previous experiments is only sufficient to provide the initial condition for understanding breakdown.

It appears most likely that breakdown of the laminar flow may be caused by one or both of two separate instabilities: a secondary instability and an absolute instability. The secondary instability consists of high-frequency fluctuations that have been observed just upstream of breakdown in several crossflow experiments. Flow-visualization experiments on rotating disks and for Görtler boundary layers have identified what may be equivalent high-frequency modes, and these instabilities appear to be responsible for transition in those cases, so the existing experimental evidence points to a secondary instability. In light of this, computational models of the phenomenon have been created and these seem to support this view. However, the second possibility, that transition is caused by the presence of an absolute instability, is supported by the fact that an absolute instability has been conclusively demonstrated to exist for rotating disk flows, the model problem for swept-wing boundary layers. Moreover, the results of Reibert *et al.* (1996) show that in certain circumstances the transition location for crossflow is insensitive to the leading-edge roughness amplitude, and insensitivity to initial conditions can frequently be a symptom of an absolute instability. Because of this evidence, both of these mechanisms need to be examined closely if one is to understand the breakdown of crossflow boundary layers.

Given these two possible breakdown mechanisms, the objectives of the current work are as follows. The first is to establish a swept-wing model that provides a crossflow boundary layer with a very well controlled primary instability. The second is to determine if a secondary instability does exist, and if so, to determine under what conditions it becomes unstable, its growth characteristics, and ultimately where it triggers breakdown. The data presented will be suitable for comparison with numerical simulations. The third objective is to determine whether the swept-wing boundary layer shows any evidence of supporting an absolute instability. Although this has been observed in a rotating disk boundary layer, no evidence has been observed for swept wings. However, the absolute instability experiment poses special challenges for maintaining a good basic state, even beyond those of the secondary instability, so it may simply be that the absolute instability experiment could not be performed before now. In parallel with these three experimental objectives, the fourth objective is to design, install and test MEMS-based roughness actuators for use as laminar-flow-control devices on a swept-wing model.

The layout of this document is structured around these four objectives. This introductory chapter has presented a review of the receptivity and primary instability aspects of crossflow stability—features that are important both for the secondary instability and absolute instability experiments. In Chapter 2, a description of the experimental facility, hardware, and techniques that are common to both the secondary instability and absolute instability experiments is presented. That chapter includes a description of the design philosophy of the swept-wing experiment. The philosophy is not restricted to just the present work but encompasses the experience of the last decade of swept-wing experiments. This section also includes a detailed description of the MEMS development efforts. Chapter 3 consists of the investigation of the secondary instability as a crossflow breakdown mechanism. The chapter begins with a review of the literature specific to the secondary instability, then progresses to specific experimental techniques, results, and discussion. Chapter 4 presents the absolute instability in the same manner: a self-contained literature review, experiment description, and results and discussion. Overall conclusions that compare the two instabilities are presented in Chapter 5.

## Chapter 2

# Experimental Design, Facility, and Techniques

### 2.1 General philosophy

The present experiment is the latest in a series at the Arizona State University Unsteady Wind Tunnel involving the stability of crossflow-dominated swept-wing boundary layers. It is to the great advantage of the current work to have inherited much of the approach and physical setup from the previous experiments of Dagenhart (1992), Radeztsky (1994), Reibert (1996), Carrillo (1996), and Chapman (1996). However, two substantial features differentiate this experiment from its predecessors. The first is that the subject of the current experiment is a detailed examination of the *breakdown* stage of crossflow transition, whereas the previous experiments were chiefly concerned with the primary instability behavior or with receptivity to surface roughness. The other principal difference is that the swept-wing model used in all of the previous experiments has been replaced with a new model that incorporates a modular leading edge and provides a pressure contour that is somewhat more advantageous for experimental simplicity. The modular design has great advantages in terms of experimental flexibility, but it has proven to be a challenge to incorporate into a highly sensitive stability experiment.

The old and new swept-wing models share a design philosophy that has its origins with the work of Dagenhart & Saric (1999) (which originally appeared as Dagenhart, 1992). The idea is to provide an experimental platform that captures all of the essential features of a swept wing that undergoes crossflow-dominated transition and yet provides the simplest possible experimental and computational problem. If all of the important physics are included in the experiment and good agreement with computations is achieved, then the computations can be used with confidence to obtain results with more realistic operating conditions. This implies that a swept wing is preferable to a swept flat plate because the wing provides surface curvature, and the results of Haynes & Reed (2000) indicate that even though the curvature is quite small, it is an essential element for correctly predicting stationary-mode growth rates. The model is not tapered. This means that a spanwise-uniform basic state can be established, greatly simplifying both the experiment and stability calculations. Taper can be included in stability calculations, of course, but the computations would simply have to be validated without taper. If subsequent calculations indicated that taper could influence the stability behavior, that discovery would require a new experiment for valida-

tion. Without an indication that this could occur, and if so, for what parameter range, there is no reason to make the experiment more complicated than necessary.

The next idea is to provide a model with boundary layers that are sufficiently thick to allow for relatively easy and well-resolved boundary-layer velocity measurements and to simultaneously provide sufficient crossflow to cause transition. These requirements conflict because thick boundary layers can be achieved by restricting the experiment to low Reynolds numbers, but at too low a Reynolds number the instability would not be strong enough to produce transition. One of the first means of improving the prospect for strong crossflow and a thick boundary layer is to select a pressure gradient that locates the pressure minimum as far back as possible. This means that the boundary layer can develop over the longest possible distance without the boundary layer becoming unstable to T-S waves and without the crossflow direction changing. The pressure gradient can also be used to enhance the crossflow by making the pressure gradient as strong as possible. Although this means that strong negative lift is preferable, experience at the Unsteady Wind Tunnel has shown that the wall liners used to maintain spanwise-uniform flow are difficult to construct and maintain when there is strong lift. Therefore a pressure contour that provides a strong pressure gradient with a late pressure minimum at zero lift is the optimum configuration. Enhanced crossflow can also be produced by increasing the sweep angle of the wing. However, exceeding  $\Lambda = 45^\circ$  becomes impractical for the hotwire traverse system.

Starting with Dagenhart (1992), all of the previous Unsteady Wind Tunnel crossflow stability experiments employed a swept-wing model with an NLF(2)-0415 profile (Somers & Horstmann, 1985) and  $45^\circ$  sweep. The NLF profile places the suction-side pressure minimum at 71% chord. Transition on this model is always observed upstream of 71% chord, so the T-S instability does not contribute to transition, nor does the Görtler instability, because the concave region also occurs downstream of 71%. The nose radius and sweep are such that leading-edge contamination is not present. The wing used in the current work, designated the ASU(67)-0315, was designed by Reibert around the same principles with the additional feature of generating significant crossflow at zero lift. The unswept chord length of the new model is 1.829 m, the sweep angle is  $45^\circ$ , and the angle of attack is set at  $-3^\circ$ , the zero-lift angle. The theoretical inviscid pressure contour for this configuration, including the influence of the wind-tunnel walls, is computed using the MCARF code of Stevens *et al.* (1971) and is shown with the wing contour in Figure 3. The code does not account for displacement thickness growth on either the model or the walls.

## 2.2 Swept-wing model

The ASU(67)-0315 wing was constructed to provide a flexible test platform on which a variety of boundary-layer transition-control experiments can be conducted. To this end, the leading edge of the wing is not continuous, but includes a leading-edge slot in the middle third of the span that extends to approximately 20% chord. This slot accepts modular leading-edge inserts that can provide any sort of boundary-layer treatment, in particular the MEMS roughness actuators. The leading 10% chord of the main body of the model is a solid aluminum piece, hand polished to a  $0.2\text{-}\mu\text{m}$ -rms surface finish. The remainder of the main body consists of an aluminum frame and foam core covered by fiberglass. The fiberglass construction means that the wing weighs approximately 350 kg, allowing it to be much more easily handled than the all-aluminum NLF wing. (The NLF wing weighs approximately 725 kg.) The model includes two lines of 29 suction-side pressure taps at various chord locations. The lines of taps are oriented in the  $X$  direction as indicated in Figure 4.

The leading-edge insert used for the current work is constructed of a solid aluminum piece machined to match the contour of the main body of the wing and to provide an exact fit at the junction between the insert and the main body. The surface of the insert is hand polished to the same 0.2- $\mu\text{m}$ -rms finish as the main body's leading edge. Figure 5 is a schematic of the leading-edge insert used in the present work. A slot centered at 2.5% chord is cut in the leading-edge insert. The slot extends 42.6 mm in the chord direction and 718 mm in the span direction. This slot accepts a smaller insert into which any one of several variable-amplitude roughness devices can be placed. Several of these smaller variable-roughness inserts are used in the present experiment. For the secondary instability measurements described in Chapter 3, a blank insert<sup>1</sup> that simply follows the contour of the wing is used. To establish a uniform disturbance field, an array of periodic static roughness similar to that used by Reibert *et al.* (1996) and Saric *et al.* (1998) for the modal growth experiments is applied to this blank insert.

## 2.3 MEMS roughness insert

The MEMS development efforts of this work focused on providing MEMS actuators that would be contained in the leading-edge insert and would provide either static, quasi-static, or unsteady control. The basic design of the actuators was developed by the Case Western Reserve University (CWRU) MEMS development group and consisted of a multi-layered structure that consisted at the top layer (in contact with the boundary layer) on an array of regularly spaced, circular, piston-like surfaces. The various designs had either 2-, 3-, or 4-mm diameter piston surfaces on 8 or 12-mm centers. Below the surface of the element, a rod connected the upper piston face to a flexible membrane that would deflect upwards, moving the piston face into the flow, several microns, when a cavity beneath the flexible membrane was heated using a small electrical resistor. This system was capable of providing several-micron deflections of the piston element either in steady or unsteady state.

The MEMS elements were manufactured on 100-mm-diameter silicon wafers using typical MEMS fabrication techniques. The principal difficulty of the assembly process was the adhesion of the piston element to the adhesive layer. This sort of bond between the silicon and elastomer layers is quite difficult to achieve and was prone to a significant failure rate. Failure of the elastomer/silicon bond became quite significant, especially in light of the particular action of the nonlinear evolution of the unstable modes in crossflow boundary layers. In particular, control of the boundary layer is achieved by applying a roughness pattern with a spacing *less than the most unstable wavelength*. In the ASU experiment, this means applying an 8-mm input when 12-mm waves are most unstable. The failure of a single roughness element leads to a 16-mm component in the input wavenumber spectrum and this leads to *enhanced transition* because 16-mm waves are nearly as unstable as 12-mm waves. Because of this, if a single element on a 100-mm strip failed to bond correctly, the entire strip could not be used. A significant bond failure rate at the time of manufacturing meant that nearly every strip produced by the MEMS production facility was unsuitable for the experiment. Beyond being simply an issue of manufacturing technique, the problem of single-point element failure has serious consequences for flow-control in practice. If the failure of a single MEMS element means that (at least locally) the situation on the wing

<sup>1</sup>Henceforth the term "insert" alone will refer to the smaller variable-roughness insert, because the same large leading-edge insert is used for the entire work. Where the context could be unclear, "variable-roughness insert" or "leading-edge insert" will be used for the smaller and larger inserts, respectively.



may be worse than if no control had been attempted, a much-more-robust actuator design must be developed for use in practice.

The work performed by the ASU group implementing the few defect-free MEMS actuators raised other serious questions about the applicability of MEMS actuators to *external* flow control given the current level of MEMS technology. Some of the key difficulties encountered were (1) implementing a flat silicon surface into a curved wing surface, (2) bonding the silicon wafer slices permanently to the aluminum wing, (3) maintaining a flush, no-roughness surface at the wing/wafer surface, and (4) maintaining the elements and replacing failed elements without damaging nearby operative elements. The first and third problems, implementing a flat silicon surface into a curved wing surface and maintaining a good-quality, no-roughness junction are particularly important for control of the crossflow instability because of its sensitivity to leading-edge roughness. The MEMS devices, as designed, essentially required hand installation, and because this could not be accomplished while maintaining sub-micron-level surface quality at the silicon/aluminum or silicon/silicon junctions, the application of the MEMS wafers actually led to larger levels of *uncontrolled* surface roughness than the actuators themselves were capable of providing. The fact that the actuator strips were much longer (on the order of 100 mm) than the most unstable crossflow waves (10–16 mm) does not prevent difficulties, because even isolated roughness sites can be detrimental, as demonstrated by the experiments of Radeztsky *et al.* (1999).

Because the experiments require roughness with better quality control than the MEMS-based elements provide, a decision was made to manufacture at ASU a pneumatically activated roughness insert. This insert provides uniform activation of an entire array of elements on a slow time scale. This action is sufficient to perform the experiments of interest, but does not extend into the unsteady or non-uniform roughness forcing the MEMS-based actuators might provide. The pneumatically driven insert has the capability to vary the roughness height, a necessary component of the absolute-instability experiments. It has an interior chamber that is pressurized from a supply outside the wind tunnel, and a 12-mm-spaced spanwise array of 3-mm-diameter holes is drilled from the contoured upper surface of the insert into the interior pressure chamber. The array of holes is covered with a 25-mm-wide, 40- $\mu$ m-thick strip of polyester tape, and when the interior of the insert is pressurized, the tape deforms into a periodic array of artificial roughness. The variable-amplitude roughness system provides a means of producing transient roughness forcing that is used to search for an absolute instability. A schematic of the small variable-roughness device is shown in Figure 6. In the future, such an insert could be manufactured with a MEMS-based valve controlling each element in the roughness array with the MEMS valves located inside the wing.

The chief difficulty associated with the new model is the quality of the surface that results from the installation of the modular pieces. It is known from the earlier work of Radeztsky *et al.* (1999) that micron-scale isolated roughness features of a surface are sources of crossflow receptivity. This means that even the smallest imperfections at the junctions between the small and large inserts and the large insert and the wing can produce deformations of the mean flow that could overwhelm any boundary-layer features generated by the roughness arrays that are intended to provide a uniform disturbance field. Fortunately, while crossflow boundary layers are extremely sensitive to 3-D roughness, they are not sensitive to 2-D (spanwise-constant) roughness. Crossflow requires a source of streamwise vorticity that 3-D roughness provides, but 2-D roughness does not. So, while the corners of the junctions pose a problem, the long sides of the variable-roughness insert and the large leading-edge insert that run in the span direction do not adversely affect the flow. Because of the large

spanwise extent of the inserts, the corners are far enough from the measurement region that the crossflow waves generated from their corners do not affect the measurement region. This is confirmed with a simple naphthalene flow visualization.

The variable-roughness inserts present a more challenging problem because application of the polyester tape over the hole array cannot be achieved without introducing several types of 3-D roughness. It is particularly important that the residual roughness level be as low as possible when the roughness is nominally inactive. Reibert *et al.* (1996) have shown that because of nonlinear saturation of sufficiently large amplitude disturbances, the state of the flow in the breakdown region can be nearly independent of the leading-edge roughness amplitude. Recall that in Reibert *et al.*'s experiment 6- $\mu\text{m}$  roughness and 48- $\mu\text{m}$  roughness produced nearly identical transition behavior at  $Re_c = 2.4 \times 10^6$ . On the other hand, Radeztsky *et al.* (1999) found a strong dependence on surface-roughness level for isolated roughness in the micron to submicron range, so this low level must be within the capabilities of the variable-roughness device.

There are several disturbance sources when the roughness is inactive. These are discrete flaws due to bubbles and small particles under the tape surface, sections of surface waviness in the tape, and a small degree of surface pucker associated with the application of the tape over the holes. The discrete flaws appear randomly and are quite small, not only in height but also in diameter, so it is shown that these will not cause a significant response. Radeztsky *et al.* (1999) observed that isolated roughness elements are most effective at crossflow-wave generation when their diameter is on the order of one-quarter of the most amplified crossflow wavelength (10–14 mm for the present experiment, depending on Reynolds number), and the small random flaws are much smaller than this, always less than 1 mm in diameter. The surface waviness is a more significant concern because this imperfection occurs over several millimeters of span and extends over the entire tape width. However, spanwise hotwire scans of the type described below are performed at chord locations just aft of the roughness insert location at 10%, 15%, and 20% chord, and these measurements indicate that the most significant source of crossflow-wave generation when the insert is inactive is the deformation of the tape over the holes. Some deformation is inevitable simply because of the geometry of the device. Because the holes are at the most amplified crossflow wavelength and their diameter is exactly one-quarter of that spacing, it should not be surprising that these flaws appear to dominate the flow on the forward section of the wing. A spanwise hotwire scan at constant offset from the surface illustrates the extent of mean-flow deformation at  $x/c = 0.20$  and  $Y = 1.0\text{ mm}$  for  $Re_c = 2.4 \times 10^6$  (Figure 7). The spatial spectrum of this mean-flow data (Figure 8) shows that the dominant wavelength of the deformation is 12 mm at this position when the roughness is inactive. Despite the fact that there is some mean-flow deformation when the roughness is nominally inactive, the device is suitable for the absolute instability experiment. This is demonstrated in Chapter 4 where it is used to change the transition location for a particular Reynolds number flow. The fact that this is possible allows the experiment to be performed. If the magnitude of the residual, inactive roughness were too large, the disturbances it produced would saturate and produce transition at the same location as the activated roughness state.

As for the active variable roughness, what is needed is the general relationship between the pressure difference across the tape surface and the height at the center of each roughness element relative to the undeformed surface. Also, the shape of the roughness elements is important for inclusion in receptivity models such as that of Collis & Lele (1999). To produce deformation of the tape surface a computer-controlled pressure system is employed. An external supply tank is maintained at 5.5 atm and a regulator valve supplies air from

this tank at 0.15 atm to a computer-controlled valve that regulates the pressure inside the variable-roughness insert. The system includes a pressure transducer, the test-section static pressure sensor, and the pressure coefficient data that give the pressure difference across the tape membrane. With no air flow in the tunnel, the relationship between the pressure difference and the displacement is measured using a confocal laser displacement sensor that is described below. A family of pressure-versus-displacement curves is shown in Figure 9. While precise control of the roughness height could not be achieved using the system, the general trend is acceptable for the purposes of the absolute instability experiment where simply high and low roughness amplitudes are needed. The shapes of the activated roughness elements for two pressure levels are shown in Figures 10 and 11.

## 2.4 Wind tunnel, test section, and traverse

The experiments are conducted in the Arizona State University Unsteady Wind Tunnel. The Unsteady Wind Tunnel is a closed-loop, low-speed, atmospheric-pressure facility originally built and operated by Dr. Philip Klebanoff at the National Bureau of Standards. Following Dr. Klebanoff's retirement, the tunnel was moved to Arizona State University and reconstructed between 1984 and 1988 with numerous flow-quality improvements. The design and operation of the wind tunnel are intended to provide the best possible conditions for conducting transition-to-turbulence experiments. With this in mind, quite a significant investment has been made in high-quality screens, honeycomb, a settling chamber, a contraction cone, turning vanes, and vibration-isolation strategies. The fan consists of a 1.8-m-diameter, 9-rotor, 11-stator axial stage, powered by a 150-hp DC motor. The motor is computer controlled and can maintain speed to within 0.01% of the set point. Further details of the facility's design and capabilities are given by Saric (1992), and details of the computer-control capabilities are described by Reibert (1996). An schematic layout of the Unsteady Wind Tunnel is shown in Figure 12.

The key features of the tunnel that bear directly on the present experiment are the freestream conditions in the test section. The maximum freestream speed that can be achieved in the test section is 35 m/s, and as noted above, any fan speed can be held to within 0.01% (although this level of precision is beyond the accuracy to which the freestream speed can be reliably measured). The maximum speed corresponds to a chord Reynolds number of approximately  $3.8 \times 10^6$  for the swept-wing model. The baseline operating point for the current experiment is  $Re_c = 2.4 \times 10^6$ , and for the temperatures at which the tunnel operates, this corresponds to freestream speeds between 22 and 23 m/s. The baseline Reynolds number provides the best combination of experimental parameters. Breakdown occurs near 50% chord, in the middle of the traverse's range, and the boundary layer is reasonably thick (3 mm) in the transition region, so well-resolved boundary-layer profiles are easy to obtain. Wind-tunnel heating is a concern at this speed but it is not so severe as to be unmanageable. The freestream turbulence level that is achieved in the test section is exceptionally low due to the very careful attention that is paid to turbulence-control devices upstream and vibration control. At 20 m/s, the turbulence level  $u'/U_\infty$  is less than 0.02% (using a 2-Hz high-pass filter). Both the  $v'$  and  $w'$  fluctuation levels are less than half that of  $u'$ . The sound level in the test section at the same conditions is below 85 dB. Recall that Deyhle & Bippes (1996) found that stationary waves dominate crossflow boundary layers only below  $Tu = 0.15\%$  (where  $Tu$  includes contributions of all three fluctuating-velocity components), so the low turbulence level of the Unsteady Wind Tunnel is essential for conducting a stationary-wave-dominated experiment. Perhaps the most significant limitation

of the Unsteady Wind Tunnel is the lack of temperature control. There is no active heat removal mechanism, and the fan motor is inside the tunnel so all of the excess heat generated by the motor increases the temperature of the flow. This is reflected in the approach to speed control and hotwire calibration. During all extended-duration experiments, the speed is adjusted regularly to maintain a constant Reynolds number because the kinematic viscosity of air increases as its temperature increases. Additionally, the hotwire calibration (discussed below) includes a sophisticated temperature compensation.

The test section is  $1.4\text{ m} \times 1.4\text{ m} \times 4.9\text{ m}$ . The contraction cone preceding the test section is a fifth-degree polynomial with a 5.3:1 contraction ratio. The test-section floor drops by 50 mm over its length to minimize the decrease in axial pressure gradient that accompanies boundary-layer growth on the model and the test-section walls. The test section includes a pitot tube for steady freestream static and dynamic pressure measurements and an RTD thermometer for freestream temperature measurements. The wing is mounted vertically in the test section both to simplify the supporting structure and to provide easy access to the suction side of the wing by the instrumentation mounted on the front wall of the test section. Moving from bottom to top, the sweep of the wing is forward, which prevents dust particles from settling on the leading edge and becoming unwanted receptivity sources. A support shaft runs through the wing at  $x/c = 0.25$ , parallel to the leading edge. This shaft mounts in a bearing just below the test-section floor that allows the wing to be set at  $1^\circ$  angle-of-attack increments. Unfortunately, after the wing was installed, it was discovered that the keyway in the shaft that adjusts the angle of attack was machined incorrectly. Because of this problem, the wing is not at the  $-3^\circ$  design position, but is at  $-3.4^\circ$ .

A high-precision, computer-controlled traverse mechanism is situated outside the front wall of the test section with access to the suction side of the wing. The traverse supports a sting that holds a boundary-layer and freestream hotwire. The traverse consists of a frame that moves 1.25 m in the axial direction along rails powered by a lead screw controlled by micro-stepping motors. The traverse frame includes stepper motors that move the sting that holds the hotwires in the vertical and wall-normal directions. The system includes optical encoder feedback to improve its reliability. The resolution and travel in the various coordinate directions are indicated in Table 2.1. Two views of the traverse system are given in Figures 13 and 14. The traverse is designed so that only the sting extends into the test section; the traverse mechanism is enclosed in a pressure box outside the test section. The pressure box nearly eliminates flow through the slot in the front of the test section that admits the sting. The panel through which the sting extends is driven vertically by two additional stepper motors that are coordinated with the vertical motion of the traverse. The slot itself is closed with a zipper that follows the sting, further reducing disturbances associated with the sting and access slot. The sting is designed to allow the boundary-layer hotwire probe support to be rotated toward the wing so that the sting itself need not be close to the wing. Additionally, the boundary-layer hotwire can be rotated about the probe-support axis so that the hotwire can be positioned parallel to the wing surface. The sting is shown in Figure 15 and additional details regarding its design are given by Radeztsky (1994). Further details regarding computer control of the traverse are given by Reibert (1996).

For the swept-wing model to meet the design goals of providing thick boundary layers and strong crossflow, while simultaneously maintaining spanwise uniformity, the use of contour wall liners is required. The liners are intended to enforce root and tip boundary conditions that mimic what would exist for an infinite-span wing, despite the fact that the model must be quite large relative to the test-section dimensions to achieve an acceptable

Direction	X, axial	Y, wall normal	Z, vertical
Travel	1250 mm	100 mm	175 mm
Step Size	12 $\mu$ m	0.7 $\mu$ m	1.3 $\mu$ m

Table 2.1: Traverse Capabilities.

Reynolds number range. A schematic of a  $45^\circ$  swept wing and liners for the zero-lift condition is shown in Figure 16. The liner design and construction techniques are thoroughly documented by Dagenhart & Saric (1999) and Radeztsky (1994), but the basic idea is as follows. First the pressure distribution predicted by the MCARF code is used to determine the surface of all streamlines passing through an arbitrary horizontal ( $X, Z$  constant) line upstream of the model. The two sides of the surface are constructed in full scale using styrofoam, and these two pieces are attached to the ceiling and floor of the test section to provide the root and tip boundary conditions, respectively. The suction-side and pressure-side walls of the test section are not treated with liners because these surfaces do not adversely affect the difficulty of stability calculations. The pressure field about the wing is slightly different from what it would be in free flight, but computations can use the pressure field calculated with these walls in place. From an experimental standpoint, suction-side and pressure-side wall liners would be significantly more challenging to implement, so not including these is a significant advantage in terms of experimental simplicity.

The extent to which the model and liners produce the conditions predicted by the inviscid code can be assessed by comparing the pressure measured using the surface pressure taps to the pressure distribution that is shown in Figure 3. The pressure at each tap is measured relative to the freestream static pressure and the difference is normalized by the freestream dynamic pressure,  $\rho U_\infty^2/2$ . This gives 3-D pressure coefficients  $C_{p,3}$ . (The data are acquired using a 10-torr differential pressure transducer described below.) The  $C_{p,3}$  measurements differ from  $C_{p,2}$  predictions shown in the figure only in terms of the normalizing pressure. The  $C_{p,2}$  values are normalized using the component of velocity perpendicular to the leading edge, whereas the  $C_{p,3}$  data use the total freestream velocity. The relationship is  $C_{p,3} = C_{p,2} \cos^2 \Lambda$ . Because  $\Lambda = 45^\circ$  for this experiment,  $C_{p,3}$  is simply one-half of  $C_{p,2}$ .

Figures 17–19 give the 3-D pressure coefficient distribution at  $Re_c = 2.0 \times 10^6$ ,  $2.4 \times 10^6$ , and  $2.8 \times 10^6$ , respectively. The measurements are for the actual  $-3.4^\circ$  angle of attack, but the computed curve reflects the design angle,  $-3^\circ$ , for which the liners were constructed. The results at the three Reynolds numbers are nearly indistinguishable. In each case the actual pressure is higher than the predicted value at all points upstream of 90% chord. However, the pressure gradient—the feature that affects boundary-layer stability—is approximately what is predicted by MCARF throughout the region of interest for the experiments,  $0.30 < x/c < 0.60$ . Furthermore, there is not an appreciable pressure difference across the span in this region. Such a difference would clearly render crossflow velocity predictions inaccurate. These results are quite similar to those obtained by Reibert *et al.* (1996) for the NLF wing. The exceptionally good agreement between those experimental results and the computations of Haynes & Reed (2000) indicates that the experiment can proceed with these pressure contours.

## 2.5 Instrumentation

### 2.5.1 General instrumentation

Because of the sensitive nature of the boundary-layer stability experiments performed at the Unsteady Wind Tunnel, a special emphasis is placed on automated control of the experiments. Repeatability and consistency demand that a completely automated system be responsible for controlling the experiment, collecting data, and processing the results. Moreover, the sheer volume of data required to track the evolution of a number of instability modes throughout their evolution means that the experiment is not possible without full automation. All of the experiments are controlled by an IBM personal computer with an Intel Pentium III running the Linux 2.2 operating system. The computer features a National Instruments GPIB controller through which all of the experimental hardware including the tunnel motor is controlled. All of the control and data analysis software is written at the Unsteady Wind Tunnel using the C and Perl programming languages.

Tunnel velocity measurements are performed using a freestream pitot tube. The static pressure is measured using an MKS 390HA 1000-torr absolute pressure transducer, and the dynamic pressure is measured with an MKS 398HD 10-torr differential pressure transducer. Temperature is measured with an Omega model DP116 RTD thermometer. The detailed freestream and boundary-layer velocity measurements are performed with hotwire anemometers. The probes used feature 2.5- $\mu\text{m}$ -diameter and 5.0- $\mu\text{m}$ -diameter tungsten wires, 1 mm long. The probes are the Dantec 55P15 design with the wire offset 3 mm from the probe axis to allow good access to the surface. The system is completed with Dantec 55M10 CTA bridges. The fluctuating-velocity signals are conditioned using a Stewart VBF44 two-channel filter/amplifier. Each channel has low- and high-pass filters that can vary from 1 Hz to 255 kHz with a best resolution of 1 Hz. Amplification is from -10 to 70 dB. The signals from the various devices are acquired using an IOtech ADC488/8SA analog-to-digital converter with 16-bit resolution and input ranges of  $\pm 1$  V to  $\pm 10$  V. The maximum sampling rate is 100 kHz.

The roughness measurements of the variable-amplitude roughness insert are performed using a Keyence model LT8120 confocal laser roughness meter. The device provides non-contact surface-height measurements over a 1-mm range with 0.2- $\mu\text{m}$  resolution at a 28-mm standoff distance. The spot on the surface for which the height is measured is 7  $\mu\text{m}$ .

### 2.5.2 Hotwire procedures

The instruments used to obtain the mean- and fluctuating-velocity measurements of the next two chapters are constant-temperature hotwire anemometers. Because careful attention to hotwire techniques is essential to a successful stability experiment, their use is described here in detail. Although a variety of more modern systems exists, hotwires provide a number of features that make them ideal for boundary-layer stability measurements. First, the very small wire diameters provide the best spatial resolution in the wall-normal direction among all possible velocity-measurement techniques. This resolution is absolutely necessary when one considers the boundary-layer scales typically encountered in the experiment, 1–3 mm, with data desired to within 150  $\mu\text{m}$  of the wall. The length of the sensor is 1 mm, but this is sufficient for the desired measurements because the spanwise length scale is 12 mm. Second, the even more attractive feature of hotwires is that the output signals can be high-pass filtered and then amplified so very accurate measurements of small, fluctuating-velocity components—exactly the feature of interest in stability measurements—can be

effectively measured. With any other system (e.g., LDV or PIV) no such filtering technique is available, so measurements of small velocity fluctuations are impossible. There is always some concern that introduction of a flow-intrusive device such as a hotwire can change the behavior of a system being studied. This is especially true for stability experiments where very small influences can become quite significant. For the present experiment this need not be a concern for several reasons. First, extensive naphthalene flow-visualization experiments of the previous investigators (in particular Dagenhart & Saric, 1999; Radeztsky *et al.*, 1999; Reibert *et al.*, 1996) show that hotwire measurements correspond exactly to behavior indicated by the flow visualization, for which no intrusive devices exist. Second, there is excellent correspondence between the experimental results of Reibert *et al.* (1996) and the computational results of Haynes & Reed (2000), so there is additional reason to believe that the boundary-layer behavior is unchanged by the presence of a boundary-layer hotwire. Finally, in the breakdown region the instability mechanism is driven by an inviscid Kelvin-Helmholtz-type instability that does not depend on the pressure gradient (the feature of the flow that would be modified by the presence of the hotwire and sting), but instead depends on the shear layer that is established by the stationary crossflow waves well upstream of the transition location.

Although in large part the fluctuating components are the most interesting features of these experiments, the correlation of the fluctuating components to the underlying mean flow is also of interest. This means that a very careful mean-flow calibration procedure is required that must include an accurate temperature compensation. The calibration procedure is performed daily to minimize long-term variations in the hotwire response. The calibration approach is somewhat different from other recent projects at the Unsteady Wind Tunnel (Reibert, 1996; Carrillo, 1996), so it will be described here in detail.

The basic idea is that the voltage output of the hotwires must be calibrated with respect to the upstream pitot tube and that this calibration must be valid for any temperature encountered during the experiment. To perform the calibration, the wind tunnel is run through a range of speeds at two temperature levels, and from this the output of the hotwires is related to the velocity/temperature state measured by the upstream pitot tube and thermometer. The pitot tube is an excellent velocity-calibration standard for steady flows because the instruments used to measure the static and dynamic pressures and the temperature all have good accuracy, precision, and long-term stability. Additionally, because the pressure transducers include independent heaters, they are immune to environmental temperature variations.

The calibration approach consists of three elements: a one-time position calibration, velocity calibration, and temperature compensation. The first, position calibration, is necessary because the entire region of the test section that is accessible by the traverse is within the zone affected by the pressure field of the wing, so the velocity measured by the pitot tube is not the velocity measured by the hotwires. To account for this, arbitrary calibration positions for the hotwires are chosen and the velocities at those points are measured using a temporary pitot tube. Then these velocities are related to the freestream velocities measured by the fixed pitot probe. For the current work, the calibration position is defined as 60% chord, midspan, with full retraction of the sting. Full retraction places the boundary-layer probe approximately 55 mm from the wall and the freestream probe approximately 180 mm from the wall. This position is selected because it minimizes the  $V$  and  $W$  components of velocity and thus offers the best velocity measurement using the temporary pitot probe. At the calibration position, the pitot probe measurements show that the velocity ratio between the boundary-layer calibration position and the upstream

pitot tube is  $1.120 \pm 0.017$  and the ratio between the freestream calibration position and the upstream pitot tube is  $1.061 \pm 0.017$ , where the errors are the standard error of the linear fit from 1–30 m/s. The ratios found during the position calibration are applied to all subsequent hotwire velocity calibrations.

The velocity calibration and temperature compensation are performed in a unified manner and will be described together. The basic equation governing the response of a hotwire is the empirical heat-transfer relationship known as King's Law. This law describes the forced-convection heat transfer from a cylinder perpendicular to a flow. The general form is written in terms of the Nusselt number and Reynolds number:

$$Nu = A' + B'Re_D^{1/2}. \quad (2.1)$$

Following Bearman (1971), this general relationship can be written in terms of the applied voltage, wire resistance, and the transport properties of air. The properties of air vary with temperature, but Bearman suggests that if one assumes that the correct temperature at which to evaluate these properties is the wire temperature (which is constant), then the variable properties can be grouped with the other constants: the sensor length and diameter and the wire resistance. Applying these assumptions yields the following expression:

$$E^2 = A(T_w - T_a) + B(T_w - T_a)U^{1/n}, \quad (2.2)$$

where  $E$  is the voltage across the sensor,  $T_w$  is the wire temperature,  $T_a$  is the ambient temperature, and  $U$  is the velocity component perpendicular to the wire. The constants  $A$ ,  $B$ , and  $n$  are to be determined. The exponent  $1/n$  is used instead of  $1/2$  because equation (2.1) is empirical and because better results can be obtained by allowing this value to vary.

To separate the effects of temperature and velocity, a temperature-compensation coefficient is generated that can correct voltage outputs to a certain standard temperature. To determine this coefficient, one measures the voltage for a certain velocity at high and low temperatures. Applying this approach to equation (2.2) gives

$$C_T(U) = \frac{E_h^2 - E_l^2}{T_h - T_l} = -A - BU^{1/n}, \quad (2.3)$$

where  $C_T(U)$  is the temperature-compensation coefficient and the subscripts refer to the high and low temperatures. The compensated hotwire voltage is then

$$E_{\text{comp}}^2 = E^2 + C_T(U)(T_{\text{comp}} - T), \quad (2.4)$$

where the subscript "comp" refers to the temperature-compensated voltage and an arbitrary compensation temperature. This approach removes the wire temperature (which is not known) as a parameter, but the resulting coefficient depends on the velocity. In practice this means that calculating velocity from the anemometer voltage output and ambient temperature requires an iterative procedure because the velocity  $U$  is unknown. Recalling equation (2.2) and replacing  $(T_w - T_a)$  with the constant  $(T_w - T_{\text{comp}})$ , the velocity is obtained using the expression

$$U = (A + BE_{\text{comp}}^2)^n. \quad (2.5)$$

The constants  $A$ ,  $B$ , and  $n$  in this equation are allowed to differ from those in equation (2.3) because, as before, King's Law is not exact, and better results can be obtained by setting these values independently.



The actual procedure used to find the constants in equations (2.3) and (2.5) is as follows. First, the tunnel speed is varied from 1 m/s to 27 m/s (as measured by the pitot probe) in increments of 1–3 m/s while the pitot velocity, temperature, and hotwire voltages are recorded at each speed. Then the tunnel is run at high speed (typically 31 m/s) until the temperature has increased by some increment, typically 5 °C. Once the higher temperature is reached, the tunnel velocity is decreased and again the pitot velocity, temperature, and voltages are recorded. During the ramp-down phase, the velocity targets are changed to the actual values observed during the ramp-up phase. This eliminates the need for a strict velocity tolerance for the ramp-up phase (thus reducing calibration time) but increases the overall calibration quality by reducing the velocity differences of the hot/cold data pairs. Using the data obtained in these two series of measurements, the temperature-compensation coefficient is calculated for each of the velocities using equation (2.3). Using these compensation coefficients, the ramp-down voltages are adjusted to yield the velocity as a function of temperature-compensated voltage, and these data are fit to equation (2.5).

The velocity target adjustment mentioned above is one improvement to the hotwire techniques employed during this experiment. Two other significant improvements over previous experiments are made as well. First, the voltages obtained during the ramp-down phase are modified via linear interpolation to the exact speed measured during the ramp-up phase. This greatly improves the temperature-compensation coefficient calculation because errors in  $E^2$  due to small velocity errors ( $\sim 0.1$  m/s) can be on the order of those due to 5 °C temperature variations, especially at low speeds. Second, instead of using second- and fourth-order polynomial fits to model equations (2.3) and (2.5), respectively, the fully nonlinear models are used. To perform the nonlinear<sup>2</sup> least-squares fit, the Levenberg-Marquardt method described by Press *et al.* (1992) is employed. The principal advantage is that the nonlinear equations provide a model that describes the heat transfer more accurately than the polynomial basis functions, resulting in reduced deviations of the data from the computed curve. Bevington (1969) shows that expected variance of data points relative to a fit is the reduced chi squared,  $\chi^2/\nu$ . This term is the sum of the squared deviations, normalized by the number of degrees of freedom of the fit (i.e., the number of data points minus the number of model parameters). The nonlinear models improve the reduced chi squared relative to the polynomial models not only by reducing the squared deviations but also by reducing the number of model parameters from eight (five for the calibration and three for the temperature compensation) to six (three each for the calibration and compensation). The effect of the various improvements on the temperature-compensation curve is shown in Figures 20 and 21. Figure 20 shows a polynomial and nonlinear fit without interpolation. Figure 21 shows the nonlinear fit using interpolated data. The reduced chi squared is  $2.6 \times 10^{-5}$  for the polynomial fit without interpolation,  $2.1 \times 10^{-5}$  for the nonlinear fit without interpolation, and  $1.8 \times 10^{-6}$  for the nonlinear fit with interpolation. Clearly the nonlinear model with interpolation produces the best result. Beyond simply reducing experimental uncertainty, the benefits of this approach are that the time and heating level required each day during calibration are reduced. Sufficiently good results can be obtained with a relatively small temperature rise.

<sup>2</sup>In this context, nonlinear refers to the form of the model parameters. For linear fits, the model parameters must appear linearly, but the basis functions may be nonlinear.

## 2.6 Measurement techniques

### 2.6.1 Coordinate systems

Prior to describing the measurement techniques that are common to the secondary instability and absolute instability experiments, a comment regarding the coordinate systems that are used to describe the experiment space is needed. This is of particular importance for anyone who wishes to compare computational results to the experimental measurements. The coordinate systems are the streamline-oriented system, the model-oriented system, and the global- or test-section-oriented system. The streamline-oriented system is most convenient for stability calculations. Here the direction tangent to the local inviscid streamline is denoted  $x_t$ , the wall-normal direction is  $y_t$ , and  $z_t$  is perpendicular to the other two directions. The crossflow velocity can be either in the positive or negative  $z_t$  direction depending on the local streamline curvature. The velocities in this system are denoted  $(u_t, v_t, w_t)$ . The model-oriented system is defined by  $x$  perpendicular to the leading edge,  $y$  perpendicular to the chord line, and  $z$  parallel to the leading edge. Here the velocities are denoted  $(u_n, v_n, w_n)$ . Finally, the global- or test-section-oriented system is denoted by  $X$  perpendicular to the freestream-flow direction,  $Y$  normal to the front wall of the test section, and  $Z$  vertical (with positive  $Z$  down to maintain a right-handed system). The global velocities are  $(u, v, w)$ . The various systems are shown in Figures 1 and 22. The coordinate definitions are consistent with the earlier Unsteady Wind Tunnel crossflow experiments.

The distinction between the model-oriented and global systems will be most pertinent for the present work because the results will be presented as a mixture of the two. The orientation of the traverse and sting provides an operational definition of the global coordinate system, so capabilities of the traverse system given in Table 2.1 relate to the global coordinates. Clearly, the best resolution is in the  $Y$  direction. Unfortunately, the wall-normal direction,  $y_t$ , which would be the correct direction in which to obtain boundary-layer velocity-profile measurements, is not aligned with the  $Y$  direction (although in the mid-chord regions of the wing they are aligned to within a few degrees). To obtain data in the  $y_t$  direction, very small traverse movements in  $X$  and  $Z$  would have to accompany steps in  $Y$ . The  $X$  and  $Z$  steps would be smaller than the limiting step size of the system. Therefore, including movement in these directions would actually render the measurements less accurate than if the small angle between the  $y_t$  and  $Y$  directions is ignored. Computational results can of course be obtained for any direction with arbitrarily good accuracy, so comparisons taken in the  $Y$  direction are best. The other direction in which traverse movement is required during an experiment is perpendicular to the local stationary-disturbance orientation. Measurements that scan along this direction would be used to produce information on the growth and energy distributions of the various stationary instability modes in their natural frame. However, because the local orientation varies over the wing and because moving along lines that are not constant chord lines presents difficulties for hotwire alignment, it is impractical for the experimentalist to continually adapt the scanning direction to the local behavior. Instead, the spanwise  $z$  direction is chosen for all such measurements, regardless of position. Because traverse movements in the span direction are much larger than the minimum traverse step sizes, there is not a resolution problem in this direction. With this approach to traverse movements, boundary-layer data are always acquired in the  $(Y, z)$  plane.

It is important that the orientation of the boundary-layer hotwire be properly understood in terms of the various sets of coordinates. (For this discussion, the schematic of the sting in Figure 15 and the coordinate axes in Figures 1 and 22 are helpful.) For each run, the

sting and boundary-layer hotwire are manually adjusted for the upcoming experiment and every experiment is restricted to a particular chord location. Prior to any adjustments, the boundary-layer wire is vertical and the probe support extends in the negative  $X$  direction. First, the boundary-layer probe support is pivoted (about the  $Z$  axis) so that it swings toward the wing in the  $(X, Y)$  plane. This rotation is required so that when the sting is moved in the  $-Y$  direction (toward the wing) during the experiment, the boundary-layer wire itself, and not the sensor's tines, the probe holder, or the sting, contacts the wing first. This orientation allows the boundary-layer measurements to be taken as close as possible to the wing. Next, the probe support is rotated about its axis so that the hotwire sensor is parallel to the surface of the wing. The rotation angle of the probe support depends on the chord location, but not on span. This is why measurements always proceed in the span direction. Because the hotwire's orientation changes depending on the measurement location, it is particularly important that comparisons between computations and the experiments described here be performed with special attention to the velocity-field projection. Because of the nature of the experiment (i.e., the hotwire senses only a projection of the local velocity), it is impossible for the full velocity vector to be reconstructed from single hotwire measurements. However, because all components of velocity are available from a computation, a projection of the computational data that mimics the physical transformation introduced by the hotwire orientation can be performed to yield a valid comparison between the experiment and computational models. In the experimental results presented in this document, velocities are referred to as  $U$ ,  $U_{\text{edge}}$ , and  $u'$ . These represent the projection of the mean-flow, boundary-layer-edge, and fluctuating-velocity components, respectively, onto the hotwire's orientation.

### 2.6.2 Boundary-layer velocity profiles

Boundary-layer velocity-profile measurements serve to acquire the projection of the mean-flow velocity onto the hotwire as the wire is traversed in the  $Y$  direction from outside the boundary layer to very close to the wing. The purpose of the scans in the present experiment is typically not to find the profiles themselves, but to locate the surface of the wing very accurately in the traverse's coordinate system. When performing an experiment, the position of the traverse can be controlled very precisely in the global frame of reference. However, in this frame the hotwire sensor's position relative to the surface is not known. This is because the hotwire is adjusted manually prior to measurements at each new chord location, so its position in the absolute traverse frame changes. Moreover, the surface of the swept-wing model is not in perfect alignment with the traverse-oriented coordinate system, nor is the surface of the model flat along the chord lines over which the measurements are obtained. The misalignment of the model and traverse is quite small, less than 1 mm over the 175-mm  $Z$  range of the traverse. Irregularities that are a result of the curing process of the fiberglass surface and subsequent hand finishing produce variations on the order of 100–200  $\mu\text{m}$  along constant chord lines. These irregularities cannot be accounted for in an overall way and must be taken into account locally. Because of these issues, the position of the wall is determined using boundary-layer profiles for every series of measurements in the boundary layer.

Using boundary-layer profiles to locate the surface utilizes the fact that the velocity at the surface is zero because of the no-slip condition. Approaching the wing while taking a series of velocity measurements and fitting these velocity data to a velocity-profile model produce a surface-position estimate via extrapolation to zero velocity. The operation must

be performed with the utmost care because the wire must be brought to within 150–200  $\mu\text{m}$  of the surface, and yet if the wire actually contacts the surface, it is destroyed. The 150- $\mu\text{m}$  limit is a consequence of the fact that hotwire measurements depend on the assumption that heat transfer from the wire is exclusively via forced convection to the air. Within 150  $\mu\text{m}$  of the wing, heat transfer to the surface becomes significant and hence the measurements overestimate the true velocity. The profile measurements are stopped before velocity errors occur due to surface heat transfer.

To address the need for caution while performing the profile measurements without spending too much time on this setup phase of the experiment, the measurements are started outside the boundary layer using a fairly large  $Y$  step between measurements. As the hotwire approaches the wing, the step size is progressively decreased so that better resolution is obtained where the data for the surface estimate are obtained. Once the hotwire has moved inside the region where  $U/U_{\text{edge}} < 0.5$ , the data fitting and extrapolation are performed after acquiring each new data point. This does not slow the measurement process because the calculations can be performed much more rapidly than the data can be acquired or the traverse can be moved. At each point in the inner portion of the boundary layer, the distance from the hotwire to the surface is calculated by subtracting the current surface estimate from the traverse coordinate. Monitoring this distance allows the stopping criteria to be distance based rather than velocity based. In previous Unsteady Wind Tunnel experiments, these sorts of measurements were terminated once a certain velocity ratio was achieved, typically  $U/U_{\text{edge}} = 0.15\text{--}0.20$ . However, in crossflow boundary layers the mean-flow distortion means that the distance from the wall at which a certain velocity ratio is reached varies significantly. The previous measurements reflected a compromise between a ratio that would allow all the measurements to come close enough to the wall to be effective and a ratio that would not allow the hotwire to contact the surface. This compromise is avoided here by simply supplying a distance, not a velocity, criterion, since it is a distance criterion that is truly important for avoiding surface collisions. Using this method, velocity profiles are obtained significantly closer to the wing at most span locations with a commensurate improvement in the surface-position estimates. The ability to achieve good estimates under a variety of conditions is especially important for the current experiment because much of the work is performed at chord locations where some portions of the boundary layer are turbulent while others remain laminar, so the range of velocity-profile types is especially wide.

The velocity-profile model is also different from that used in previous experiments. As before, only the points closest to the surface are used, but instead of a linear model a second-order model is employed:

$$U = a(Y - Y_0) + b(Y - Y_0)^2, \quad (2.6)$$

where  $a$ ,  $b$ , and  $Y_0$ , the surface position, are to be determined. This choice reflects the fact that there is a pressure gradient and therefore  $\partial^2 U / \partial Y^2$  is not zero at the surface. The second derivative is quite small, but its inclusion does not impose a time penalty on the experiment because the computation can be performed so rapidly. The more physical model means that better estimates can be achieved with fewer boundary-layer points and that points farther from the wing can be utilized. So overall, the use of the higher-order model actually serves to reduce the time spent performing boundary-layer velocity-profile measurements.

### 2.6.3 Spanwise-line and full-field scans

Once the boundary-layer profiles have been used to find accurate surface-position estimates, the measurements of interest can begin. There are two principal types used: spanwise-line velocity scans for the absolute instability experiments and full-field velocity scans for the secondary instability experiments. The line scans proceed along the  $z$  direction at constant chord,  $x/c$ , and distance from the surface,  $Y$ . The mean flows measured by these scans are useful for producing stationary-mode amplitudes. These are obtained by taking the Fourier transform of the velocity data along the span direction. This technique is similar to that used by Reibert *et al.* (1996) and Saric *et al.* (1998). To begin such a scan, the following parameters are supplied: the starting and ending span locations, the span step size, the offset in the  $Y$  direction at which the measurements are to be performed, the sampling duration, and the sampling rate. The first task performed is surface-position estimation using the boundary-layer-profile approach described above. The wall location is found at the starting, middle, and ending span positions, and the resulting data are fit to a polynomial that provides a surface estimate at all points along the span. With this estimate, the hotwire is moved to the position at the starting span location and the correct surface offset, and the first point is acquired. After this point, the traverse is moved one step in  $z$  and the  $Y$  position is adjusted to maintain the correct offset. After a number of acquisitions, the tunnel parameters are checked and the speed is adjusted if necessary to account for any heating that would increase the boundary-layer thickness. For the absolute instability measurements, multiple scans at the same  $x/c$  location are desired, so after each scan in  $z$ , the hotwire is returned to the starting position and the operator is given the option of changing parameters or ending the experiment.

Whereas the line scans are designed to be performed very rapidly, the full-field scans used for the secondary instability measurements are designed to provide very detailed velocity data for all points in the boundary layer. These scans provide mean- and fluctuating-velocity data on a 2-D grid of points at a particular  $x/c$  location. Typically the spacing in  $Y$  is 200–300  $\mu\text{m}$  and the spacing in  $z$  is 1.0 or 1.2 mm. This provides 15–20 points in the  $Y$  direction from the surface to outside the boundary layer and 12–15 points in the  $z$  direction, enough to span somewhat more than one crossflow wavelength. Full-field scans begin with a boundary-layer-profile measurement to locate the surface at the starting  $z$  position. Once the surface is located, the hotwire is moved to the starting  $Y$  position that is specified in the control program, and the mean and fluctuating data are acquired. Then the wire is moved out to the next  $Y$  location. After the desired points at the first  $z$  station are acquired, the hotwire is moved to the next span location and a new boundary-layer profile is obtained. The second and subsequent profiles are obtained more quickly than the first because a fairly good surface-location estimate exists from the previous profile, so these scans need not start outside the boundary layer. Instead they are begun well inside using the previous point's surface-location estimate and boundary-layer-edge velocity as parameters. The process is repeated until the entire domain is mapped.

### 2.6.4 Fluctuating-velocity spectra

When the line and full-field scans are performed, both mean-flow and fluctuating-velocity data are obtained. Because the interest here is in the process by which the instabilities grow and turbulence appears, the fluctuations are of particular interest. At each measurement position the mean output of the hotwire anemometer is obtained in the usual way, and the fluctuating output is obtained by high-pass filtering (typically at 20 Hz) to remove the

steady component and low-pass filtering to ensure that the subsequent Fourier transform of the data is not aliased. For acquisition at 20 kHz an 8.0-kHz filter is applied; for acquisition at 50 kHz a 20.0-kHz filter is applied. After filtering, the voltage output is amplified so that it covers a  $\pm 5$ -V range utilizing the full range of the data-acquisition electronics.

Analysis of the mean and fluctuating voltages acquired from the anemometers consists of first computing the temperature-compensated mean velocity. Next, the gain is removed from the fluctuating voltages and the mean is added to each fluctuating voltage so that the correct temperature-compensated velocity can be computed for each. The mean velocity is then subtracted from each of the instantaneous velocities yielding temperature-compensated fluctuating-velocity components. These are normalized by the boundary-layer-edge velocity to yield nondimensional velocity fluctuations.

Rather than the fluctuations themselves, power spectra of the fluctuations provide the most useful data regarding instability growth. To compute these spectra, the fluctuations are processed using a fast Fourier transform. A Bartlett window is employed to reduce leakage and averaging is used to reduce the variance of the power spectrum. Long samples are obtained that allow 10–20 averages to be performed while maintaining spectral resolution of about 10 Hz. The power-spectrum normalization is such that the sum of the discrete power components is equal to the sum of the discrete velocity fluctuations squared; Parseval's theorem is preserved in the discrete sense. To compute the rms amplitude of a particular frequency band, the components that lie in the band are summed, and the square root of that sum represents the rms velocity fluctuations for that band.

## Chapter 3

# Secondary Instability

The review of the crossflow instability on swept wings presented in Chapter 1 concentrated on two aspects: receptivity and the primary instability. Work of the past decade has shown the primary instability to be subject to nonlinear growth, stationary-wave interactions, and amplitude saturation. This aspect of the flow is now well understood both experimentally and computationally. Excellent agreement between these approaches has been demonstrated by the experiments of Reibert *et al.* (1996) and the computations of Haynes & Reed (2000) and Malik *et al.* (1999). Receptivity is not as well understood, but progress continues, and the recent computational results of Collis & Lele (1999) have provided a renewed impetus for experimental work. Despite achievements on these fronts, the actual mechanism responsible for the breakdown of laminar flow remains unclear.

Most of the important data regarding breakdown have come from observations of transition location. These observations give only general information and do not yield any specific clues about breakdown mechanisms. What transition location data have shown is that in some cases, the transition location is insensitive to roughness amplitude, while for other conditions, transition location is very sensitive to roughness. Specifically, recall that the early randomly distributed roughness studies by Radeztsky *et al.* (1999) showed that for  $Re_c = 2.7 \times 10^6$ , a decrease of the roughness amplitude from  $0.5 \mu\text{m}$  rms to  $0.25 \mu\text{m}$  rms delayed transition from  $x/c = 0.61$  to  $x/c = 0.68$ . Contrast this with the results of Reibert *et al.* (1996) for  $Re_c = 2.4 \times 10^6$  that show a change in transition location from  $x/c = 0.49$  to only  $x/c = 0.52$  when 12-mm-spaced, 6- $\mu\text{m}$ -high artificial roughness is replaced with 12-mm-spaced, 48- $\mu\text{m}$ -high roughness. Although the Radeztsky *et al.* (1999) experiment is for naturally occurring roughness and the Reibert *et al.* (1996) experiment uses artificial arrays of periodic roughness, the wide variety of transition behavior observed indicates that transition of crossflow boundary layers can be quite complicated. In order to better understand—and eventually predict—this behavior, one must be capable of understanding breakdown. In particular it is important to understand what triggers breakdown at the specific location at which it is observed.

There are at least two explanations for why the transition behavior is insensitive to roughness amplitude for a sufficiently large initial condition. The first of these is that a secondary instability grows in the saturated mean-flow region produced by sufficiently large amplitude leading-edge roughness, and it is this secondary instability that leads to transition. There have been a few experimental observations that suggest that this is the mechanism, and these will be discussed below. Another possibility is that at some point in the boundary layer, the flow becomes absolutely unstable. This would mean that disturbances could grow in time to large amplitudes at a fixed spatial location. If this is the

case, then breakdown would occur at or near the location where the flow becomes absolutely unstable, and this location would be independent of the initial disturbance amplitude and hence roughness amplitude.

It is the objective of this work to experimentally investigate both of these possibilities. The focus of the present chapter is the secondary instability. The first section is a review of the literature relevant to the secondary instability. The second is a description of the experiments. Results and discussion are presented in the third section. A similar approach to the possibility of an absolute instability is presented in Chapter 4.

### 3.1 Literature review

The first crossflow experiment for which a high-frequency disturbance was observed prior to transition was by Poll (1985). Part of Poll's experiment consisted of placing a fixed hotwire at the position of the maximum crossflow Reynolds number,  $x/c = 0.306$ , on a  $63^\circ$  swept cylinder. At this location, traveling crossflow waves were observed with a dominant frequency of 1100 Hz for  $Re_c = 0.9 \times 10^6$ . Increasing the chord Reynolds number to  $1.2 \times 10^6$  increased the traveling crossflow frequency to 1500 Hz. In addition to the primary waves an intermittent signal at 17.5 kHz was superposed on the underlying traveling crossflow waves at the higher Reynolds number. Poll noted that increasing the Reynolds number beyond  $1.2 \times 10^6$  resulted in turbulent flow at  $x/c = 0.306$ , so the high-frequency signal appeared only in a narrow range just prior to transition. Poll attributed the existence of the high-frequency component to intermittent turbulence.

Around the same time as Poll's experiment, work regarding the secondary instability behavior of streamwise vortices similar to those that exist on swept wings was being conducted for several other flows: rotating disk and cone boundary layers and Görtler boundary layers. Rotating disk and cone flows were the subject of flow-visualization studies by Kohama (1984, 1985). These geometries produce the same system of co-rotating streamwise vortices that exist in swept-wing boundary layers. Kohama's experiments showed that the streamwise vortices develop a pattern of secondary vortices around the perimeter of the main vortex structure just prior to breakdown. Drawing an analogy between the rotating disk configuration and swept wings, Kohama (1987) predicted that the same type of secondary instability mechanism would be active in swept-wing boundary layers as well. Furthermore, Kohama *et al.* (1987) suggested that this secondary instability was responsible for the 17.5-kHz signals observed by Poll (1985).

The Görtler instability on concave-curvature walls has been the subject of very extensive research and was the subject of a review by Saric (1994). This instability is similar to crossflow in that the primary instability is manifested as stationary streamwise vortices. Just as for crossflow, these vortices produce significant mean-flow distortion and undergo amplitude saturation due to nonlinearities. The difference between the crossflow and Görtler instabilities is that Görtler vortices are counter-rotating while crossflow vortices are co-rotating. In the Görtler literature, the experiment that is most relevant for this discussion is that of Swearingen & Blackwelder (1987), which (among other tasks) examined the secondary instability of the primary Görtler vortices using smoke flow visualization and detailed velocity-fluctuation maps. The flow visualization revealed two secondary instability modes: a horseshoe vortex structure around the perimeter of the primary vortices and a sinuous, transverse oscillation of the primary vortices. Of these, the sinuous oscillation mode was observed more frequently. This result is in contrast to the Kohama (1984, 1985) flow-visualization experiments in which the crossflow vortices clearly show a horseshoe-type



mode. The reason for the difference in the observed secondary instability modes is unclear. In a later computational work on the secondary instability of Görtler boundary layers, Li & Malik (1995) were able to determine different growth rates for both of the modes observed by Swearingen & Blackwelder (1987), and it appears as if the appearance of a particular mode depends strongly on the parameters of the Görtler boundary layer and on the receptivity of the individual modes.

The maps of velocity-fluctuation intensity produced by Swearingen & Blackwelder (1987) are 2-D sections in the spanwise/wall-normal plane. These maps show that the fluctuations are confined to a stationary multilobed structure. Two lobes exist high in the boundary layer at maxima of  $\partial U/\partial z$  and a single mode exists close to the wall near the center of the low-momentum upwelling region. The maximum amplitude of the fluctuations was found to grow exponentially at a rate two to five times more rapidly than the primary instability. The conclusions are that it is the secondary instability that is responsible for transition, and that the secondary instability is the result of inflection points of the streamwise flow when the second derivative is taken in the spanwise, not the wall-normal, direction.

With the investigations described above as a background, a high-frequency secondary instability was specifically investigated as a source of breakdown by Kohama, Saric & Hoos (1991). This experiment combined hotwire measurements and flow visualizations and was intended first to determine the location and behavior of the secondary instability mode relative to breakdown patterns that had been observed in naphthalene flow-visualization experiments conducted by Dagenhart & Saric (1999), and second to test the conjecture of Kohama (1987) that swept-wing breakdown is due to a secondary instability of the same type that affects rotating disk flow. The hotwire experiments consisted of two phases: single-point velocity-fluctuation spectrum measurements for various Reynolds numbers and single-line spanwise scans at constant chord and boundary-layer height. The flow-visualization tests were intended to correlate specific features of the hotwire measurements with surface shear-stress patterns.

A velocity spectrum result is given for  $x/c = 0.4$ ,  $y/\delta = 0.5$  ( $\delta$  is not explicitly defined), and  $U_\infty = 25$  m/s or  $Re_c = 2.66 \times 10^6$ . The spectrum (figure 8 in Kohama *et al.*, 1991) shows traveling crossflow wave activity at 350 Hz and a very broad high-frequency peak centered near 3 kHz. The claim is that the high-frequency activity is a secondary instability caused by a Rayleigh instability of the inflection points in the wall-normal profiles of the streamwise mean flow,  $U(y)$ . The authors report that increasing the Reynolds number increases the amplitude of the high-frequency peak until the signal (as determined by the hotwire time trace) becomes turbulent, although no quantitative data are given characterizing this development.

Using a characteristic secondary instability frequency of 3.5 kHz and a 350-Hz traveling primary-wave frequency, Kohama *et al.* (1991) undertake a series of spanwise line scans meant to demonstrate the spatial correlation between secondary instability and mean-flow deformation features. The scans are obtained between  $x/c = 0.40$  and  $0.45$  with the transition location at  $x/c = 0.50$ . The data reveal that both the low- and high-frequency disturbance amplitudes vary significantly over each wavelength of the stationary structure and that each mode has an amplitude peak close to the low-momentum upwelling location. The authors claim that the instability is located on opposite sides of this region, but this is difficult to observe in the data that are presented. In any case, the claim is that the streamwise velocity inflection points near the low-momentum region drive the flow to turbulence. The mechanism is an energy-production term involving  $v'$ , and this activity is located near the boundary-layer edge at the location of the multiply inflected wall-normal

velocity profiles.

Although it is clear from the Kohama *et al.* (1991) experiments that there is a growing high-frequency mode in the region upstream of transition, a number of concerns can be raised regarding the authors' techniques and results. First is the fact that the hotwire experiments consist of single-line scans rather than whole-field scans. Because the mean- and fluctuating-velocity data are obtained at a single height, there is some ambiguity about the actual location of the secondary instability behavior relative to the stationary mean-flow structure. Moreover, single-line scans become less reliable if one considers that the experiment was conducted without a well-controlled primary disturbance state. Experiments that were conducted subsequent to this work used arrays of micron-sized roughness elements near the leading edge. These arrays greatly improved the spanwise uniformity of both the stationary vortex amplitudes and the transition location. Without the benefit of this technique, the data obtained by Kohama *et al.* (1991) in all likelihood cover a wide range of stability behavior despite having been obtained at a single chord position. Additionally, it is apparent from a drift of the mean velocity in the span direction (e.g., Kohama *et al.*, 1991, figure 14) that there is a misalignment between the hotwire traverse and the model. This may be a result of the chain-driven  $X$  axis of the hotwire traverse used for those experiments. The precision with which a particular chord location could be maintained during an experiment was not nearly as good as can be obtained now. This alignment issue would not be a problem were the secondary instability mode confined to a single spanwise position within the stationary structure. However, as will be shown in the following chapter, the dominant secondary instability mode actually extends over a relatively large extent of the stationary structure, and the spanwise position of the peak fluctuation amplitude depends on the distance from the wall. Clearly, to obtain reliable secondary instability data, one must be very careful in controlling the position of the sensor both in terms of distance from the wall and in terms of span location relative to the underlying vortex.

Perhaps the most serious problem is in the approach to the signal amplitudes at particular frequencies. For all of the single-line scans, 3.5 kHz is intended to represent the secondary instability behavior. However, a close inspection of the spectrum that is presented (Kohama *et al.*, 1991, figure 8) reveals not one but two high-frequency peaks that are superposed. As will be described below, these peaks represent at least two independent instability modes, and the choice of 3.5 kHz is particularly unfortunate because it falls in the overlap band between the modes. This choice of representative frequency makes the true locations of the instability modes unclear because it includes contributions from two spatially distinct modes. Given this, it is apparent why the results are so ambiguous. What is clearly required is a more detailed experimental examination of the secondary instability process for the swept-wing configuration. For quite some time this experiment stood as the only source of secondary instability data for a crossflow boundary layer. The current experiment uses a more careful approach and provides data that will be useful for comparison with computations.

Following the experimental works of the mid 1980s and early 1990s, the focus shifted more toward computations. One of the first such investigations was by Fischer & Dallmann (1991). This work was undertaken as a computational analog to the DLR swept-plate experiments conducted concurrently by Müller (1990). The computational approach consisted of three phases. First, an FSC boundary-layer flow whose parameters (Reynolds number, sweep angle, and Hartree parameter) matched the experiment parameters at 80% chord was computed as a basic state. Then the stationary-wave stability characteristics of the FSC flow were computed. Finally, the most unstable stationary wave was superposed on

the FSC basic state and stability characteristics of this field were calculated. The mode shape of the stationary wave was taken from the earlier calculation and the amplitude was adjusted to match the experiment. Both the primary and secondary stability calculations were performed using local, temporal stability analysis.

The primary instability calculations successfully identified the most amplified stationary wavenumber,  $\beta_0 = 0.4788$ , where the nondimensionalizing length is the boundary-layer scale,  $\delta = (\nu x / U_c^{\text{ext}})^{1/2}$ . The orientation of this mode was also in good qualitative agreement with experimental observations,  $4.73^\circ$  from the inviscid streamline. Amplitude saturation was not captured because these were linear calculations.

The secondary instability calculations were performed at the same chord location using the saturated stationary-mode amplitude from the experimental measurements,  $\epsilon_0 = 7.89\%$ , where  $\epsilon_0$  is the maximum spanwise mean-flow velocity difference for all heights. The secondary-mode behavior was calculated using Floquet theory. In Fischer & Dallmann's approach, the perturbations of the spanwise-periodic mean flow,  $q'$ , are written as  $q' = \epsilon_1 q_1$ , where

$$q_1 = \text{real} \left[ \hat{q}_1(y, z) e^{i(\alpha_1 x - \omega_1 t)} \right], \quad (3.1)$$

$$\hat{q}_1(y, z) = e^{-i\sigma\beta_0 y} \sum_{k=-K_1}^{K_2} \hat{q}_{1,k}(y) e^{ik\beta_0 z}. \quad (3.2)$$

(Fischer & Dallmann, 1991, use  $y$  to indicate the spanwise coordinate and  $z$  to indicate the wall-normal coordinate. For consistency with the rest of this document,  $y$  is the wall-normal coordinate and  $z$  is the spanwise coordinate in equations 3.1 and 3.2.) The variable  $\sigma$  is a detuning parameter used to specify a harmonic, subharmonic, or mixed response.

The secondary instability calculations show that maximum temporal amplification occurred at  $\alpha = 0.03$  for  $\sigma = 0$  (harmonic resonance) and  $\alpha = 0.08$  for  $\sigma = 0.35$  (combination resonance). The dimensional frequencies of these modes are 73 and 145 Hz, respectively. These frequencies are in the range of the most amplified traveling disturbances obtained by the primary stability analysis. Similarly, the growth rates of the secondary modes ( $\omega_i = 0.0063$  and  $0.0068$ , respectively) are commensurate with the primary instability traveling-wave growth rates (although the growth rates computed using the linear code are not valid at 80% chord due to amplitude saturation). The conclusion that can be drawn from these results is that the strong mean-flow distortion produces a spanwise modulation of the traveling-wave intensity. It seems that this effect should not be considered a secondary instability, because the amplified modes exist without mean-flow deformation, and because progressively larger values of the stationary-mode amplitude simply modify the growth rate and frequency of the existing traveling-wave mode. No stable modes are rendered unstable to produce entirely new behavior. What is demonstrated, however, is that the stationary vortices produce strong spanwise modulation of the traveling waves.

An interesting feature of the computations of Fischer & Dallmann (1991) was that they did not identify the high-frequency fluctuations observed by Kohama *et al.* (1991) in the ASU swept-wing experiment. To resolve this inconsistency, Fischer, Hein & Dallmann (1993) impose a stationary disturbance amplitude larger than that observed in the DLR experiment. They point out that such large amplitudes would clearly be subject to nonlinear interactions, but those interactions could not be considered. Instead, the focus was on determining if the high-frequency instability could be produced under the same linear framework as the previous Fischer & Dallmann (1991) calculations. The new analysis by Fischer *et al.* (1993) also uses parameters that match the basic state of the Müller

(1990) experiment at 80% chord. For stationary-wave amplitudes exceeding 11%, a high-frequency mode was observed. At the 11% threshold, a high-frequency mode becomes unstable at 1500 Hz ( $F = 4.6 \times 10^{-4}$ ) and streamwise wavenumber  $\alpha = 0.556$  for  $\sigma = 0.5$  subharmonic resonance. Increasing the stationary-wave amplitude dramatically increased the growth rate and enlarged the amplified frequency band. In the calculations, the high-frequency secondary instability growth rate first exceeds the traveling-wave growth rate for a stationary-wave amplitude between 12% and 14%. By 16% amplitude, the maximum growth rate  $\omega_i$  is 0.027 at 2000 Hz ( $F = 6.1 \times 10^{-4}$ ). This growth rate is nearly three times that of the low-frequency traveling wave as given by linear theory.

The next computational approach to the secondary instability was presented by Malik *et al.* (1994). For their study, the authors use a nonlinear PSE to calculate the primary stability behavior for a swept Hiemenz flow. As described previously, the nonlinear PSE approach successfully captures the nonlinear effects including amplitude saturation of the primary stationary disturbances. The authors use a stationary-wave-only boundary-layer calculation to provide a basic state for a local, temporal secondary instability calculation. The calculation is started with a 0.1% amplitude primary wave at  $R = 186$ . No high-frequency modes are unstable at  $R = 450$  where the stationary-wave amplitude is 8%. At  $R = 500$  where the stationary-wave amplitude is 17%, the secondary instability is detected with a growth rate about equal to the stationary crossflow disturbance's growth rate. By  $R = 550$  where the stationary amplitude is saturated at 22%, the secondary instability growth rate has reached  $\omega_i = 0.02$  for  $\alpha = 0.6$  at  $F = 1.5 \times 10^{-3}$ . Recall that Fischer *et al.* (1993) obtained a most amplified value of  $\omega_i = 0.27$  at  $F = 6.1 \times 10^{-4}$  for 16% amplitude, and increasing the stationary amplitude increases the frequency of maximum amplification, so these results are quite similar. The most unstable frequency is approximately one order of magnitude greater than the most unstable primary traveling wave as reported by Kohama *et al.* (1991), and the peak mode amplitude is "on top" of the stationary crossflow vortex structure. This location corresponds to what will be referred to below by Malik *et al.* (1996) as the mode-II secondary instability.

In order to obtain a more direct comparison to experimental data, Malik *et al.* (1996) used the approach of Malik *et al.* (1994) to compute the secondary instability behavior of an FSC boundary layer with parameters designed to match the conditions found for the swept-cylinder experiment of Poll (1985) and the swept-wing experiment of Kohama *et al.* (1991), both of which contain secondary instability frequency data. To match the data of Kohama *et al.* (1991), a dominant stationary wavelength of 11.5 mm was imposed. Two secondary instability modes were generated, both with similar growth rates. The lower frequency of these at 2.1 kHz with a streamwise wavelength of 10.6 mm is referred to as mode I. The higher frequency mode, mode II, is at 3.9 kHz with a streamwise wavelength of 6.2 mm. The spanwise modulation of the traveling crossflow wave predicted by Fischer & Dallmann (1991) was also detected. Malik *et al.* (1996) claim that the fluctuations observed by Kohama *et al.* (1991) are mode-II instabilities because the calculated mode-II peak at 3.9 kHz is the closer of the two peaks to the experimentally quoted value of 3.5 kHz. However, as discussed above, the spectral data presented by Kohama *et al.* (1991) likely include contributions of both the type-I and type-II modes.

The calculations of Malik *et al.* (1996) reveal that the energy production for the mode-I instability is dominated by the term  $-\langle u_2 w_2 \rangle \partial U_2 / \partial z_2$  and the mode-II instability is dominated by  $-\langle u_2 v_2 \rangle \partial U_2 / \partial y_2$  where the subscript "2" refers to a primary-vortex-oriented coordinate system. This energy-production behavior suggests that the mode-I instability is generated primarily by inflection points of the streamwise flow in the *spanwise*

direction and the mode-II instability is generated by inflection points in the *wall-normal* direction. Although one or the other production mechanism may dominate for a particular mode, it is too simplistic to assume that *only* the spanwise or wall-normal inflection points are responsible for the appearance of a particular mode; with such a highly distorted 3-D boundary layer, all possible instabilities must be evaluated.

Malik *et al.* (1996) also compute the secondary instability behavior observed by Poll (1985). The computations for a stationary-wave-dominated boundary layer predict a 17.2-kHz mode; Poll's high-frequency signal occurred at 17.5 kHz. Based on the shape of this disturbance, Malik *et al.* (1996) claim that this is a type-II mode. Calculations were also performed for a traveling-wave-dominated boundary layer. These yielded three high-frequency secondary modes at 15.7, 14.8, and 12.8 kHz.

As part of the ongoing crossflow stability experiment at DLR, Lerche & Bippes (1996) and Lerche (1996) obtain measurements of the high-frequency secondary instability while examining the effect of forcing traveling and stationary crossflow waves. Forcing the most amplified traveling wave is denoted a (1,1) case; forcing the most amplified stationary wave is denoted a (0,1) case. For (1,1) and (0,1) forcing, the distortion of the mean flow alone is not sufficient to render the boundary layer unstable to the secondary instability. The saturation levels of these cases are 2% and 10%, respectively. However, superposition of the stationary and traveling waves can produce sufficient distortion to destabilize the secondary instability. Using phase-locked hotwire measurements, Lerche (1996) observes that the high-frequency secondary instability appears to be linked to a particular phase range of the traveling wave. Bippes (1999) states that in these cases, the secondary instability is located near the *instantaneous* wall-normal inflection point,  $\partial^2 U / \partial y^2$ , with the larger velocity gradient  $\partial U / \partial y$ ,<sup>1</sup> where  $U$  now represents the basic state plus the primary instability (stationary and traveling) disturbances. Bippes claims that the region of secondary instability activity is not tied to a particular inflection point of the steady flow (either wall-normal or spanwise), but rather is moving in the span direction with the traveling waves induced by the upstream forcing. This is likely the case when traveling waves dominate, but in low-disturbance environments for which stationary waves dominate, the secondary instability does seem to be located at particular span locations.

The fact that for some configurations the superposition of a certain phase range of the traveling crossflow mode with the stationary mode is required to trigger the secondary instability may reveal why some earlier observers (e.g., Poll, 1985) believed the high-frequency hotwire signals to be intermittent turbulence. The result obtained by Lerche (1996) shows this is not the case. The occurrence of the secondary instability is deterministic if one is careful to control both the traveling and stationary waves. It appears that to destabilize the secondary instability, there is a critical amplitude of the streamwise-flow deformation that is necessary, but this deformation need only occur instantaneously. This result should not be surprising if one considers that secondary instability frequencies are much higher than the primary traveling-wave frequencies. What could be considered "instantaneous" with respect to the slow primary-wave time scale is quite long on the secondary instability time scale.

The velocity fluctuation data obtained by Lerche (1996) for the case of (0,1)+(1,1) forcing have the same type of spectral structure as seen by Kohama *et al.* (1991). The secondary instability appears as a broad high-frequency peak an order of magnitude higher (in frequency) than the most amplified mode of the primary instability. For Lerche's case,

<sup>1</sup>The DLR group uses  $z$  as the wall-normal coordinate.  $y$  is used here for consistency with the definition used throughout this document.

the secondary instability peak is centered at 2 kHz while the most amplified primary wave is at 82 Hz. Using spectra from an array of points, Lerche constructs maps of the secondary instability amplitude, filtered from 1.6 to 2.4 kHz. For (1,1) forcing, the high-frequency data do not show a distinct spanwise structure. For (0,1)+(1,1) forcing, however, the amplitude distribution in  $(y, z)$  clearly resembles the type of structure predicted by Malik *et al.* (1994). Because only one high-frequency peak appears in the velocity spectrum (figures 2 and 28, respectively, in Lerche, 1996; Bippes, 1999), it is impossible to classify this as a type-I or type-II mode using the spectrum. Likewise, the shape of the mode (figures 3 and 29, respectively, in Lerche, 1996; Bippes, 1999) does not clearly suggest a classification either. Although the amplitude maximum appears to correspond to the mode-II location high in the boundary layer, there is significant activity in the mode-I region as well. Clearly there is a need for additional experiments to fully understand the conditions under which these modes appear and what techniques can be used to detect and classify them.

A DNS approach to the problem of the stationary-vortex saturation and the ensuing secondary instability was pursued by Högberg & Henningson (1998). Recall that the stationary-wave behavior of the primary instability was well described by the DNS of Wintergerste & Kleiser (1996) and that these simulations captured the nonlinear interaction of the low-frequency traveling crossflow wave with the stationary mean-flow structure. This interaction is what Fischer & Dallmann (1991) refer to as a secondary instability, although it is only modified, not new, stability behavior. To assess the high-frequency secondary instability, Högberg & Henningson (1998) artificially impose a random disturbance at  $x = 209.5$  (nondimensional) where the stationary vortices are saturated. These disturbances enhance both the low- and high-frequency disturbances downstream, and each frequency band has a distinct spatial location, with the high-frequency disturbance located in the upper part of the boundary layer and the low-frequency disturbance located in the lower part. Spectral analysis of the resulting disturbance field shows that the most amplified high frequency is at  $\omega = 0.957$ . Another high-frequency peak at approximately twice this frequency is also evident in the spectrum (figure 12 in Högberg & Henningson, 1998). This peak likely corresponds to the type-II mode, although this feature is not described by the authors. The other significant result is the growth rate of the high-frequency secondary instability mode relative to the primary instability growth rates. The neutral point of the secondary instability is  $x = 270$ , very far downstream, but the subsequent growth is so rapid that the secondary mode quickly is observed to produce breakdown in the computations. In fact, this process is so rapid that the authors suggest that the neutral point of the secondary instability may provide a good prediction of transition location.

This idea is modified by Malik *et al.* (1999). With the results of an NPSE simulation of the ASU swept wing, they compute the local, temporal stability of the stationary crossflow vortices that are established by the primary instability. Malik *et al.* (1999) find that better transition correlation results can be obtained by actually following the growth of the secondary instability in an  $N$ -factor calculation rather than simply basing a prediction on the location at which the secondary instability destabilizes.

A swept flat-plate experiment was performed by Kawakami, Kohama & Okutsu (1999) to investigate secondary instability growth in crossflow boundary layers. The model features  $45^\circ$  sweep and a chord Reynolds number of about  $4.9 \times 10^5$ . Using a very wide (600 Hz–2.5 kHz) band-pass filter, mode shapes that are similar to those found by Lerche & Bippes (1996) are identified. From the spectral data presented, the lowest frequency mode's peak appears to be between 1.0 and 1.2 kHz. This mode becomes unstable between  $x/c = 0.35$  and  $x/c = 0.40$ . Just upstream of  $x/c = 0.50$ , a mode identified with a 2.5–4.0-kHz filter

becomes unstable and grows slightly less rapidly than the 600-Hz–2.5-kHz mode. Kawakami *et al.* (1999) also use a small speaker embedded in the plate to force the secondary instability. Using various forcing frequencies, the authors find that the maximum growth rate is about three times that of the most amplified primary instability and occurs at 1.5 kHz.

### 3.2 Experimental approach

What is lacking from the experiments described above is a careful, thorough approach to the secondary instability that can be used to validate the computational models. There are numerous spatial and spectral details that have not been explored that could significantly improve our understanding of the secondary instability, including the beginnings of a predictive understanding into where it will appear and how it causes breakdown. One detail that is particularly interesting is the issue of what secondary instability modes appear and under what conditions. Much of the past work has been hindered by rather broad generalizations of the secondary instability features, the best example of which is the fact that none of the experiments has distinctly demonstrated either the type-I or type-II modes predicted by Malik *et al.* (1996). It is a goal of the present experiment to provide a detailed catalog of secondary instability features that is capable of validating computational models.

The secondary instability experiment is quite simple. The approach is to first establish a spanwise-uniform primary disturbance field and then track the evolution of the fluctuating velocities associated with all of the instability modes that exist in a particular stationary structure. Because Reibert *et al.* (1996) demonstrated that the spanwise uniformity of the primary instability is quite good when periodic leading-edge roughness is used, periodic roughness is applied here at  $x/c = 0.0025$ , near the crossflow neutral point. Because of the uniformity, only a single stationary structure need be interrogated for each case and its behavior is taken to be representative of the behavior of the entire boundary layer. Following the notation used by Reibert *et al.* (1996) and Saric *et al.* (1998), the artificial roughness arrays will be designated with the notation  $[k|\lambda]$ , where  $k$  is the amplitude of the roughness in micrometers and  $\lambda$  is the spanwise wavelength in millimeters.

Measurements are taken by performing the full-field scans that were described previously to obtain the mean and fluctuating velocities at all points in a 2-D grid in the  $(Y, z)$  plane at various chord locations,  $x/c$ . The mean-flow data are used to determine the stationary-mode amplitude growth. This is done by considering the spanwise rms of the stationary disturbance,  $\text{rms}[(U - U_{\text{mean}})/U_{\text{edge}}]$ . The amplitude of the stationary-disturbance mode is represented by the integral of the mode-amplitude curve taken from the surface,  $Y = 0$ , to the edge of the boundary layer. This measure is convenient and robust for experimental data both because it includes the contribution of all the data and thus is resistant to errors at individual points and because there is no ambiguity that results from arbitrary definitions such as a point in the flow at which to evaluate the amplitude. The fluctuating data are processed using a fast Fourier transform to yield fluctuation spectra, and a narrow band-pass filter is applied to these spectra to yield rms velocity-fluctuation amplitudes for individual modes. To obtain the instability growth rates, an integration over the whole field is required rather than an amplitude maximum or the amplitude at a particular location. Without considering changes in the spatial extent of an instability mode, much of the growth in its energy content could be lost as more of the area participates. As will be apparent below, the spatial distributions of the modes vary through the boundary layer, so to obtain an accurate picture of the instability growth rates, the velocity-fluctuation amplitudes are integrated over the entire field to give the total mode amplitudes. Because the stationary

distortion is such a large amplitude, and such strong spanwise periodicity is observed in the instability modes, simply finding the maximum or the amplitude at a certain point would not yield correct amplitude growth data. The integration of each mode is carried out over 12 mm of span, one stationary crossflow wavelength. The integration in  $Y$  is carried out to the edge of the measurement region because all of the fluctuations go to zero at the top of the range. For each location, the individual starting points in the span are adjusted to better accommodate the location of the modes relative to the stationary structure.

The secondary instability measurements presented here consist of four cases. The first of these is performed at  $Re_c = 2.4 \times 10^6$  with an 18- $\mu\text{m}$ -high, 12-mm-spaced roughness array at  $x/c = 0.025$ , [18|12] roughness. This first case serves as a baseline for comparison with the other runs and will therefore be presented in the greatest detail. Despite the new swept-wing model, this case will be close enough to the behavior observed previously to be considered a continuation of the experiments of Reibert *et al.* (1996), whose baseline was  $Re_c = 2.4 \times 10^6$  with [6|12] roughness. The larger roughness amplitude used here is a single layer of the smallest rub-on elements that could be obtained for this experiment. The 6- $\mu\text{m}$  elements used by Reibert *et al.* can no longer be obtained. Because saturation occurs prior to breakdown, it is thought that the appearance and growth of the secondary instability may not be affected by the initial amplitude.

To determine whether the secondary instability is affected by the initial roughness amplitude despite saturation by way of an increased amplitude of stationary-mode harmonics, a second case is performed at  $Re_c = 2.4 \times 10^6$  using three layers of artificial roughness to give a [54|12] array. To determine the behavior with weakly supercritical roughness forcing, the third case is performed with the same [54|12] roughness at  $Re_c = 2.8 \times 10^6$ . The higher Reynolds number means that the most amplified stationary crossflow wavelength is somewhat less than 12 mm. Spanwise spectra of the mean flow for this Reynolds number indicate that the most amplified wave is about 10.2 mm. Similarly, the behavior with weakly subcritical forcing is obtained from the fourth and last case performed with [54|12] roughness at  $Re_c = 2.0 \times 10^6$ . Here the most amplified stationary wave is about 13.5 mm. Finally, several tests are performed with enhanced freestream acoustic and turbulent fluctuations to assess whether varying these features can impact the behavior of the secondary instability.

### 3.3 Results and discussion

#### 3.3.1 Baseline case

The baseline configuration is  $Re_c = 2.4 \times 10^6$  with [18|12] roughness at  $x/c = 0.025$ . At this Reynolds number the most amplified stationary crossflow wavelength is about 12 mm, so the roughness spacing forces the most amplified wavelength. The first station considered is at  $x/c = 0.30$ . This is the first position for which the quantity  $\partial U / \partial Y$  equals zero somewhere inside the boundary layer, indicating that significant mean-flow distortion exists.<sup>2</sup> We first examine the boundary-layer velocity profiles spanning a single wavelength of the stationary vortex. Figure 23 shows the mean-flow profiles along with the spanwise mean of the individual profiles. The rms curve is the stationary-disturbance mode shape. For this location, it appears that although there is some distortion of the mean flow, the flow is still essentially linear because the rms curve has not yet developed the upper lobe that

<sup>2</sup>In this chapter and the following, the velocity  $U$  will be the mean velocity detected by the boundary-layer hotwire aligned parallel to the local wing surface as described in Chapter 2. Recall that this is not exactly aligned with the local inviscid streamwise direction, but it is within several degrees of that direction.



accompanies the advent of nonlinearities. Reibert *et al.* (1996) explain that the upper lobe is due to the rollover phenomenon that brings low-momentum fluid into the upper part of the boundary layer above the high-momentum fluid that is drawn close to the surface. Using the mean-flow velocity profiles from Figure 23, a velocity contour plot is constructed. This plot is shown in Figure 24. This layout reveals the structure of the stationary vortex better than the collection of profiles. In this figure the streamwise flow is into the page and the crossflow velocity is from right to left. The stationary vortex rotates in the clockwise direction. The dark shades are low-momentum regions and the light shades are high-momentum regions. The low-momentum upwelling region falls between  $z = 121$  and  $123$  mm. What is particularly important for understanding the breakdown of the boundary layer is the distribution of velocity fluctuations within this structure. Figures 25–27 show the velocity-fluctuation spectra at points on three vertical (constant  $z$ ) lines. The first of these, Figure 25, is at  $z = 119$  mm, to the left of the low-momentum upwelling. The spectra here show extremely low fluctuation levels. However, several features are detected. First, the most amplified disturbances are between 150 and 200 Hz. These fluctuations are the most amplified traveling crossflow waves. Second, there are fluctuations near 800 Hz. These may be T-S fluctuations that exist in spite of the favorable pressure gradient, since 800 Hz corresponds to about  $F = 140$ . All of the fluctuations die off quickly as the distance from the wall increases. For  $z = 122$  mm (Figure 26), the center of the low-momentum upwelling region, the spectra are about the same as at  $z = 119$  mm, except now the disturbances exist much farther from the wall where the boundary layer is thicker. The final span location,  $z = 125$  mm, with spectra shown in Figure 27, is what is referred to as the overturning region. This is where the low-momentum fluid that has been lifted away from the wall moves over the high-momentum fluid that is drawn in toward the wall. For this chord station, the spectra are very similar to those in the upwelling region of the previous figure.

The best means of understanding the stability behavior in the distorted boundary layer is to plot the spatial distribution of the amplitudes of the various fluctuating modes and compare these to the underlying structure of the mean flow at the same location. To do this, all of the velocity-fluctuation spectra for a particular chord location are integrated over the frequency band of interest, and the result is plotted against  $Y$  and  $z$  in a manner similar to the mean-flow contours. In the velocity-fluctuation amplitude-distribution figures, the intensity is given as the rms velocity fluctuation in the frequency band, the square root of the integral of the spectrum. Figure 28 is the rms velocity-fluctuation distribution for the frequency band centered at 200 Hz, the frequency band corresponding to the traveling crossflow mode. Before the boundary layer undergoes mean-flow modification because of the stationary crossflow vortices, the traveling crossflow waves are uniform in span. Here, the mean-flow modification has produced some deformation of the traveling crossflow amplitude distribution. This is the effect termed a secondary instability by Fischer & Dallmann (1991), who predicted that just such a modification should exist. As was argued above, this should not be considered an absolute instability because it is only a modification of existing unstable modes and not a destabilization of a new mode.

It is not obvious that this experiment should be capable of detecting the traveling crossflow fluctuations as well as we see them here. The primary disturbance consists of streamwise vorticity and the velocity fluctuations associated with this are  $v', w'$ . The hotwire is situated to detect  $u', v'$  fluctuations. Furthermore, because the streamwise  $U$  component is large relative to the fluctuations, the hotwire is more capable of detecting the  $u'$  fluctuations that are aligned with  $U$  than the  $v'$  fluctuations that simply change the velocity vector's direction, but don't significantly change its amplitude. The fluctuating velocity detected by

the hotwire is  $[(U + u')^2 + v'^2]^{1/2} - U$ , which is approximately equal to  $u'$  for  $u', v' \ll U$ . What this does not consider, however, is the fact that the inviscid streamlines and crossflow vortices are inclined relative to the  $X$  axis. This means that the hotwire actually detects a component of the  $w'$  fluctuations that appears with mean velocity,  $U$ , in the simple analysis presented above. This arrangement is shown schematically in Figure 29.

Moving to  $x/c = 0.35$ , the earliest stage of nonlinear evolution is apparent in the mean flow. An upper node of the stationary-disturbance mode shape can be seen in Figure 30. The composite velocity contour plot (Figure 31) shows that overturning is under way here. Comparing the velocity-fluctuation spectra at  $z = 105, 108$ , and  $111$  mm (Figures 32–34) to those obtained at  $x/c = 0.30$  shows that the traveling crossflow mode amplitude has increased while the higher-frequency fluctuations near  $800$  Hz have decreased somewhat. Overall, however, the spectra are quite similar to those upstream, and none shows evidence of a high-frequency secondary instability. What is not clear from the spectra is the extent to which the  $200$ -Hz disturbances are being redistributed within the structure. Figure 35 shows that just like the mean velocity, the fluctuations are acted on by the clockwise  $v', w'$  disturbance of the stationary crossflow mode. We observe very strong spanwise modulation of what was originally a spanwise-uniform feature. In fact, it may not be appropriate to refer to these fluctuations as traveling crossflow waves once the modulation is so severe. However, the experimental evidence shows that the origin of this mode is consistent with what is predicted for traveling waves by linear theory, and there is a continuous progression from that state to what is seen here.

At  $x/c = 0.40$ , the stationary-mode amplitude is increased substantially as can be seen in the velocity profiles and contours of Figures 36 and 37. Here, spectra at all three of the typical span locations show evidence of a high-frequency mode. At  $z = 91$  mm (Figure 38),  $3$  mm to the left of the center of the upwelling region, there is a broad band of fluctuations from about  $1$  kHz to about  $5$  kHz, with a maximum amplitude near  $3.0$  kHz. At  $z = 91$  mm, this feature only appears in the spectra obtained at  $Y = 0.8$  mm, close to the wall; at  $Y = 1.6$  mm, the feature disappears. At the center of the upwelling region,  $z = 94$  mm (Figure 39), the same band is active, now at  $Y = 2.4$  mm. In the overturning location,  $z = 97$  mm (Figure 40), the same band can just be detected high in the boundary layer. At all of these stations, the  $200$ -Hz fluctuations (Figure 41) are also strongly amplified.

The amplitude distribution of the  $3.0$ -kHz fluctuations at  $x/c = 0.40$  is shown in Figure 42. These fluctuations meet the secondary instability criteria because there is not a region that would be predicted to be unstable without mean-flow modification. These fluctuations lie along the shear layer to the right of the upwelling region and extend over much of the span of the stationary structure. This location is not what was reported by Kohama *et al.* (1991) but instead agrees with the computations of Malik *et al.* (1999) and measurements on swept plates by Lerche (1996) and Kawakami *et al.* (1999). The location of the  $3.0$ -kHz mode relative to the mean-flow distribution indicates that its production is likely dominated by the *spanwise* gradient of the streamwise velocity,  $\partial U / \partial z$ . This is what Malik *et al.* (1996) termed a mode-I secondary instability. The shape and extent of this mode reinforce the need for full-field as opposed to single-line scans to adequately understand the secondary instability. Obviously, the choice of wall offset  $Y$  for a single-line scan is tremendously important for the relationship of the mode-I amplitude distribution to the underlying mean flow.

Because the secondary instability is situated where it is, aligned on the high-velocity shear layer along the right edge of the low-momentum upwelling, it would appear that this is a Kelvin–Helmholtz-type instability. As such it will be manifested as vortex lines

that lie in the  $(Y, z)$  plane and convect in the stream direction. If this is the case, a visualization of the secondary instability would consist of rolls that wrap along the left side of and extend above the stationary structure. This is exactly what is observed in the rotating disk flow-visualization experiments of Kohama (1984). In the secondary instability phase of the Görtler experiment carried out by Swearingen & Blackwelder (1987), two types of secondary instability modes were observed. One is termed a horseshoe mode and resembles the crossflow rolls observed by Kohama (1984). The other mode is termed a sinuous mode and consists of an oscillation of the structure in the span direction. The difference between the crossflow and Görtler boundary layers is the fact that while crossflow boundary layers appear to have only a single secondary instability location, the Görtler structure has symmetric instability lobes that can operate either in or out of phase to produce one or the other type of secondary instability. Because there is no such symmetry in crossflow boundary layers, only the horseshoe-type mode can exist. This is exactly what is observed by Kohama (1984) and is what is thought to exist here.

The distribution of 200-Hz fluctuations continues to diverge from what is expected for traveling crossflow waves. Now there is almost no significant activity in this band in the high-velocity regions that are being drawn into the surface by the stationary vortex, and the fluctuations that were once distributed along the surface as the traveling crossflow waves are being lifted by the vortex in the low-momentum upwelling region. It is very surprising that a mode whose origin is in spanwise-traveling waves could reach a stationary state that is so highly modulated in span. The behavior of this mode is certainly worthy of much more detailed attention. However, to do it justice would require a different technique than is used here. Because it is (or at least starts as) a  $v', w'$  disturbance, if one wishes to understand its evolution unambiguously, a multi-element hotwire probe should be used to obtain the projection of the velocity field onto the plane parallel to the wing instead of simply the projection onto the single-element wire used here. With the data that are available now, nothing more conclusive can be said about this mode. This does not prevent us from moving forward with the high-frequency mode that appears here at  $x/c = 0.40$ . Because this mode lies along a streamwise shear layer, the disturbances are  $u', w'$  (or  $u', v'$ , depending on the particular location being considered), so the single hotwire is sufficient to obtain good data on this mode.

Moving downstream, the next position considered is  $x/c = 0.41$ . The mean-flow contours, velocity-fluctuation spectra, and the rms velocity distributions are nearly identical to those at  $x/c = 0.40$ , except of course for growth of the fluctuation amplitudes. Figures 43–47 are the mean-flow profiles; mean-flow contours; and fluctuation spectra at  $z = 87, 90$ , and 93 mm, respectively.

At  $x/c = 0.42$ , the mean flow (profiles and contours are given in Figures 48 and 49) is again about the same, but here a subtle difference in some of the fluctuation spectra (Figures 50–52) exists. Close examination of the  $Y = 0.80$  mm spectrum at  $z = 84$  mm (Figure 50) and the  $Y = 1.60$  mm spectrum at  $z = 87$  mm (Figure 51) reveals that a second peak in the fluctuation spectra exists at about 1.8 kHz. It is easy to miss the existence of this peak because of the proximity of the mode-I peak at 3.0 kHz. Plotting the rms velocity from 1.7–1.9 kHz (Figure 53) reveals an amplitude distribution that is almost identical to that seen previously for the mode-I instability. It is easy to imagine that much of this similarity is due to spillover from the 3.0-kHz mode. Consider, for instance, the  $Y = 2.4$  mm spectrum at  $z = 87$  mm (the highest amplitude secondary instability peak in Figure 51). That feature of the spectrum is quite strong at 1.8 kHz, and yet it appears to have only a single mode centered near 3 kHz. If there is 1.8-kHz activity here it is swamped

by the higher amplitude mode. Notwithstanding this, comparing the 1.8-kHz distribution in Figure 53 to the distribution of 3.0-kHz fluctuations in Figure 54 reveals that the lower frequency distribution extends much closer to the wall on the left side of the low-momentum upwelling region. Also, the mode extends well beyond the span of the figure to the left, just as the tail of the 1.8-kHz fluctuations from the structure to the right side of the figure ( $z > 94$ ) extends into the span range being considered. Contrast this with the 3.0-kHz mode that is much more compact. Unfortunately, the spatial and spectral proximity of these two modes makes it impossible to do more than speculate about the details of the lower amplitude 1.8-kHz mode. One could imagine that if the two could be separated, perhaps using phase information if it were available, then the 1.8-kHz mode would appear *only* close to the wall and all of the activity higher in the boundary layer would be simply spillover from the 3.0-kHz mode.

Moving to  $x/c = 0.43$ , the mean-flow profiles and contours are unchanged (Figures 55 and 56). Individual spectra at  $z = 81$  and  $84$  mm in Figures 57 and 58, respectively, again show evidence of a 1.8-kHz mode, but here the spatial distribution is even less distinct than in the previous case. The spectra at  $z = 87$  mm in Figure 59 show no sign of this mode, similar to Figure 52, the equivalent position in the stationary structure at  $x/c = 0.42$ , the previous chord location.

At the next location,  $x/c = 0.44$ , the mean-flow behavior remains the same as before (see Figures 60 and 61). The fluctuation spectra show very large secondary instability amplitudes both at the mode-I frequency, 3.0 kHz, and now for the first time at a higher frequency, 6.1 kHz. To the left of the upwelling region at  $z = 78$  mm, the spectra (Figure 62) only show a hint of this higher frequency mode and the position closest to the wall retains some activity that appears to be associated with the possible 1.8-kHz structure. However, at  $z = 81$  mm, the center of the upwelling region (Figure 63), the growth of the new 6.1-kHz mode is quite dramatic. In the overturning region, the spectra for  $z = 84$  mm (Figure 64) do not show evidence of the highest frequency mode and show relatively low amplitudes for the 3.0-kHz mode. It is interesting to note that the overturning location,  $z = 84$  mm, is exactly the location for which a secondary instability might be expected based solely on the  $U(Y)$  profiles. These profiles include multiple inflection points in regions of high shear stress and high velocity at the top of the vortex structure. However, at this location there is almost no secondary instability activity. The spatial distributions of the 3.0-kHz and 6.1-kHz modes are given in Figures 65 and 66. These show that the two modes are spatially coincident, so it is only because of their frequency separation that they can be recognized as distinct modes.

Moving to  $x/c = 0.45$ , the situation is very similar to  $x/c = 0.44$ , except now there is some indication that the fine structure of the mean flow cannot persist given the increased fluctuation levels. The individual profiles shown in Figure 67 from which the contour map is assembled cannot be distinguished from those of the previous station. However, the mean-flow contours in Figure 68 actually show a break and a separate zone of low-momentum fluid high in the boundary layer. This may only be an artifact of the grid on which the data are acquired, but it is certainly a harbinger of breakdown. The fluctuation spectra for  $z = 76$ ,  $79$ , and  $82$  mm in Figures 69–71 show that the 3.0-kHz and 6.1-kHz modes continue to grow rapidly, now with points at all three of these span locations participating. The spatial distribution of the 6.1-kHz peak (Figure 72) has matured significantly since  $x/c = 0.44$ ; it now lies clearly along the shear layer to the left of the low-momentum upwelling zone, whereas before it was a rather ambiguous blob.

Finally at  $x/c = 0.46$ , breakdown occurs. The mean-flow profiles shown in Figure 73

are not markedly different, but the contour map constructed from them (Figure 74) shows that much of the fine structure of the mean flow has been eliminated. The low-momentum upwelling no longer has a narrow apex; instead this region is wider and flatter. The region of low-momentum fluid high in the boundary layer still extends over nearly the whole stationary structure's length, but now the lowest velocities in this feature,  $U < 0.7 U_{\text{edge}}$ , are gone. What is most important in Figure 74, however, is the velocity gradient near the wall to the left of the low-momentum upwelling. Notice that this region looks quite different from previous cases; in particular the contour lines are now very close together, indicating that the wall shear here is quite high.

What are responsible for these changes in the mean flow are of course the much-increased velocity fluctuations brought on by breakdown to turbulence. At  $z = 72$  mm, the high wall-shear region to the left of the low-momentum upwelling, the fluctuation spectra in Figure 75 show a flat, very high amplitude, fully turbulent spectrum at  $Y = 0.8$  mm, the position in the figure closest to the wall. The spectra higher in the boundary layer are nearly fully turbulent, but in these curves some evidence of the 3.0-kHz mode remains. The situation is much the same for  $z = 75$  mm (Figure 76), the low-momentum upwelling position, except the spectrum of the point closest to the wall shows a somewhat lower fluctuation level, especially beyond 2 kHz. This position is below the zone affected by the secondary instabilities at the upstream stations and below the traveling crossflow fluctuations that persist throughout the preceding development, just as they appeared in Figure 41. The spectra for  $z = 78$  mm that are shown in Figure 77 are not turbulent; they maintain distinct spectral features associated with traveling crossflow fluctuations near 200 Hz and the 3.0-kHz mode-I secondary instability despite their very high amplitude.

In Figure 78 the distribution of the *total* velocity-fluctuation rms amplitude is plotted. It is evident from this figure that the overall energy distribution is exactly coincident with the 3.0-kHz and 6.1-kHz modes. Their rapid growth just prior to breakdown and the spatial location of the subsequent turbulent fluctuation maximum make it quite obvious that the secondary instability is the route to breakdown for this flow. Notice that the total rms velocity-fluctuation distribution shows somewhat more activity close to the wall between  $z = 71$  and 73 mm than do the 3.0-kHz distributions upstream. This has an important consequence in that it helps to explain the high wall shear in this region; the turbulent fluctuations promote enhanced mixing of the high-momentum fluid with the low-momentum fluid near the wall, resulting in increased shear. As a result, the behavior of the turbulent wedges that indicate breakdown in naphthalene flow-visualization experiments is now clear. The upstream tips of the wedges appear at the points where the mode-I instability makes its closest approach to the wall on the left side of the low-momentum upwelling location. The reason the wedges appear as they do, with the breakdown tip on the left edge of the low-shear part of the naphthalene streaks, has been a subject of some interest since the first systematic swept-wing flow-visualization experiments were undertaken by Dagenhart (1992). Understanding the location and amplitude of boundary-layer features relative to the associated wall shear in this manner is essential if one is to conduct an experiment using only wall measurements with hot films or some other technique as would be required in a flight experiment. In particular, consider the quantitative transition-detection technique developed by Chapman *et al.* (1998) using hot films. In this approach the hot films are aligned in an array along a particular stationary structure and must be positioned within the structure to detect the secondary instability fluctuations and the high shear of the turbulent wedge. With the data presented here it is now possible to correctly place the sensors to achieve optimum performance with this technique.

The appearance of the total fluctuation amplitude distribution raises the question: Why do these features extend so close to the surface and cause the wall-shear behavior that is observed? Comparing Figure 78 to the upstream 3.0-kHz and 6.1-kHz distributions shows that while the maxima are located in the same region of the stationary structure, the total fluctuation contours come much closer to the wing than the individual mode contours that we have been tracking. There are at least two potential explanations. The first is that the 1.8-kHz mode that was detected at  $x/c = 0.42$  and  $x/c = 0.43$  persists below an amplitude level that can be detected, but that it is able to enhance the fluctuation levels in this zone. The other possibility is that the small counter-rotating stationary vortex that was predicted by the computations of Malik *et al.* (1994) and the DNS study of Wintergerste & Kleiser (1996) is of sufficiently high amplitude to either participate in breakdown or transport fluctuation energy closer to the wall in this region. Neither of these mechanisms is directly supported by the present data, but there is some means by which enhanced fluctuations are generated near the surface, and these two scenarios are both candidates based on the upstream measurements and results from the literature.

Downstream of the breakdown location we can expect the stationary structure to dissolve quickly in the face of the enhanced fluctuation levels. This is evident at  $x/c = 0.47$  in the stationary profile rms curve in Figure 79 where both the upper node and the region below the lower node are already significantly reduced. This is reflected in the contours in Figure 80 that show the continuing breakup of the low-momentum zone high in the boundary layer and the extension of the high wall-shear zone. These trends continue at  $x/c = 0.48$ , the last measurement station of the baseline case. Here the stationary mode shown in Figure 81 continues to dissolve as the high wall-shear zone that can be observed in the contour plot (Figure 82) extends. For this final location, spectra at four span locations are presented. At the three span locations we have been tracking 3 mm to the left of, centered on, and 3 mm to the right of the low-momentum upwelling region (Figures 83–85), the spectra are all nearly fully turbulent, with amplitudes decreasing away from the wall. For this last chord station, spectra from  $z = 74$  mm, 6 mm to the right of the low-momentum upwelling center, are also included (Figure 86). These spectra show that although the parts of the stationary structure that contain the 3.0-kHz and 6.1-kHz fluctuations upstream are now turbulent, parts of the structure still exhibit relatively low fluctuation levels.

The growth of the instabilities is tracked by integrating the fluctuation levels over entire  $(Y, z)$  sections as described above. The reason for the whole-field integration should now be evident from the redistribution of energy throughout transition for both the 6.1-kHz fluctuations seen in Figure 66 and Figure 72 and for the 200-Hz fluctuations in Figures 28, 35, and 41. The rms fluctuation growth curves are shown in Figure 87. Each curve is normalized using the amplitude of its first occurrence. In this figure we see that the stationary disturbance grows between  $x/c = 0.30$  and  $x/c = 0.35$  and between  $x/c = 0.35$  and  $x/c = 0.40$ . Downstream of  $x/c = 0.40$ , the stationary disturbance is saturated. Throughout the chord range the traveling crossflow amplitude is slowly growing. Its development past  $x/c = 0.45$  is not plotted because once the flow becomes turbulent, the spectral band that defines this mode, 100–300 Hz, contains significant fluctuation levels that are clearly not associated with the same mode. The most important and dramatic features of this plot are the 3.0-kHz- and 6.1-kHz-mode amplitude curves. These modes appear in quick succession at  $x/c = 0.40$  and  $x/c = 0.43$ , respectively. The 3.0-kHz mode does not amplify rapidly at first, but starting at  $x/c = 0.42$  it undergoes very rapid exponential growth until breakdown at  $x/c = 0.46$ . It is rather curious that the 3.0-kHz mode exists for 2% chord before undergoing rapid growth. One might think from this behavior that the 2.9–3.1-kHz band includes two distinct modes:

a weaker early mode and the strongly amplified mode that becomes unstable at  $x/c = 0.42$ . This may indeed be the case, but if so it would be difficult or impossible to detect experimentally because the 3.0-kHz fluctuations are always observed at exactly the same spatial location, regardless of the chord location. The 6.1-kHz mode is first detected at  $x/c = 0.43$  and it undergoes even more rapid growth than the 3.0-kHz mode. What is interesting about the growth rates of the two high-frequency modes is that the 6.1-kHz mode *is not* twice that of the 3.0-kHz mode, meaning that the 6.1-kHz mode is not simply a harmonic of the 3.0-kHz mode, despite the fact that they are spatially coincident. Rather, it appears that the 3.0-kHz and 6.1-kHz modes are distinct.

### 3.3.2 Increased roughness amplitude case

With a fairly complete description of the secondary instability for the baseline case of  $Re_c = 2.4 \times 10^6$  with [18|12] roughness, we wish to understand the effect of the roughness-array amplitude on the appearance of the secondary instability. The results of Reibert *et al.* (1996) show that if the stationary crossflow waves saturate, then the transition location is nearly independent of the roughness amplitude. Those authors observed that changing from [6|12] to [48|12] roughness moved the transition location from  $x/c = 0.49$  to only  $x/c = 0.52$  at  $Re_c = 2.4 \times 10^6$ . This result suggests that because the stationary crossflow disturbances were saturated by  $x/c = 0.40$  in the previous section, an increase in the roughness amplitude will not change the stationary-mode amplitude in the transition region. Essentially, one could expect that if the gross transition behavior is unchanged, the secondary instability is unchanged as well.

One aspect of the higher amplitude roughness case that will be different from the baseline is the amplitude of the stationary-mode harmonics. Nonlinearities in the development of the mean-flow field are not just responsible for saturation, they also generate harmonics of the stationary mode. So if 12-mm input waves are applied, 12-mm waves are observed to dominate the flow field, but sufficiently far downstream, 6-mm, 4-mm, etc. waves are observed to grow as well, and these grow even after the principal wave has saturated.

For this second case with [54|12] roughness, the boundary-layer velocity profiles will not be shown; instead only the contour plots will give mean-flow information because the contours are better at describing the mean-flow modification. The stationary-mode amplitudes are calculated in the same manner as before using the integration of the rms stationary profile. The stationary boundary-layer structure that is followed for the [54|12] case saturates somewhat earlier than the structure that is followed for the [18|12] case, so the measurements begin at  $x/c = 0.25$ . Here the mean flow shown in Figure 88 is distorted but has not yet developed a distinct overturning feature. Spectra at  $z = 118.6, 122.2$ , and  $125.8$  mm (Figures 89–91) are very similar to what was seen in the upstream stations for the previous case. They indicate low disturbance amplitudes with activity confined to the traveling crossflow frequency band. The stationary structure has developed the overlap feature at  $x/c = 0.30$  (Figure 92), and the spectra show much higher amplitude fluctuations near 200 Hz (Figures 93–95). The spatial distribution of the 200-Hz fluctuations shown in Figure 96 is very similar to the type of distribution seen earlier.

At  $x/c = 0.33$ , there is still no secondary instability activity in the spectra, so the mean flow and spectra are not shown. At  $x/c = 0.34$ , there is the first indication of secondary instability activity near 3.0 kHz. The mean-flow velocity contours for this location are shown in Figure 97 and representative spectra are given in Figures 98–100. The distributions of 200-Hz and 3.0-kHz fluctuations are shown in Figures 101 and 102, respectively. Despite

the fact that the 3-kHz fluctuations are very low amplitude and can just be detected above the background, they are still clearly the same mode that was observed in the baseline case. It appears that this is a type-I mode that corresponds to the calculations performed by Malik *et al.* (1996). Both the 200-Hz and 3.0-kHz modes continue to develop as shown here for the next several chord stations.

By  $x/c = 0.37$ , there is evidence of 6.1-kHz activity. By  $x/c = 0.38$ , this activity has grown to the extent that it can be extracted into a distinct mode shape. The mean flow at  $x/c = 0.38$  is shown in Figure 103 and the representative spectra at  $z = 91, 94$ , and  $97$  mm are shown in Figures 104–106. What is striking about these spectra, especially the two at the low-momentum upwelling location and to its right (Figures 105 and 106), is that the low-frequency fluctuations appear to be much more important than they did in the previous [18|12] roughness experiment. The peak of the low-frequency spectrum is not above what was observed before, but the band of amplified frequencies extends to beyond 1 kHz, whereas before, these fluctuations did not extend past 400 Hz. So perhaps one of the most important features of the increased roughness amplitude is not the appearance of higher amplitude harmonics of the dominant stationary wave, but is instead the enhanced low-frequency velocity fluctuations. The distribution of 200-Hz fluctuations given in Figure 107 remains much the same as it was both in the previous figures and for [18|12] roughness, but here there is the additional feature of a local amplitude maximum to the left of the low-momentum upwelling location, situated close to the surface at  $Y = 0.5$  mm. It is possible that this feature is a consequence of the small stationary counter-rotating vortex whose existence was predicted by both PSE and DNS codes. That vortex may be drawing fluid that was lifted away from the surface by the main crossflow vortex back toward the wing.

The 3.0-kHz distribution at  $x/c = 0.38$  (Figure 108) is about the same as the other 3-kHz distribution figures for this and the previous configurations. However, the 6.1-kHz distribution (Figure 109) is quite different from what is observed in the baseline [18|12] roughness experiment. Now, the peak amplitude is not located at the same point on the high-velocity shear layer as the 3.0-kHz mode. Instead, the 6.1-kHz fluctuations are located on the top of the overturning region, the region with strong *wall-normal* gradients of the streamwise velocity and weak *spanwise* gradients of the streamwise velocity. This mode is different from what was observed for [18|12] roughness and instead appears to be what Malik *et al.* (1996) term a type-II secondary instability. It is still a Kelvin–Helmholtz instability, but now the energy production is dominated by the velocity gradient in  $Y$  and the  $u', v'$  fluctuation terms, whereas the mode-I instability is driven primarily by the velocity gradient in  $z$  and the  $u', w'$  fluctuations. Figure 109 shows that there is 6.1-kHz activity in the same part of the structure where the 3.0-kHz activity is greatest, so it appears that there are two separate modes at 6.1 kHz that are simultaneously active.

For  $x/c = 0.39$ , the mean-flow contour is given in Figure 110 and the representative spectra are shown in Figures 111–113. The fluctuation amplitude distributions for the 200-Hz, 3.0-kHz, and 6.1-kHz bands are given in Figures 114, 115, and 116, respectively. All of these modes retain their earlier character. The 6.1-kHz type-II mode is still not a high enough amplitude to render the background fluctuation level unimportant, so an energy integral would include a large contribution from the regions outside the mode. This is one drawback of the whole-field integration technique; it cannot be used to pinpoint very low amplitude modes. The mode-II zone continues to droop into the mode-I region of the figure. It is impossible to determine whether we are detecting a single mode or whether there continue to be two separate mechanisms that overlap both spatially and spectrally.

At  $x/c = 0.40$ , breakdown occurs. The mean-flow contours in Figure 117 indicate that



the mean-flow velocity has already lost much of its structure high in the boundary layer and the shear is increased to the left of the low-momentum upwelling as it was in the baseline case. The velocity-fluctuation spectra given in Figures 118–120 are not as dramatic as the spectra that indicated breakdown for the baseline [18|12] case, but the mode-I and the mode-II secondary instabilities have actually decreased, and lacking a more clear indication, we take this as the breakdown criteria in this case. What is new here is that following breakdown, the total rms velocity fluctuations that are shown in Figure 121 are coincident with the location of 200-Hz activity and not with either of the secondary instability modes. This suggests that although the secondary instability growth is obviously a major factor in triggering breakdown, for the increased roughness amplitude case, we cannot ignore the contribution of the lower frequency fluctuations.

The growth rates of the stationary crossflow vortex, the 200-Hz mode, and the 3.0-kHz mode are shown in Figure 122. The 6.1-kHz mode is not shown both because it never appears as a distinct mode and also because its amplitude is so low that the amplitude integration would include a significant contribution from the background. The 200-Hz mode grows throughout the entire boundary layer, with a growth rate that does not change nearly as much as one might expect given the dramatic variations that occur in the underlying mean flow. The 3.0-kHz mode-I instability has a lower growth rate here than was observed in the baseline case. It is not known whether this is a consequence of the growth being observed upstream of the baseline case or whether it is a purely local effect that only depends on the details of the stationary structure. The overall growth from where the mode can be detected until breakdown is much lower than for the baseline case, but here we believe that the lower frequency fluctuations are jointly responsible for breakdown, and this would mean that the secondary instability need not reach as high an amplitude before transition occurs.

The stationary-mode growth curve displays a notched appearance, that is, growth and saturation followed by a slight decrease in amplitude, then slightly more growth before breakdown. Although it is more obvious here, the same phenomenon occurs for the baseline case (Figure 87). This behavior was observed by Reibert *et al.* (1996), who performed similar mean-flow measurements over many wavelengths on another model. It would appear that this is a real effect and cannot be dismissed as experimental error. In Reibert *et al.*'s experiments, this phenomenon was observed for [18|12] and [48|12] roughness but not for [6|12] roughness. Here we observe the same phenomenon; higher-amplitude leading-edge roughness leads to a more pronounced two-stage saturation. Although the mechanism is not clear, the effect of roughness amplitude suggests that larger-amplitude harmonics of the dominant stationary wave, increased low-frequency fluctuation amplitudes, or a combination of both of these is responsible. One possible scenario is that downstream of saturation of the dominant wave, its harmonics continue to grow, but at too low an amplitude to be detected immediately. Saturation of the largest-amplitude harmonic gives the second saturation plateau observed in the overall mode amplitude curve. The effect would clearly be more pronounced for large roughness amplitudes that provide earlier saturation and higher-amplitude harmonics.

### 3.3.3 Decreased Reynolds number case

We now move to the case of [48|12] roughness with  $Re_c = 2.0 \times 10^6$ . This will demonstrate what effect slightly subcritical forcing has on the secondary instability and breakdown, because the lower Reynolds number means that the most amplified stationary wavelength is shorter than 12 mm. The lower Reynolds number will produce transition at a larger

value of  $x/c$ , but what is of primary interest is the identification of the secondary instability modes and the relative importance of the secondary modes to the fluctuations of the primary instability. The measurements for this case begin at  $x/c = 0.40$ , where there is already some overturning of the stationary structure (Figure 123). The fluctuation spectra (Figures 124–126) are all very low amplitude here, but a low-frequency mode at 200 Hz can be extracted (Figure 127) from the data.

The structure continues to develop with only the low-frequency mode detected until  $x/c = 0.46$ , where a secondary mode first appears. For this location, the mean-flow contours are shown in Figure 128 and representative spectra are shown in Figures 129–131. The 200-Hz low-frequency mode shown in Figure 132 is much more distinct here and it demonstrates the same sort of redistribution that was observed for the previous cases. The secondary instability fluctuation distributions at 2.4 kHz are given in Figure 133. The location demonstrates that in this case, as in the previous cases, the type-I mode is the dominant secondary instability mode.

Moving to  $x/c = 0.50$ , the mean-flow contour is given in Figure 134 and example spectra are given in Figures 135–137. The spectra show that for this Reynolds number and roughness configuration, the boundary layer has more of the character of the baseline case rather than of the high-amplitude roughness case that was presented in Section 3.3.2. The low-frequency mode does not extend to higher frequencies and the mode-I secondary instability frequency is growing significantly. The 200-Hz mode amplitude distribution is shown in Figure 138 and the mode-I secondary instability is shown in Figure 139. Both modes have very good definition. Although it is not apparent from the spectra, a 4.9-kHz mode can be extracted at this location. Its amplitude distribution (Figure 140) shows this to be a type-II mode produced by the wall-normal shear layer.

At  $x/c = 0.55$ , the appearance of the instability modes is quite dramatic. The mean-flow contours are typical (Figure 141), but now the spectra (Figures 142–144) show dramatic growth of the mode-I peak as well as at least two additional higher frequency modes at two and three times the frequency of the mode-I peak. The spatial distributions of the 200-Hz, 2.4-kHz, 4.9-kHz, and 7.5-kHz modes are shown in Figures 145–148. The 200-Hz mode appears in its usual position relative to the mean-flow structure. At this chord location, all of the high-frequency modes lie in the mode-I orientation where the  $\partial U/\partial z$  shear is strongest. There is no evidence of mode-II behavior.

Breakdown is first detected at  $x/c = 0.57$ . The mean-flow contour is not visibly changed (Figure 149), but the spectra near the wall to the left of the low-momentum upwelling region (Figure 150) have a flat, turbulent character. The other spectra (Figures 150–152) do not show turbulent characteristics, which explains why the structure high in the boundary layer persists. The total velocity-fluctuation rms is shown in Figure 153. This figure shows that the low-frequency activity and high-frequency activity are about equally important for this breakdown scenario because the two regions of the stationary structure have equal intensities. The fluctuation growth curves in Figure 154 confirm rapid growth of both the 2.4-kHz and 4.9-kHz type-I modes.

### 3.3.4 Increased Reynolds number case

As a fourth case we consider  $Re_c = 2.8 \times 10^6$  with [54|12] roughness. In this case the 12-mm crossflow waves produced by the roughness array are supercritical; without artificial roughness a 10.2-mm wave is detected. Because the basic secondary instability processes are now well established by the previous cases, the present case begins at  $x/c = 0.30$ , where the

secondary instability is first detected. What is immediately apparent from the mean-flow contour plot (Figure 155) is that short wavelength harmonics of the 12-mm mode are quite important here. To the left of the low-momentum upwelling that is centered at  $z = 85$  mm, there is a distinct plateau where there is not a strong  $\partial U/\partial z$  gradient. The mean-flow contours immediately suggest that the mode-I instability will not be as important in this case as in the previous cases because the region in which it is most strongly amplified has been reduced. Instead the type-II mode may play a more important role.

Velocity-fluctuation spectra for  $x/c = 0.30$  are given in Figures 156–159 for  $z = 80.2, 82.6, 85.0$ , and  $87.4$  mm. Four stations are used here instead of the three that are used above because of the more complex stationary structure. In all of these, a broad, high-amplitude band centered at 300 Hz is amplified. The very low amplitude secondary instability is just visible at  $z = 85.0$  mm, directly above the low-momentum upwelling center. For this  $Re_c = 2.8 \times 10^6$  case, 300 Hz is representative of the most amplified traveling crossflow wave and 3.6 kHz is representative of the mode-I instability. Distributions of these two modes are given in Figures 160 and 161, respectively. The 300-Hz mode is somewhat different from the shapes that occur for critical- and subcritical-wavelength forcing; here there are distinct maxima within the structure. The highest fluctuation amplitudes occur just to the right of the low-momentum upwelling region as in the previous cases, but the region near the wall to the left of the upwelling also contains significant low-frequency fluctuations, as does the upper part of the overturning region. Although the highest amplitude part of the structure occurs in roughly the same span position as in previous cases, it is somewhat lower in the boundary layer and elongated in span. The 3.6-kHz mode is barely detectable over the background fluctuations, but it can be identified as a type-I mode based on its location within the stationary structure.

Several stations downstream at  $x/c = 0.35$ , the mean flow (Figure 162) has a character similar to the mean flow at  $x/c = 0.30$ . The representative spectra at  $z = 66, 68, 70$ , and  $72$  mm (Figures 163–166) indicate that while the secondary instability has grown significantly, it does not exist as close to the wing on the left side of the stationary structure as it does in other cases that do not feature supercritical roughness forcing. The minor lobes of the 300-Hz mode (Figure 167) have disappeared by this station, but the mode retains the elongated shape it demonstrated at  $x/c = 0.30$ . Figure 168 confirms that the 3.6-kHz mode is not close to the wall and is in fact creeping along the stationary structure into the region occupied by the type-II instability. Previously, the behavior was the opposite. A type-II mode might be observed early, but it would tend to shift down into the mode-I region. The type-II mode is apparent in Figure 169.

Moving to  $x/c = 0.37$ , the mean-flow contours are given in Figure 170. The most interesting feature of this location is that the spectra (Figures 171–174) show that above the overturning region, the center of mode-II activity, the 6.5-kHz type-II mode is of nearly equal amplitude to the 3.6-kHz type-I mode, despite having started growing farther downstream. Mode II is more highly amplified, so this case appears to conform to the expectation that supercritical forcing can suppress the mode-I instability in favor of the mode-II instability. The 3.6-kHz and 6.5-kHz fluctuation distributions are given in Figures 175 and 176, respectively.

Breakdown is observed at  $x/c = 0.385$ . The mean-flow contours shown in Figure 177 do not appear markedly different; only the spectra above the low-momentum upwelling appear to have undergone breakdown. Figures 178–181 show that there is mode-I activity to the far left of the center of the vortex at  $z = 58$  mm, that breakdown has occurred in the overlap region between the type-I and low-frequency modes, and that mode-I and mode-II activity

is still present high in the boundary layer at  $z = 64$  mm. The total rms fluctuations for this location are given in Figure 182, and for this distribution they indicate that the amplitude of the mode-II secondary instability is nearly as large as the low-frequency mode.

Finally, the growth rates for the  $Re_c = 2.8 \times 10^6$  case are given in Figure 183. This figure shows that even though the traveling waves are higher amplitude, transition still appears to be triggered by the secondary instability modes. Breakdown occurs almost immediately following their detection. The growth of the secondary instability modes from the initially detected amplitude to their amplitude at breakdown for this case is the lowest level seen in any of the experiments, yet their presence appears to be critical. The most interesting feature of this case is the confirmation that the mode-II instability has a higher growth rate than the mode-I instability for this level of supercritical forcing because of the modified characteristic of the underlying mean flow.

### 3.3.5 Enhanced freestream fluctuation cases

If one is to claim that the secondary instability is solely responsible for breakdown of the laminar boundary layer, an important piece of supporting evidence could be that an increase in initial secondary instability amplitude leads directly to enhanced breakdown. In this subsection two means of introducing such an initial amplitude increase are attempted, freestream acoustic forcing and enhanced freestream turbulence. In both of these cases the idea is to choose a location just upstream of the breakdown location and observe whether the introduction of increased initial disturbance amplitude at the secondary instability frequencies moves transition location. The location just upstream of breakdown is used because this position includes the integrated effect of the entire instability process, and if there is to be any effect of enhanced initial amplitude it will be most obvious there. Detection of a positive result would then prompt more-detailed measurements.

The experimental results of Radeztsky *et al.* (1999) would tend to discount the likelihood of observing such a result for acoustic forcing, since in those experiments no effect on transition was observed with up to 95-dB acoustic forcing at various frequencies, including the secondary instability frequency range. However, those experiments were conducted without periodic leading-edge roughness and hence with a lower-amplitude, less-organized stationary-disturbance state. Introduction of periodic roughness for an acoustic forcing experiment might yield different results. Also, because the secondary instability grows so rapidly (as was shown in the previous section), even a significant increase in the initial amplitude of the secondary instability might not be manifested in a dramatic change in the transition location. Because breakdown occurs within a few percent chord of where the secondary modes destabilize, an increase in the initial amplitude could at most move the transition location upstream by this same few percent chord. Because the change in transition location could be quite subtle, it is not clear that this would have been detected, because at that time, the details that we now understand regarding the secondary instability growth were not known.

Acoustic forcing is more straightforward than turbulence forcing because it simply requires activating the speakers in the plenum upstream of the test section during an experiment. This means that it is possible to obtain high and low acoustic levels during a single run without any experimental hardware changes. Two tests are conducted, both with [54|12] roughness. The first test is conducted at  $Re_c = 2.4 \times 10^6$ ,  $x/c = 0.39$ ,  $z = 86$ – $89$  mm, the location of maximum secondary instability activity (see Figures 110 and 115). At these locations, sound frequencies between 2.0 kHz and 4.0 kHz were applied at the max-

imum amplitude available in the facility, 125 dB. At frequencies above 2.8 kHz, the sound amplitude decreased significantly due to the capability of the speakers (woofers designed for frequencies in the hundreds of Hertz). For the entire range of secondary instability frequencies, no change in the boundary-layer velocity-fluctuation spectrum was observed at any position within the stationary-vortex structure at the 39% chord position. The second test is conducted at  $Re_c = 2.0 \times 10^6$ ,  $x/c = 0.55$ ,  $z = 88$  mm (see Figures 141 and 146). These conditions are better than in the previous case because the mode-I secondary instability is centered near 2.4 kHz, within the capability of the speakers, and because the maximum amplitude of the secondary instability is much greater than the surrounding frequency band, so the spectral signal is unambiguous. However, as with the higher Reynolds number case, maximum-amplitude acoustic input from 1.5–3.0 kHz had no discernible effect on the boundary layer.

To assess the effect of freestream turbulence on the secondary instability, a small turbulence-generating grid is positioned in the contraction cone upstream of the test section. The grid produces  $u'_{\text{rms}}/U_\infty$  as high as 0.0029, high enough that traveling-wave-dominated flow might result. Spectra of the  $u'$  are flat up to about 800 Hz and roll off thereafter, reaching a minimum by 4 kHz. Tests at all three chord Reynolds numbers are performed with the turbulence grid in place. In all cases the traveling waves are enhanced, but in no case does the transition behavior change, and no changes are detected in the behavior of the secondary instability. The fundamental problem with this approach is the problem of applying high-frequency turbulence without also inducing the low-frequency content that will produce overwhelmingly large traveling primary crossflow waves.

These tests underscore a fundamental difficulty associated with boundary-layer stability experiments. One must always consider the mode of receptivity when attempting a controlled means of forcing an instability. For secondary instabilities, the problem is even more pronounced. Here, the receptivity encompasses both the initial entrainment of the freestream disturbance of the desired frequency and the subsequent evolution of that mode until the secondary instability becomes amplified.

## Chapter 4

# Absolute Instability

As described in the introduction, an alternative mechanism to saturation and secondary instability growth that could explain the insensitivity of the transition location to surface-roughness amplitude is the existence of an absolute instability. An absolute instability is a mode with zero group velocity and a positive temporal growth rate. The ramification of this behavior is that such a disturbance will grow to large amplitude at a particular location regardless of the initial disturbance amplitude or duration. The location at which the group velocity goes to zero depends on the local boundary-layer-scale Reynolds number and disturbance wavenumber, but not the disturbance amplitude. So in some sense, the existence of an absolute instability can guarantee transition at a particular location because initial disturbances of low amplitude are unavoidable. Previous researchers have found that for the related rotating disk problem, both a secondary instability (see Kohama, 1984, for example) and an absolute instability (Lingwood, 1995, 1996, described below) are possible. For the rotating disk, the selection mechanism for the transition process appears to be surface-roughness amplitude. For high roughness amplitudes, the secondary instability appears, whereas in low-disturbance environments, the absolute instability is observed (Lingwood, 1995). The possibility that swept-wing crossflow boundary layers are subject to an absolute instability and that this produces transition behavior insensitive to initial roughness amplitude is explored in this chapter.

### 4.1 Foundation

A rigorous mathematical framework exists to determine if a flow is stable, convectively unstable (i.e., unstable only for non-zero group velocity disturbances), or absolutely unstable. This method is referred to as Briggs' method (named after Briggs, 1964, who developed the method in connection with instabilities encountered in plasma physics). A review of the method with application to fluid stability is given by Huerre & Monkewitz (1990). In essence, to identify an absolute instability, one considers the long-time response of a linearized system to impulsive forcing. This problem is represented by  $\mathcal{L}G(x, t) = \delta(x)\delta(t)$ . The solution for the Green's function,  $G(x, t)$ , is

$$G(x, t) = \frac{1}{(2\pi)^2} \int_F \int_L \frac{e^{i(kx - \omega t)}}{D(k, \omega, R)} d\omega dk, \quad (4.1)$$

where the term in the denominator is the dispersion relation,  $D(k, \omega, R) = 0$ , that results from the solution of the homogeneous problem,  $\mathcal{L}\phi(x, t) = 0$ . Evaluating this integral re-

quires choosing contours in the complex  $\omega$ - and  $k$ -planes that maintain causality (i.e., no response for  $t < 0$ ) and properly treat singularities introduced by the dispersion relation.

The correct approach to choosing the integration contours for (4.1) is Briggs' method. First, causality requires that the contour  $L$  be a line located above any poles in the  $\omega$ -plane and be closed in the upper-half plane for  $t < 0$  (or the lower-half plane for  $t > 0$ ). Second, if there is to be an absolute instability, at least two poles,  $k(\omega)$ , must exist in the  $k$ -plane. For an  $L$  contour far enough above any  $\omega$ -plane singularities, the two singularities,  $k^+(\omega)$  and  $k^-(\omega)$ , are located above and below the real axis, respectively. As the  $L$  contour is lowered toward the real axis, the  $k^\pm(\omega)$  curves deform and the  $F$  contour (which was originally along the real  $k$ -axis) must be deformed as well to avoid the singularities. At some point, the  $k^\pm(\omega)$  curves touch at a so-called pinch point. This pinch point is denoted  $k_0$  and is where the group velocity,  $\partial\omega/\partial k$ , is zero, and where the upstream- and downstream-traveling modes merge. If the temporal growth rate  $\text{Im}(\omega_0)$  at  $k_0$  is positive, then this point represents an absolute instability. The mode is stationary and has positive temporal growth. If the temporal growth rate at  $k_0$  is negative, then the flow is not absolutely unstable; it may be convectively unstable (i.e., positive temporal growth rate for a non-zero group velocity) or stable.

## 4.2 Literature review

There are two reasons to consider an absolute instability in swept-wing boundary layers. First is the result obtained by Reibert *et al.* (1996) that the *amplitude* of roughness arrays near the first crossflow neutral point has almost no effect on the transition location. Recall that for 12-mm-spaced roughness arrays at 2.5% chord, roughness amplitudes of 6, 18, and 48  $\mu\text{m}$  produced transition at 49%, 51%, and 52% chord, respectively, at  $Re_c = 2.4 \times 10^6$ . This type of behavior would be expected for an absolute instability because regardless of the initial disturbance amplitude, the point at which the instability ceases to be convective and becomes absolute determines the point of transition. For Reibert *et al.*'s experiment, this would be between 49% and 52% chord. Different transition locations result from different *wavelength* disturbances, but this is simply because different wavelengths have different stability characteristics. Similarly, different chord Reynolds numbers produce different transition locations for identical roughness conditions because the critical Reynolds number (based on boundary-layer thickness) for the absolute instability is achieved at different chord locations.

One aspect of the transition-location data that does not fit with the *linear* Briggs' method model outlined in the previous section is the case of no artificial roughness. Radeztsky *et al.* (1999) found that for the same model and Reynolds number considered by Reibert *et al.* (1996) above, transition did not occur until 77% chord for a 0.25- $\mu\text{m}$ -rms surface finish. This means that a linear model may not be sufficient to describe the absolute instability present on the swept wing (if such an instability exists). Obviously the existence of artificial roughness is important for providing mean-flow distortion and modification of the basic state. So what must be considered is the possibility that the modified mean-flow field that results from the stationary crossflow disturbance supports an absolute instability. That possibility is a subject of the present investigation.

The other reason to consider an absolute instability for swept-wing transition is that an absolute instability is known to be present for the rotating disk boundary layer, a model problem for swept wings. The presence of an absolute instability was predicted by Lingwood (1995) using Briggs' method. Lingwood shows that the onset of the absolute instability occurs at  $R = 510$ , and experimentally determined transition Reynolds numbers for low-disturbance environments are centered about  $R = 513$ . In an experiment designed



specifically to investigate absolute instability behavior, Lingwood (1996) traced the evolution of transiently forced disturbances and showed that the radial group velocity does indeed go to zero with positive temporal growth and cause transition.

The rotating disk result is quite convincing, but the extension to swept wings is not as direct as might be imagined. Although each geometry is a 3-D crossflow boundary layer, the axial symmetry of the rotating disk means that one need only consider whether the *radial* group velocity goes to zero, because any disturbance that exists at a fixed radius will spread in the circumferential direction and contaminate an entire radial band. On swept wings, there is no such symmetry, so if the disturbance velocity goes to zero in only one direction the disturbance will still convect in the other direction, leaving the initial position disturbance free. Thus what could be thought of as an absolute instability of one direction is not sufficient for a true absolute instability. An extension of Briggs' method to the swept-wing boundary layer requires *simultaneous* pinching of the contours in both the streamwise- and crossflow-wavenumber planes.

The difficulty of achieving such simultaneous pinching is acknowledged by Lingwood (1997). She applies the generalized approach to an FSC boundary layer to determine whether swept-wing-type flows can support an absolute instability despite the more stringent criteria. The FSC geometry is a closer approximation to the swept wing than the rotating disk because it provides for pressure gradient and sweep and because it does not possess the symmetry inherent to the rotating disk. However, the FSC configuration retains an advantageous feature of the rotating disk: a similarity solution for the mean flow exists, making parametric studies relatively easy. Lingwood finds that a pinch point does exist for the chordwise wavenumber plane for very strong favorable pressure gradients ( $\beta_H = 1.0$ , i.e., near the attachment line) and high sweep angles (greater than  $80^\circ$ ), but no simultaneous spanwise pinching is observed. Thus a true linear absolute instability does not exist for FSC boundary layers, and furthermore, the parameter range for which a single direction becomes nonconvective is quite restricted.

Lingwood's approach was extended by Taylor & Peake (1998), who consider both FSC and true swept-wing configurations. These authors determine that the parameter range that supports single-direction pinch points is larger than the region identified by Lingwood (1997), but despite this, the flow still does not support an absolute instability. Taylor & Peake (1999) make yet another extension to compressible FSC and swept-wing flows and still find no absolute instabilities. For these more realistic configurations, even the attachment-line region identified by Lingwood (1997) is not absolutely unstable.

A critical feature that is not considered by any of these computations is that stationary crossflow waves on the swept wing render the disturbance evolution highly nonlinear. The modification of the mean-flow basic state means that the velocity profiles considered by Lingwood (1997) and Taylor & Peake (1998, 1999) do not represent what actually exists in the boundary layer near the transition location. In light of the saturation data of Reibert *et al.* (1996), it is conceivable that although the nondeformed linear basic state does not support an absolute instability, the highly modified nonlinear boundary layer does. It is with this possibility in mind that a transient forcing experiment is performed as part of the current swept-wing transition program.

### 4.3 Experimental approach

The most robust experimental means of determining whether an absolute instability exists is to apply a transient initial disturbance and observe the spatial and temporal evolution of

the resulting wave packet. If the group velocity goes to zero somewhere in the flow while the disturbance grows to large amplitude, an absolute instability exists at that location. This approach is the experimental equivalent to the Green's function solution that forms the basis of Briggs' method. This constitutes the "hard" but convincing approach suggested by Huerre & Monkewitz (1990) and is exactly the technique employed by Lingwood (1996) in the rotating disk experiment. In that work, Lingwood was able to position a hotwire at a single point for each radial position and construct a complete picture of the wave-packet growth both spatially and temporally using phase-locked averaging of the velocity signals and taking advantage of the disk's axial symmetry. The situation is somewhat more difficult for swept wings because the lack of symmetry and the importance of stationary structures mean that one cannot capture all of the necessary data at a single measurement location. Instead, measurements over a range of span for each chord location are required to provide information about the entire flow. For this reason, it is more efficient to consider step-function-type forcing rather than delta-function forcing so that measurements at many span locations can be obtained for a single forcing cycle.

The approach used here to determine whether swept-wing crossflow transition can support an absolute instability is to apply variable-amplitude leading-edge roughness and to determine whether there is a true insensitivity to initial conditions during a single experiment. For this experiment, we first supply low-amplitude (denoted "inactive") roughness using the variable-amplitude roughness insert described in Chapter 2 and observe that the flow is laminar for a particular chord location and Reynolds number. Then upon increasing the roughness amplitude (denoted by "active roughness") we observe that the flow becomes turbulent for the same location and Reynolds number. Inactive roughness is flush with the undeformed surface (except for the inherent flaws that were described previously); the active roughness is approximately 50  $\mu\text{m}$  displacement. For the inactive-roughness case, the flow at the measurement station is laminar and thus there is no absolute instability. For the active-roughness case, the flow is turbulent and if the transition mechanism is an absolute instability, it is active for the larger-amplitude roughness. Finally, the roughness amplitude is decreased to the original inactive amplitude. If the state of the flow reverts to laminar when the roughness is deactivated, then the transition mechanism must be purely convective because the large-amplitude disturbance has convected away from the measurement location. If the flow remains turbulent after the roughness amplitude is decreased, then the instability must be absolute somewhere upstream of the measurement location so that the large-amplitude disturbance can continue to exist without a disturbance source. Hysteresis is the marker for the absolute instability.

The experimental measurements consist of hotwire scans along lines of constant chord and constant wall offset. Each experiment sequence begins with three boundary-layer profiles at the starting, middle, and ending span positions. These profiles are used to identify the position of the wing surface in the traverse-oriented coordinate system using the nonlinear, progressive wall-search procedure described earlier. With the span points, a polynomial wall-position estimate is constructed. Using this estimate, the hotwire is positioned at a predetermined distance from the wall and the mean and fluctuating components of velocity are obtained in the same manner as in the secondary instability experiment. Once again the hotwire is oriented parallel to the local surface in the manner described in Chapter 2. The wall distance is selected to give an average value of the boundary-layer-to-edge velocity ratio of about 0.85. The exact value of this ratio is unimportant because the desired experimental output is simply turbulent/laminar, and this will be apparent at any point sufficiently close to the wall. The ratio 0.85 is simply a value for which large mean-velocity variations can

be expected and for which the hotwire will be far enough from the surface that it can be moved without danger of hitting the surface. The hotwire is stationary at each point while the velocity data are obtained, and following each point the traverse is moved in the positive span direction,  $z$ , and adjusted in  $Y$  to maintain the correct offset from the local wing surface. Following a complete run along the span, the hotwire is returned to the starting position, the pressure input to the variable-roughness insert is adjusted, and the next run is begun.

Several aspects of the experimental data are most revealing. The basic output of the experiment is the mean flow,  $U/U_{\text{edge}}$ , as a function of the span,  $z$ . For each Reynolds number and chord station considered, these curves are presented for an initial inactive-roughness case, an active-roughness case, and a second inactive-roughness case. The three states are acquired sequentially during a single, continuous wind-tunnel run. If the second inactive case is the same as the first, the boundary layer does not support an absolute instability. If the second inactive case is somehow fundamentally different from the first, then there is reason to believe that an absolute instability *may* be present in the boundary layer.<sup>1</sup> It is useful to observe the behavior of the stationary crossflow modes by calculating the spatial (spanwise) mean-flow power spectra. For each Reynolds number, at least two chord locations are considered and the behavior of the stationary modes (i.e., growing, saturated, or dissipating due to turbulent fluctuations) helps to demonstrate the laminar or turbulent state of the particular cases. Another means of understanding the flow is gained by examining the spanwise distribution of the fluctuating-velocity power at the most amplified frequency of the secondary instability. In the previous chapter it was observed that this amplitude grows by many orders of magnitude through transition, so the high-frequency fluctuations provide a more sensitive indication of the state of transition than the mean flow. Moreover, the results of the previous chapter provide a means of evaluating what is represented by the various high-frequency fluctuations. Finally, velocity-fluctuation spectra at particular locations are provided as another means of indicating the laminar, transitional, or turbulent state of the boundary layer.

## 4.4 Results and discussion

### 4.4.1 Baseline case

For the baseline case of  $Re_c = 2.4 \times 10^6$ , the two most revealing measurement stations are at  $x/c = 0.43$  and  $x/c = 0.45$ . However, to place the results at those locations in context, it is useful to first examine results from  $x/c = 0.40$ , a (nearly) purely laminar case for both active and inactive leading-edge roughness. Figure 184 shows the mean flow at  $x/c = 0.40$  and  $Y = 1.5$  mm. It is evident in this figure that although the active-roughness case has larger-amplitude mean-flow deformation, the inactive-roughness case shows significant deformation as well. The spatial power spectra of these spanwise mean-flow data (Figure 185) reveal that in the active-roughness case nearly all the stationary disturbance power is concentrated in the 12-mm mode, with some growth of the 6- and 4-mm harmonics. These spectra are generated from 128 span locations as shown in Figure 184. The original data are spaced at 1-mm increments of  $z$ . For the inactive roughness, there is a broader but much lower amplitude distribution of stationary-disturbance power centered about the most amplified

<sup>1</sup>If an absolute instability is suspected based on the initial experiments, a more convincing set of experiments is required. These would consist of point-by-point phase-locked averaging over many forcing cycles to reconstruct the disturbance velocities throughout the boundary layer.

stationary wavelength. This is exactly what should be expected for low-amplitude, randomly distributed leading-edge roughness. It is clear that although the variable-amplitude roughness insert is not capable of producing zero-amplitude stationary-mode distortion, the amplitudes of the disturbances that result are much lower than those of the activated state. Returning to the mean-flow curves of Figure 184, notice that there is a strong feature near  $z = 75$  mm. The velocity minimum that exists for both the high- and low-amplitude roughness configurations is a nascent turbulent wedge. It is nearly impossible to remove all the isolated receptivity sources from the variable-roughness insert, and features like the isolated wedge in Figure 184 cannot be eliminated from the experiment. A close inspection of the roughness insert failed to reveal any potential sources of this particular disturbance. As long as features such as this are isolated and can be reasonably demonstrated not to dominate the transition behavior being investigated, they do not interfere with the ability to draw conclusions about an absolute instability. Admittedly it would be preferable to work with an absolutely clean basic state, but nature of the variable-roughness system makes it impractical to achieve such a condition.

Moving to  $x/c = 0.43$ , Figure 186 provides the first indication that an absolute instability is *not* responsible for transition. This figure represents three back-to-back spanwise mean-flow scans at  $Y = 2.0$  mm that were obtained during a continuous wind-tunnel run for which the roughness was first nominally inactive, then activated, and finally deactivated. The two inactive cases are indistinguishable to the degree that can be reasonably expected from the experiment. The spatial spectra given in Figure 187 show that here the active-roughness case has a higher-amplitude 12-mm mode than the inactive cases, but the amplitude is much lower than the active case at  $x/c = 0.40$ , whereas for the inactive cases the entire amplified crossflow wavelength band is still growing. In the active case, the flow has ended, or it is in the final stages of breakdown, at all spanwise locations when the roughness is activated. With the possible exception of the turbulent wedge, the flow is entirely laminar for both inactive-roughness cases. If an absolute instability were responsible for transition, then the second inactive-roughness case would be markedly different from the first. Clearly this is not so. For this parameter set, at least, the instability is convective.

Velocity-fluctuation data are useful to demonstrate that breakdown has occurred for the active-roughness case but not the inactive case, and to further demonstrate that the two inactive cases are essentially identical. Figure 188 shows the spanwise distribution of 3.0-kHz velocity-fluctuation power. (Recall that 3 kHz is the center of the mode-I secondary instability frequency band for  $Re_c = 2.4 \times 10^6$ .) The active-roughness case has reached turbulent or nearly turbulent fluctuation levels everywhere, whereas the inactive cases are still completely laminar, with the exception of the rogue turbulent wedge centered at  $z = 66$  mm. Near  $z = 108$  mm and  $z = 120$  mm there are signs that the secondary instability is amplified for the inactive case, but the fluctuation levels at these points indicate that the flow is still laminar.

Figure 189 includes velocity-fluctuation spectra for the first inactive- and active-roughness cases at  $z = 24$  mm. For the active-roughness setting, this is a region of minimal 3.0-kHz disturbance amplitude in a neighborhood of 12-mm-periodic 3.0-kHz activity. There is a band of higher frequency activity, however. This suggests that  $z = 24$  mm is one of the regions in the upper-middle or upper-right of the fluctuation distribution figures of the previous chapter where there is never mode-I activity but where there are some mode-II fluctuations. The inactive-roughness spectra are completely benign.

For  $z = 31$  mm (Figure 190), the 3.0-kHz power of the active-roughness case is at a local maximum and the spectral characteristics suggest that this is a region of mode-I

secondary instability activity just prior to the end of breakdown. The inactive-roughness case appears fully laminar without any signs of secondary instability growth. At  $z = 46$  mm (Figure 191), the onset of breakdown in the active case is farther upstream than it is for the structure at  $z = 31$  mm, because at  $z = 46$  mm, active roughness produces fully turbulent flow. At  $z = 66$  mm, the center of the turbulent wedge (Figure 192), the active-roughness case is indeed turbulent, but the inactive case is still in the midst of secondary instability growth as evident from the distinct bands of mode-I and mode-II activity in the velocity-fluctuation spectrum. It is somewhat surprising that the behavior produced by the two roughness configurations is different here. One might expect that whatever feature inherent to the roughness device that produces the wedge would be sufficient to cause earlier transition regardless of the amplitude of the periodic disturbances on which it is superposed. However, the breakdown of the feature generated by the isolated roughness does depend on the background periodic disturbance. The details of the primary instability interaction between a large amplitude isolated feature and a lower-amplitude periodic field have not been investigated, and this may represent an important topic for further study. It is easy to imagine that on an actual aircraft employing subcritically spaced roughness arrays to suppress crossflow transition, such isolated features would be plentiful, and it is unclear what the resulting behavior would be and whether isolated roughness elements could prevent such a system from working.

Moving finally to  $z = 108$  mm (Figure 193), the spectra associated with the inactive-roughness amplitude peak contain the early stages of the mode-I secondary instability growth and the active-roughness case is fully turbulent. Taken together, the spanwise mean flow (Figures 186 and 187), the 3-kHz fluctuation curves (Figure 188), and the individual point spectra (Figures 189–193) show that the instabilities present can be fully understood in terms of secondary instability growth, and that there is no indication of an absolute instability.

At the third chord location for  $Re_c = 2.4 \times 10^6$ ,  $x/c = 0.45$ , the now fully turbulent active-roughness case exhibits significantly lower spanwise mean-flow variations because of the continuing turbulent dissipation of the crossflow vortices. The amplitude of the variations in Figure 194 is visibly reduced relative to the upstream locations, and the spatial spectra in Figure 195 confirm this. Even the minimum in the mean-flow velocity associated with the turbulent wedge has disappeared. The data that are obtained prior to and following the turbulent active-roughness case are again nearly identical. There is no hysteresis and no absolute instability. The distributions of 3.0-kHz velocity-fluctuation power in Figure 196 show that the active-roughness case consists of fully turbulent flow. The inactive cases remain almost entirely laminar, except for the turbulent wedge that has grown to cover approximately 24 mm of the span.

For this chord station, the most interesting fluctuation spectra are obtained at  $z = 60$  mm and  $z = 102$  mm. At  $z = 60$  mm (Figure 197), the wedge is now turbulent for the inactive case, with some remnant of the mode-I secondary instability still visible. The active case is turbulent as it was at the upstream station. At  $z = 102$  mm (Figure 198), the active-roughness case remains turbulent but here the secondary instability is strongly amplified in the inactive case. So overall, the  $x/c = 0.45$  data confirm that the instabilities driving transition are convective.

#### 4.4.2 Increased Reynolds number case

For Reynolds number  $Re_c = 2.8 \times 10^6$ , the two chord stations considered are  $x/c = 0.38$  and  $x/c = 0.40$ . Starting at  $x/c = 0.38$ , Figure 199 indicates that, as in the baseline case, there is no hysteresis when changing from inactive to active and back to inactive leading-edge roughness. So here, too, there is no indication of an absolute instability. The spatial spectrum of the mean flow (Figure 200) shows that the active-roughness case produces a distinct 12-mm mode, whereas the inactive case again produces a broad, low-amplitude response. Note that the interesting feature of this higher Reynolds number is not necessarily the different transition location, but the fact that for this condition the most amplified stationary crossflow wave is not the 12-mm wave, but is instead a shorter wavelength. For this case the forced wavelength is detuned from the most amplified wavelength that the spatial spectrum indicates is at  $\lambda_s = 10.2$  mm. The spectral resolution is quite poor because the emphasis of the experiment is on rapid data collection rather than mode identification. The wavelength resolution is about 1.6 mm at 10.2 mm. At  $Re_c = 2.8 \times 10^6$ , 4.0 kHz is near the center of the mode-I secondary instability frequency band. The distributions of 4.0-kHz velocity-fluctuation power for the various roughness configurations are given in Figure 201. It is evident in this figure that with activated roughness the entire span range is turbulent, whereas with inactive roughness there is a large region of laminar flow and two turbulent regions. For the entire span, no hysteresis is observed in the fluctuation levels as the upstream roughness state is altered. Velocity-fluctuation spectra are given for three span locations:  $z = 23$ , 26, and 84 mm. At  $z = 23$  mm (Figure 202), the inactive-roughness case shows amplified mode-I activity centered at 4.0 kHz and the active-roughness case is turbulent. Nearby at  $z = 26$  mm (Figure 203), there is no secondary instability fluctuations in the inactive case. Finally at  $z = 84$  mm (Figure 204), the flows of both the inactive and active cases are fully turbulent. The roughness insert used for these  $Re_c = 2.8 \times 10^6$  experiments is the same as that used for the  $Re_c = 2.4 \times 10^6$  experiments, so the turbulent flow observed near  $z = 84$  mm is likely part of the same turbulent wedge structure that is discussed above.

Moving downstream to  $x/c = 0.40$ , the mean-flow curves (Figure 205) again show no evidence of an absolute instability. The two inactive-roughness cases, however, do show more significant differences than some of the previous cases. The reason for this is the difficulty in obtaining good measurements at the breakdown location, especially at high Reynolds numbers. The high Reynolds number produces a thin boundary layer and rapid tunnel heating; both make it difficult to maintain good control of the hotwire position in terms of nondimensional wall offset. The result is somewhat reduced repeatability of the experiment. Bear in mind that an absolute instability would be manifested by gross changes in the transition-region boundary-layer behavior, and clearly this does not occur. The spatial spectra of the mean-flow data (Figure 206) reinforce that the 12-mm stationary crossflow waves generated by the artificial roughness array are rapidly dissipating due to turbulent fluctuations, but the shorter wavelength natural waves continue to grow. And, finally, the distributions of 4.0-kHz fluctuations given in Figure 207 confirm again that the flow recovers an initially laminar state when the activated roughness is removed.

#### 4.4.3 Decreased Reynolds number case

As a final case consider  $Re_c = 2.0 \times 10^6$ . This Reynolds number provides a condition for which the 12-mm crossflow waves produced by the activated roughness are subcritical. Here the first measurement station is at  $x/c = 0.58$ . The mean-flow curves are given in Figure 208,

the spatial spectra of the mean-flow curves are given in Figure 209, and the distributions of 2.0-kHz mode-I fluctuations are given in Figure 210. No hysteresis is detected in any of these curves. The spatial spectra show that the dominant crossflow wavelength with zero-amplitude artificial roughness is about 13.5 mm. This station exhibits the widest band of amplified wavelengths of any examined thus far. The band of amplified fundamental wavelengths extends from 19.5 mm to 8.8 mm and both its first and second harmonics are visible. The active-roughness case is much more regular in span, and it has lower-amplitude mean-flow variations.

One consequence of the irregularity of the disturbance field is that the individual point spectra in Figures 211–214 exhibit a variety of behaviors. Even though the active-roughness case has a much higher fluctuation level across the span, the inactive cases actually break down near  $z = 16$  mm (Figure 211) where the active-roughness case does not. Furthermore, the active-roughness fluctuations at  $z = 16$  mm are centered at 3.0 kHz, not 2.0 kHz, as are the highest-amplitude inactive-roughness fluctuations. This may represent behavior nearly along the lines of that observed by Saric *et al.* (1998), who used subcritically spaced roughness arrays to suppress transition. The active case is not sufficient to prevent transition in general, however. At  $z = 53$  mm (Figure 212), the active-roughness case is fully turbulent while the inactive-roughness case has almost zero disturbance amplitude, as it does over most of the span.

Because peaks at both 2.0 kHz and 3.0 kHz are observed for  $x/c = 0.58$ , the distributions of 3.0-kHz fluctuations are given in Figure 215 to supplement the 2.0-kHz fluctuation distribution plots given in Figure 210. The 3.0-kHz mode is nearly identical to the 2.0-kHz mode. Both are active across the span for the active-roughness case, but they only appear at high amplitudes near  $z = 16$  mm for the inactive-roughness case.

The final absolute instability test is performed at  $x/c = 0.60$ . The mean flow for this case is given in Figure 216. There is no change in behavior of the inactive-roughness cases, so there is no absolute instability. In Figure 217, the spanwise spectra of the inactive-roughness cases indicate that the flow there has undergone amplitude saturation; the peak of the most amplified mode is unchanged from  $x/c = 0.58$ . The active-case spectrum indicates that the forced stationary wave is dissipating due to the higher fluctuation levels. Figures 218 and 219 show that the fluctuations are still growing for the active case and the high-amplitude peak in the inactive cases, but that across most of the span, the inactive case remains free of high-frequency disturbances.

So for three cases on the ASU(67)-0315 wing,  $Re_c = 2.4 \times 10^6$ ,  $Re_c = 2.8 \times 10^6$ , and  $Re_c = 2.0 \times 10^6$ , the data show that there is no evidence of an absolute instability prior to breakdown of the crossflow boundary layer. Moreover, in every case, the behavior of both the stationary mode and the high-frequency fluctuations may be understood in terms of secondary instability growth. Breakdown appears to be driven by that mechanism.

## Chapter 5

# Conclusions

This work consists of two parallel tasks: an experimental investigation of the breakdown mechanism of crossflow-dominated swept-wing boundary layers and a development effort intended to integrate a MEMS-based roughness-actuator system into a swept-wing experiment. The MEMS development work reveals a number of shortcomings of MEMS technology (at its present state) as applied to an external flow-control application. The MEMS actuators are not capable of providing the required surface control both because of quality control issues and because of installation difficulties. Without better manufacturing and integration capabilities, MEMS technology will not be useful for swept-wing boundary-layer control.

The experimental phase is intended to provide conclusive data regarding two potential breakdown mechanisms of crossflow-dominated swept-wing boundary layers: a high-frequency secondary instability and an absolute instability. The data presented here overwhelmingly support the idea that an absolute instability *is not* responsible for breakdown. Instead, the high-frequency secondary instability mechanism always appears to play a dominant role. If an absolute instability existed, it would be detected by a transient-forcing experiment performed in a low-disturbance environment. Chapter 4 consists of just such an experiment, and no evidence is found for this type of instability at each of three Reynolds numbers,  $Re_c = 2.0 \times 10^6$ ,  $Re_c = 2.4 \times 10^6$ , and  $Re_c = 2.8 \times 10^6$ , using variable-amplitude leading-edge surface roughness on a 12-mm-spaced array. That array provides subcritical, critical, and supercritical wavelength forcing, respectively, for these three Reynolds numbers.

On the other hand, data from this experiment show that when stationary crossflow waves reach saturation amplitudes, breakdown is always triggered via a secondary instability mechanism. The secondary instability modes observed in this experiment are destabilized in the saturated region and grow much more rapidly than the low-frequency mode that has its origins in the most amplified traveling crossflow mode predicted by linear theory. Local breakdown is always observed within a few percent chord of where the secondary instability is first detected.

The secondary instability modes that are observed may be classified into two general categories, called type-I and type-II modes. What are termed type-I modes (after Malik *et al.*, 1996) lie inboard of the low-momentum upwelling zone of the stationary crossflow vortices. These modes are Kelvin-Helmholtz instabilities of the *spanwise* shear layer of the streamwise flow. This is the same type of behavior that is observed by Swearingen & Blackwelder (1987) for secondary instabilities of Görtler vortices; spanwise gradients are more important. The type-I mode extends diagonally in the  $(Y, z)$  plane, from close to the



wall at the farthest point from the stationary vortex center to above the low-momentum upwelling center. The secondary instability can be imagined as wrapping around the outside of this portion of the stationary vortex. This is the behavior shown very clearly in the rotating disk flow visualizations of Kohama (1984, 1985). In nearly all circumstances, the lowest-frequency secondary instability is type I and is the largest amplitude secondary instability mode that is detected. In many instances, one or more higher-frequency type-I modes coexist in the same location. These are observed at close to integer multiples of the lowest-frequency type-I mode.

Although instability modes at integer multiples at the same spatial location strongly suggest harmonics of the dominant mode, the growth rates do not always support this. In the baseline case, the growth rates of the fundamental 3.0-kHz type-I mode and the 6.1-kHz type-I mode have nearly equal growth rates. The 6.1-kHz mode would be expected to have twice the growth rate of the fundamental were it a harmonic. However, growth rates are more easily obtained for the  $Re_c = 2.0 \times 10^6$ , [54|12] roughness case, and here the growth rate of the 4.9-kHz multiple of the 2.4-kHz fundamental type-I mode is about twice as large. For the same case, a 7.5-kHz type-I mode was observed as well, and the spectra show that even higher multiples exist. The other cases do not provide sufficiently good data to obtain reliable higher-frequency-mode growth-rate comparisons. In light of the limited and conflicting data, it is unclear whether these are harmonics that we cannot measure accurately, or whether they are distinct modes. In any case, these results show that to properly understand the breakdown region in as much detail as possible, narrow frequency bands should be investigated separately. As many as five or more instability modes exist in some cases, so tracking the behavior of bands as wide as a kilohertz or more can lump the behavior of many modes into a single result.

In one instance,  $Re_c = 2.4 \times 10^6$  with [18|12] roughness, a high-frequency mode of lower frequency than the most amplified type-I mode was identified. This mode existed closer to the wall than the typical type-I shape, and it may play a role in triggering breakdown where the type-I mode makes its closest approach to the wall. This mode was not identified in any other case and was difficult to separate from the higher-amplitude 3.0-kHz mode.

The second type of secondary instability mode, termed a type-II mode, was observed much less frequently than the type-I modes. This mode exists high in the boundary layer above and somewhat outboard of the low-momentum upwelling center. This instability is of the Kelvin-Helmholtz class, as is the type-I mode, but the type-II mode exists in the *wall-normal* shear layer of the streamwise flow. The type-II mode occurs at about twice the frequency of the highest-amplitude type-I mode. It is often overwhelmed by the growth of the (possible) harmonic of the type-I mode and is therefore extremely difficult to track experimentally. One exception is the supercritical forcing case,  $Re_c = 2.8 \times 10^6$  with [54|12] roughness. For this configuration, the spanwise shear region is reduced and the type-I modes do not reach the amplitude they do under more favorable conditions. In this environment, the type-II mode is detected more easily and plays an important part in triggering transition.

Although the low-frequency fluctuations that correspond to the most amplified primary disturbance are not the focus here, their behavior is quite interesting and could represent a useful topic of further study. These fluctuations start as a spanwise-uniform mode at chord locations where mean flow is not deformed by the stationary vortices. However, these fluctuations appear to be acted upon by the stationary vortices in the same manner as the mean flow, and they become highly localized within the stationary structure even before the stationary mode saturates. Despite the modification of the mean flow and the spatial

redistribution of the low-frequency mode that results, these modes appear to grow linearly throughout transition.

It is observed by comparing the high-amplitude [54|12] roughness case at  $Re_c = 2.4 \times 10^6$  to the low-amplitude [18|12] case at the same Reynolds number that an increase in roughness amplitude increases the amplitude of the low-frequency mode. However, despite the higher amplitude of the low-frequency mode, breakdown appears to be triggered by the appearance of the secondary instability. Even when the low-frequency mode is higher amplitude than the secondary instabilities, the breakdown location always occurs within a few percent chord of where the secondary instability destabilizes. Conclusive evidence for this could be provided by enhancing the initial amplitudes of the secondary instability independently and observing a change in transition behavior. Unfortunately, attempts to do this both with freestream sound and enhanced freestream turbulence were unsuccessful because of the difficulty of directly exciting the secondary instability.

Taken as a whole, the experiments demonstrate the range of behaviors that are exhibited by the secondary instability, and they emphasize that to predict transition location in crossflow boundary layers, one must be capable of predicting secondary instability behavior. What we have seen is that the most important factor for the secondary instability is the wavelength of the stationary disturbances. Different wavelengths, and their classification as subcritical, critical, or supercritical, play an important role in selecting the dominant secondary instability mode, either type I or type II. Previous experiments have shown that roughness amplitude may not be important for determining transition location because of amplitude saturation. That idea is extended here by noting that increased roughness amplitudes increase the amplitudes of low-frequency disturbances, but these do not appear to trigger breakdown independently. This may not be so for low-frequency disturbances of larger amplitudes than are produced in this experiment, but the low-disturbance environment is more representative of flight and therefore represents the most important practical case. In the low-disturbance environment, breakdown always appears to be triggered by secondary instability growth.

# Bibliography

- ARNAL, D. 1997 Laminar-turbulent transition: Research and applications in France. *AIAA Paper* 97-1905.
- BEARMAN, P. W. 1971 Corrections for the effect of ambient temperature drift on hot-wire measurements in incompressible flow. *DISA Information* 11.
- BEVINGTON, P. R. 1969 *Data Reduction and Error Analysis for the Physical Sciences*. New York: McGraw-Hill.
- BIPPES, H. 1999 Basic experiments on transition in three-dimensional boundary layers dominated by crossflow instability. *Prog. Aero. Sci.* 35 (4), 363-412.
- BRIGGS, R. J. 1964 *Electron-Stream Interaction with Plasmas*. Cambridge: MIT Press.
- CARRILLO, JR., R. B. 1996 Distributed-roughness effects on stability and transition in swept-wing boundary layers. Master's thesis, Arizona State University.
- CHAPMAN, K. L. 1996 Structure identification within a transitioning swept-wing boundary layer. PhD thesis, Clarkson University.
- CHAPMAN, K. L., REIBERT, M. S., SARIC, W. S. & GLAUSER, M. N. 1998 Boundary-layer transition detection and structure identification through surface shear-stress measurements. *AIAA Paper* 98-0782.
- CHOUDHARI, M. 1994 Roughness-induced generation of crossflow vortices in three-dimensional boundary layers. *Theor. Comput. Fluid Dyn.* 6, 1-30.
- COLLIS, S. S. & LELE, S. K. 1999 Receptivity to surface roughness near a swept leading edge. *J. Fluid Mech.* 380, 141-168.
- CROUCH, J. 1997 Transition prediction and control for airplane applications. *AIAA Paper* 97-1907.
- CROUCH, J. D. 1994 Theoretical studies on receptivity of boundary layers. *AIAA Paper* 94-2224.
- DAGENHART, J. R. 1992 Crossflow stability and transition experiments in swept-wing flow. PhD thesis, Virginia Polytechnic Institute and State University, also available as NASA-TP 1999-209344 by J. R. Dagenhart & W. S. Saric.
- DAGENHART, J. R. & SARIC, W. S. 1999 Crossflow stability and transition experiments in swept-wing flow. *NASA TP* 1999-209344. Originally appeared as a Virginia Polytechnic Institute PhD thesis by Dagenhart, 1992.

- DEYHLE, H. & BIPPES, H. 1996 Disturbance growth in an unstable three-dimensional boundary layer and its dependence on initial conditions. *J. Fluid Mech.* **316**, 73–113.
- VON DOENHOFF, A. E. & BRASLOW, A. L. 1961 The effect of distributed roughness on laminar flow. In *Boundary-layer control* (ed. Lachmann). Pergamon.
- FEDOROV, A. V. 1989 Excitation of waves of instability of the secondary flow in the boundary layer on a swept wing. *J. App. Mech. Tech. Phys.* **29**, 643–648.
- FISCHER, T. M. & DALLMANN, U. 1991 Primary and secondary stability analysis of a three-dimensional boundary layer. *Phys. Fluids A* **3** (10), 2378–2391.
- FISCHER, T. M., HEIN, S. & DALLMANN, U. 1993 A theoretical approach for describing secondary instability features in three-dimensional boundary layer flows. *AIAA Paper* 93-0080.
- GRAY, W. E. 1952 The effect of wing sweep on laminar flow. *Tech. Rep. Aero 255*. RAE.
- GREGORY, N., STUART, J. T. & WALKER, W. S. 1955 On the stability of three-dimensional boundary layers with application to the flow due to a rotating disk. *Philos. Trans. R. Soc. London Ser. A* **248**, 155–199.
- HAYNES, T. S. & REED, H. L. 2000 Simulation of swept-wing vortices using nonlinear parabolized stability equations. *J. Fluid Mech* **405**, 325–349.
- HERBERT, TH. 1997a On the stability of 3-D boundary layers. *AIAA Paper* 97-1961.
- HERBERT, TH. 1997b Transition prediction and control for airplane applications. *AIAA Paper* 97-1908.
- HERBERT, TH. & LIN, N. 1993 Studies of boundary-layer receptivity with parabolized stability equations. *AIAA Paper* 93-3053.
- HÖGBERG, M. & HENNINGSON, D. 1998 Secondary instability of crossflow vortices in Falkner–Skan–Cooke boundary layers. *J. Fluid Mech.* **368**, 339–357.
- HUERRE, P. & MONKEWITZ, P. A. 1990 Local and global instabilities in spatially developing flows. *Ann. Rev. Fluid Mech.* **22**, 473–537.
- VAN INGEN, J. L. 1956 A suggested semi-empirical method for the calculation of the boundary layer transition region. *Tech. Rep. UTH1-74*. Univ. of Tech., Delft.
- JUILLEN, J. C. & ARNAL, D. 1990 Etude expérimentale du dé clenchement de la transition par rugosités et par rainer sur de bord d'attaque d'une aile en flèche en écoulement incompressible. *Tech. Rep.* 51/5018.35. CERT/ONERA, Toulouse, France.
- KACHANOV, Y. S. 1996 Experimental studies of three-dimensional instability of boundary layer. *AIAA Paper* 96-1976.
- KAWAKAMI, M., KOHAMA, Y. & OKUTSU, M. 1999 Stability characteristics of stationary crossflow vortices in three-dimensional boundary layer. *AIAA Paper* 99-0811.
- KOHAMA, Y. 1984 Study on boundary layer transition of a rotating disk. *Acta Mechanica* **50**, 193–199.

- KOHAMA, Y. 1985 Turbulent transition process of the spiral vortices appearing in the laminar boundary layer of a rotating cone. *PhysicoChemical Hydrodynamics* **6** (5), 659–669.
- KOHAMA, Y. 1987 Some expectations on the mechanism of cross-flow instability in a swept-wing flow. *Acta Mechanica* **66**, 21–38.
- KOHAMA, Y., SARIC, W. S. & HOOS, J. A. 1991 A high-frequency, secondary instability of crossflow vortices that leads to transition. In *Proc. of the Royal Aero. Soc. Conf. on Boundary-Layer Trans. and Control*.
- KOHAMA, Y., UKAKU, M. & OHTA, F. 1987 Boundary-layer transition on a swept cylinder. In *Proceedings of the International Conference on Fluid Mechanics*. Beijing: Peking University Press.
- LERCHE, T. 1996 Experimental investigation of nonlinear wave interactions and secondary instability in three-dimensional boundary-layer flow. In *6th European Turbulence Conference, Lausanne* (ed. S. Gavrilakis, L. Machiels & P. A. Monkewitz), pp. 357–360.
- LERCHE, T. & BIPPES, H. 1996 Experimental investigation of cross-flow instability under the influence of controlled disturbance excitation. In *Trans. boundary layers in aeronautics* (ed. R. Henkes & J. van Ingen).
- LI, F. & MALIK, M. R. 1995 Fundamental and subharmonic secondary instabilities of Görtler vortices. *J. Fluid Mech.* **297**, 77–100.
- LINGWOOD, R. J. 1995 Absolute instability of the boundary layer on a rotating disk. *J. Fluid Mech.* **299**, 17–33.
- LINGWOOD, R. J. 1996 An experimental study of absolute instability of the rotating-disk boundary layer flow. *J. Fluid Mech.* **314**, 373–405.
- LINGWOOD, R. J. 1997 On the impulse response for swept boundary-layer flows. *J. Fluid Mech.* **344**, 317–334.
- MALIK, M. R., LI, F. & CHANG, C.-L. 1994 Crossflow disturbances in three-dimensional boundary layers: Nonlinear development, wave interaction and secondary instability. *J. Fluid Mech.* **268**, 1–36.
- MALIK, M. R., LI, F. & CHANG, C.-L. 1996 Nonlinear crossflow disturbances and secondary instabilities in swept-wing boundary layers. In *IUTAM Symposium on Nonlinear Instability and Transition in Three-Dimensional Boundary Layers* (ed. P. W. Duck & P. Hall), pp. 257–266. Kluwer.
- MALIK, M. R., LI, F., CHOUDHARI, M. M. & CHANG, C.-L. 1999 Secondary instability of crossflow vortices and swept-wing boundary layer transition. *J. Fluid Mech.* **399**, 85–115.
- MEYER, F. & KLEISER, L. 1989 Numerical investigation of transition in 3D boundary layers. In *Fluid Dynamics of Three-Dimensional Turbulent Shear Flows and Transition*, AGARD CP 438.
- MÜLLER, B. 1990 Experimental study of the travelling waves in a three-dimensional boundary layer. In *IUTAM Symposium on Laminar-Turbulent Transition, Toulouse* (ed. D. Arnal & R. Michel), pp. 489–499. Springer.

- MÜLLER, B. & BIPPES, H. 1989 Experimental study of instability modes in a three-dimensional boundary layer. In *Fluid Dynamics of Three-Dimensional Turbulent Shear Flows and Transition*, AGARD CP 438.
- POLL, D. I. A. 1985 Some observations of the transition process on the windward face of a long yawed cylinder. *J. Fluid Mech.* **150**, 329–356.
- PRESS, W. H., TEUKOLSKY, S. A., VETTERLING, W. T. & FLANNERY, B. P. 1992 *Numerical Recipes in C: The Art of Scientific Computing*, 2nd edn. New York: Cambridge University Press.
- RADEZTSKY, JR., R. H. 1994 Growth and development of roughness-induced stationary crossflow vortices. PhD thesis, Arizona State University.
- RADEZTSKY, JR., R. H., REIBERT, M. S. & SARIC, W. S. 1999 Effect of isolated micron-sized roughness on transition in swept-wing flows. *AIAA J.* **37** (11), 1371–1377, originally appeared as *AIAA Paper* 93-0076.
- REED, H. L. & SARIC, W. S. 1989 Stability of three-dimensional boundary layers. *Ann. Rev. Fluid Mech.* **21**, 235–284.
- REIBERT, M. S. 1996 Nonlinear stability, saturation, and transition in crossflow-dominated boundary layers. PhD thesis, Arizona State University.
- REIBERT, M. S. & SARIC, W. S. 1997 Review of swept-wing transition. *AIAA Paper* 97-1816.
- REIBERT, M. S., SARIC, W. S., CARRILLO, JR., R. B. & CHAPMAN, K. L. 1996 Experiments in nonlinear saturation of stationary crossflow vortices in a swept-wing boundary layer. *AIAA Paper* 96-0184.
- RESHOTKO, E. 1997 Progress, accomplishments and issues in transition research. *AIAA Paper* 97-1815.
- SARIC, W. S. 1992 The ASU transition research facility. *AIAA Paper* 92-3910.
- SARIC, W. S. 1994 Görtler vortices. *Ann. Rev. Fluid Mech.* **26**, 379–409.
- SARIC, W. S., CARRILLO, JR., R. B. & REIBERT, M. S. 1998 Nonlinear stability and transition in 3-D boundary layers. *Meccanica* **33**, 469–487.
- SARIC, W. S. & YEATS, L. G. 1985 Experiments on the stability of crossflow vortices in swept-wing flows. *AIAA Paper* 85-0493.
- SMITH, A. M. O. & GAMBERONI, A. H. 1956 Transition, pressure gradient and stability theory. *Tech. Rep.*. Douglas Aircraft Company.
- SOMERS, D. M. & HORSTMANN, K. H. 1985 Design of a medium-speed natural-laminar-flow airfoil for commuter aircraft applications. *DFVLR-IB* /29-85/26.
- SPALART, P. R. 1993 Numerical study of transition induced by suction devices. In *Near-Wall Turbulent Flows*. Elsevier Science Pub.
- STEVENS, W. A., GORADIA, S. H. & BRADEN, J. A. 1971 Mathematical model for two-dimensional, multi-component airfoils in viscous flow. NASA CR-1843.

- SWEARINGEN, J. D. & BLACKWELDER, R. F. 1987 The growth and breakdown of stream-wise vortices in the presence of a wall. *J. Fluid Mech.* **182**, 255–290.
- TAYLOR, M. J. & PEAKE, N. 1998 The long-time behaviour of incompressible swept-wing boundary layers subject to impulsive forcing. *J. Fluid Mech.* **355**, 359–381.
- TAYLOR, M. J. & PEAKE, N. 1999 The long-time impulse response of compressible swept-wing boundary layers. *J. Fluid Mech.* **379**, 333–350.
- WINTERGERSTE, T. & KLEISER, L. 1996 Direct numerical simulation of transition in a three-dimensional boundary layer. In *Transitional Boundary Layers in Aeronautics* (ed. R. A. W. M. Henkes & J. L. van Ingen).

## Appendix A

### Figures



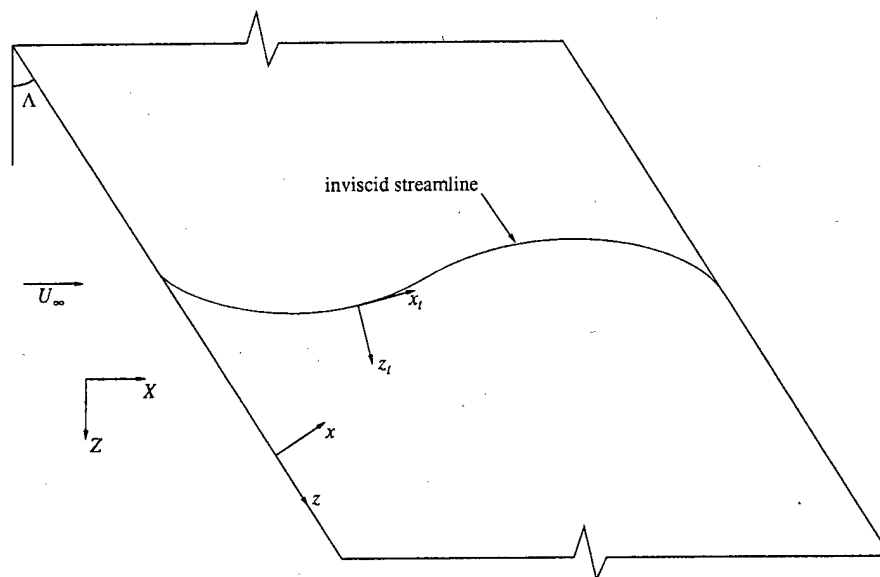


Figure 1: Swept-wing streamline and coordinate systems.

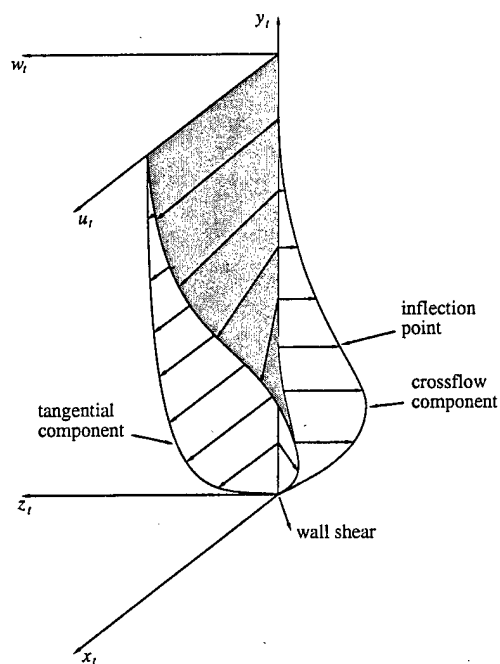


Figure 2: Crossflow boundary-layer profiles.

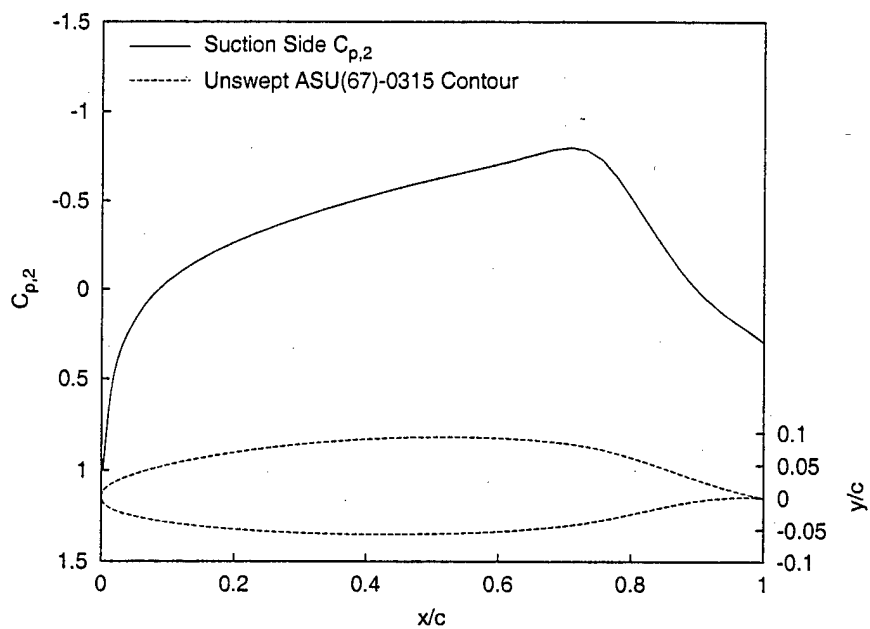


Figure 3: Airfoil shape and suction-side pressure distribution,  $C_{p,2}$ , for the ASU(67)-0315 swept wing at  $-3^\circ$  angle of attack.

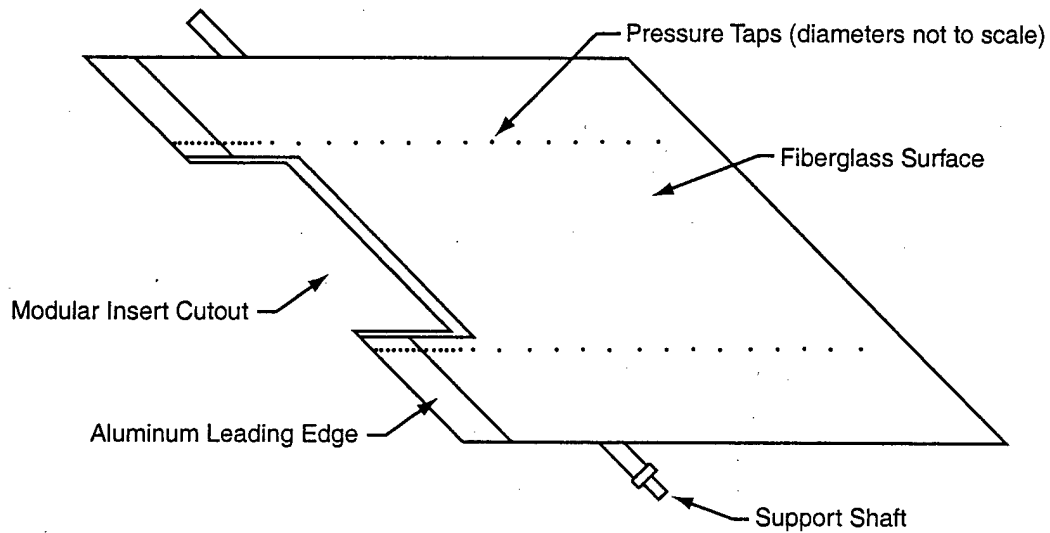


Figure 4: ASU(67)-0315 features.

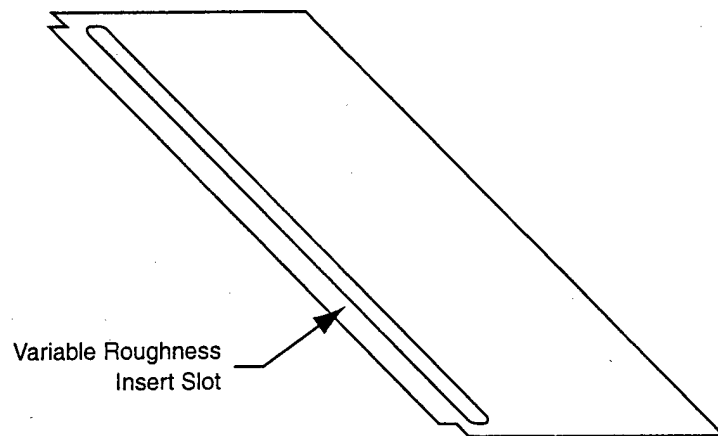


Figure 5: Modular leading-edge insert for the ASU(67)-0315.

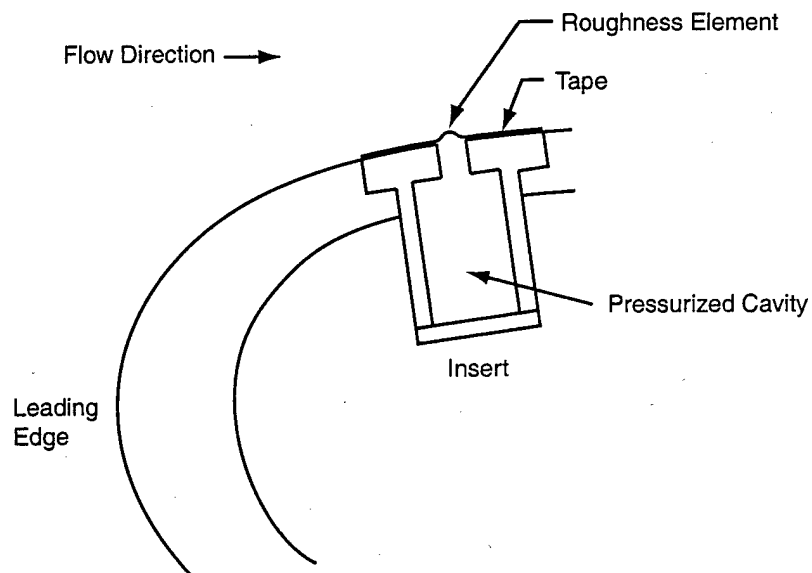


Figure 6: Schematic cross section of the variable leading-edge roughness device.

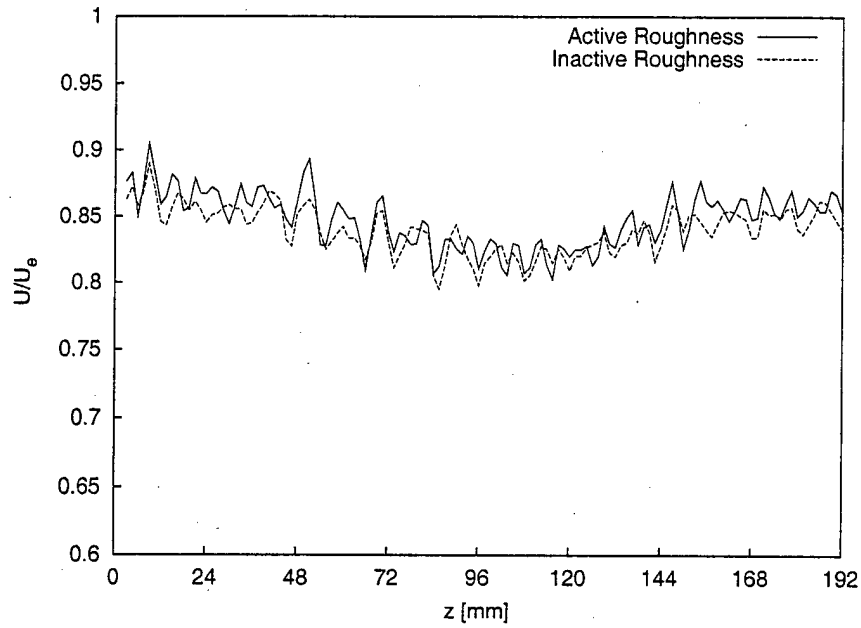


Figure 7: Spanwise mean-flow hotwire scan at  $x/c = 0.20$ ,  $Y = 1.0$  mm,  $Re_c = 2.4 \times 10^6$ .

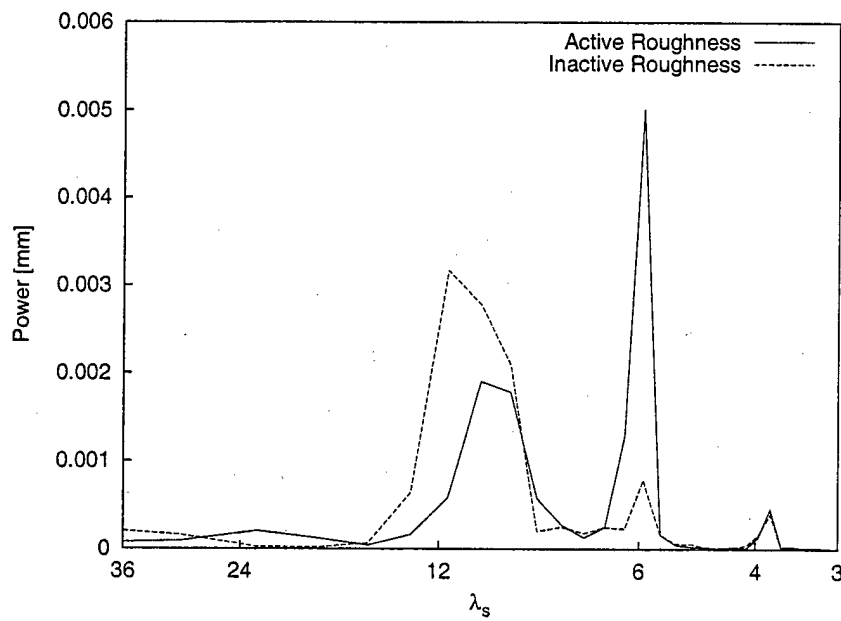


Figure 8: Spatial mean-flow spectrum of data from Figure 7.

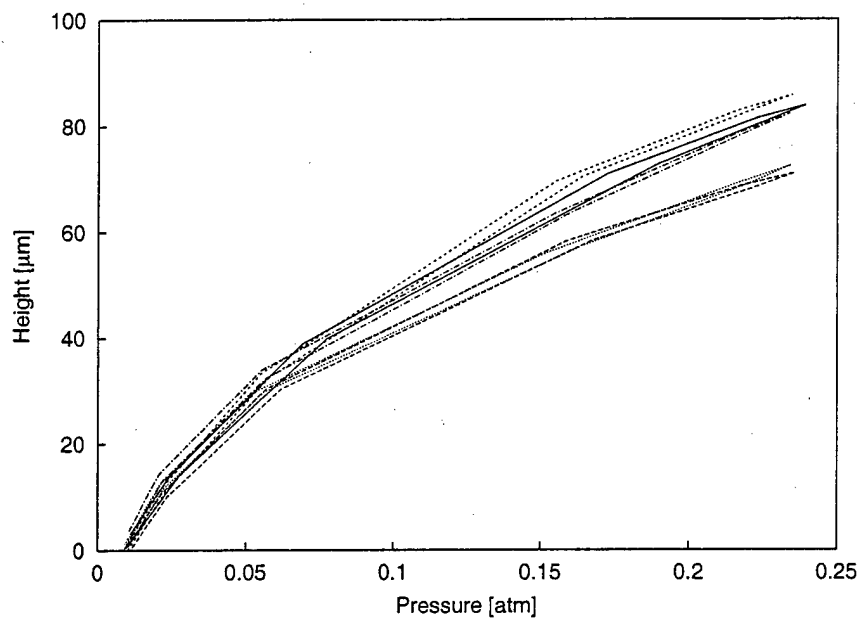


Figure 9: Center-displacement height versus pressure difference,  $\Delta p$ , across 3-mm-diameter roughness elements. Different line styles indicate different elements.

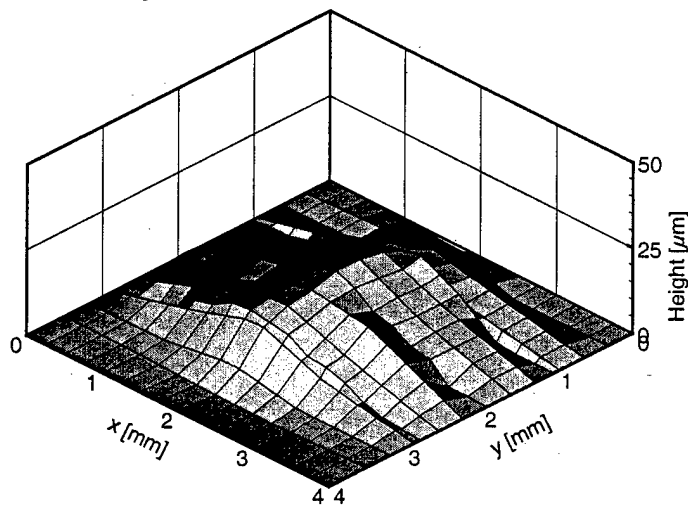


Figure 10: Activated 3-mm-diameter roughness shape of a 10- $\mu$ m-high element.

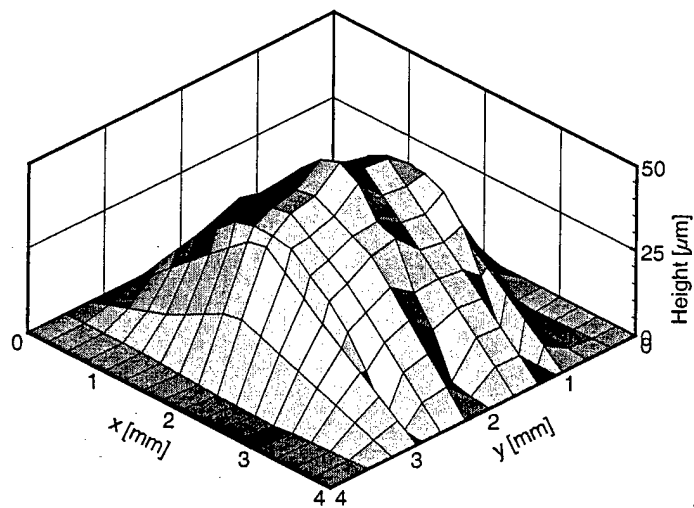


Figure 11: Activated 3-mm-diameter roughness shape of a 50-μm-high element.

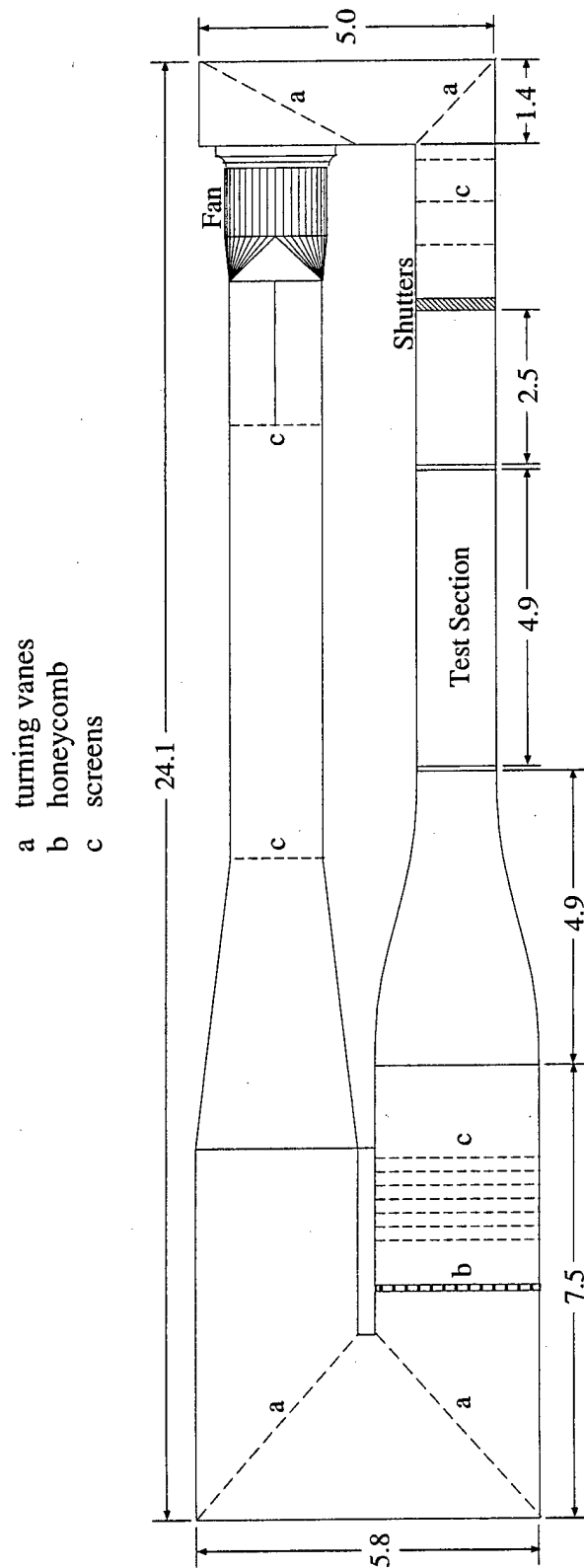


Figure 12: Schematic view of the Unsteady Wind Tunnel. All dimensions in meters.

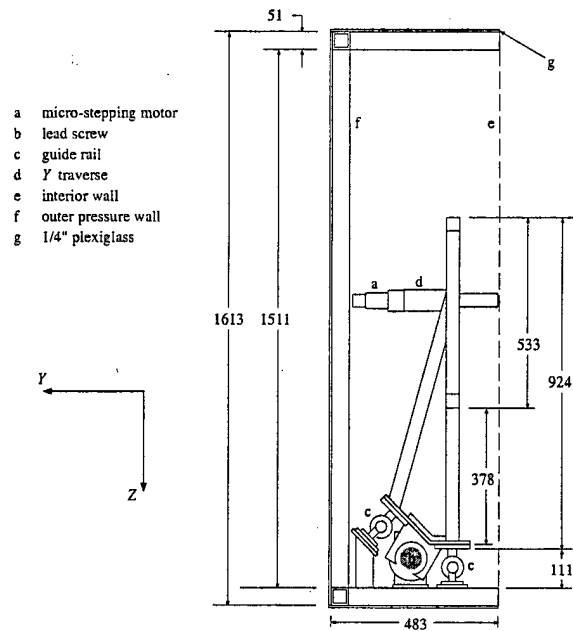


Figure 13: Side view of the traverse frame. All dimensions in millimeters.

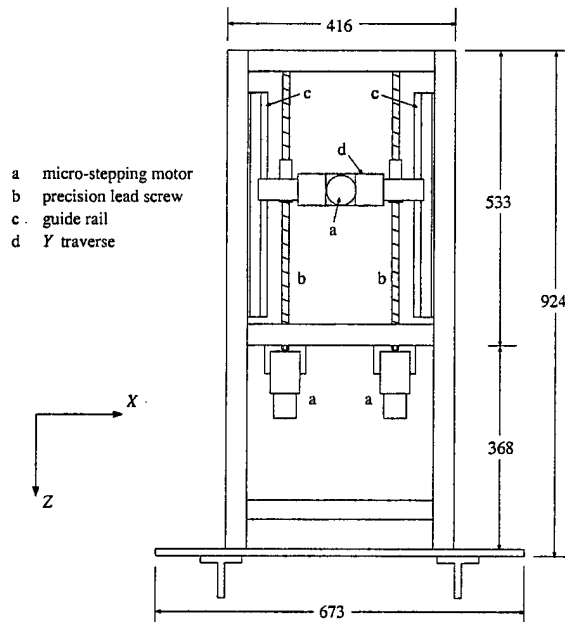


Figure 14: Front view of the traverse frame. All dimensions in millimeters.



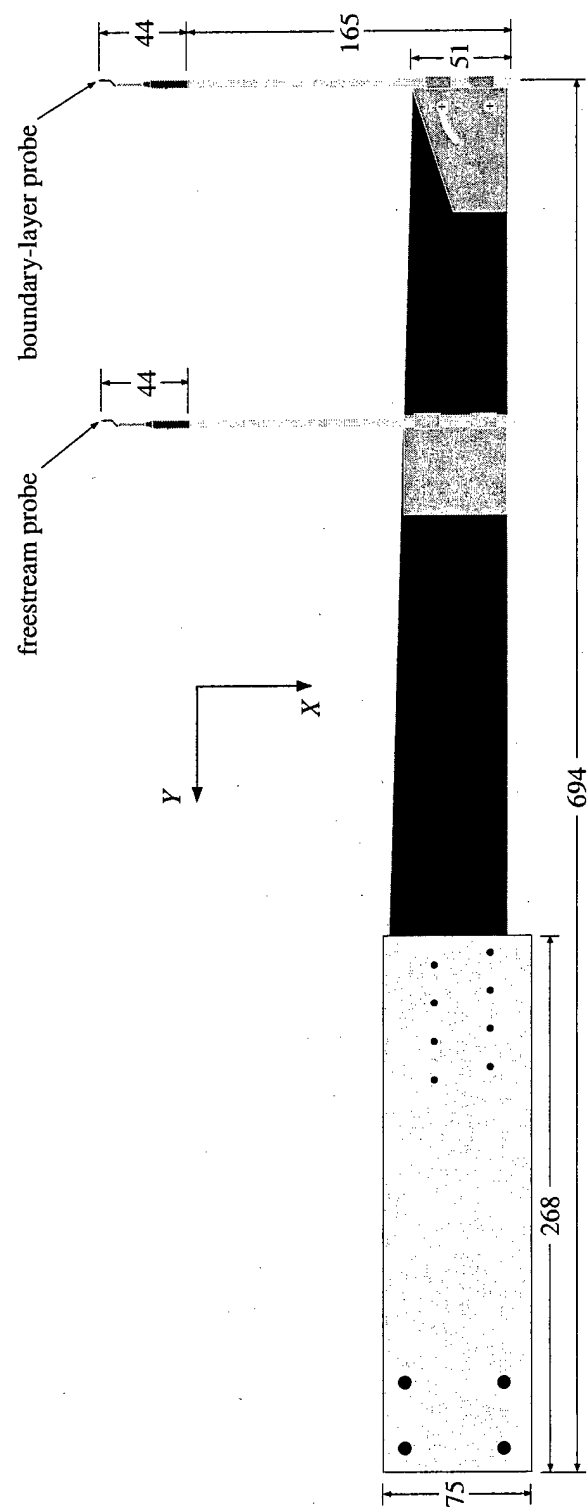


Figure 15: Top view of the hotwire sting. All dimensions in millimeters.

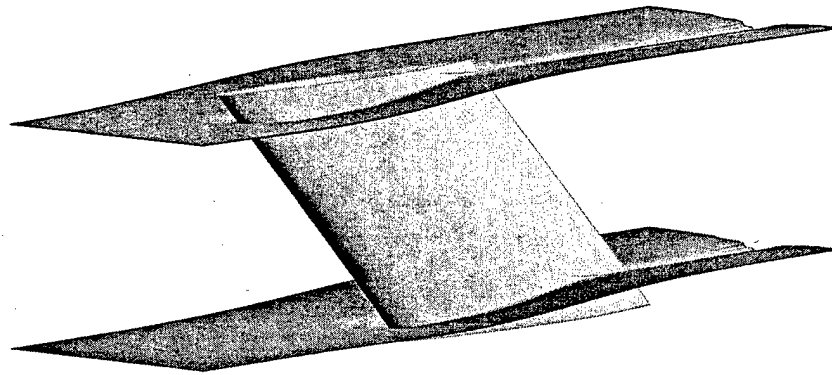


Figure 16: Schematic of root and tip wall liners for a zero-lift configuration.

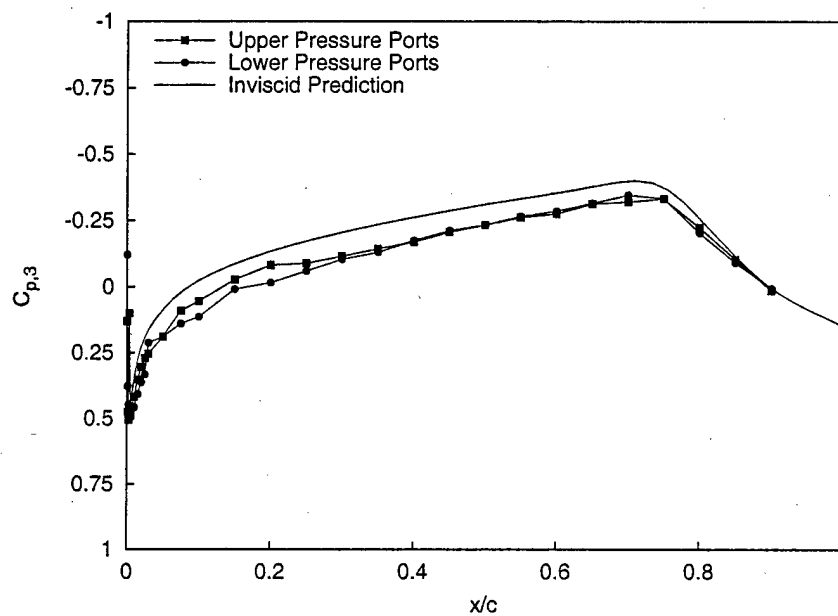


Figure 17: Upper and lower span suction-side  $C_{p,3}$  distributions at  $Re_c = 2.0 \times 10^6$ .

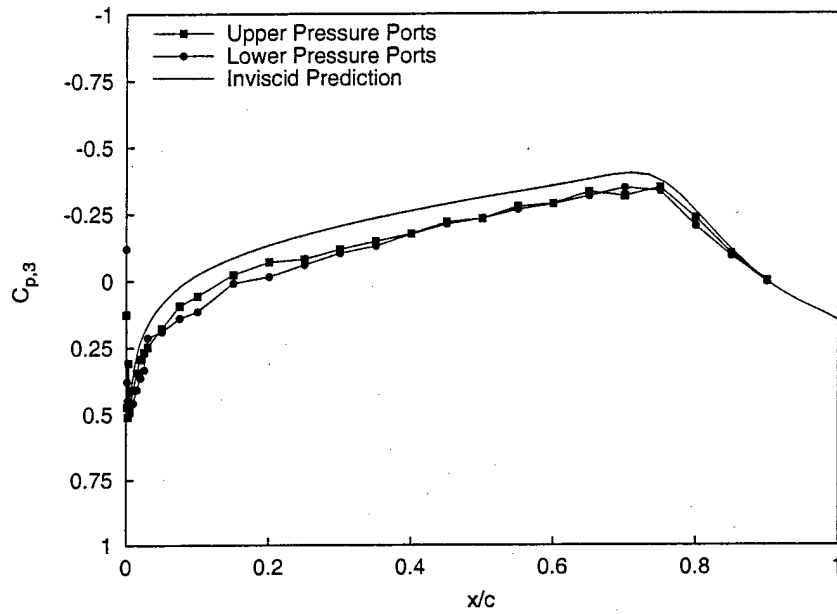


Figure 18: Upper and lower span suction-side  $C_{p,3}$  distributions at  $Re_c = 2.4 \times 10^6$ .

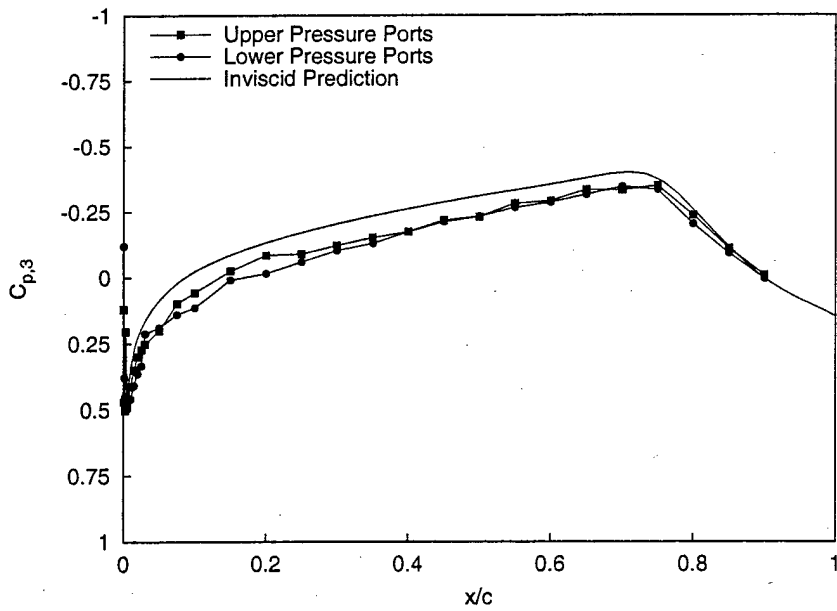


Figure 19: Upper and lower span suction-side  $C_{p,3}$  distributions at  $Re_c = 2.8 \times 10^6$ .

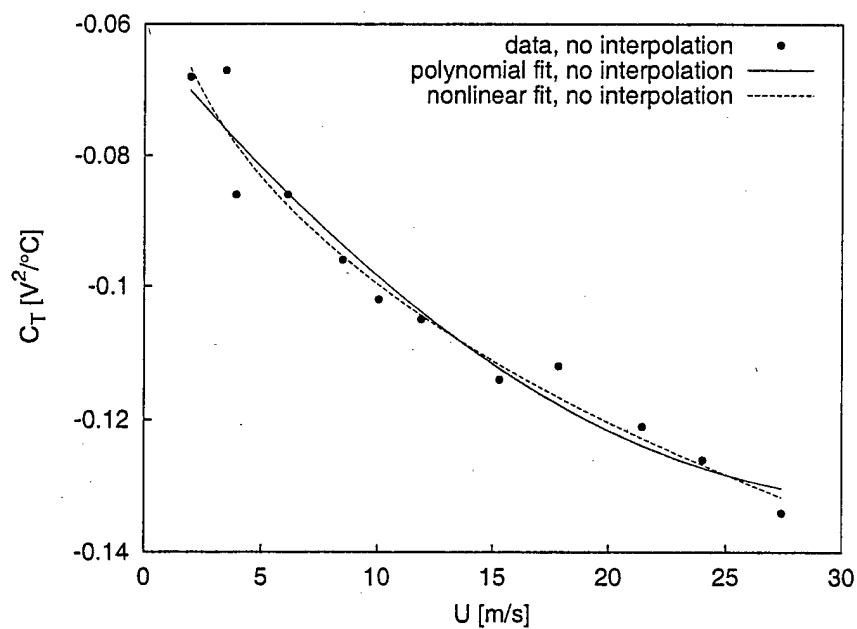


Figure 20: Polynomial and nonlinear temperature-compensation curves without interpolated data.

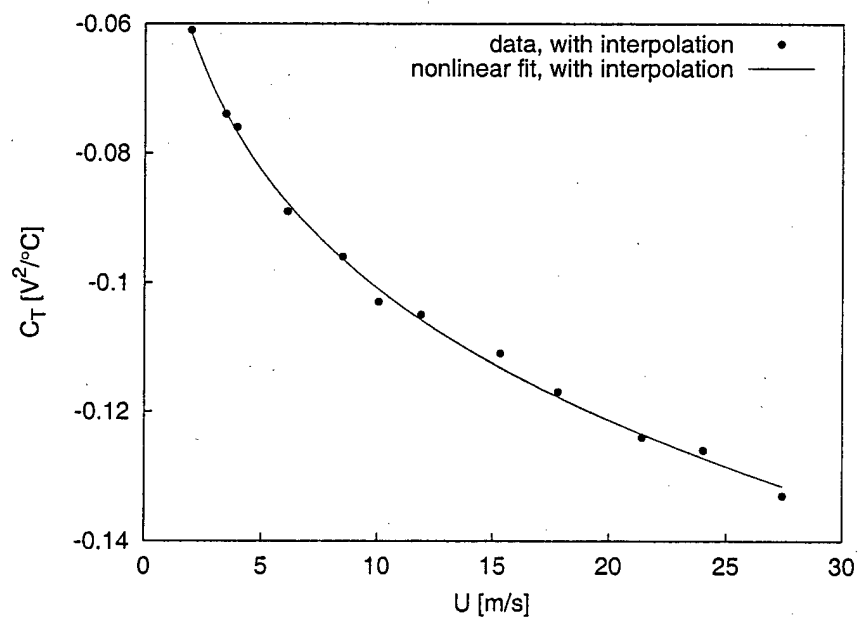


Figure 21: Nonlinear temperature-compensation curve with interpolated data.

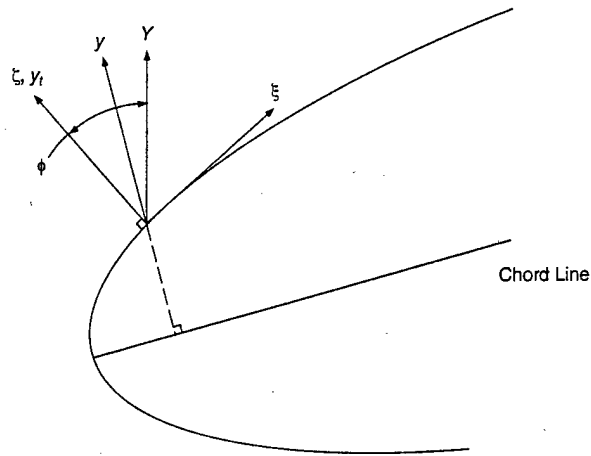
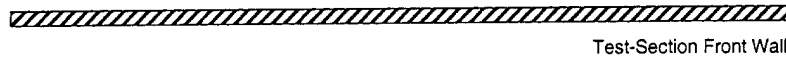


Figure 22: Coordinate systems,  $X, Y$  plane.

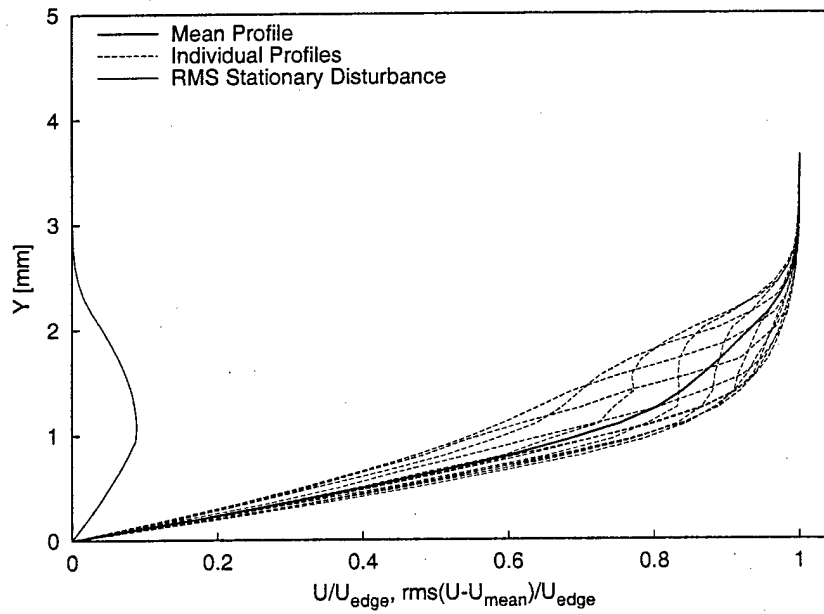


Figure 23: Mean-flow velocity profiles,  $Re_c = 2.4 \times 10^6$ , [18|12] roughness,  $x/c = 0.30$ ,  $z = 117\text{--}128$  mm.

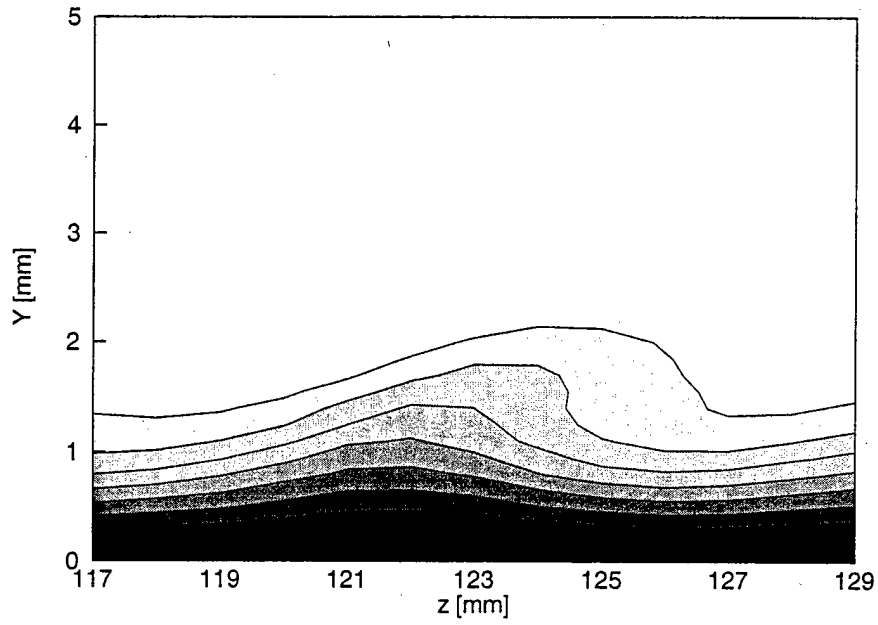


Figure 24: Mean-flow velocity contours,  $Re_c = 2.4 \times 10^6$ , [18|12] roughness,  $x/c = 0.30$ , contour lines at  $U/U_{\text{edge}} = 0.10, 0.20, \dots, 0.90$ .

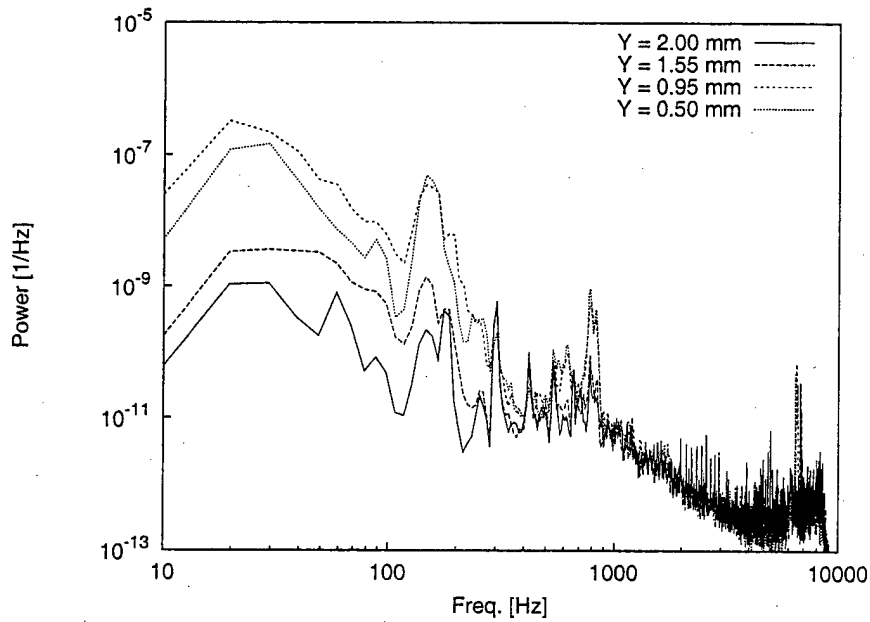


Figure 25: Fluctuating-velocity spectra,  $Re_c = 2.4 \times 10^6$ , [18|12] roughness,  $x/c = 0.30$ ,  $z = 119$  mm.

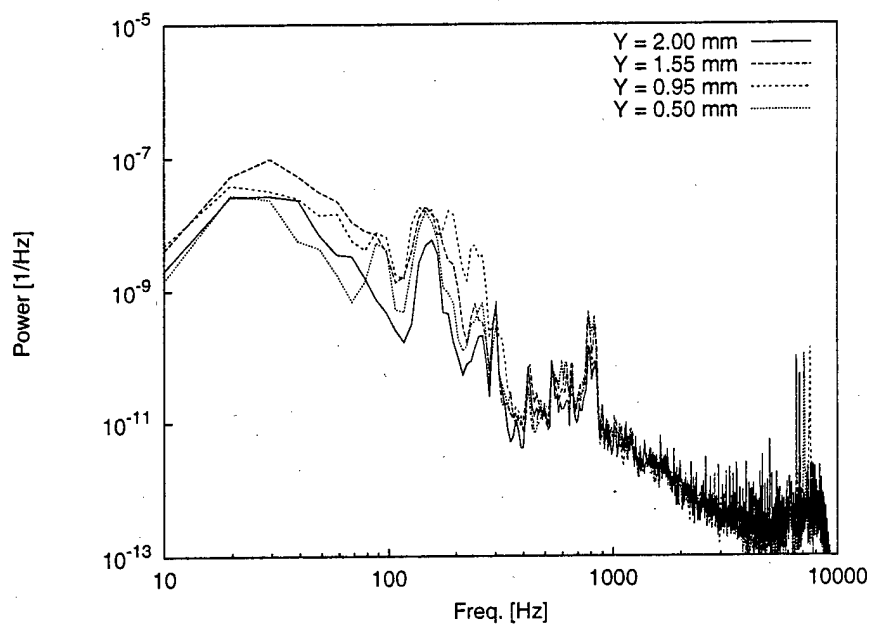


Figure 26: Fluctuating-velocity spectra,  $Re_c = 2.4 \times 10^6$ , [18|12] roughness,  $x/c = 0.30$ ,  $z = 122$  mm.

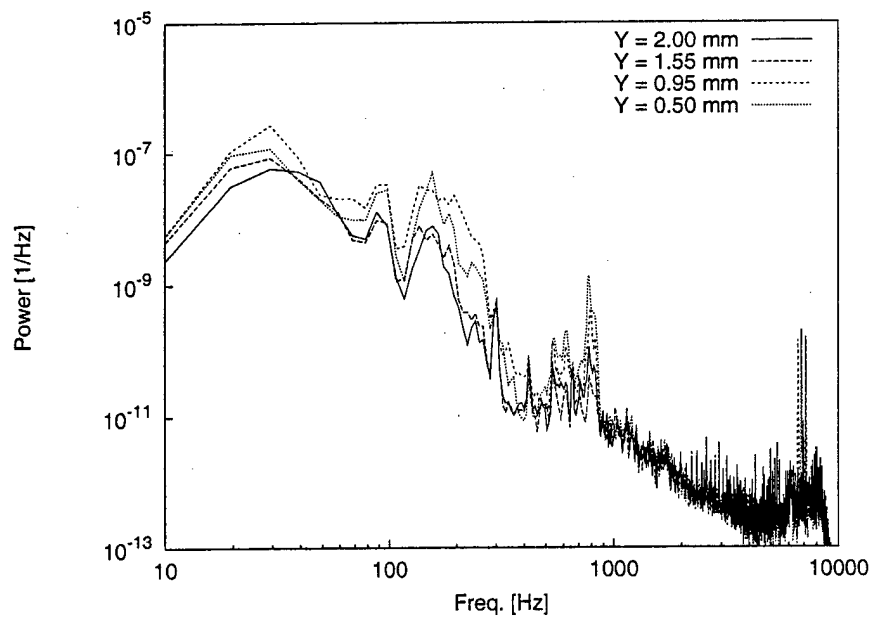


Figure 27: Fluctuating-velocity spectra,  $Re_c = 2.4 \times 10^6$ , [18|12] roughness,  $x/c = 0.30$ ,  $z = 125$  mm.

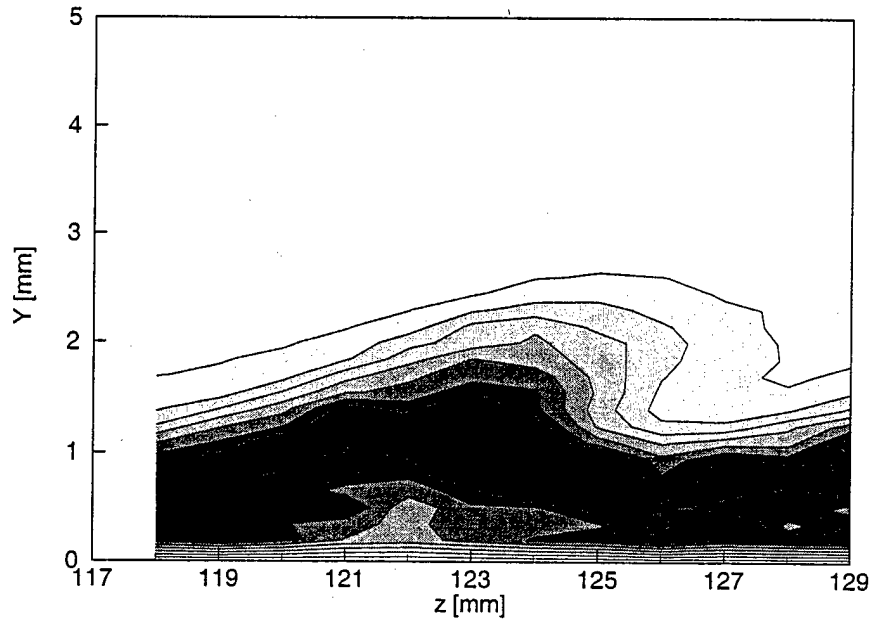


Figure 28: 200-Hz velocity-fluctuation rms distribution,  $Re_c = 2.4 \times 10^6$ , [18|12] roughness,  $x/c = 0.30$ , 100–300-Hz bandpass. Lines are 10% contours of the maximum in this band.

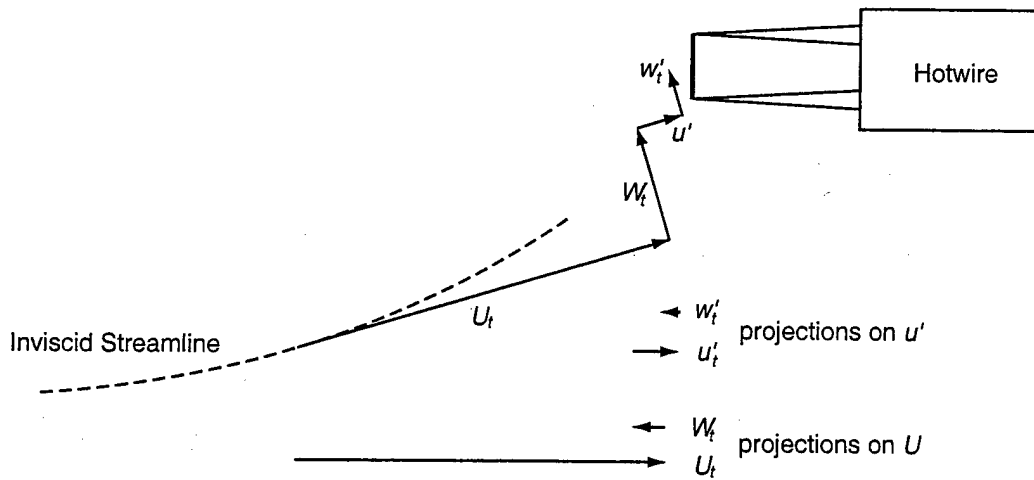


Figure 29: Schematic of the crossflow vortex velocity components and hotwire arrangement parallel to the plane of the wing's surface.



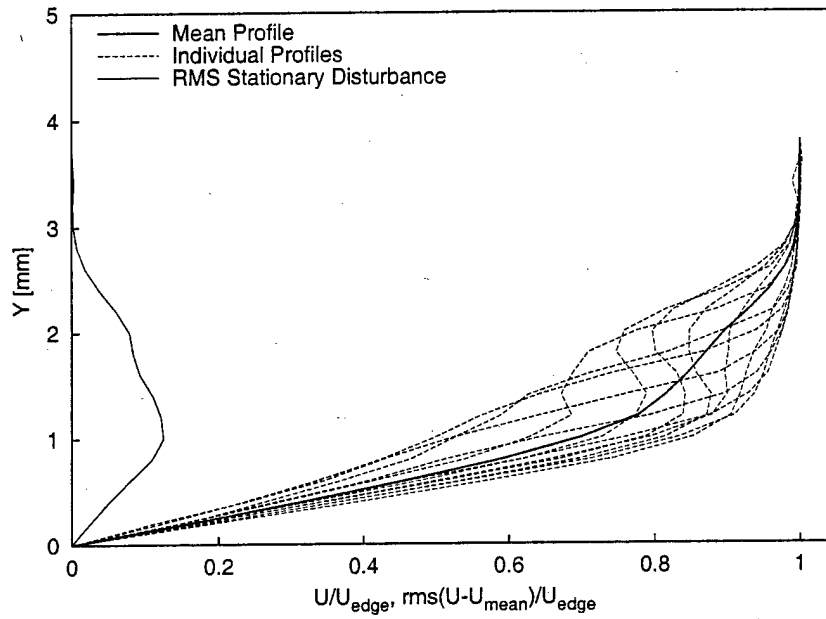


Figure 30: Mean-flow velocity profiles,  $Re_c = 2.4 \times 10^6$ , [18|12] roughness,  $x/c = 0.35$ ,  $z = 103$ – $114$  mm.

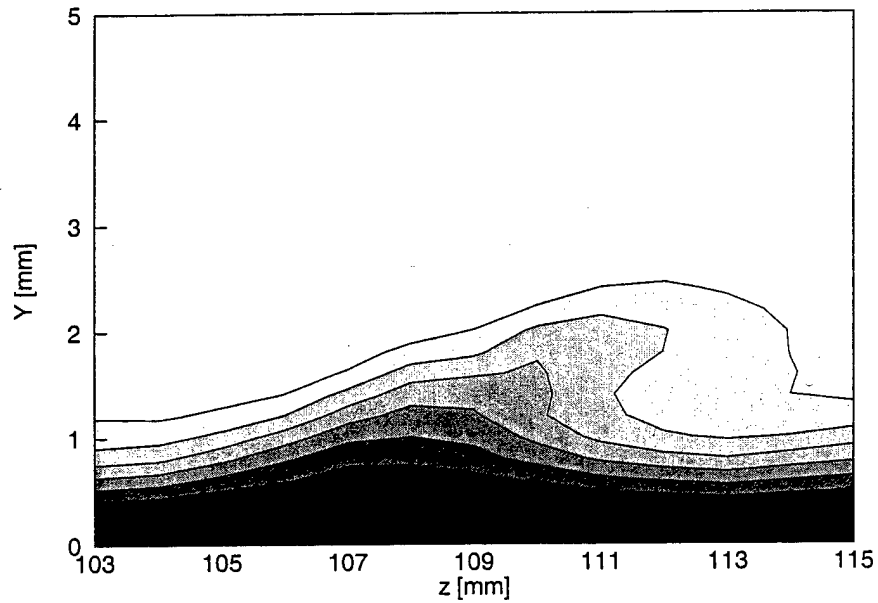


Figure 31: Mean-flow velocity contours,  $Re_c = 2.4 \times 10^6$ , [18|12] roughness,  $x/c = 0.35$ , contour lines at  $U/U_{edge} = 0.10, 0.20, \dots, 0.90$ .

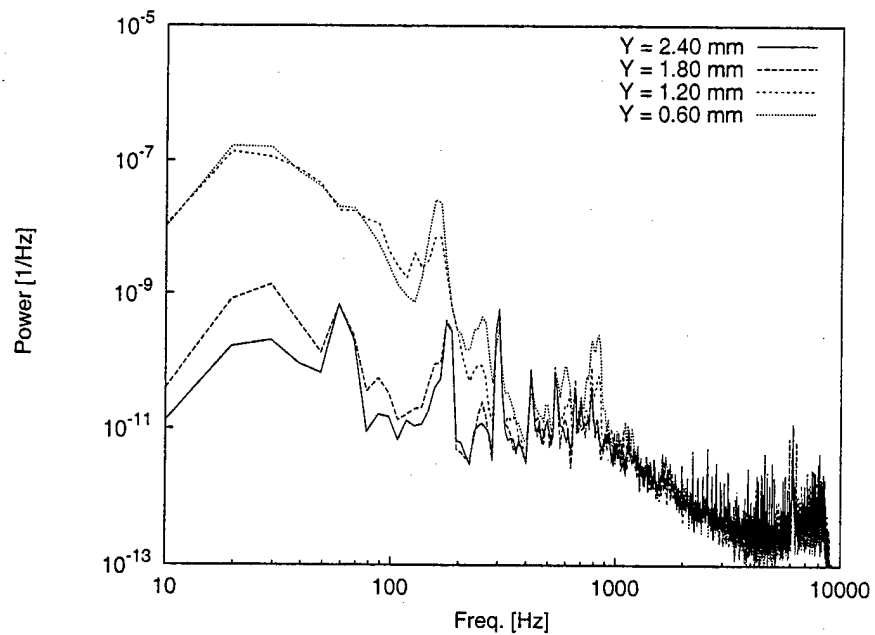


Figure 32: Fluctuating-velocity spectra,  $Re_c = 2.4 \times 10^6$ , [18|12] roughness,  $x/c = 0.35$ ,  $z = 105$  mm.

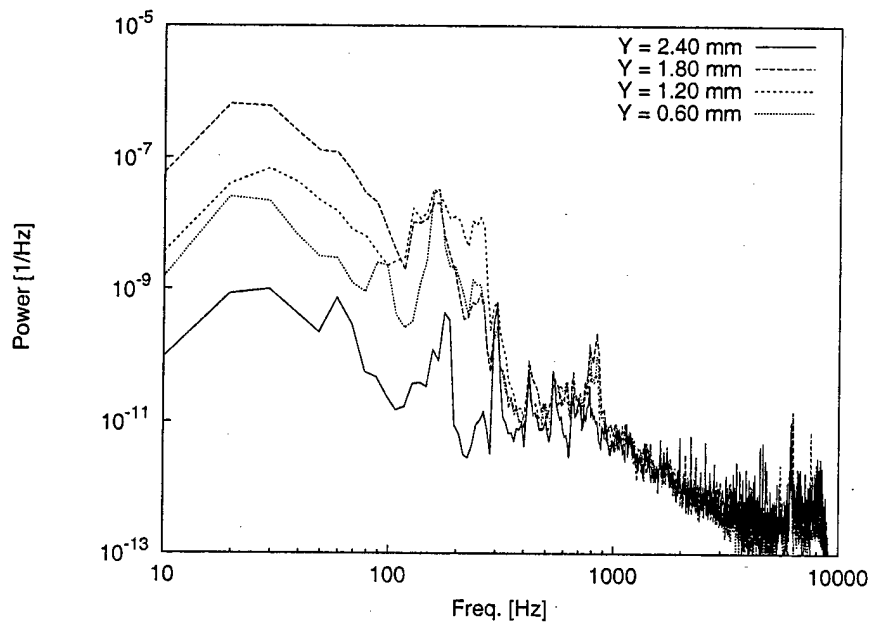


Figure 33: Fluctuating-velocity spectra,  $Re_c = 2.4 \times 10^6$ , [18|12] roughness,  $x/c = 0.35$ ,  $z = 108$  mm.

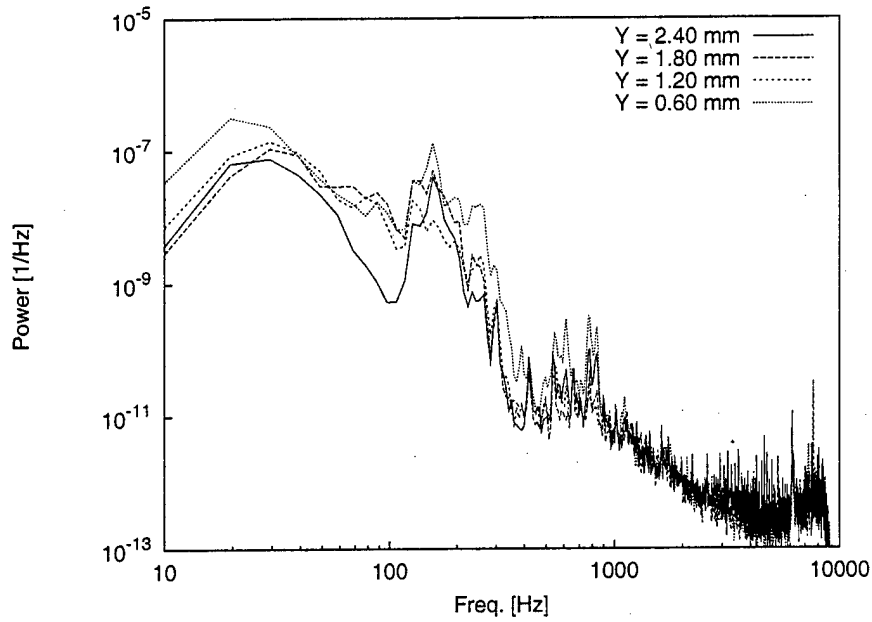


Figure 34: Fluctuating-velocity spectra,  $Re_c = 2.4 \times 10^6$ , [18|12] roughness,  $x/c = 0.35$ ,  $z = 111$  mm.

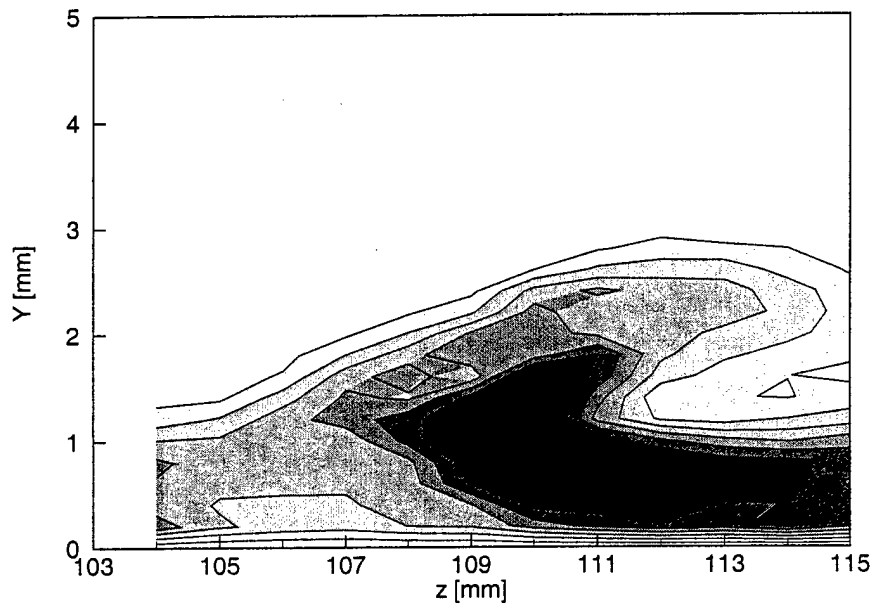


Figure 35: 200-Hz velocity-fluctuation rms distribution,  $Re_c = 2.4 \times 10^6$ , [18|12] roughness,  $x/c = 0.35$ , 100–300-Hz bandpass. Lines are 10% contours of the maximum in this band.

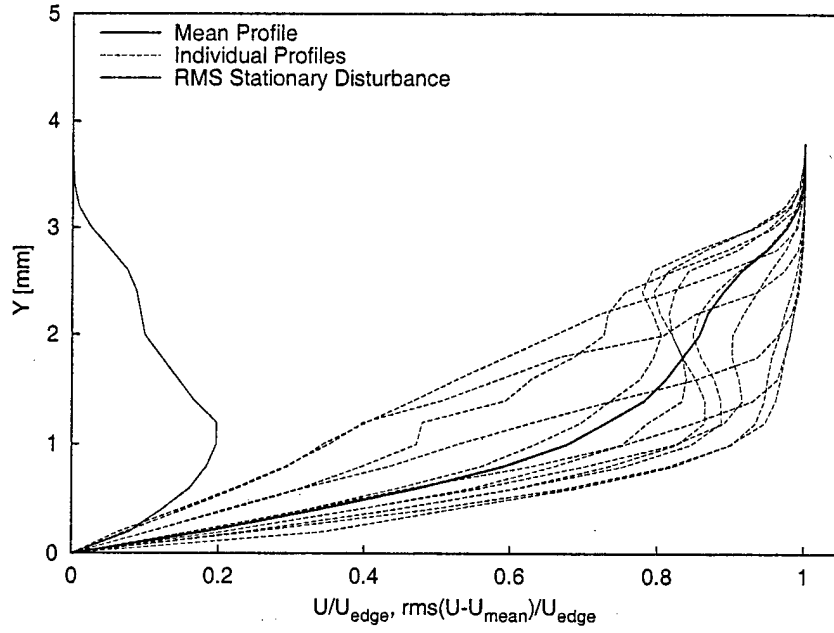


Figure 36: Mean-flow velocity profiles,  $Re_c = 2.4 \times 10^6$ , [18|12] roughness,  $x/c = 0.40$ ,  $z = 89$ – $100$  mm.

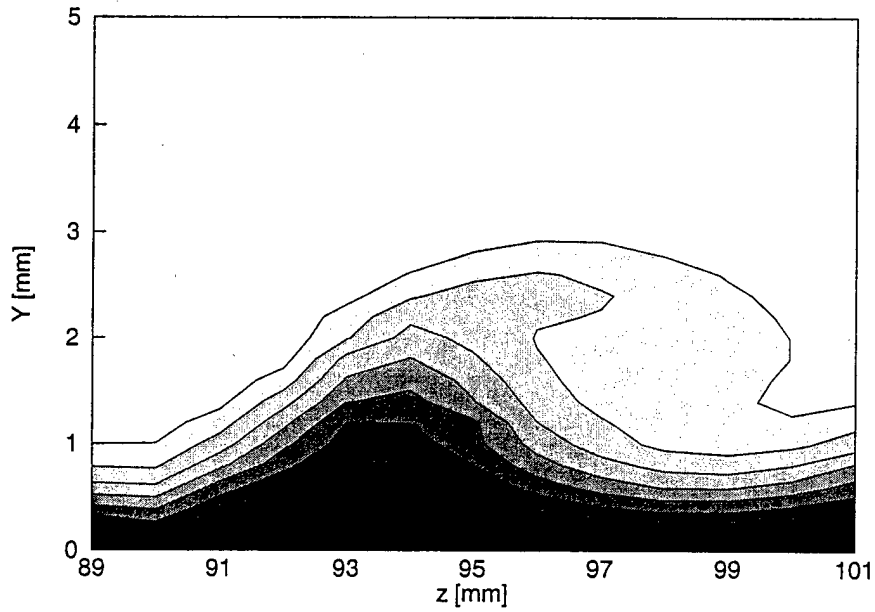


Figure 37: Mean-flow velocity contours,  $Re_c = 2.4 \times 10^6$ , [18|12] roughness,  $x/c = 0.40$ , contour lines at  $U/U_{edge} = 0.10, 0.20, \dots, 0.90$ .

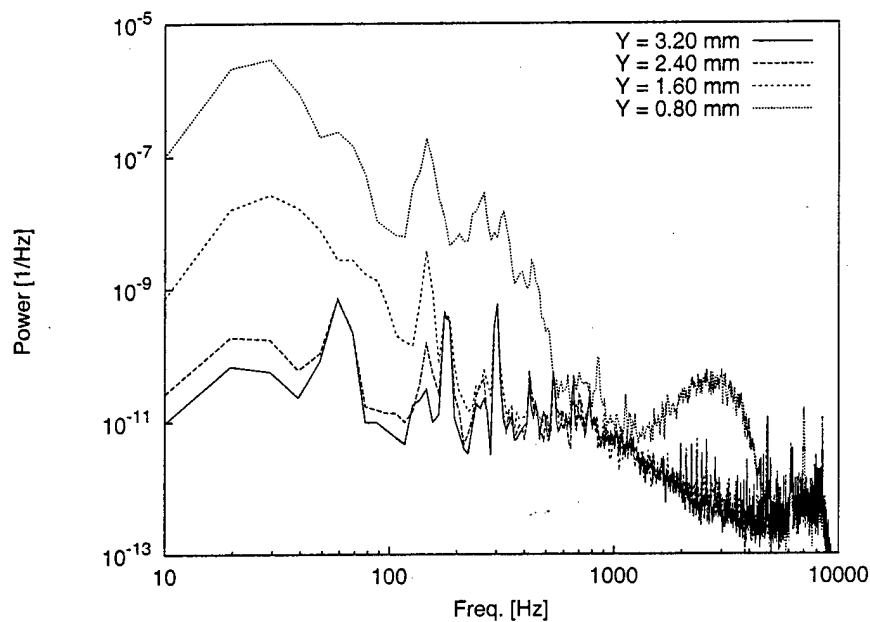


Figure 38: Fluctuating-velocity spectra,  $Re_c = 2.4 \times 10^6$ , [18|12] roughness,  $x/c = 0.40$ ,  $z = 91$  mm.

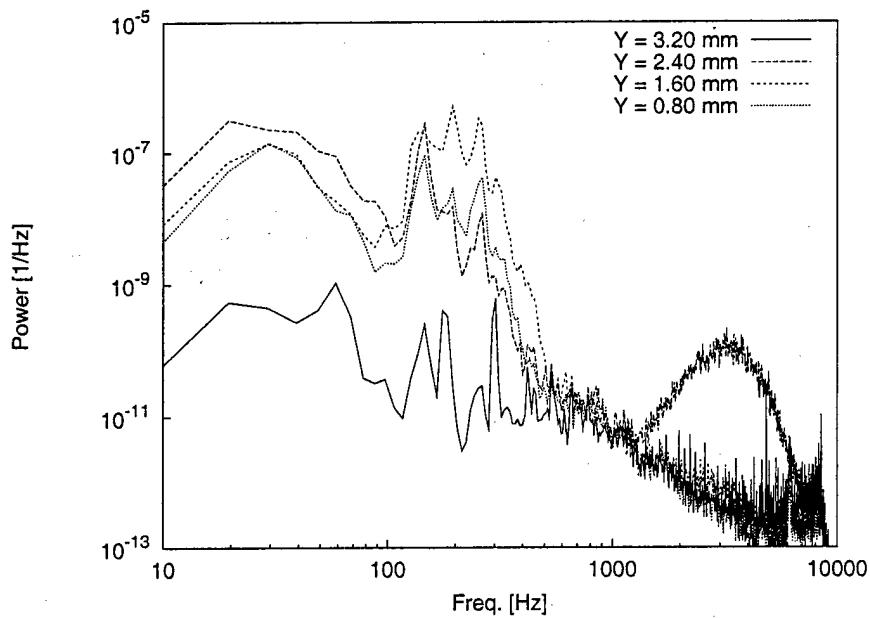


Figure 39: Fluctuating-velocity spectra,  $Re_c = 2.4 \times 10^6$ , [18|12] roughness,  $x/c = 0.40$ ,  $z = 94$  mm.

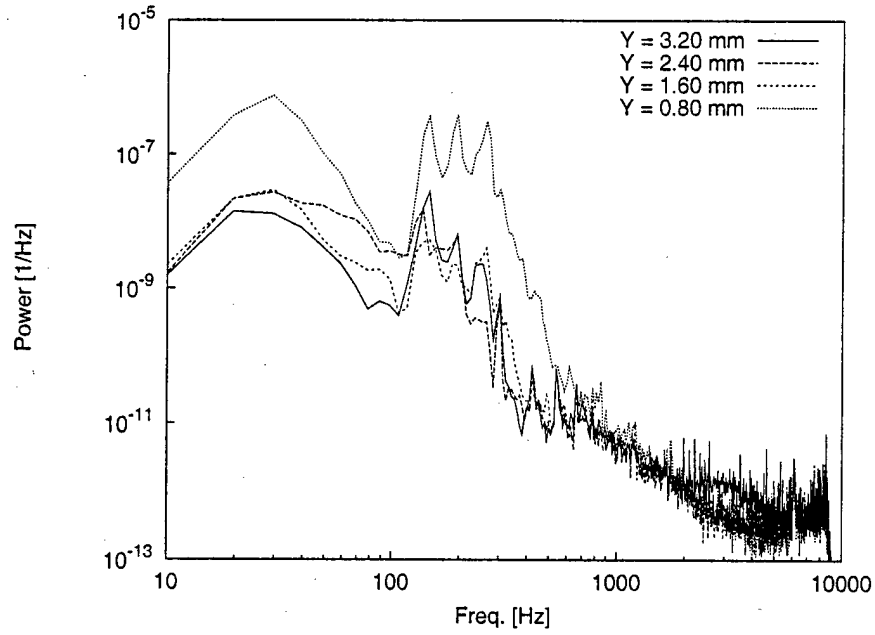


Figure 40: Fluctuating-velocity spectra,  $Re_c = 2.4 \times 10^6$ , [18|12] roughness,  $x/c = 0.40$ ,  $z = 97$  mm.

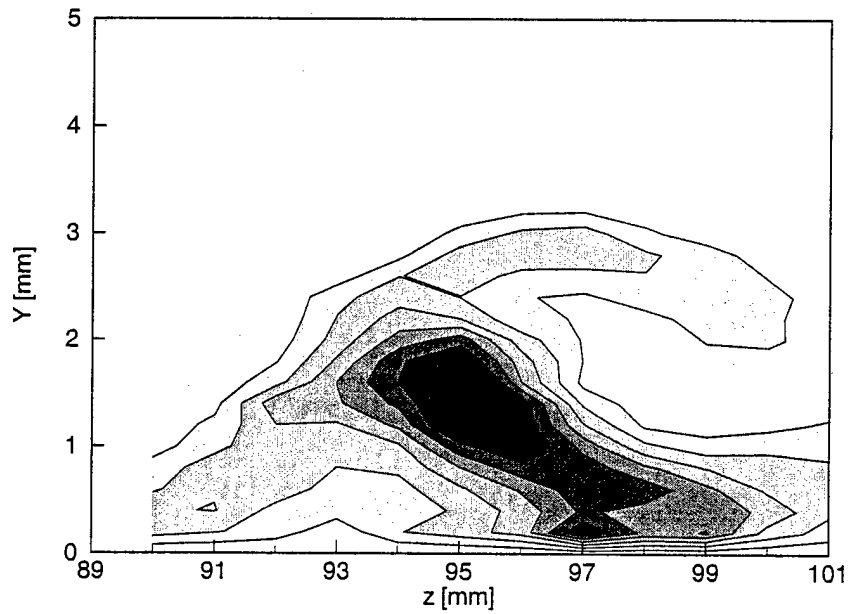


Figure 41: 200-Hz velocity-fluctuation rms distribution,  $Re_c = 2.4 \times 10^6$ , [18|12] roughness,  $x/c = 0.40$ , 100-300-Hz bandpass. Lines are 10% contours of the maximum in this band.

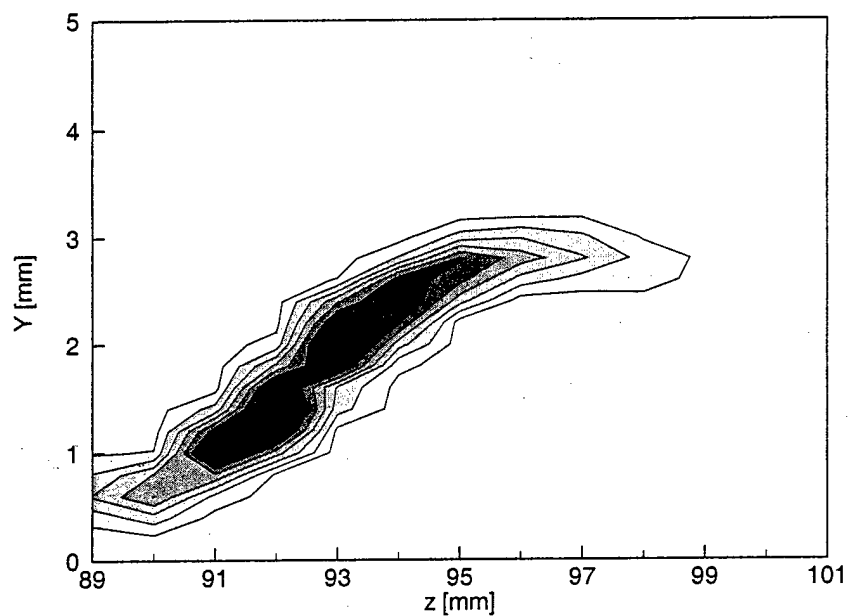


Figure 42: 3.0-kHz velocity-fluctuation rms distribution,  $Re_c = 2.4 \times 10^6$ , [18|12] roughness,  $x/c = 0.40$ , 2.9–3.1-Hz bandpass. Lines are 10% contours of the maximum in this band.

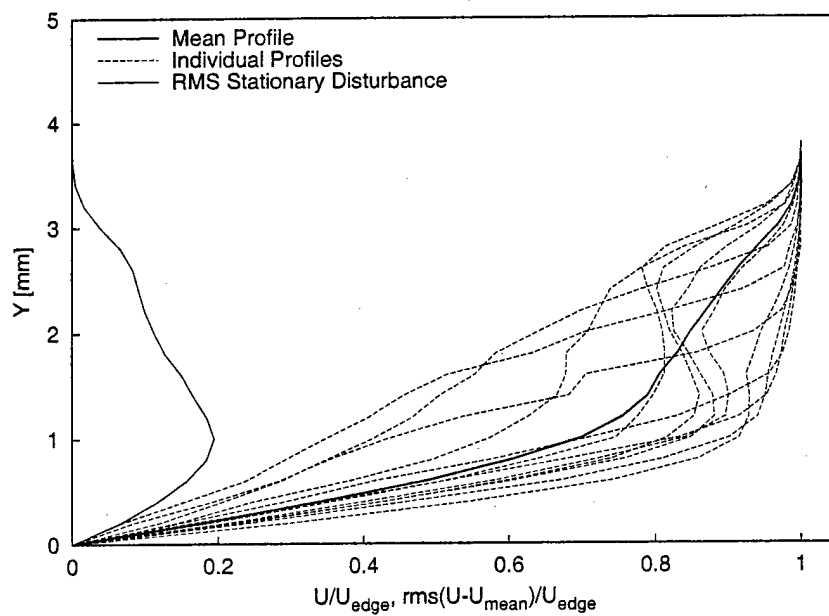


Figure 43: Mean-flow velocity profiles,  $Re_c = 2.4 \times 10^6$ , [18|12] roughness,  $x/c = 0.41$ ,  $z = 85$ – $96$  mm.

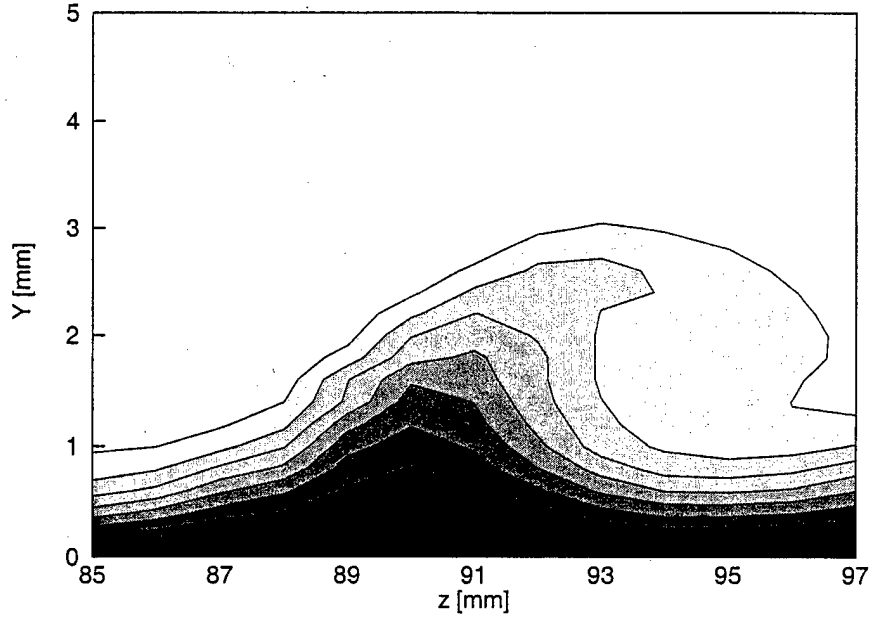


Figure 44: Mean-flow velocity contours,  $Re_c = 2.4 \times 10^6$ , [18|12] roughness,  $x/c = 0.41$ , contour lines at  $U/U_{edge} = 0.10, 0.20, \dots, 0.90$ .

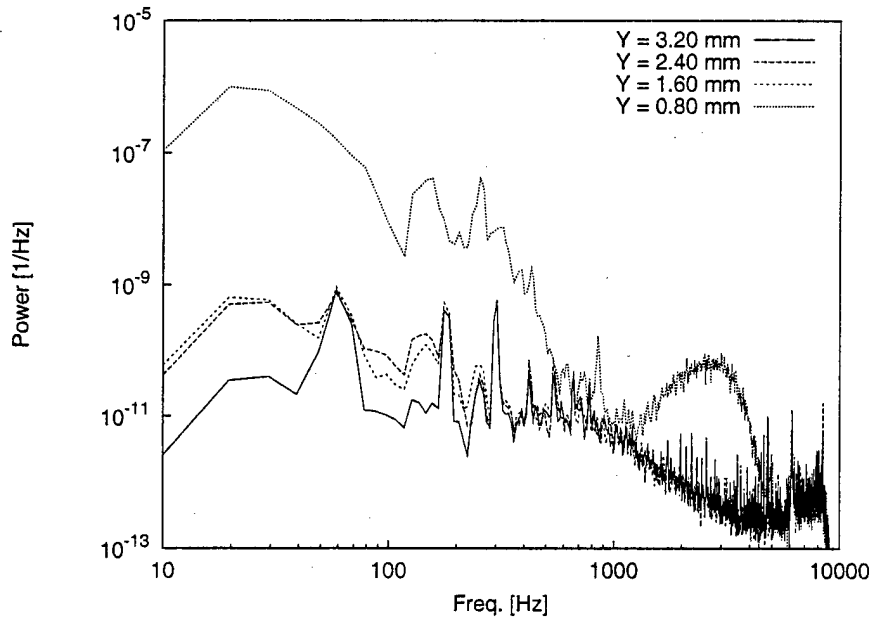


Figure 45: Fluctuating-velocity spectra,  $Re_c = 2.4 \times 10^6$ , [18|12] roughness,  $x/c = 0.41$ ,  $z = 87$  mm.



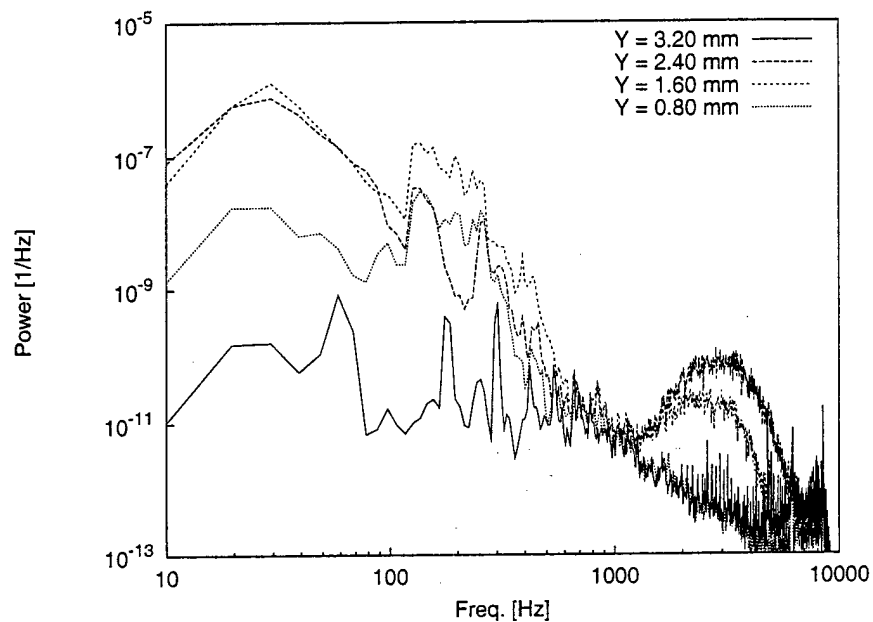


Figure 46: Fluctuating-velocity spectra,  $Re_c = 2.4 \times 10^6$ , [18|12] roughness,  $x/c = 0.41$ ,  $z = 90$  mm.

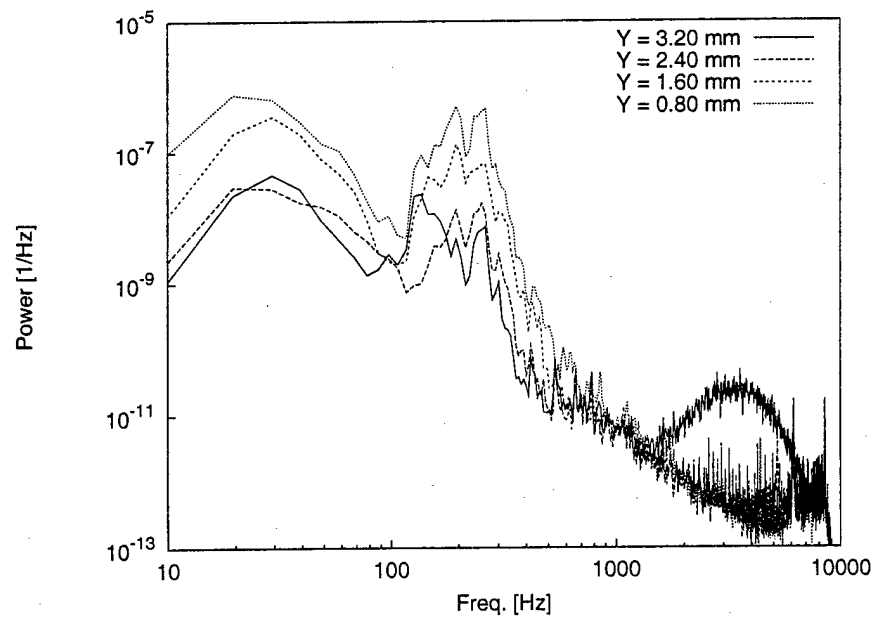


Figure 47: Fluctuating-velocity spectra,  $Re_c = 2.4 \times 10^6$ , [18|12] roughness,  $x/c = 0.41$ ,  $z = 93$  mm.

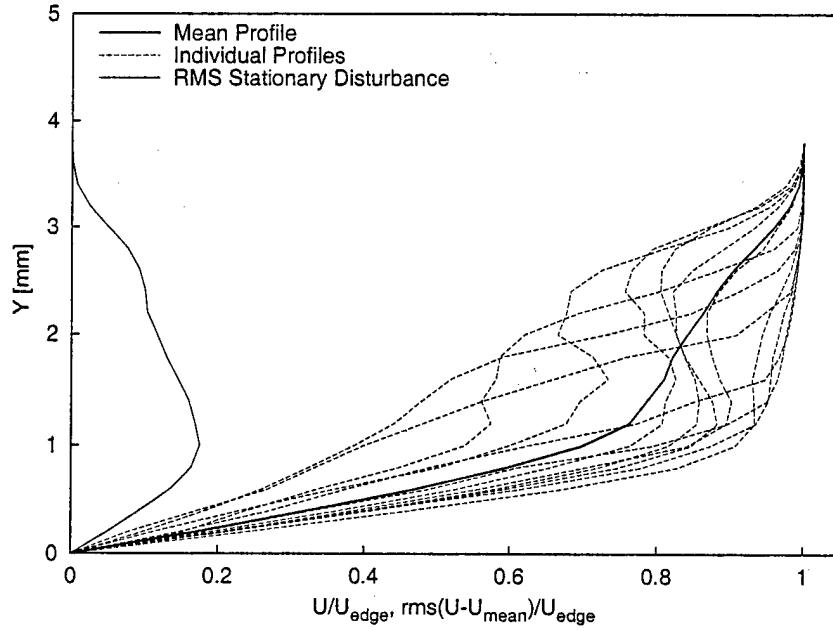


Figure 48: Mean-flow velocity profiles,  $Re_c = 2.4 \times 10^6$ , [18|12] roughness,  $x/c = 0.42$ ,  $z = 82-93$  mm.

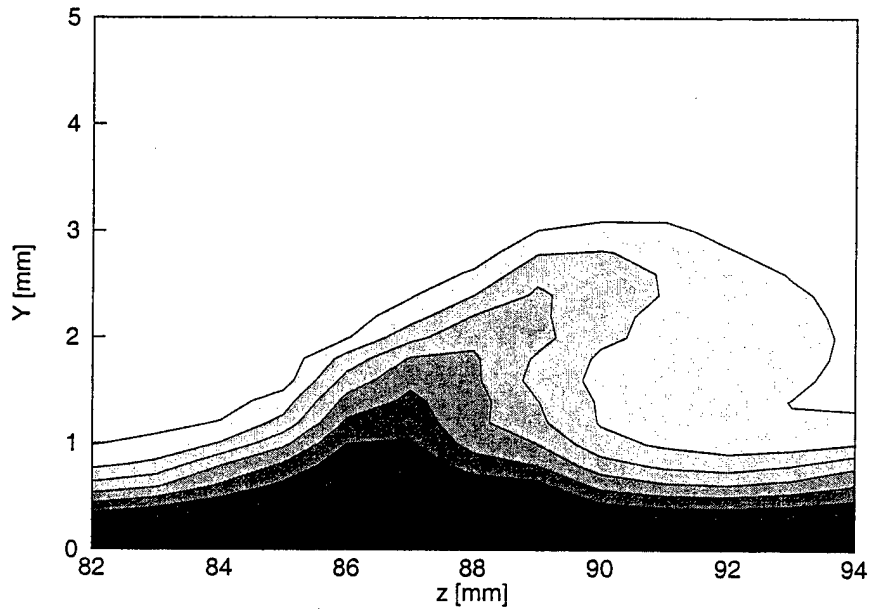


Figure 49: Mean-flow velocity contours,  $Re_c = 2.4 \times 10^6$ , [18|12] roughness,  $x/c = 0.42$ , contour lines at  $U/U_{edge} = 0.10, 0.20, \dots, 0.90$ .

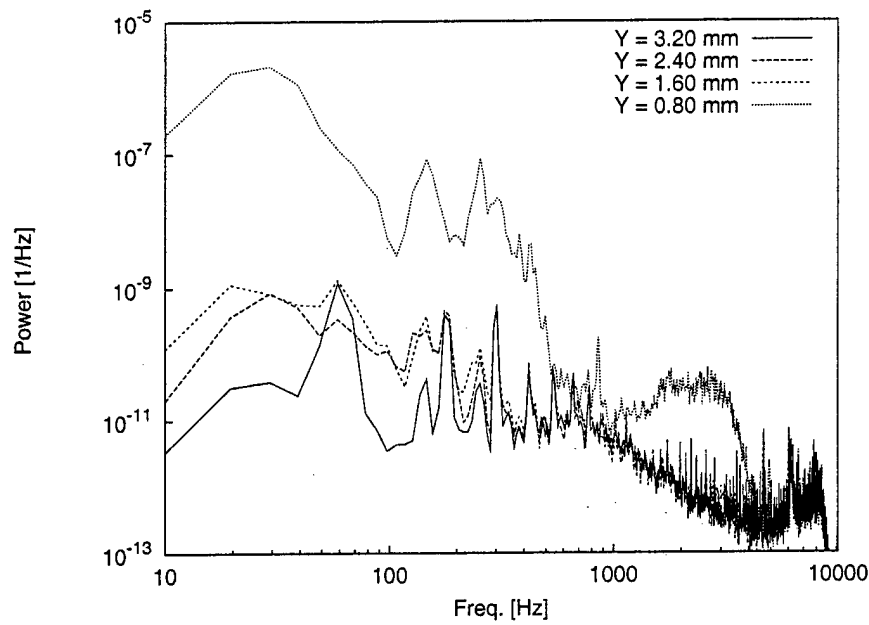


Figure 50: Fluctuating-velocity spectra,  $Re_c = 2.4 \times 10^6$ , [18|12] roughness,  $x/c = 0.42$ ,  $z = 84$  mm.

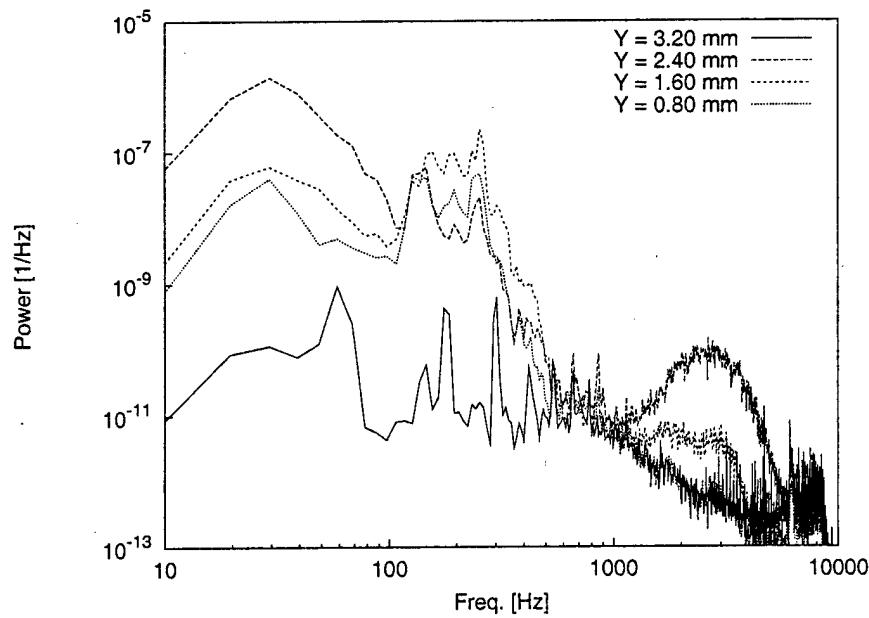


Figure 51: Fluctuating-velocity spectra,  $Re_c = 2.4 \times 10^6$ , [18|12] roughness,  $x/c = 0.42$ ,  $z = 87$  mm.

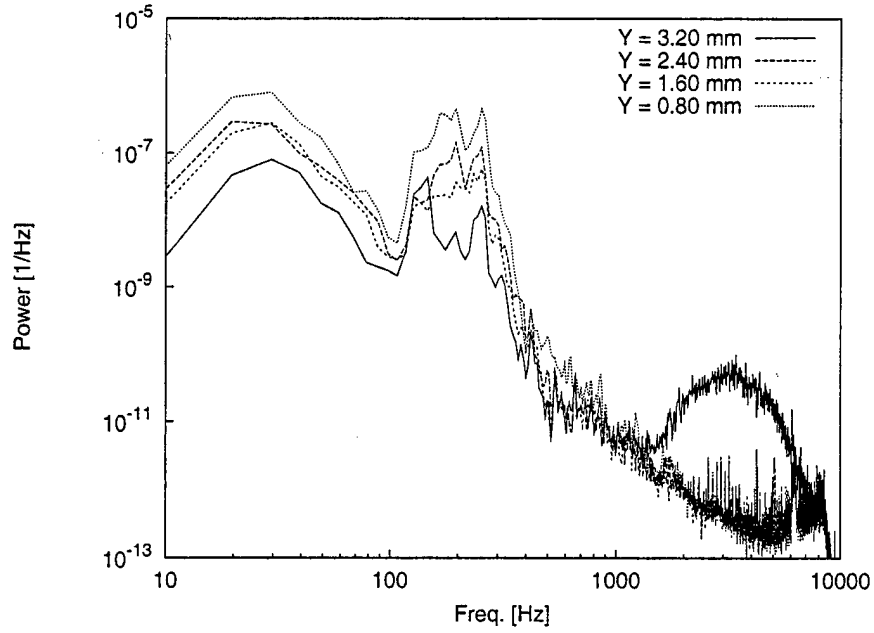


Figure 52: Fluctuating-velocity spectra,  $Re_c = 2.4 \times 10^6$ , [18|12] roughness,  $x/c = 0.42$ ,  $z = 90$  mm.

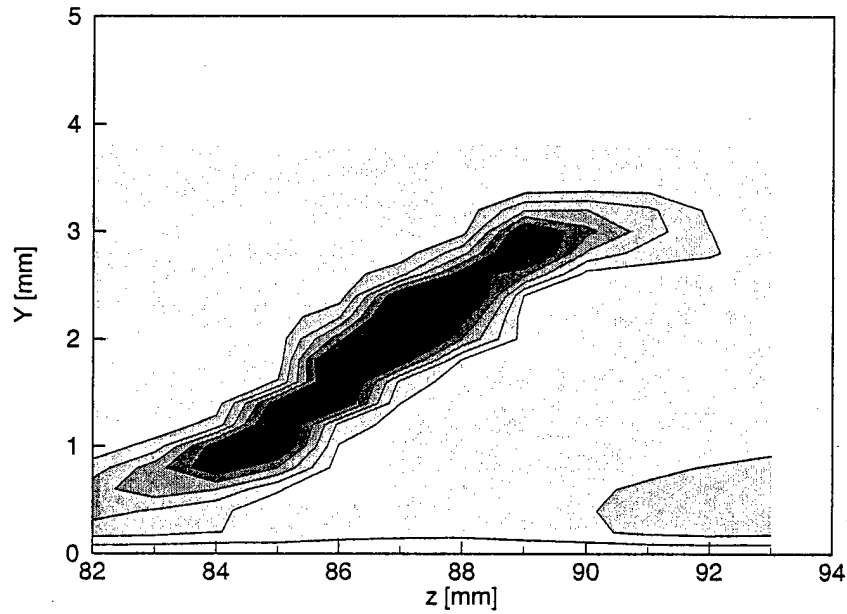


Figure 53: 1.8-kHz velocity-fluctuation rms distribution,  $Re_c = 2.4 \times 10^6$ , [18|12] roughness,  $x/c = 0.42$ , 1.7–1.9-kHz bandpass. Lines are 10% contours of the maximum in this band.

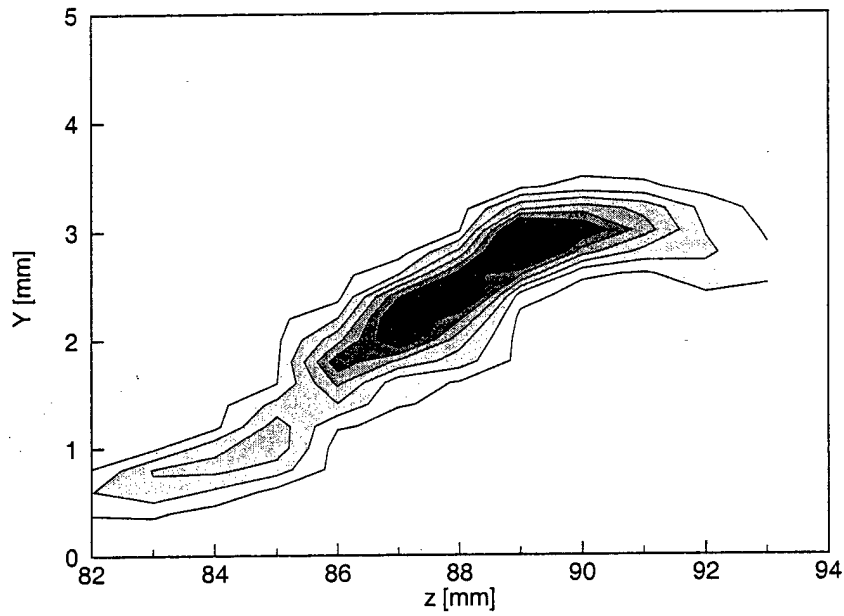


Figure 54: 3.0-kHz velocity-fluctuation rms distribution,  $Re_c = 2.4 \times 10^6$ , [18|12] roughness,  $x/c = 0.42$ , 2.9–3.1-kHz bandpass. Lines are 10% contours of the maximum in this band.

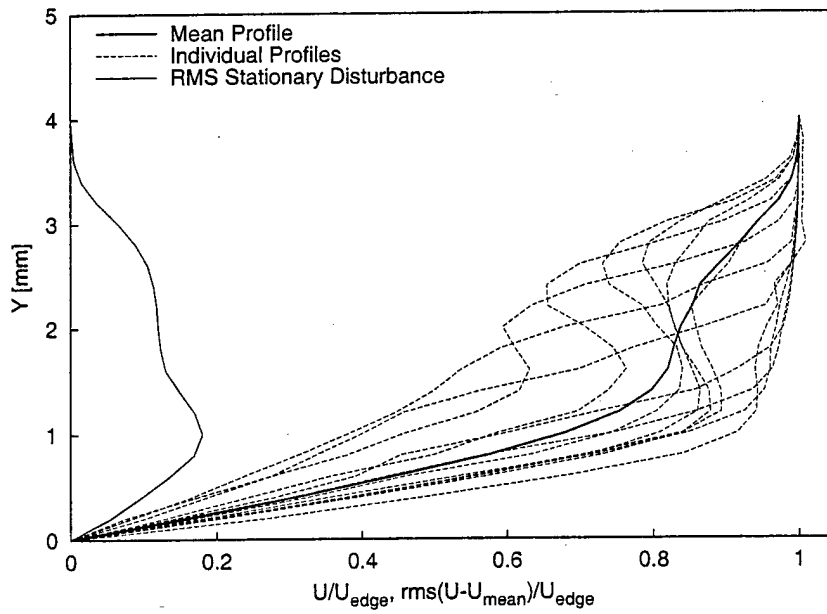


Figure 55: Mean-flow velocity profiles,  $Re_c = 2.4 \times 10^6$ , [18|12] roughness,  $x/c = 0.43$ ,  $z = 79$ – $90$  mm.

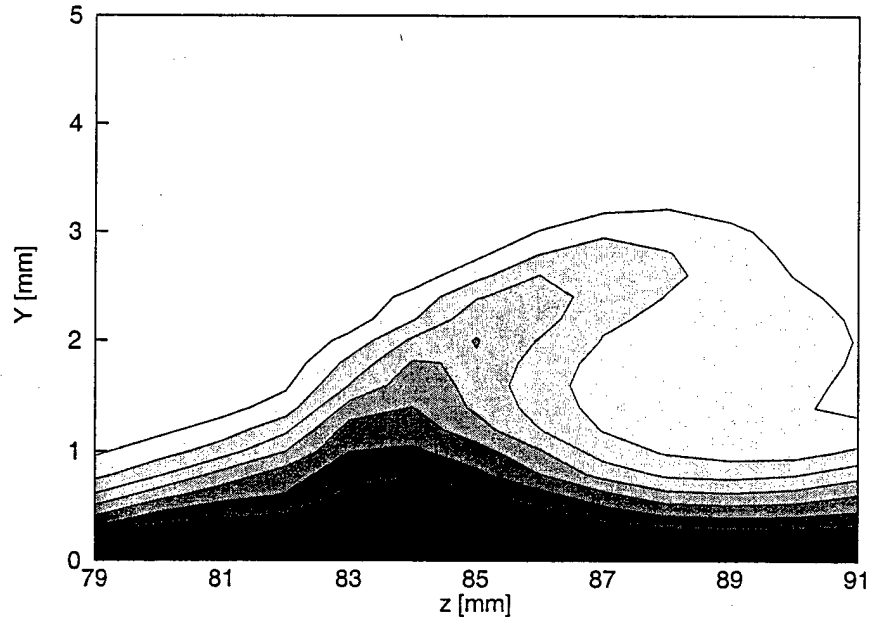


Figure 56: Mean-flow velocity contours,  $Re_c = 2.4 \times 10^6$ , [18|12] roughness,  $x/c = 0.43$ , contour lines at  $U/U_{\text{edge}} = 0.10, 0.20, \dots, 0.90$ .

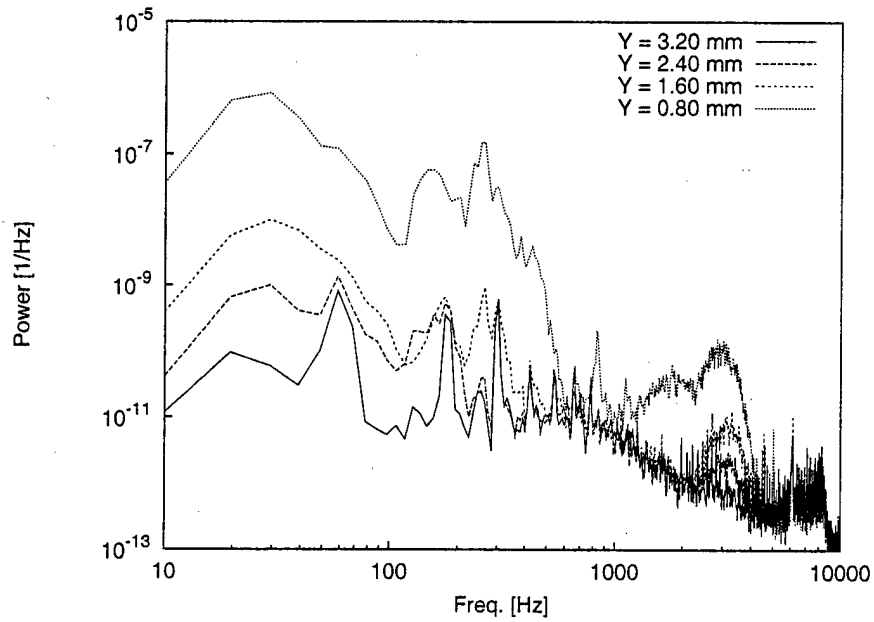


Figure 57: Fluctuating-velocity spectra,  $Re_c = 2.4 \times 10^6$ , [18|12] roughness,  $x/c = 0.43$ ,  $z = 81$  mm.

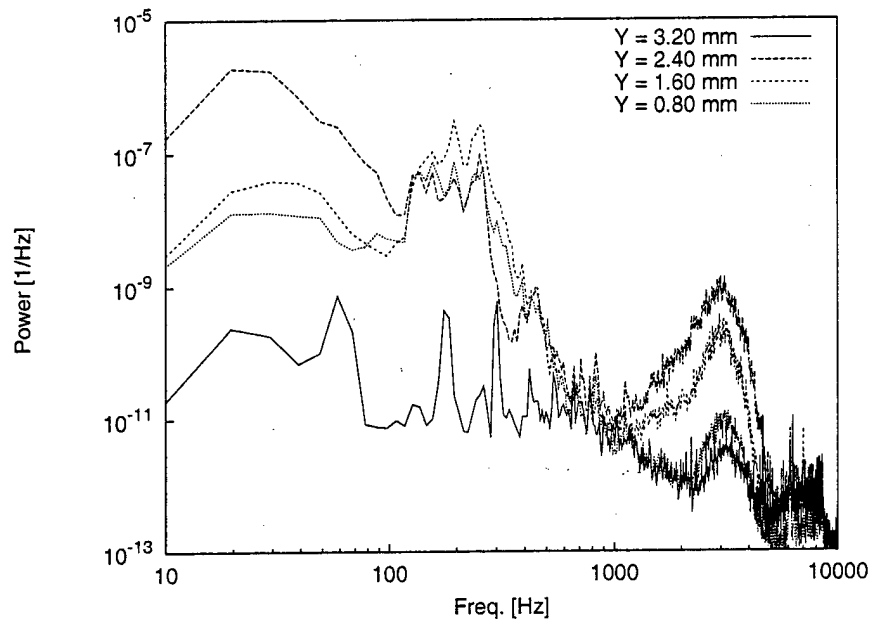


Figure 58: Fluctuating-velocity spectra,  $Re_c = 2.4 \times 10^6$ , [18|12] roughness,  $x/c = 0.43$ ,  $z = 84$  mm.

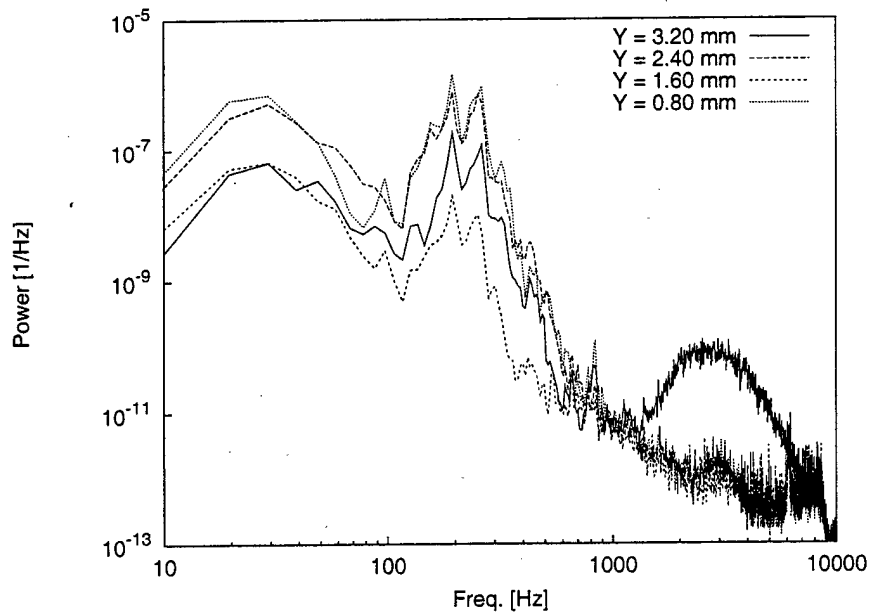


Figure 59: Fluctuating-velocity spectra,  $Re_c = 2.4 \times 10^6$ , [18|12] roughness,  $x/c = 0.43$ ,  $z = 87$  mm.

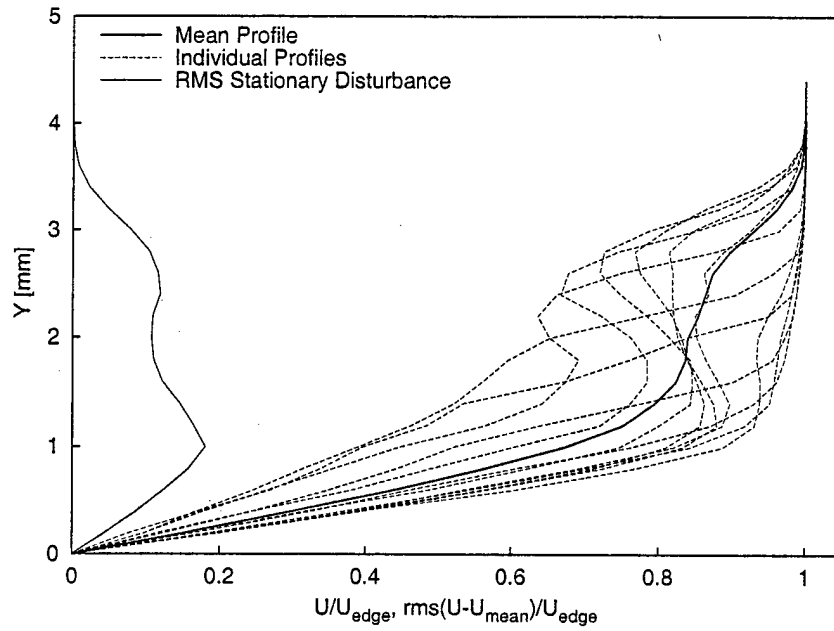


Figure 60: Mean-flow velocity profiles,  $Re_c = 2.4 \times 10^6$ , [18|12] roughness,  $x/c = 0.44$ ,  $z = 76\text{--}87$  mm.

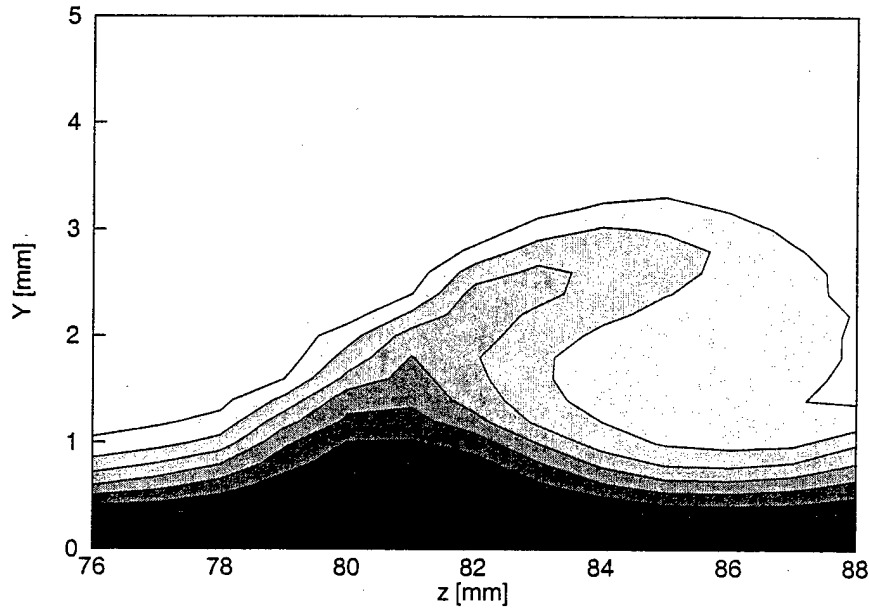


Figure 61: Mean-flow velocity contours,  $Re_c = 2.4 \times 10^6$ , [18|12] roughness,  $x/c = 0.44$ , contour lines at  $U/U_{\text{edge}} = 0.10, 0.20, \dots, 0.90$ .



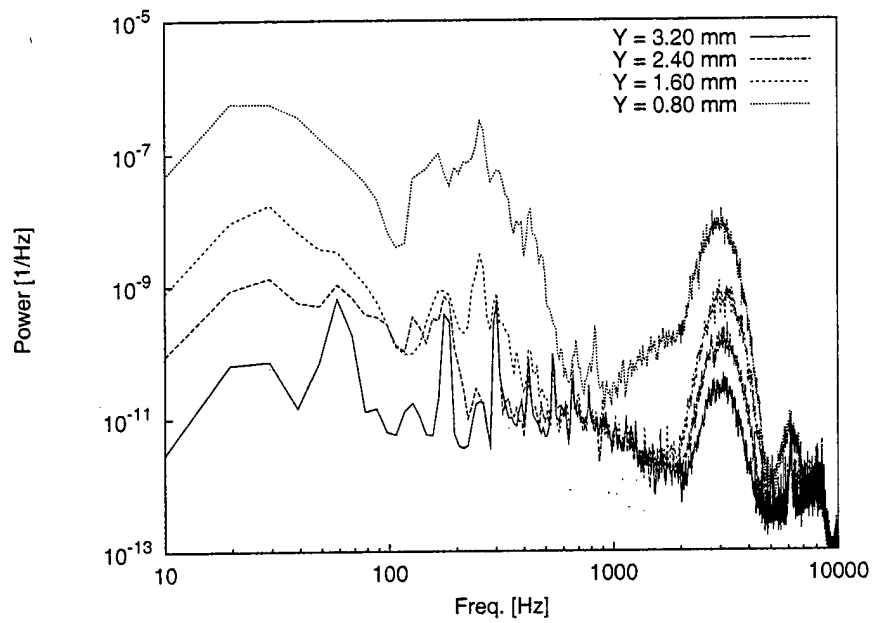


Figure 62: Fluctuating-velocity spectra,  $Re_c = 2.4 \times 10^6$ , [18|12] roughness,  $x/c = 0.44$ ,  $z = 78$  mm.

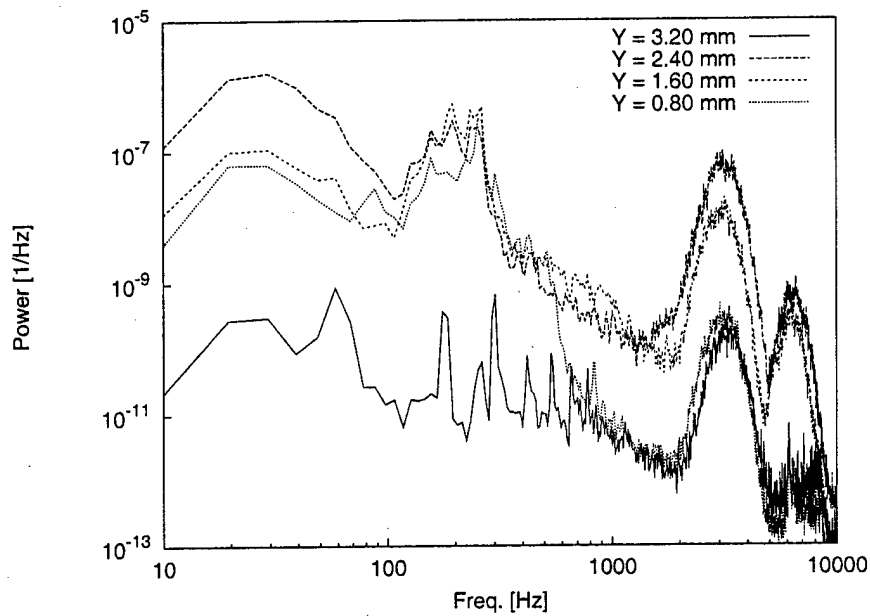


Figure 63: Fluctuating-velocity spectra,  $Re_c = 2.4 \times 10^6$ , [18|12] roughness,  $x/c = 0.44$ ,  $z = 81$  mm.

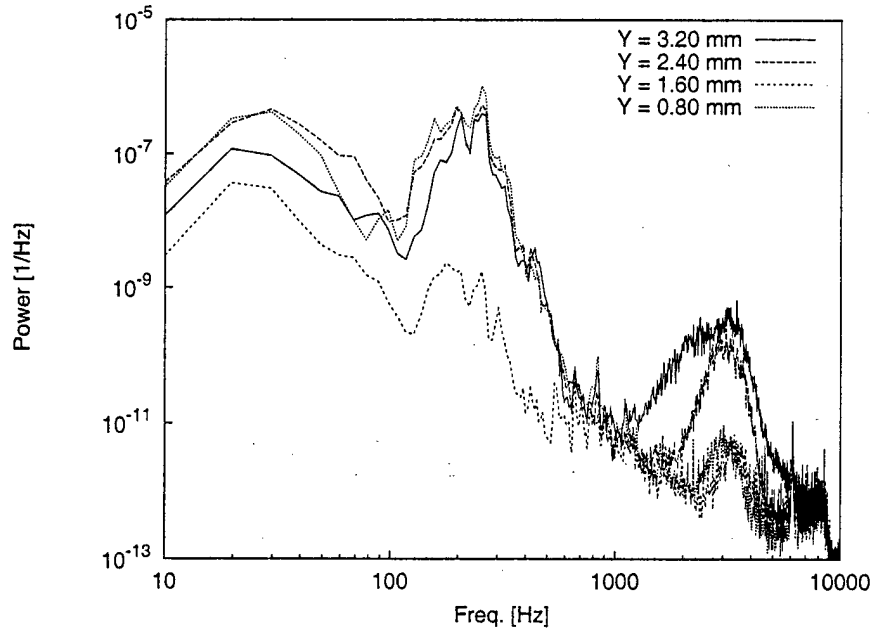


Figure 64: Fluctuating-velocity spectra,  $Re_c = 2.4 \times 10^6$ , [18|12] roughness,  $x/c = 0.44$ ,  $z = 84$  mm.

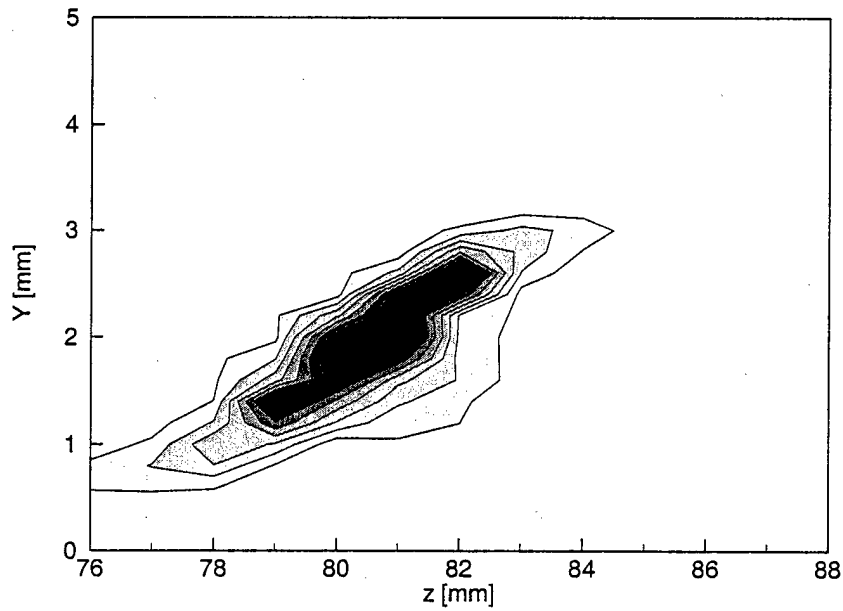


Figure 65: 3.0-kHz velocity-fluctuation rms distribution,  $Re_c = 2.4 \times 10^6$ , [18|12] roughness,  $x/c = 0.44$ , 2.9–3.1-Hz bandpass. Lines are 10% contours of the maximum in this band.

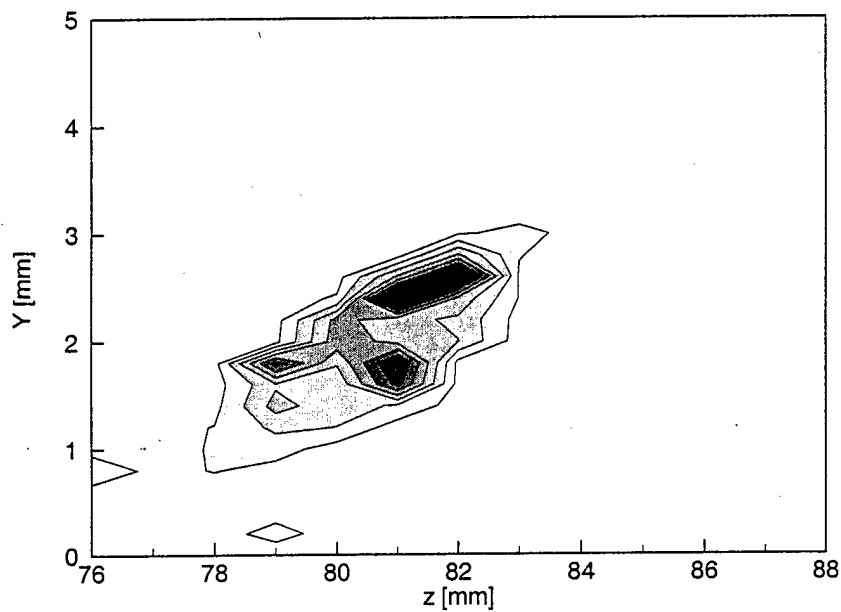


Figure 66: 6.1-kHz velocity-fluctuation rms distribution,  $Re_c = 2.4 \times 10^6$ , [18|12] roughness,  $x/c = 0.44$ , 6.0–6.2-Hz bandpass. Lines are 10% contours of the maximum in this band.

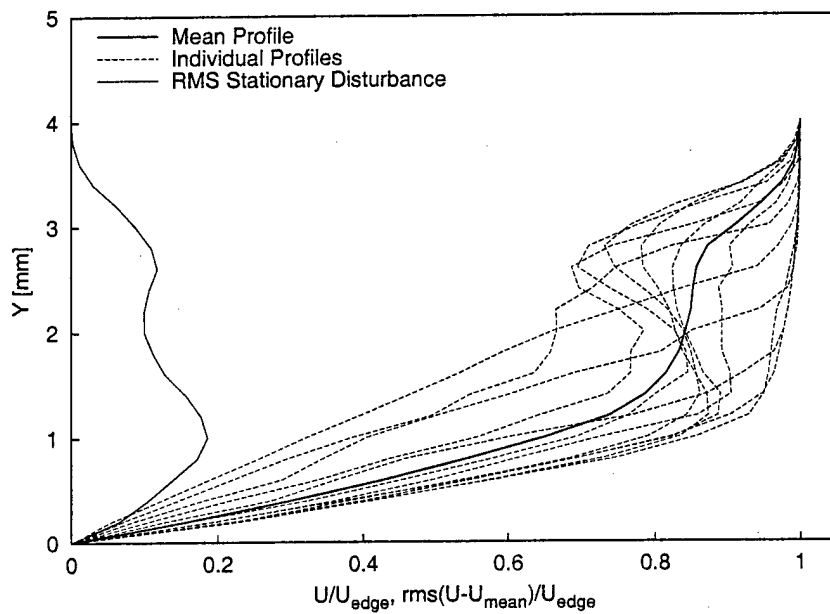


Figure 67: Mean-flow velocity profiles,  $Re_c = 2.4 \times 10^6$ , [18|12] roughness,  $x/c = 0.45$ ,  $z = 75$ – $86$  mm.

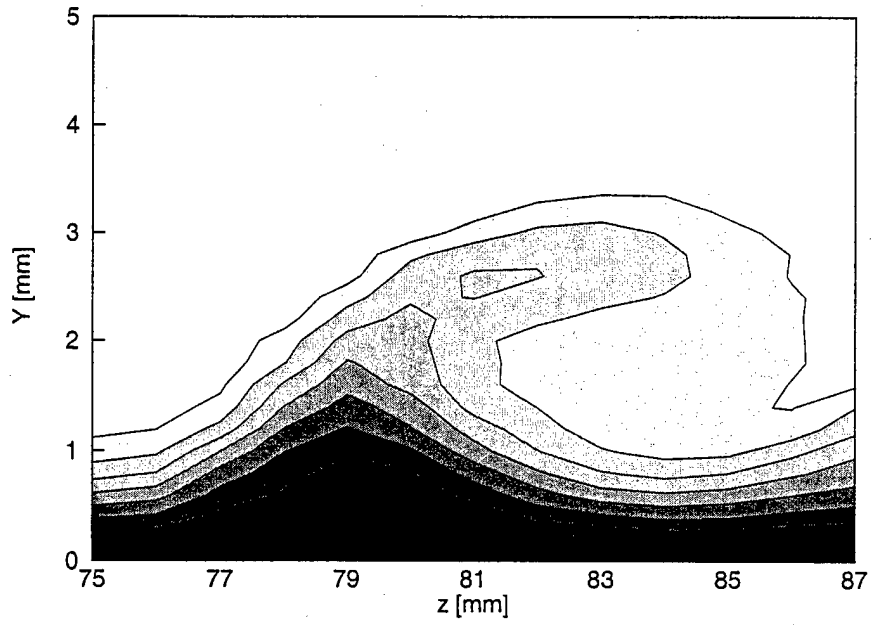


Figure 68: Mean-flow velocity contours,  $Re_c = 2.4 \times 10^6$ , [18|12] roughness,  $x/c = 0.45$ , contour lines at  $U/U_{\text{edge}} = 0.10, 0.20, \dots, 0.90$ .

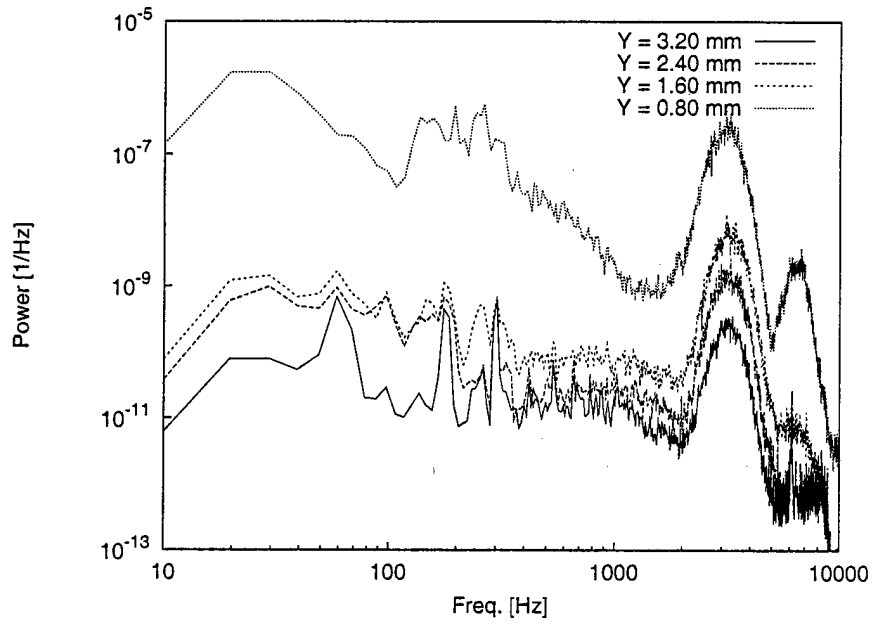


Figure 69: Fluctuating-velocity spectra,  $Re_c = 2.4 \times 10^6$ , [18|12] roughness,  $x/c = 0.45$ ,  $z = 76$  mm.

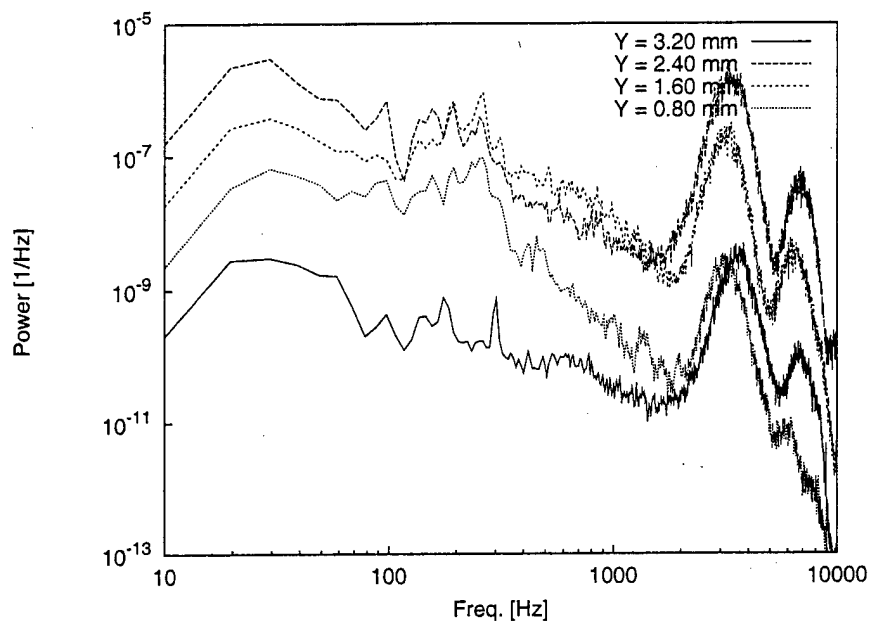


Figure 70: Fluctuating-velocity spectra,  $Re_c = 2.4 \times 10^6$ , [18|12] roughness,  $x/c = 0.45$ ,  $z = 79$  mm.

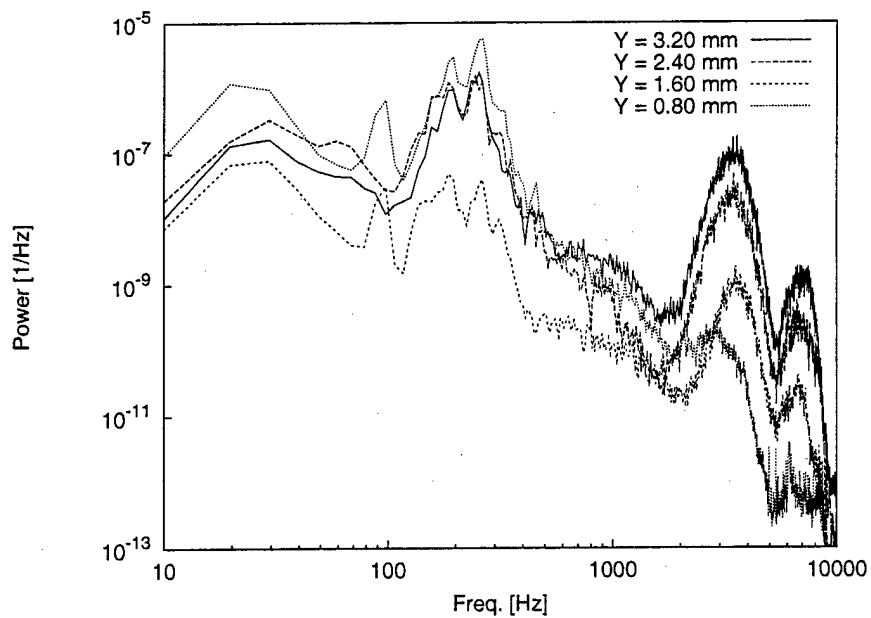


Figure 71: Fluctuating-velocity spectra,  $Re_c = 2.4 \times 10^6$ , [18|12] roughness,  $x/c = 0.45$ ,  $z = 82$  mm.

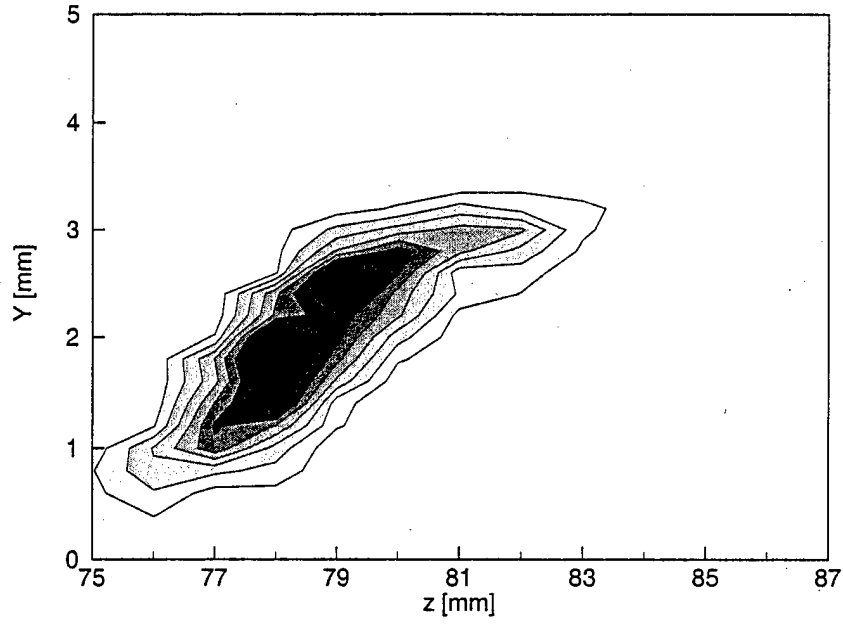


Figure 72: 6.1-kHz velocity-fluctuation rms distribution,  $Re_c = 2.4 \times 10^6$ , [18|12] roughness,  $x/c = 0.45$ , 6.0–6.2-Hz bandpass. Lines are 10% contours of the maximum in this band.

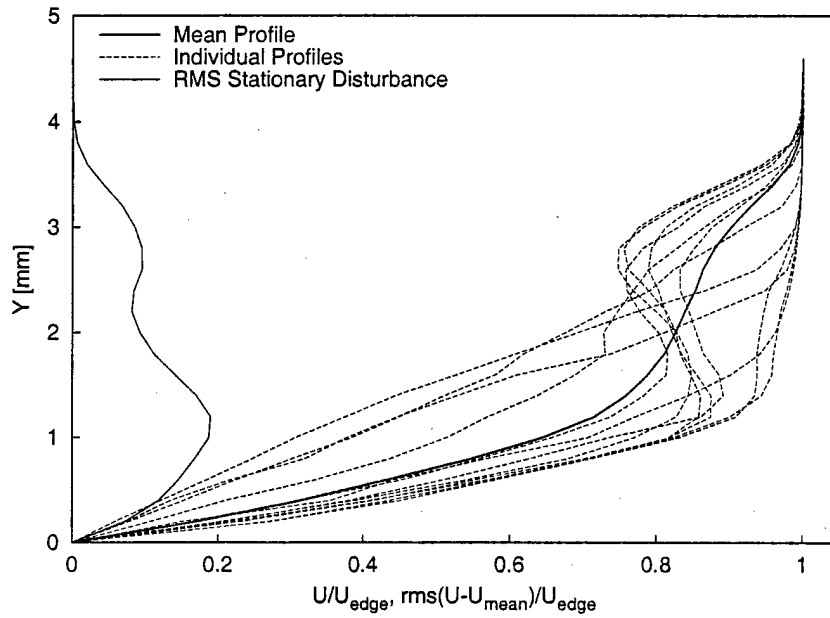


Figure 73: Mean-flow velocity profiles,  $Re_c = 2.4 \times 10^6$ , [18|12] roughness,  $x/c = 0.46$ ,  $z = 71$ –82 mm.

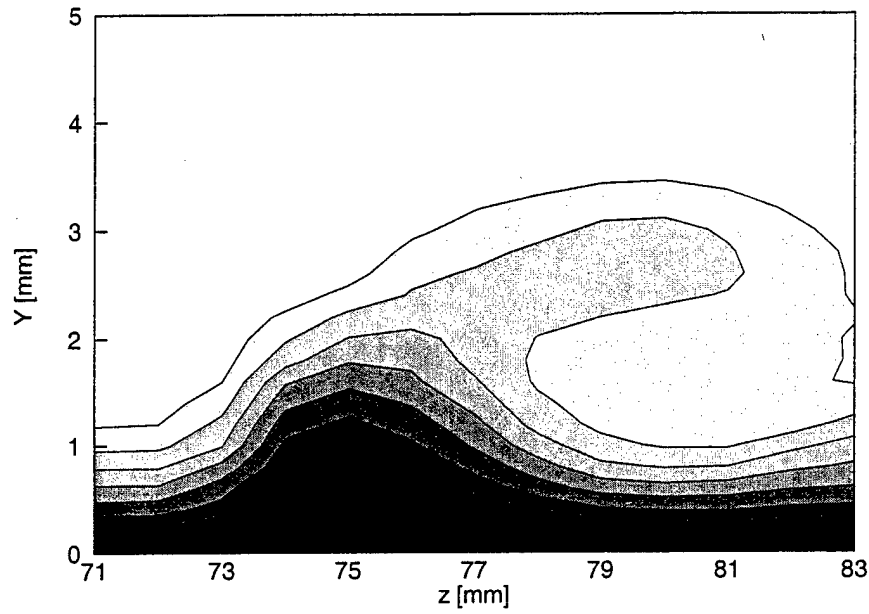


Figure 74: Mean-flow velocity contours,  $Re_c = 2.4 \times 10^6$ , [18|12] roughness,  $x/c = 0.46$ , contour lines at  $U/U_{\text{edge}} = 0.10, 0.20, \dots, 0.90$ .

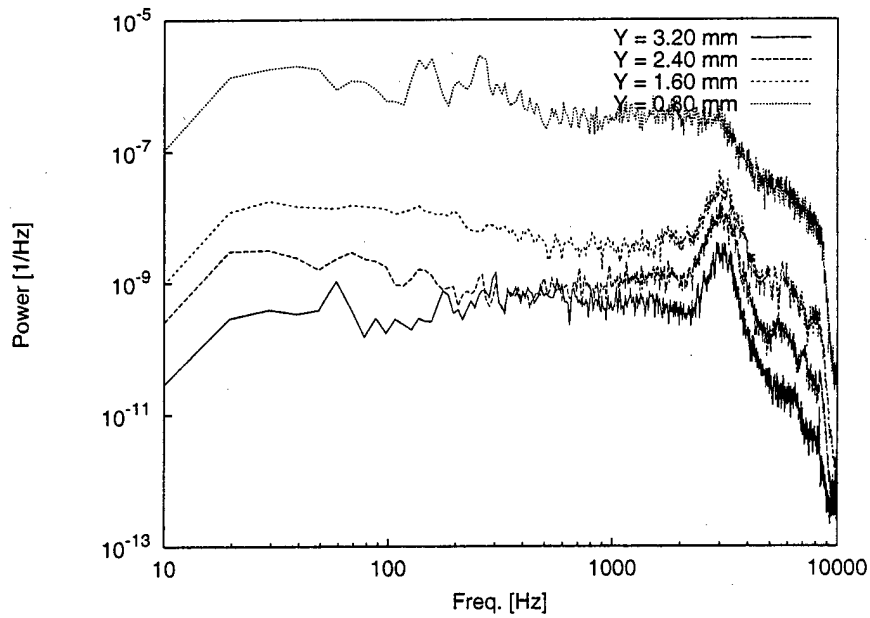


Figure 75: Fluctuating-velocity spectra,  $Re_c = 2.4 \times 10^6$ , [18|12] roughness,  $x/c = 0.46$ ,  $z = 72$  mm.

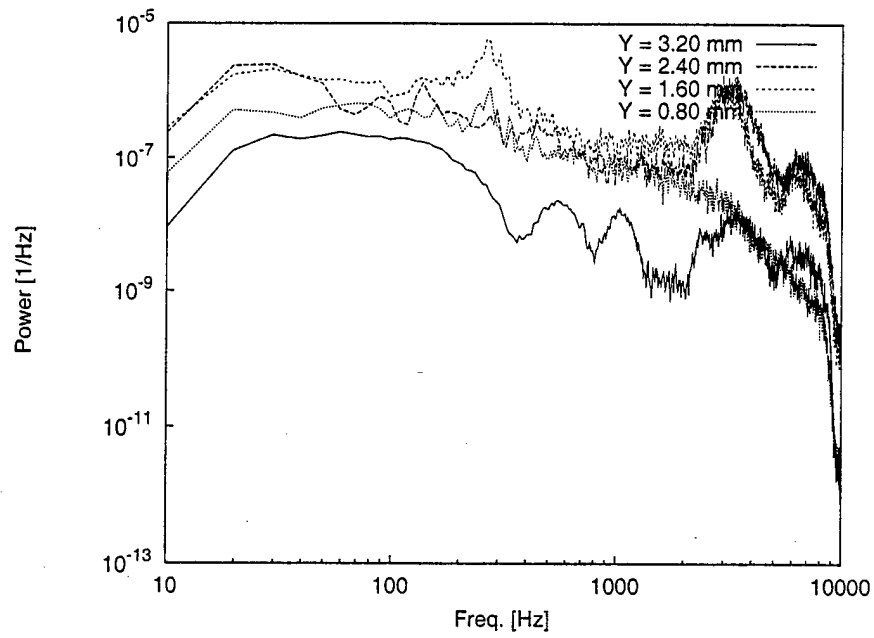


Figure 76: Fluctuating-velocity spectra,  $Re_c = 2.4 \times 10^6$ , [18|12] roughness,  $x/c = 0.46$ ,  $z = 75$  mm.

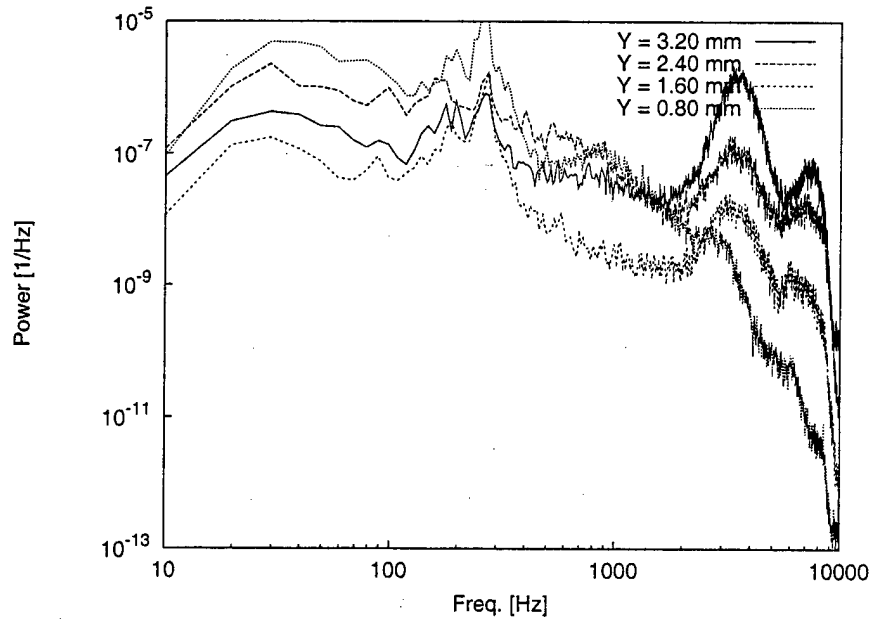


Figure 77: Fluctuating-velocity spectra,  $Re_c = 2.4 \times 10^6$ , [18|12] roughness,  $x/c = 0.46$ ,  $z = 78$  mm.



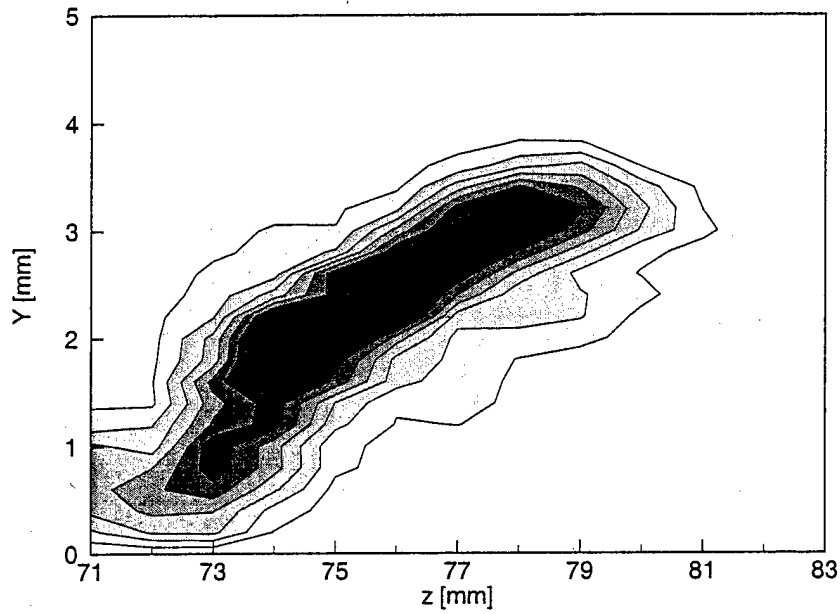


Figure 78: Total velocity-fluctuation rms distribution,  $Re_c = 2.4 \times 10^6$ , [18|12] roughness,  $x/c = 0.46$ , 20 Hz–8.0-kHz bandpass. Lines are 10% contours of the maximum rms fluctuations.

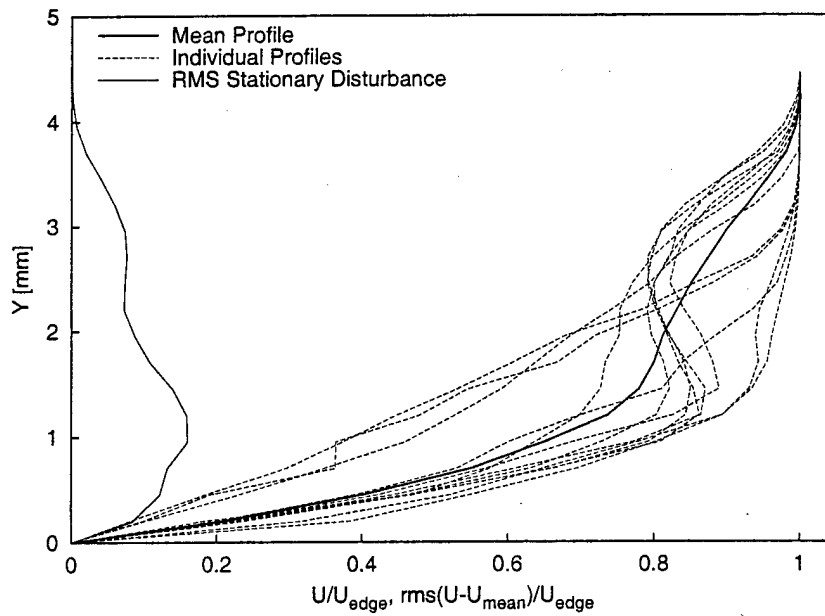


Figure 79: Mean-flow velocity profiles,  $Re_c = 2.4 \times 10^6$ , [18|12] roughness,  $x/c = 0.47$ ,  $z = 68$ –79 mm.

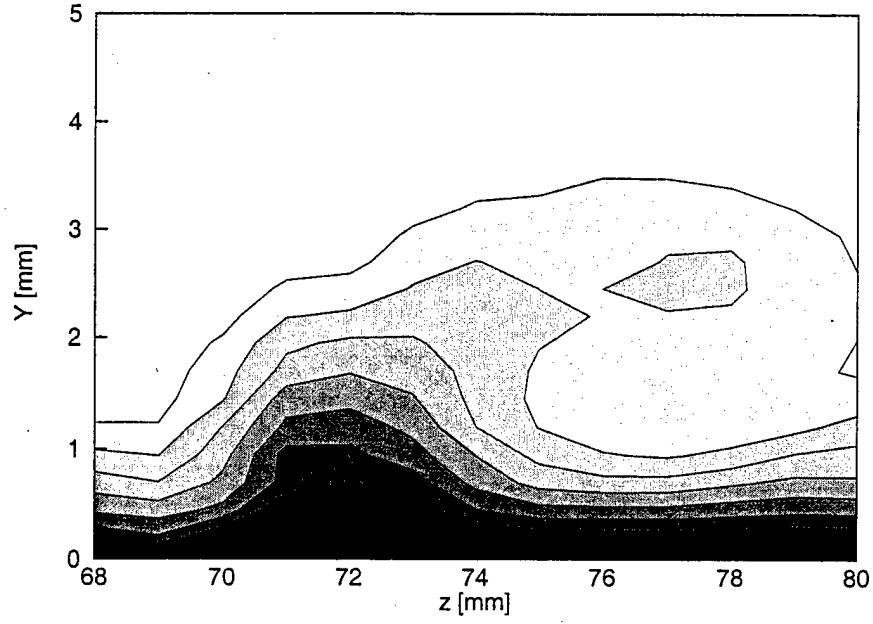


Figure 80: Mean-flow velocity contours,  $Re_c = 2.4 \times 10^6$ , [18|12] roughness,  $x/c = 0.47$ , contour lines at  $U/U_{\text{edge}} = 0.10, 0.20, \dots, 0.90$ .

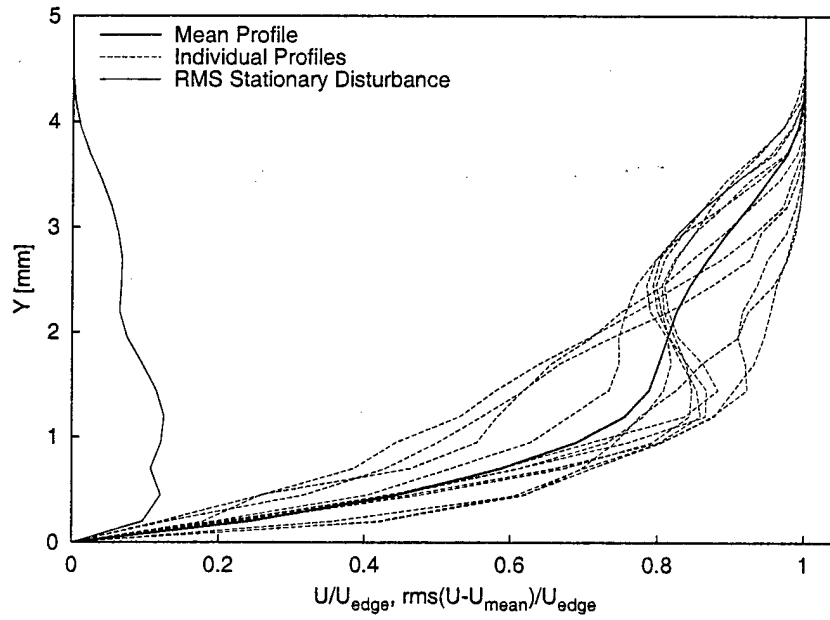


Figure 81: Mean-flow velocity profiles,  $Re_c = 2.4 \times 10^6$ , [18|12] roughness,  $x/c = 0.48$ ,  $z = 64-75$  mm.

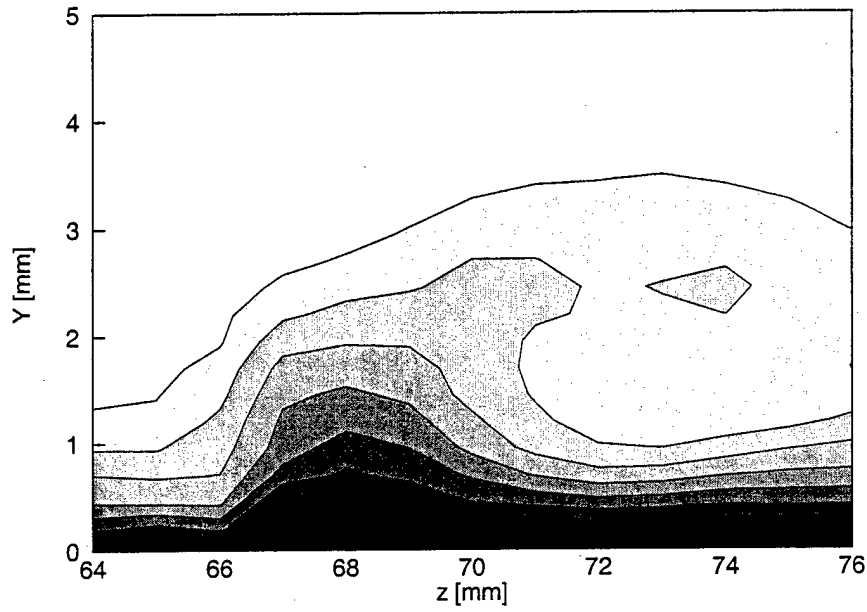


Figure 82: Mean-flow velocity contours,  $Re_c = 2.4 \times 10^6$ , [18|12] roughness,  $x/c = 0.48$ , contour lines at  $U/U_{\text{edge}} = 0.10, 0.20, \dots, 0.90$ .

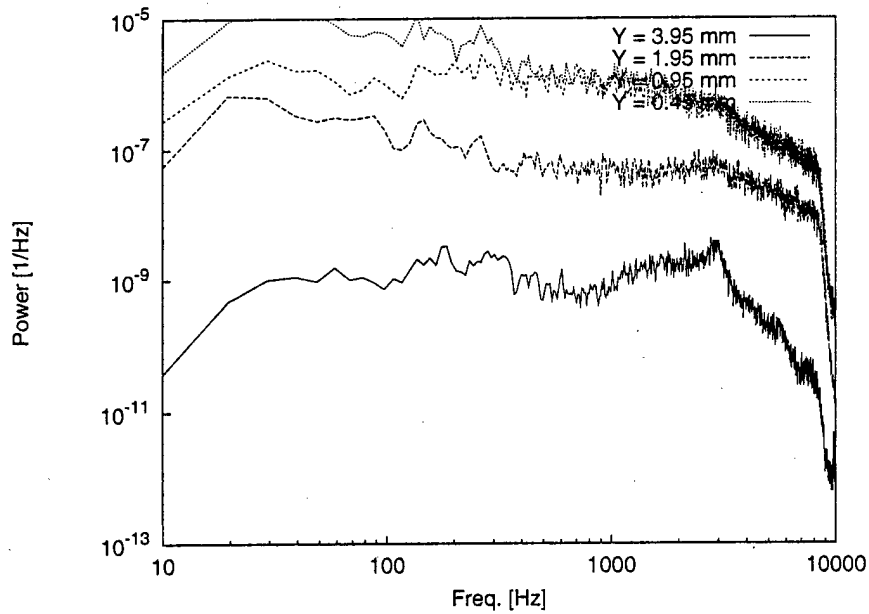


Figure 83: Fluctuating-velocity spectra,  $Re_c = 2.4 \times 10^6$ , [18|12] roughness,  $x/c = 0.48$ ,  $z = 65$  mm.

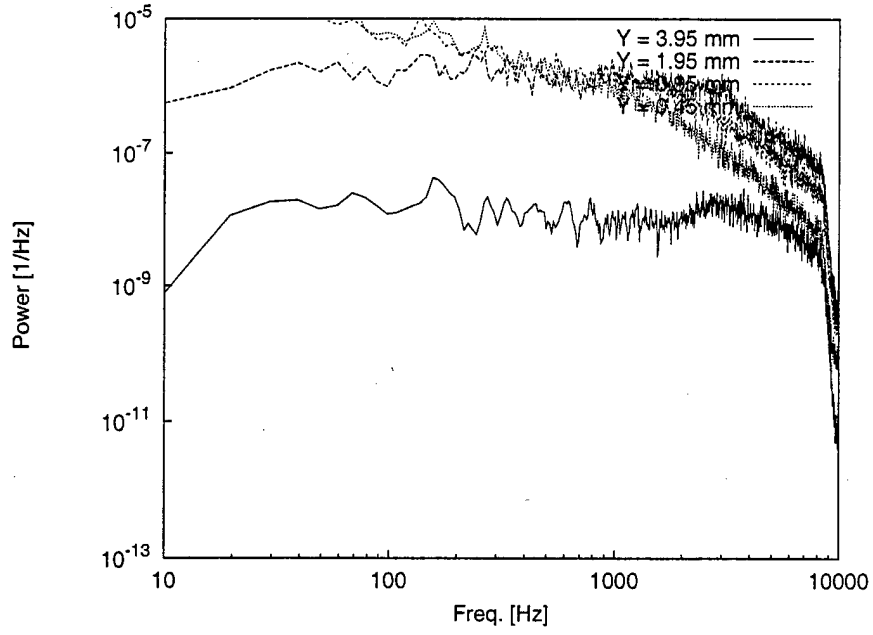


Figure 84: Fluctuating-velocity spectra,  $Re_c = 2.4 \times 10^6$ , [18|12] roughness,  $x/c = 0.48$ ,  $z = 68$  mm.

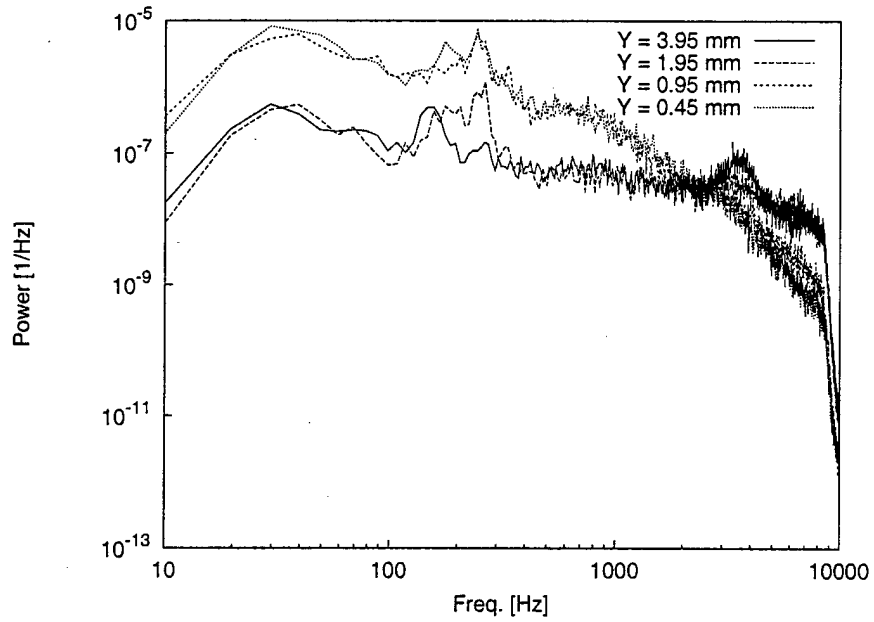


Figure 85: Fluctuating-velocity spectra,  $Re_c = 2.4 \times 10^6$ , [18|12] roughness,  $x/c = 0.48$ ,  $z = 71$  mm.

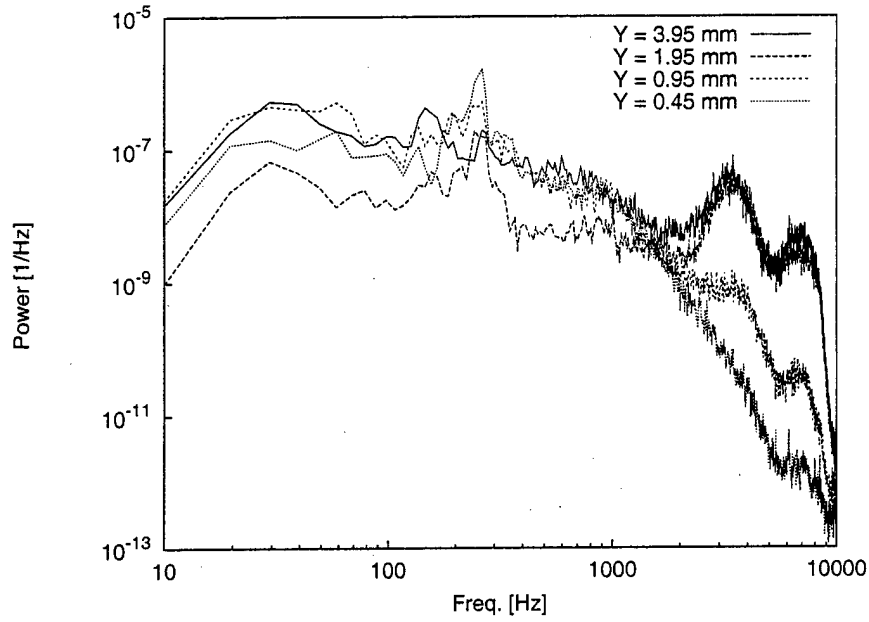


Figure 86: Fluctuating-velocity spectra,  $Re_c = 2.4 \times 10^6$ , [18|12] roughness,  $x/c = 0.48$ ,  $z = 74$  mm.

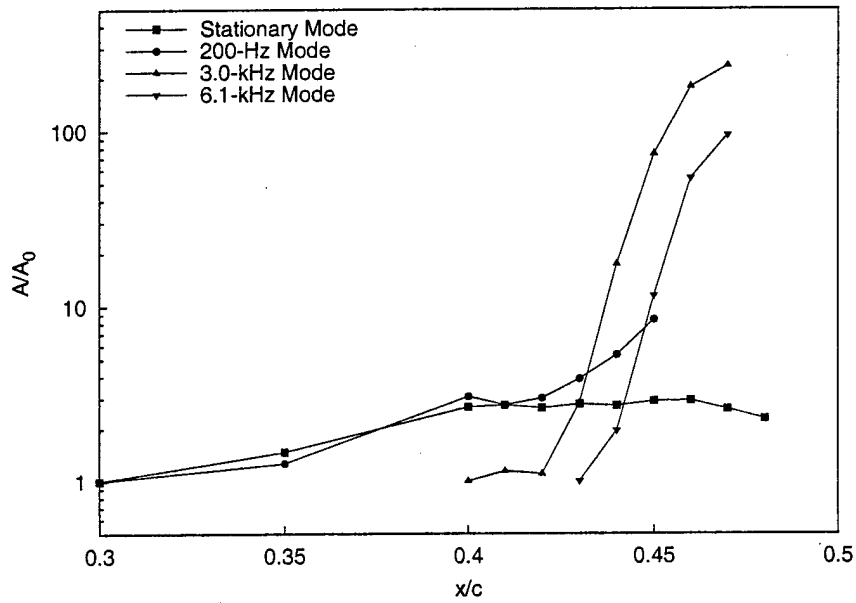


Figure 87: Velocity-fluctuation rms growth,  $Re_c = 2.4 \times 10^6$ , [18|12] roughness.

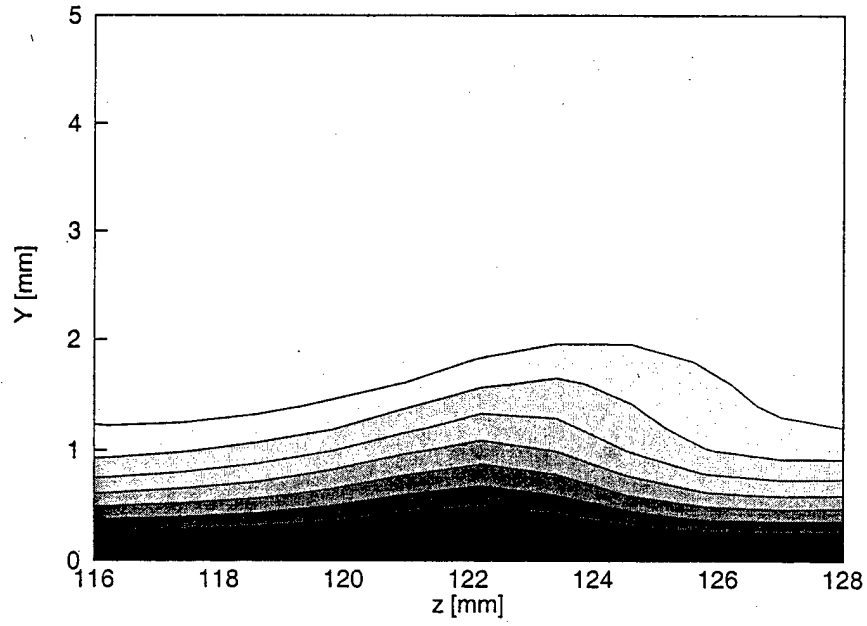


Figure 88: Mean-flow velocity contours,  $Re_c = 2.4 \times 10^6$ , [54|12] roughness,  $x/c = 0.25$ , contour lines at  $U/U_{\text{edge}} = 0.10, 0.20, \dots, 0.90$ .

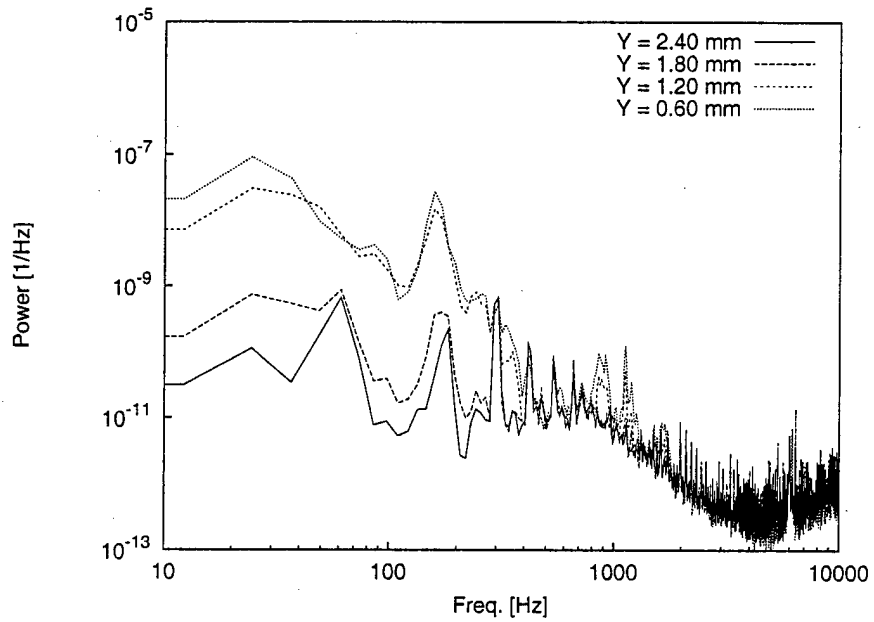


Figure 89: Fluctuating-velocity spectra,  $Re_c = 2.4 \times 10^6$ , [54|12] roughness,  $x/c = 0.25$ ,  $z = 118.6$  mm.

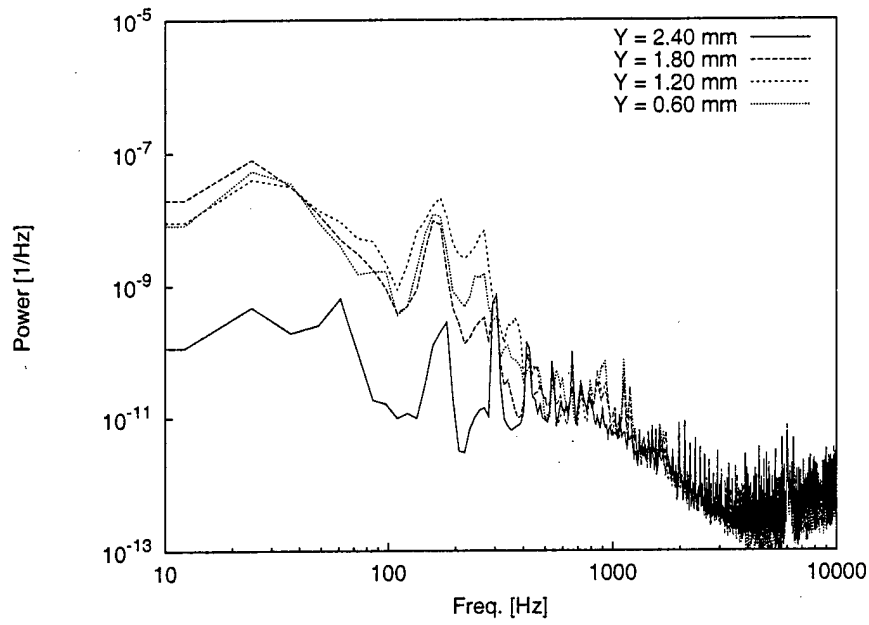


Figure 90: Fluctuating-velocity spectra,  $Re_c = 2.4 \times 10^6$ , [54|12] roughness,  $x/c = 0.25$ ,  $z = 122.2$  mm.

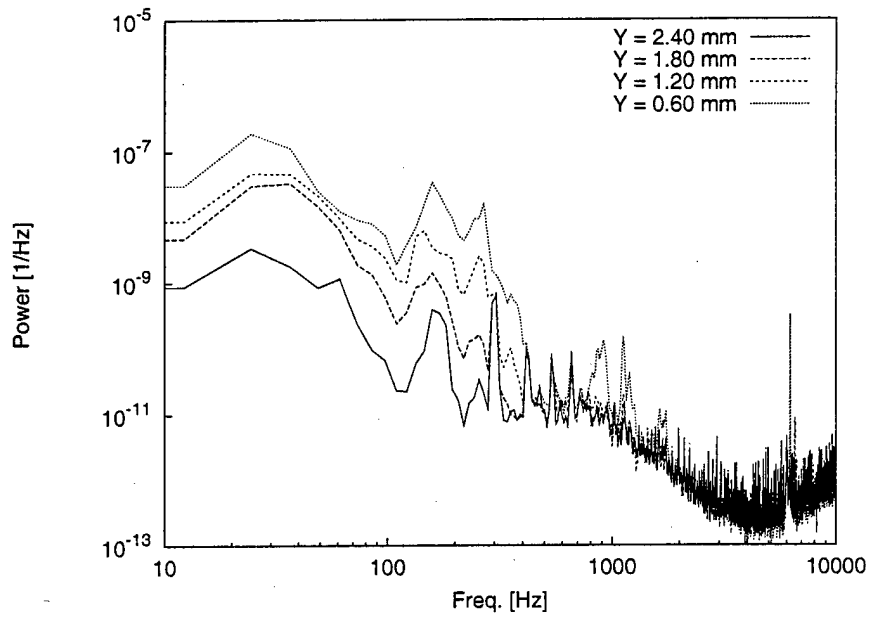


Figure 91: Fluctuating-velocity spectra,  $Re_c = 2.4 \times 10^6$ , [54|12] roughness,  $x/c = 0.25$ ,  $z = 125.8$  mm.

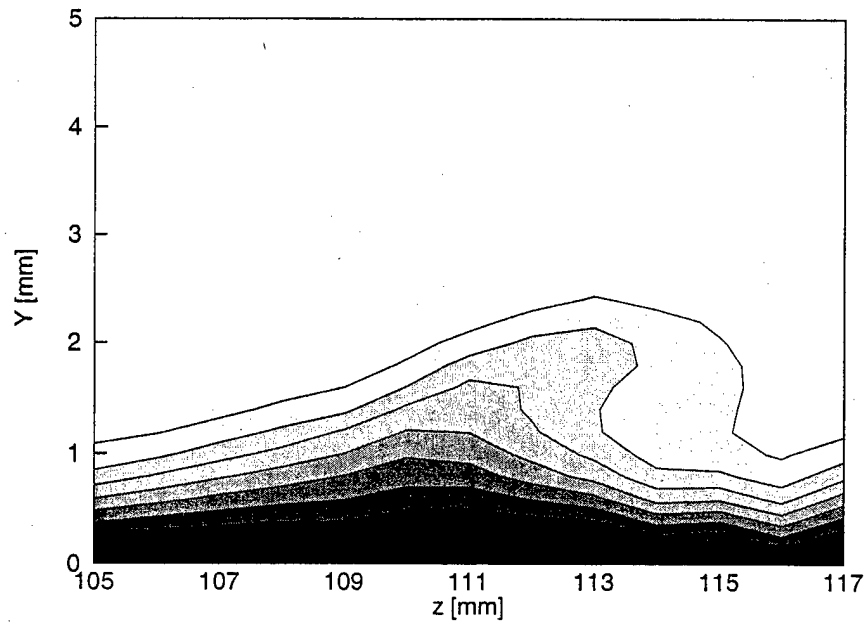


Figure 92: Mean-flow velocity contours,  $Re_c = 2.4 \times 10^6$ , [54|12] roughness,  $x/c = 0.30$ , contour lines at  $U/U_{\text{edge}} = 0.10, 0.20, \dots, 0.90$ .

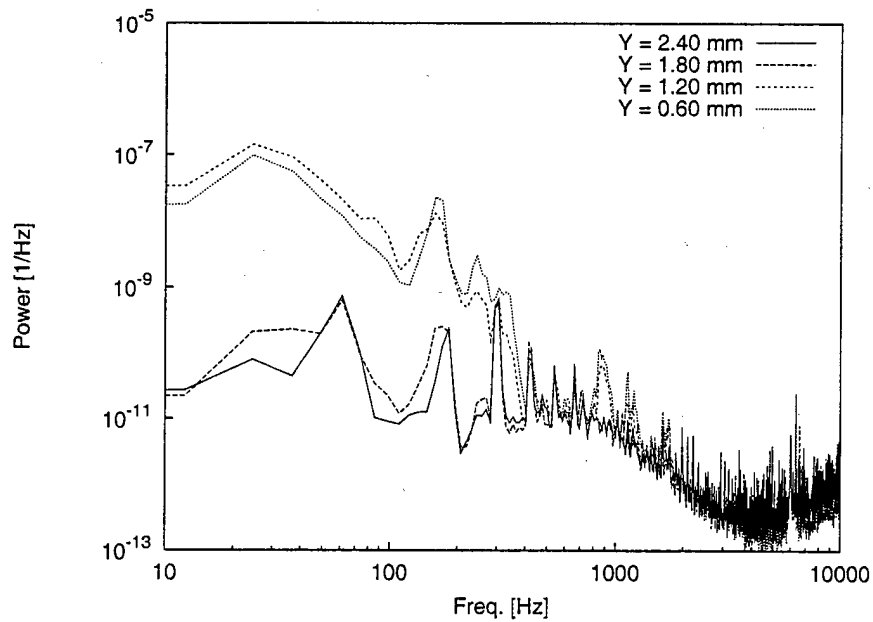


Figure 93: Fluctuating-velocity spectra,  $Re_c = 2.4 \times 10^6$ , [54|12] roughness,  $x/c = 0.30$ ,  $z = 107$  mm.



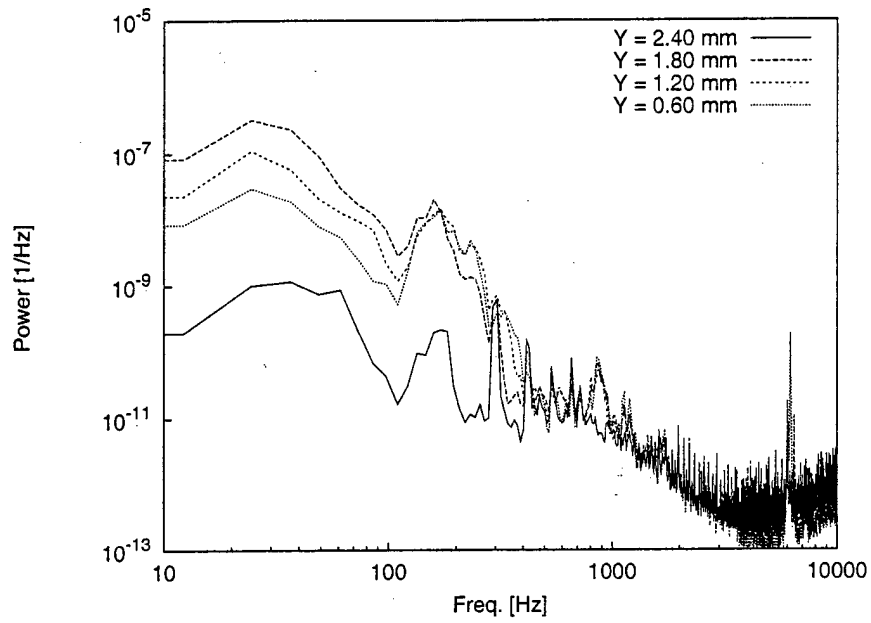


Figure 94: Fluctuating-velocity spectra,  $Re_c = 2.4 \times 10^6$ , [54|12] roughness,  $x/c = 0.30$ ,  $z = 110$  mm.

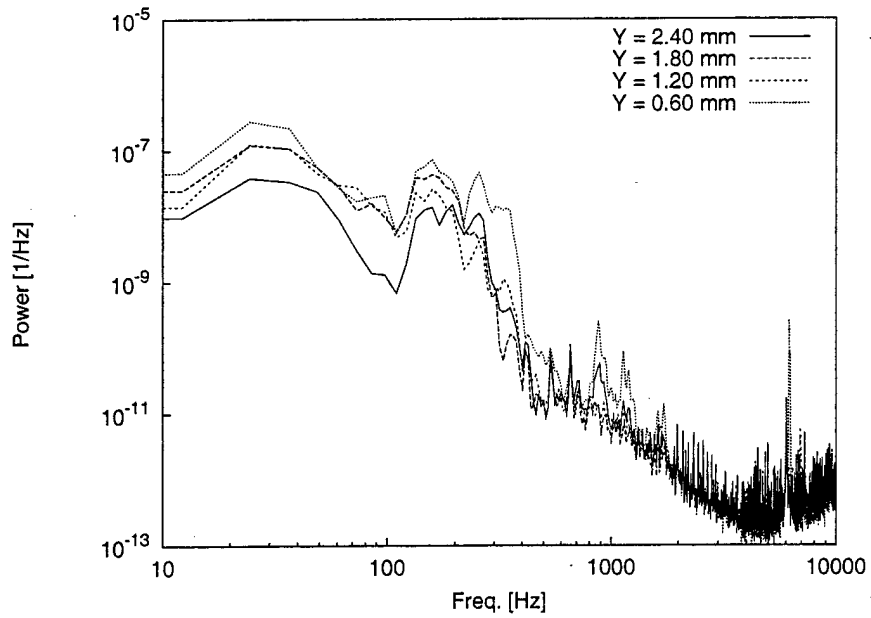


Figure 95: Fluctuating-velocity spectra,  $Re_c = 2.4 \times 10^6$ , [54|12] roughness,  $x/c = 0.30$ ,  $z = 113$  mm.

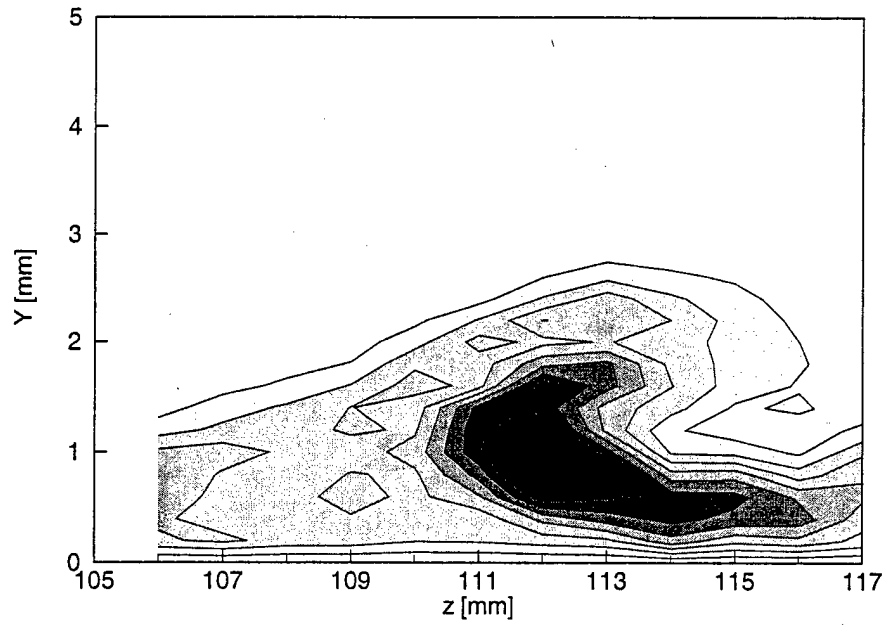


Figure 96: 200-Hz velocity-fluctuation rms distribution,  $Re_c = 2.4 \times 10^6$ , [54|12] roughness,  $x/c = 0.30$ , 100–300-Hz bandpass. Lines are 10% contours of the maximum in this band.

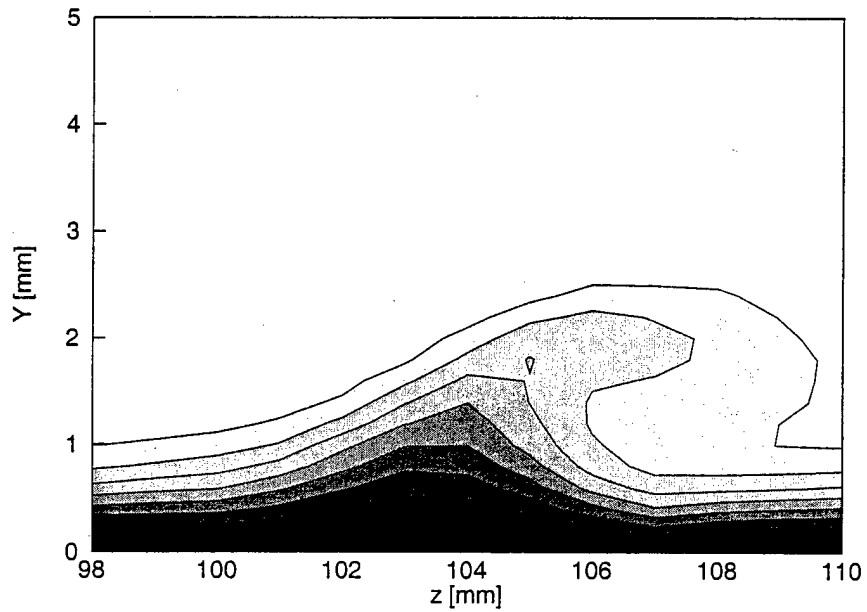


Figure 97: Mean-flow velocity contours,  $Re_c = 2.4 \times 10^6$ , [54|12] roughness,  $x/c = 0.34$ , contour lines at  $U/U_{\text{edge}} = 0.10, 0.20, \dots, 0.90$ .

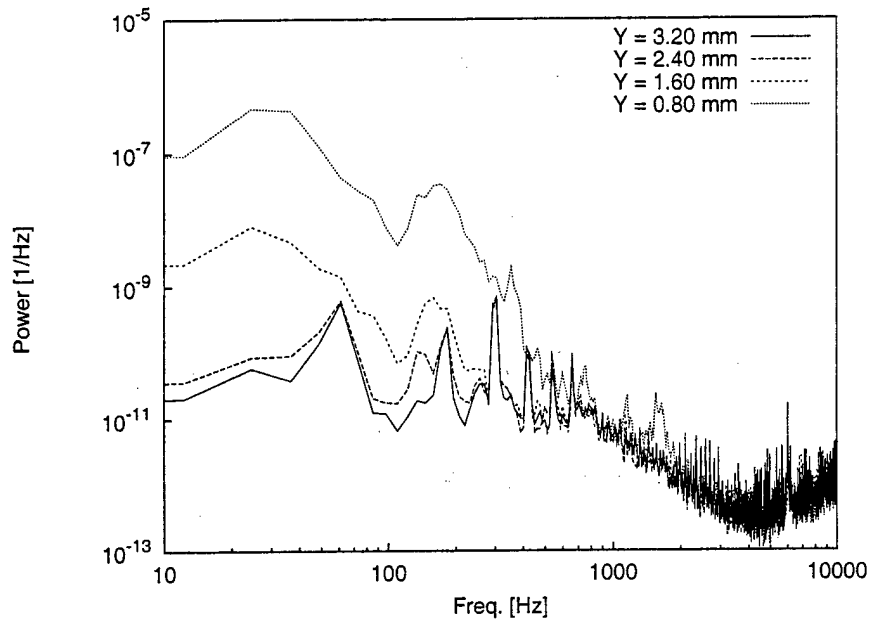


Figure 98: Fluctuating-velocity spectra,  $Re_c = 2.4 \times 10^6$ , [54|12] roughness,  $x/c = 0.34$ ,  $z = 101$  mm.

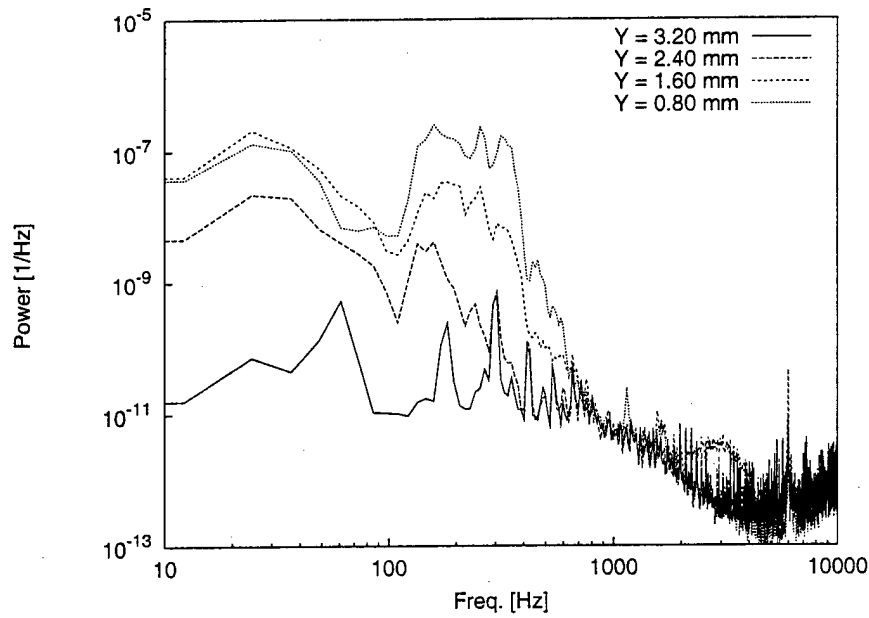


Figure 99: Fluctuating-velocity spectra,  $Re_c = 2.4 \times 10^6$ , [54|12] roughness,  $x/c = 0.34$ ,  $z = 104$  mm.

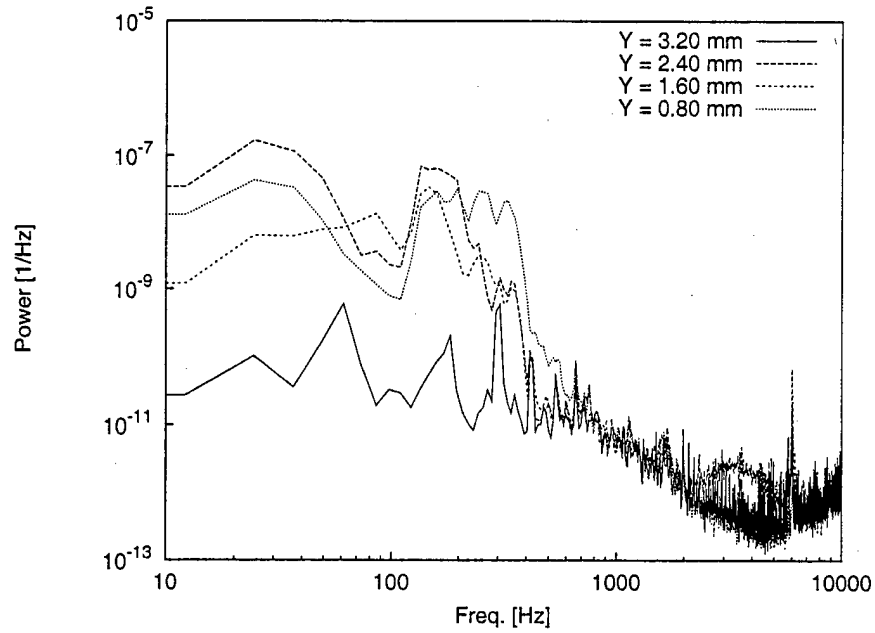


Figure 100: Fluctuating-velocity spectra,  $Re_c = 2.4 \times 10^6$ , [54|12] roughness,  $x/c = 0.34$ ,  $z = 107$  mm.

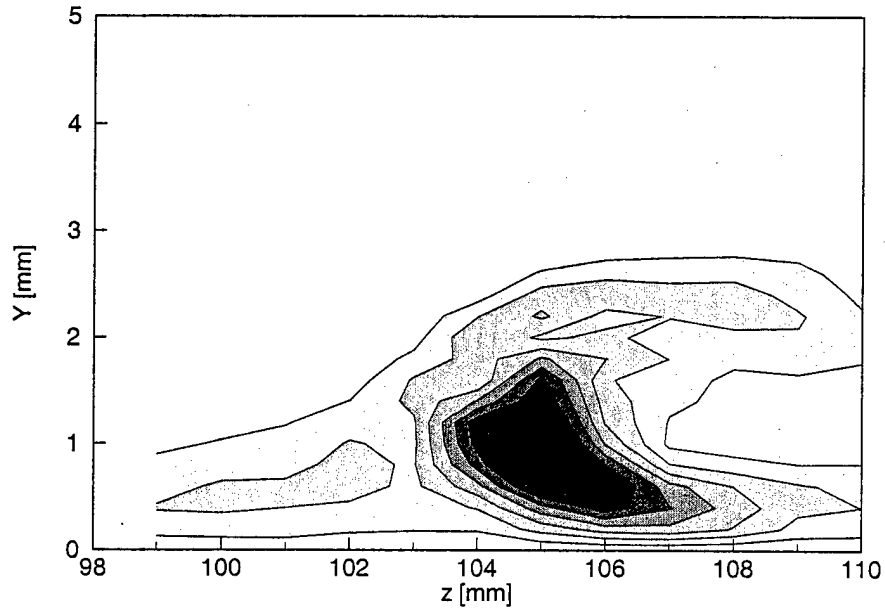


Figure 101: 200-Hz velocity-fluctuation rms distribution,  $Re_c = 2.4 \times 10^6$ , [54|12] roughness,  $x/c = 0.34$ , 100–300-Hz bandpass. Lines are 10% contours of the maximum in this band.

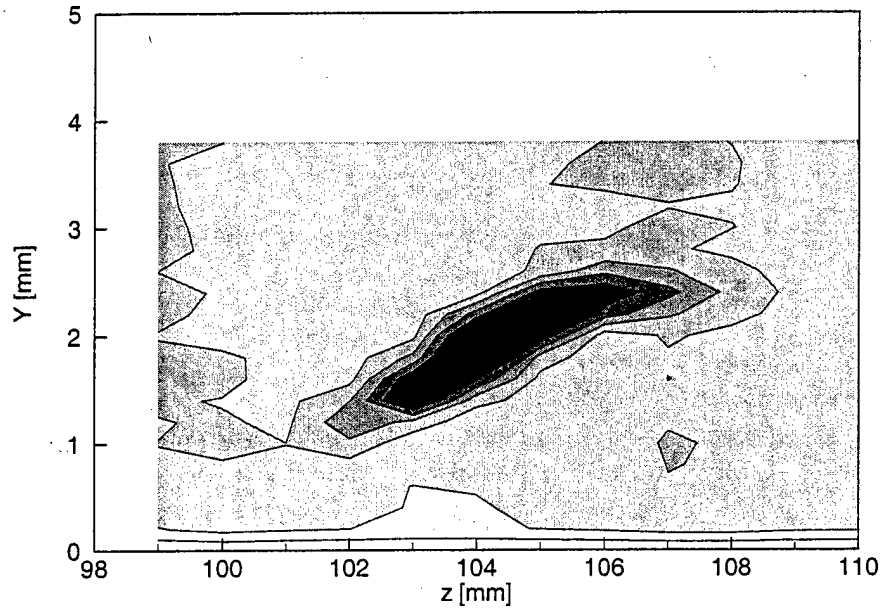


Figure 102: 3.0-kHz velocity-fluctuation rms distribution,  $Re_c = 2.4 \times 10^6$ , [54|12] roughness,  $x/c = 0.34$ , 2.9–3.1-kHz bandpass. Lines are 10% contours of the maximum in this band.

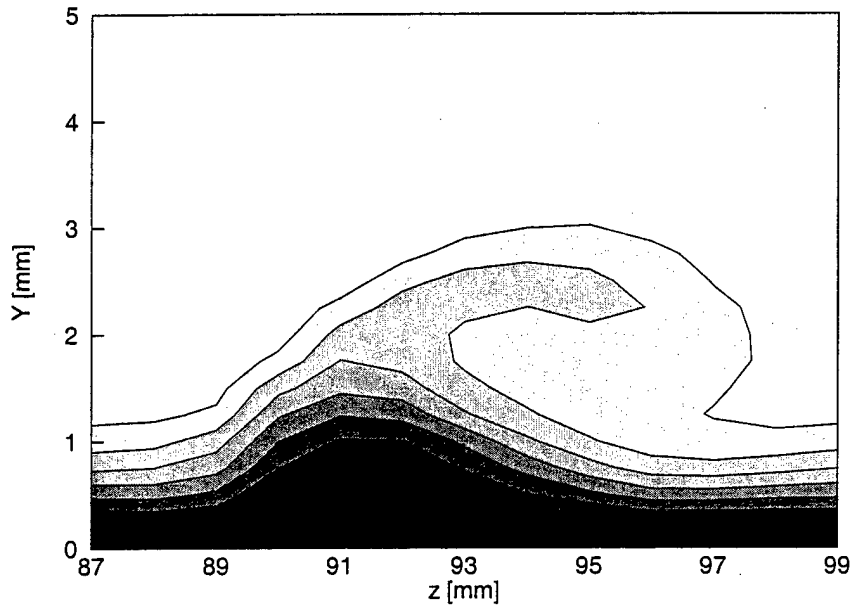


Figure 103: Mean-flow velocity contours,  $Re_c = 2.4 \times 10^6$ , [54|12] roughness,  $x/c = 0.38$ , contour lines at  $U/U_{\text{edge}} = 0.10, 0.20, \dots, 0.90$ .

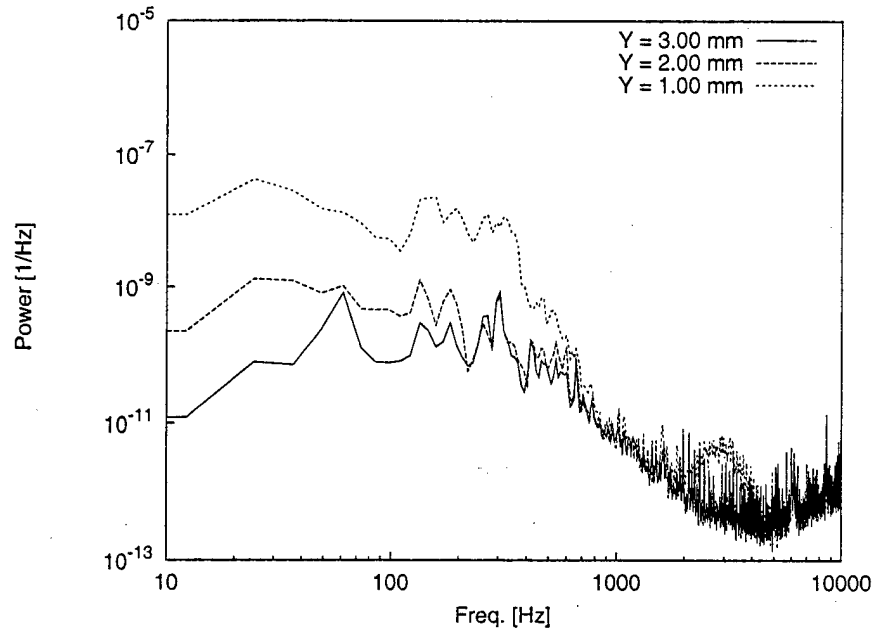


Figure 104: Fluctuating-velocity spectra,  $Re_c = 2.4 \times 10^6$ , [54|12] roughness,  $x/c = 0.38$ ,  $z = 88$  mm.

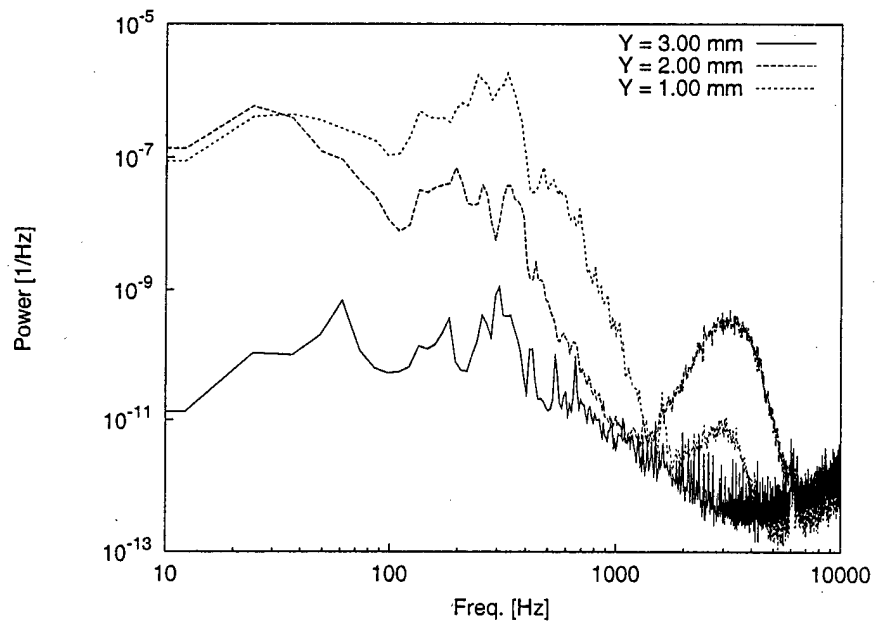


Figure 105: Fluctuating-velocity spectra,  $Re_c = 2.4 \times 10^6$ , [54|12] roughness,  $x/c = 0.38$ ,  $z = 91$  mm.

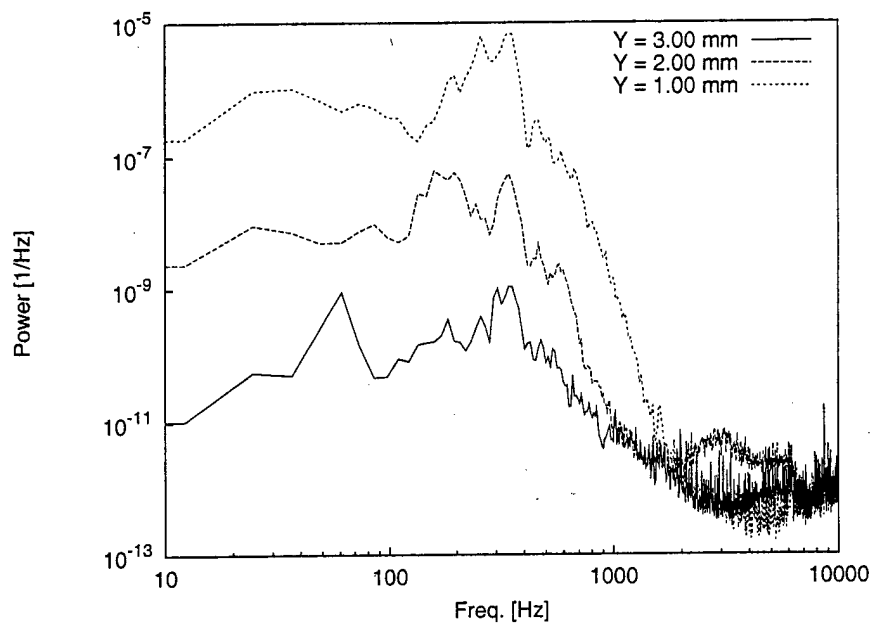


Figure 106: Fluctuating-velocity spectra,  $Re_c = 2.4 \times 10^6$ , [54|12] roughness,  $x/c = 0.38$ ,  $z = 94$  mm.

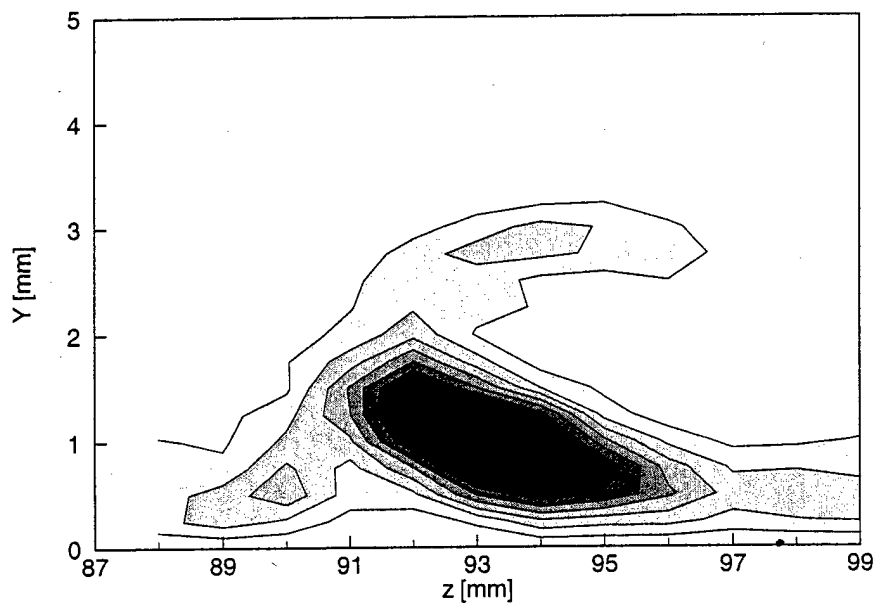


Figure 107: 200-Hz velocity-fluctuation rms distribution,  $Re_c = 2.4 \times 10^6$ , [54|12] roughness,  $x/c = 0.38$ , 100-300-Hz bandpass. Lines are 10% contours of the maximum in this band.

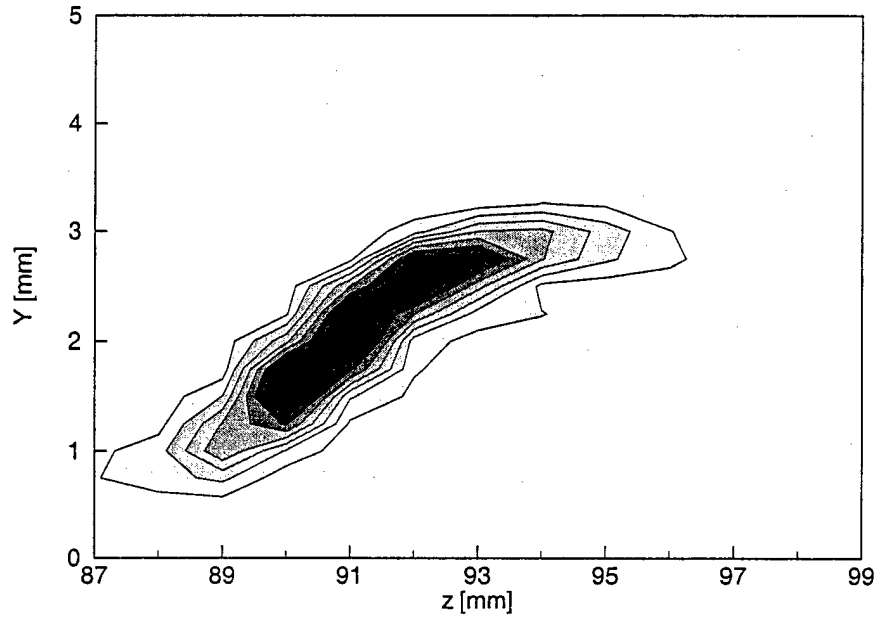


Figure 108: 3.0-kHz velocity-fluctuation rms distribution,  $Re_c = 2.4 \times 10^6$ , [54|12] roughness,  $x/c = 0.38$ , 2.9–3.1-Hz bandpass. Lines are 10% contours of the maximum in this band.

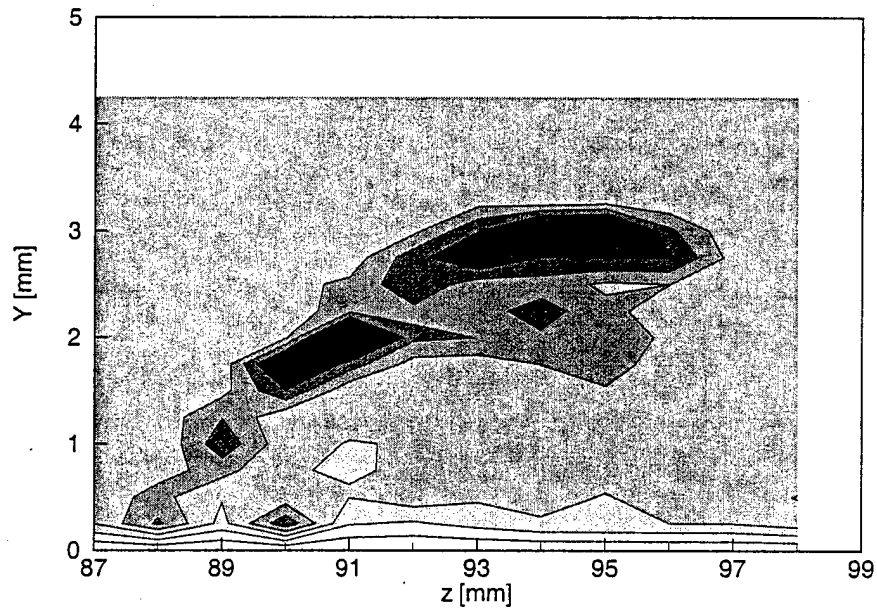


Figure 109: 6.1-kHz velocity-fluctuation rms distribution,  $Re_c = 2.4 \times 10^6$ , [54|12] roughness,  $x/c = 0.38$ , 6.0–6.2-kHz bandpass. Lines are 10% contours of the maximum in this band.



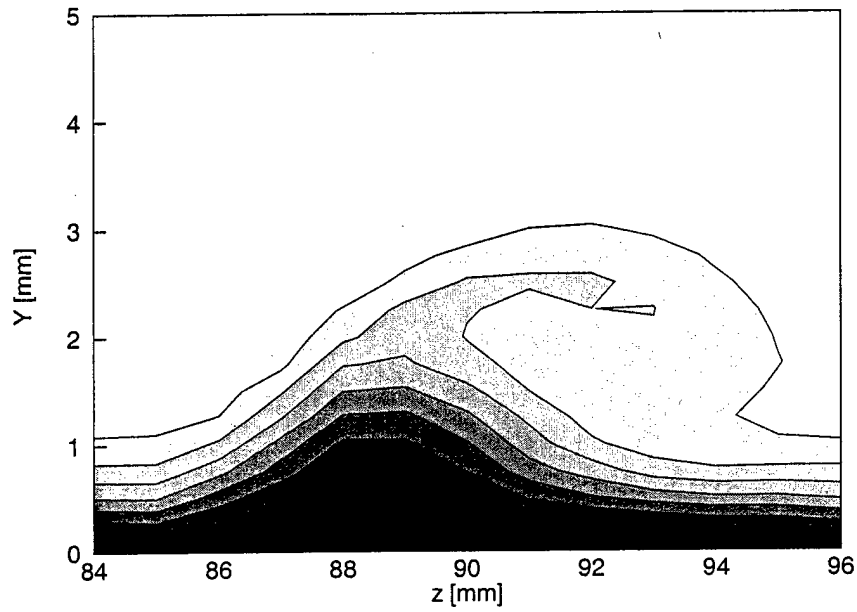


Figure 110: Mean-flow velocity contours,  $Re_c = 2.4 \times 10^6$ , [54|12] roughness,  $x/c = 0.39$ , contour lines at  $U/U_{edge} = 0.10, 0.20, \dots, 0.90$ .

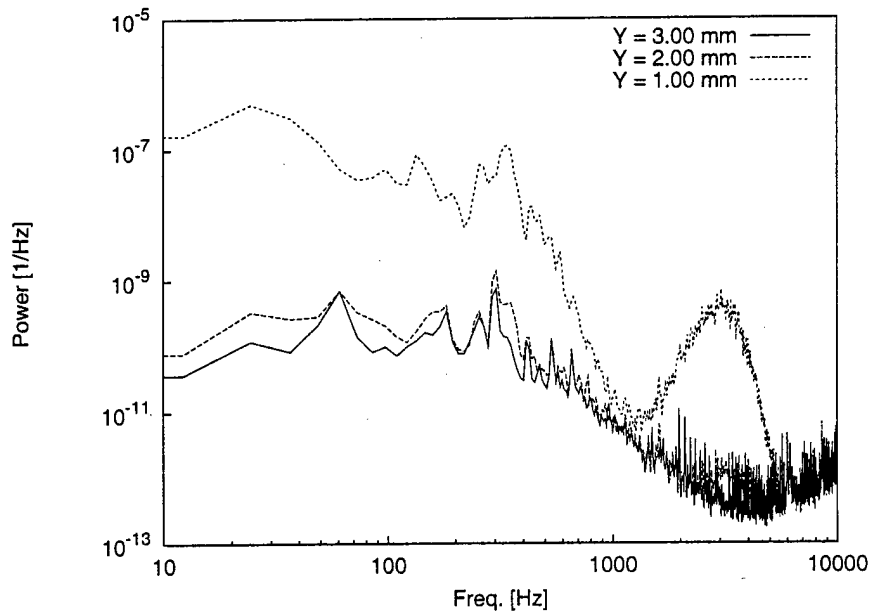


Figure 111: Fluctuating-velocity spectra,  $Re_c = 2.4 \times 10^6$ , [54|12] roughness,  $x/c = 0.39$ ,  $z = 86$  mm.

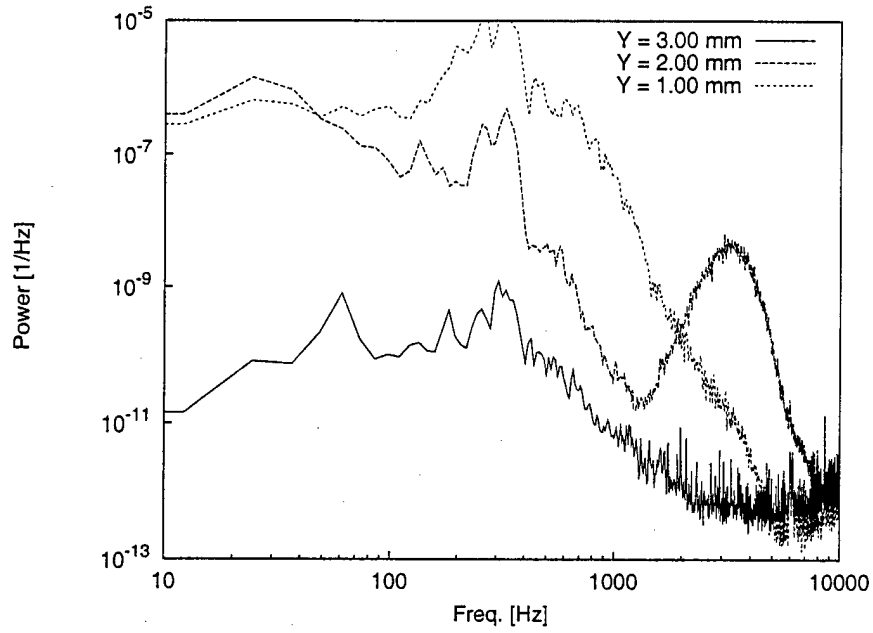


Figure 112: Fluctuating-velocity spectra,  $Re_c = 2.4 \times 10^6$ , [54|12] roughness,  $x/c = 0.39$ ,  $z = 89$  mm.

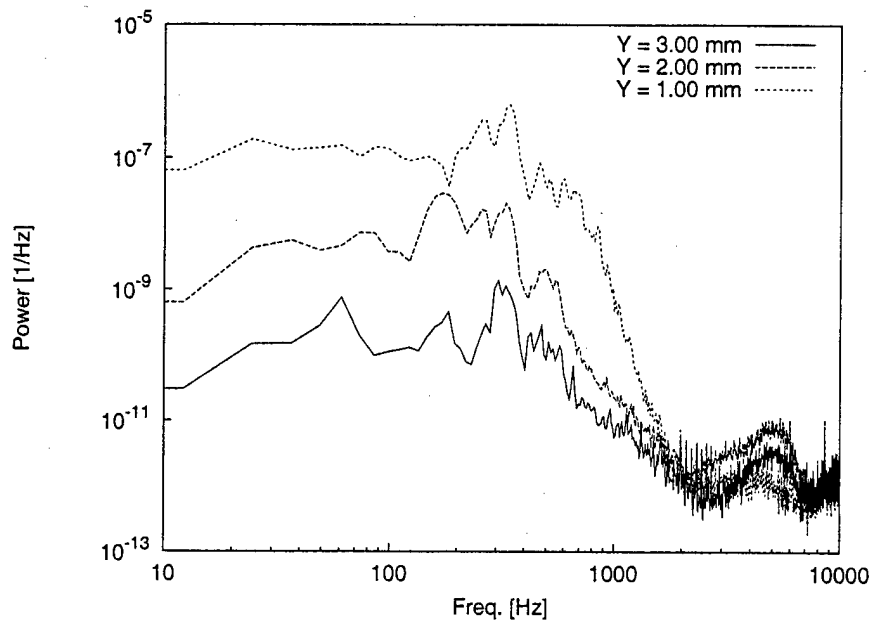


Figure 113: Fluctuating-velocity spectra,  $Re_c = 2.4 \times 10^6$ , [54|12] roughness,  $x/c = 0.39$ ,  $z = 92$  mm.

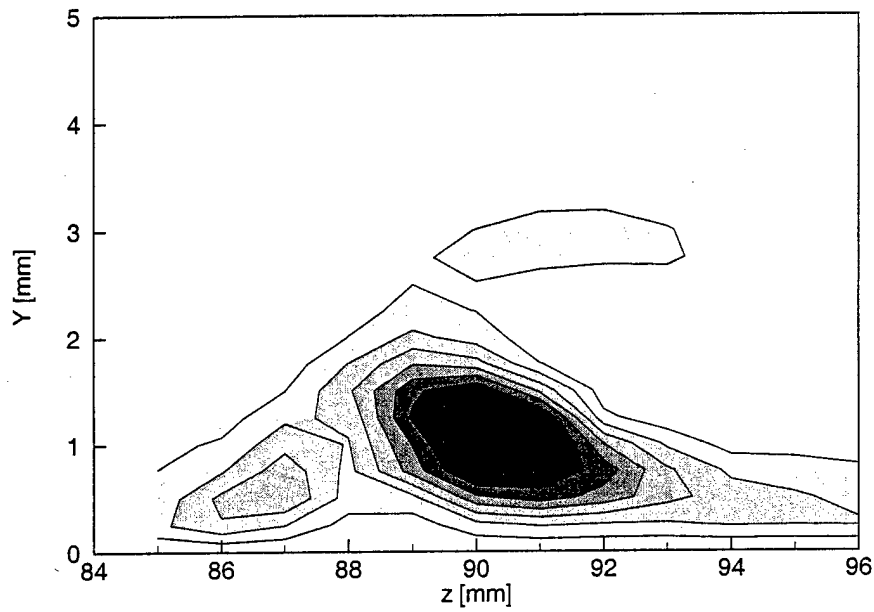


Figure 114: 200-Hz velocity-fluctuation rms distribution,  $Re_c = 2.4 \times 10^6$ , [54|12] roughness,  $x/c = 0.39$ , 100–300-Hz bandpass. Lines are 10% contours of the maximum in this band.

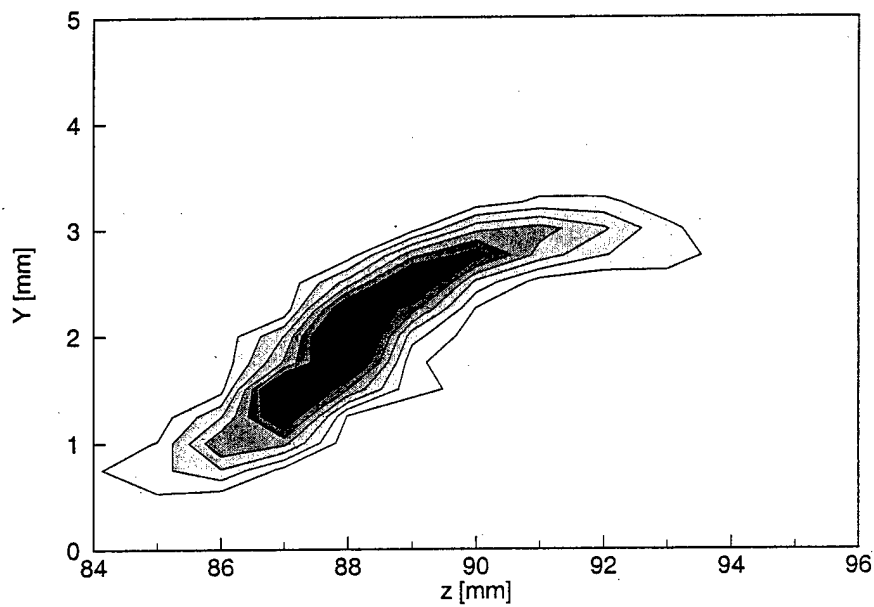


Figure 115: 3.0-kHz velocity-fluctuation rms distribution,  $Re_c = 2.4 \times 10^6$ , [54|12] roughness,  $x/c = 0.39$ , 2.9–3.1-kHz bandpass. Lines are 10% contours of the maximum in this band.

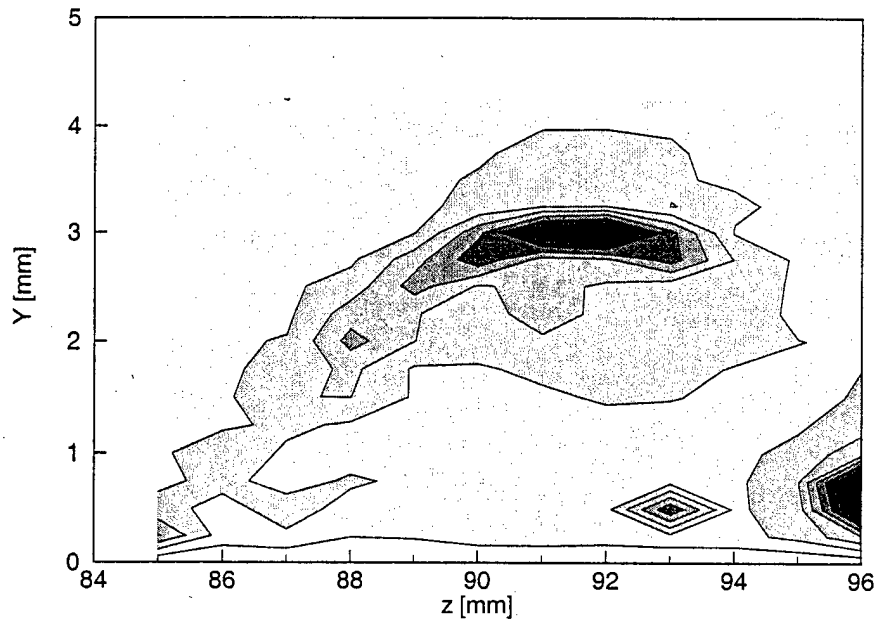


Figure 116: 6.1-kHz velocity-fluctuation rms distribution,  $Re_c = 2.4 \times 10^6$ , [54|12] roughness,  $x/c = 0.39$ , 6.0–6.2-kHz bandpass. Lines are 10% contours of the maximum in this band.

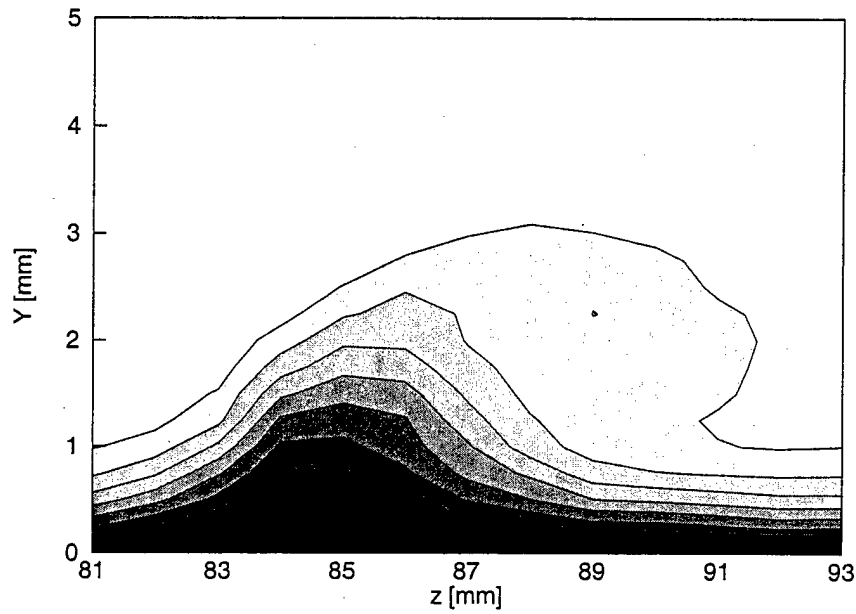


Figure 117: Mean-flow velocity contours,  $Re_c = 2.4 \times 10^6$ , [54|12] roughness,  $x/c = 0.40$ , contour lines at  $U/U_{\text{edge}} = 0.10, 0.20, \dots, 0.90$ .

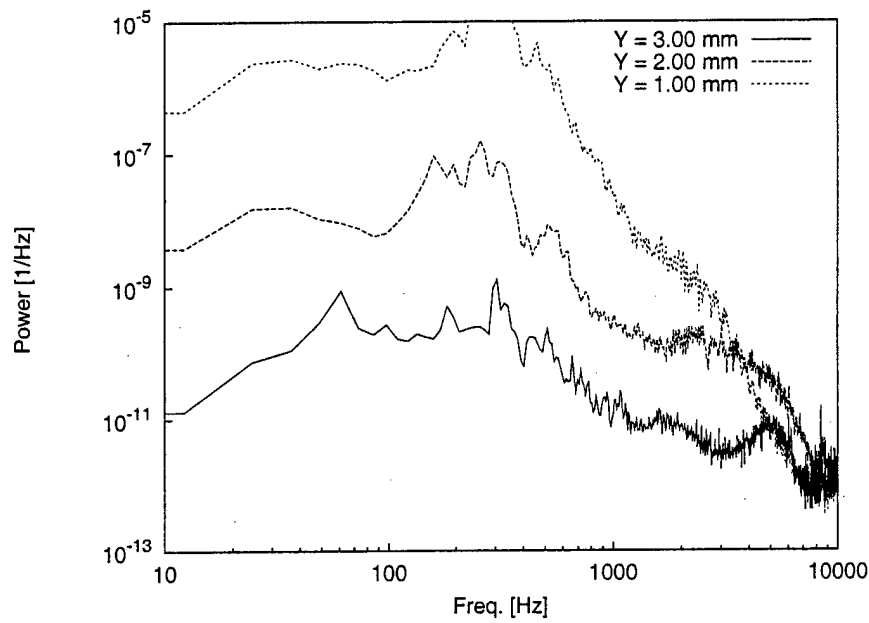


Figure 118: Fluctuating-velocity spectra,  $Re_c = 2.4 \times 10^6$ , [54|12] roughness,  $x/c = 0.40$ ,  $z = 82$  mm.

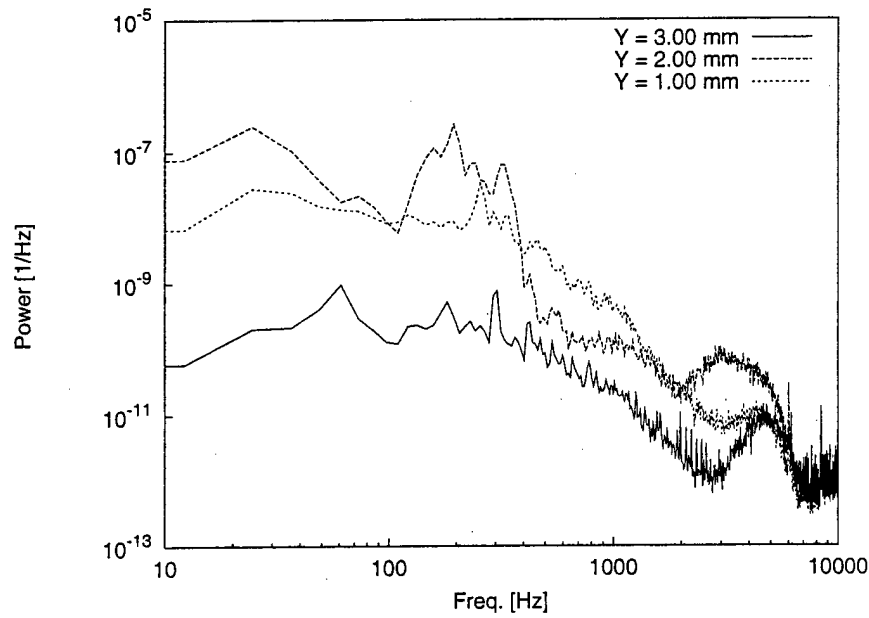


Figure 119: Fluctuating-velocity spectra,  $Re_c = 2.4 \times 10^6$ , [54|12] roughness,  $x/c = 0.40$ ,  $z = 85$  mm.

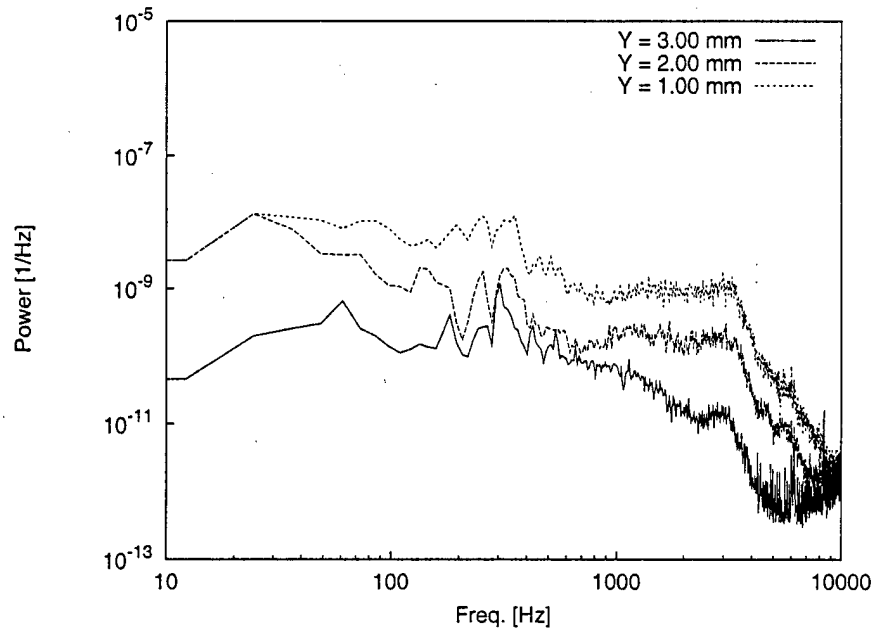


Figure 120: Fluctuating-velocity spectra,  $Re_c = 2.4 \times 10^6$ , [54|12] roughness,  $x/c = 0.40$ ,  $z = 88$  mm.

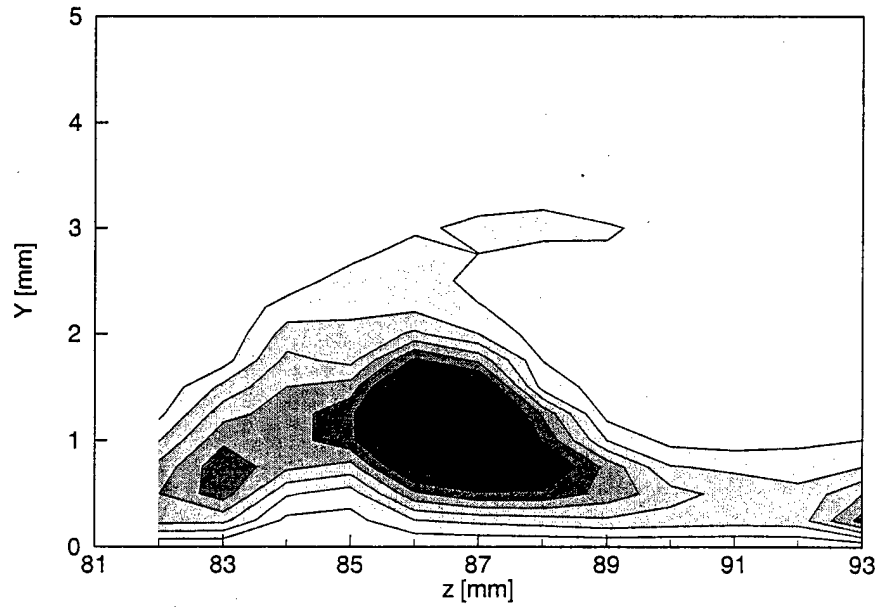


Figure 121: Total velocity-fluctuation rms distribution,  $Re_c = 2.4 \times 10^6$ , [54|12] roughness,  $x/c = 0.40$ , 20 Hz–8.0-kHz bandpass. Lines are 10% contours of the maximum rms fluctuations.

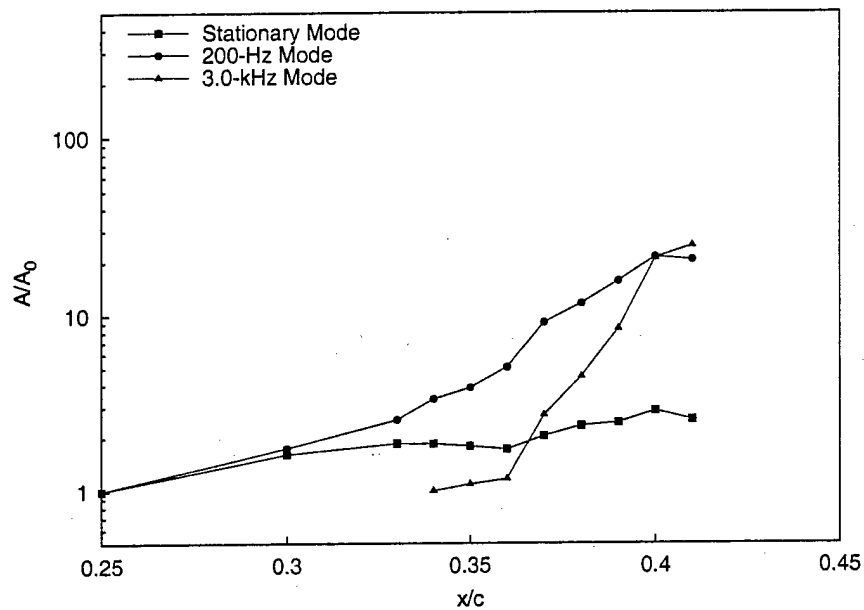


Figure 122: Velocity-fluctuation rms growth,  $Re_c = 2.4 \times 10^6$ , [54|12] roughness.

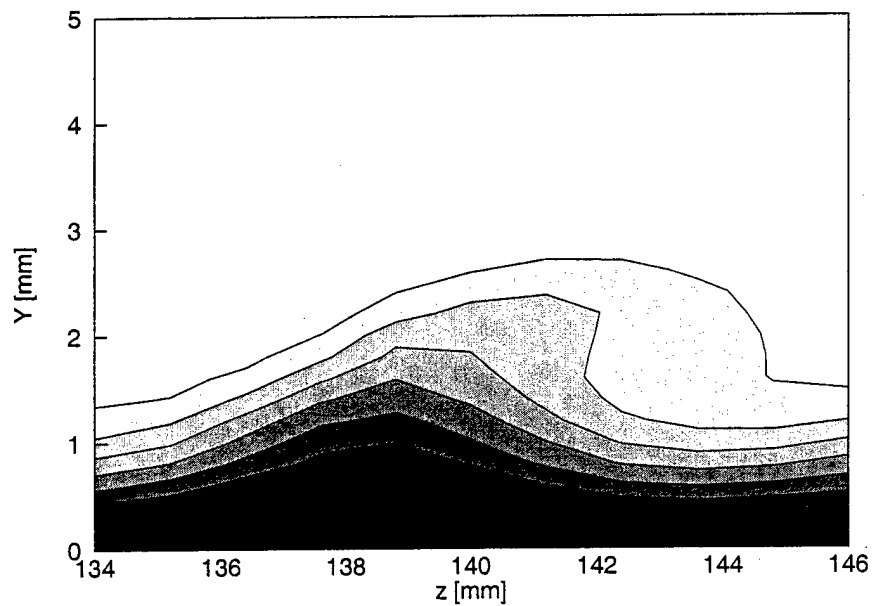


Figure 123: Mean-flow velocity contours,  $Re_c = 2.0 \times 10^6$ , [54|12] roughness,  $x/c = 0.40$ , contour lines at  $U/U_{edge} = 0.10, 0.20, \dots, 0.90$ .

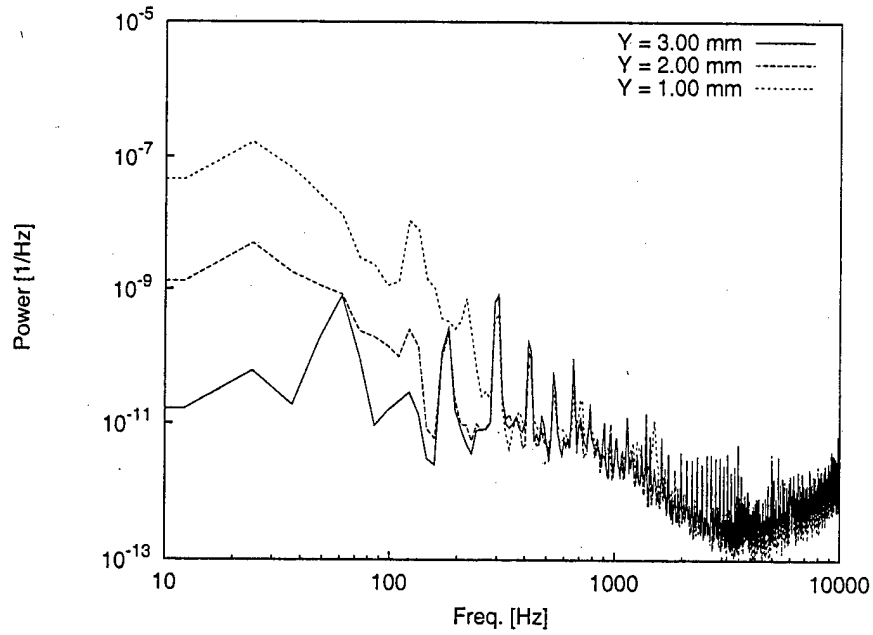


Figure 124: Fluctuating-velocity spectra,  $Re_c = 2.0 \times 10^6$ , [54|12] roughness,  $x/c = 0.40$ ,  $z = 136.4$  mm.

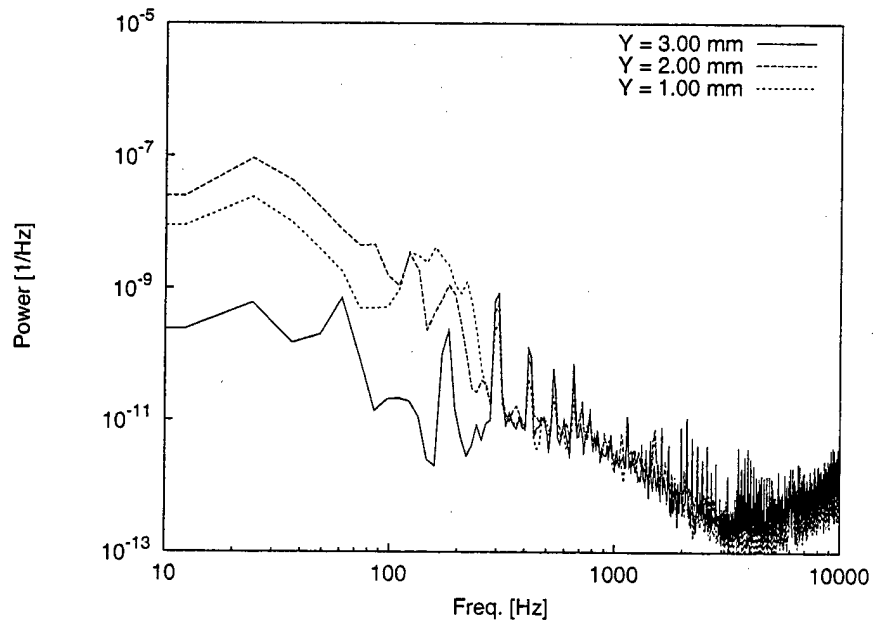


Figure 125: Fluctuating-velocity spectra,  $Re_c = 2.0 \times 10^6$ , [54|12] roughness,  $x/c = 0.40$ ,  $z = 138.8$  mm.



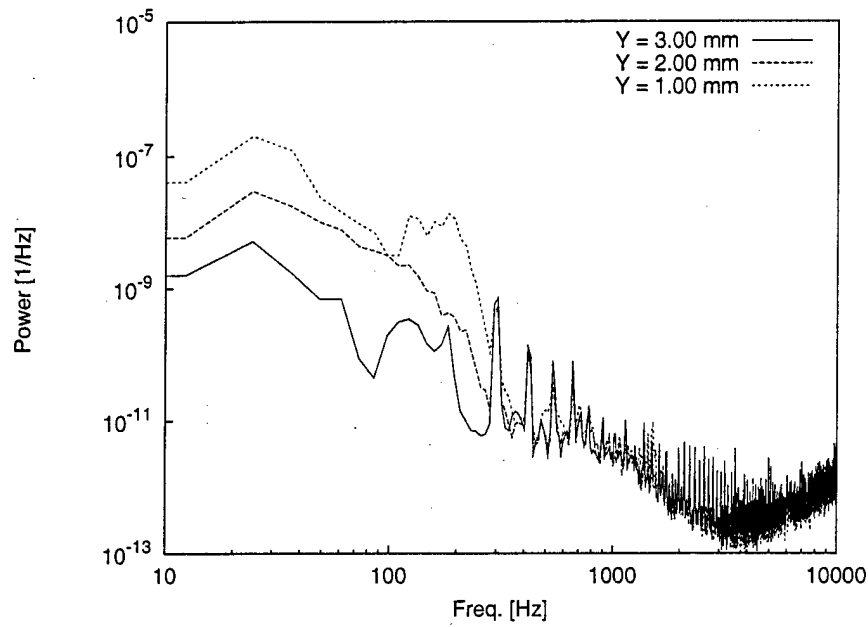


Figure 126: Fluctuating-velocity spectra,  $Re_c = 2.0 \times 10^6$ , [54|12] roughness,  $x/c = 0.40$ ,  $z = 141.2$  mm.

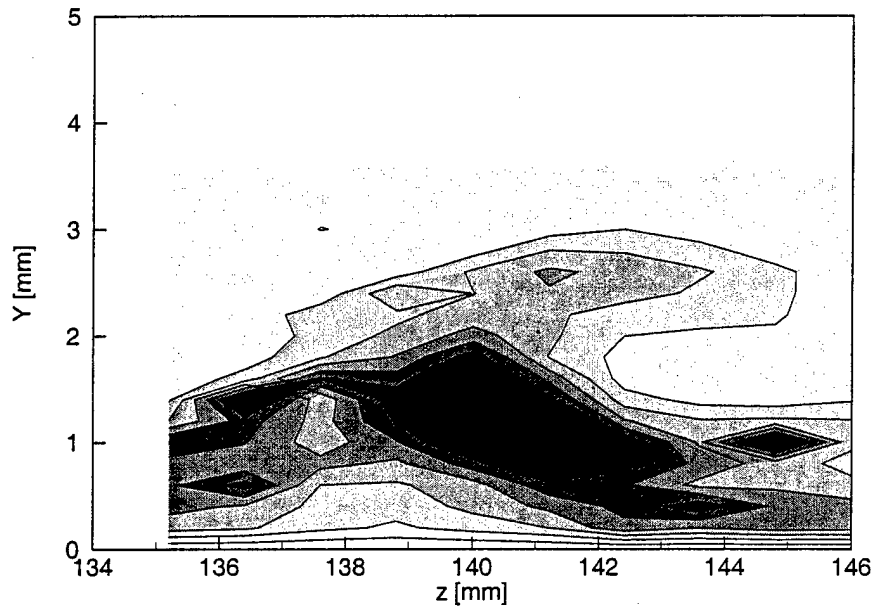


Figure 127: 200-Hz velocity-fluctuation rms distribution,  $Re_c = 2.0 \times 10^6$ , [54|12] roughness,  $x/c = 0.40$ , 100-300-Hz bandpass. Lines are 10% contours of the maximum in this band.

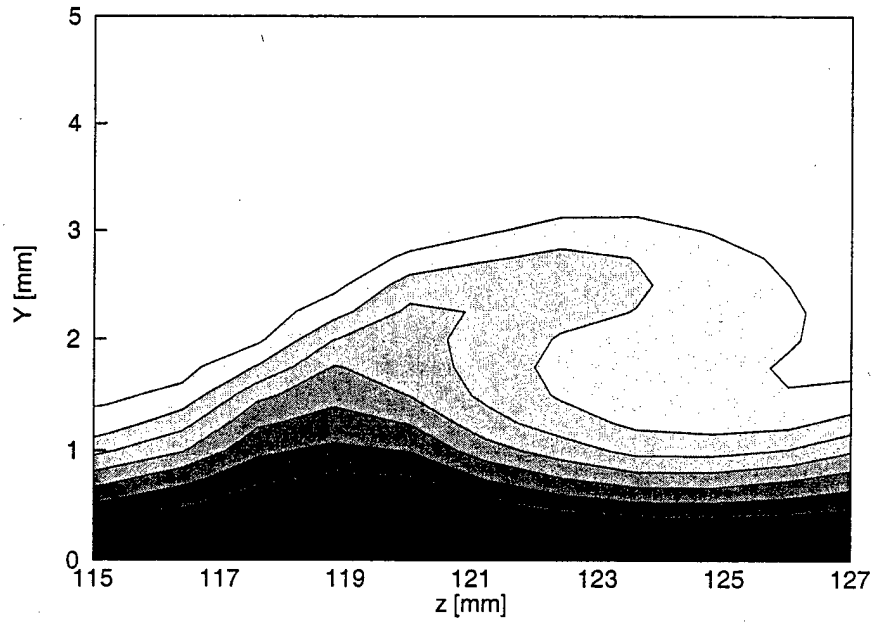


Figure 128: Mean-flow velocity contours,  $Re_c = 2.0 \times 10^6$ , [54|12] roughness,  $x/c = 0.46$ , contour lines at  $U/U_{edge} = 0.10, 0.20, \dots, 0.90$ .

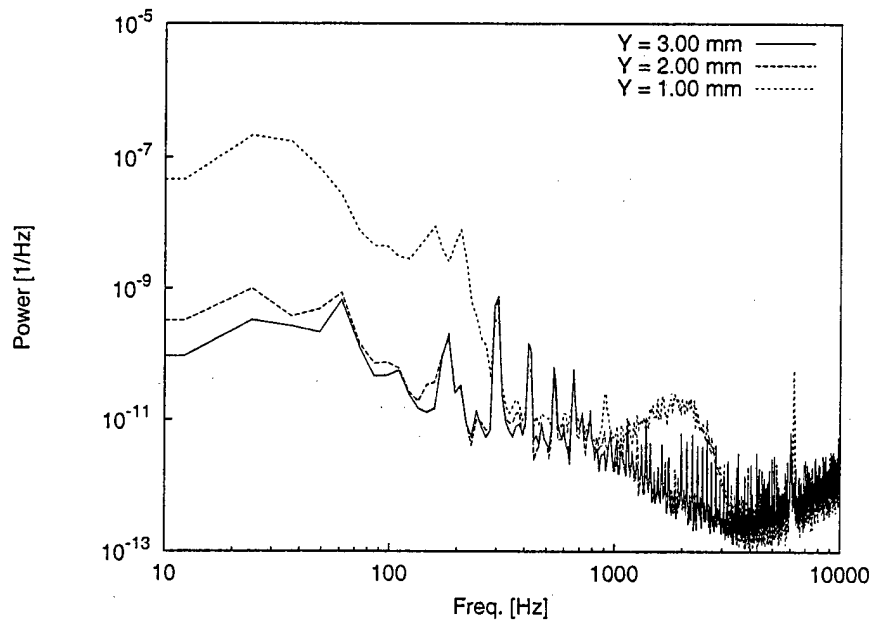


Figure 129: Fluctuating-velocity spectra,  $Re_c = 2.0 \times 10^6$ , [54|12] roughness,  $x/c = 0.46$ ,  $z = 116.4$  mm.

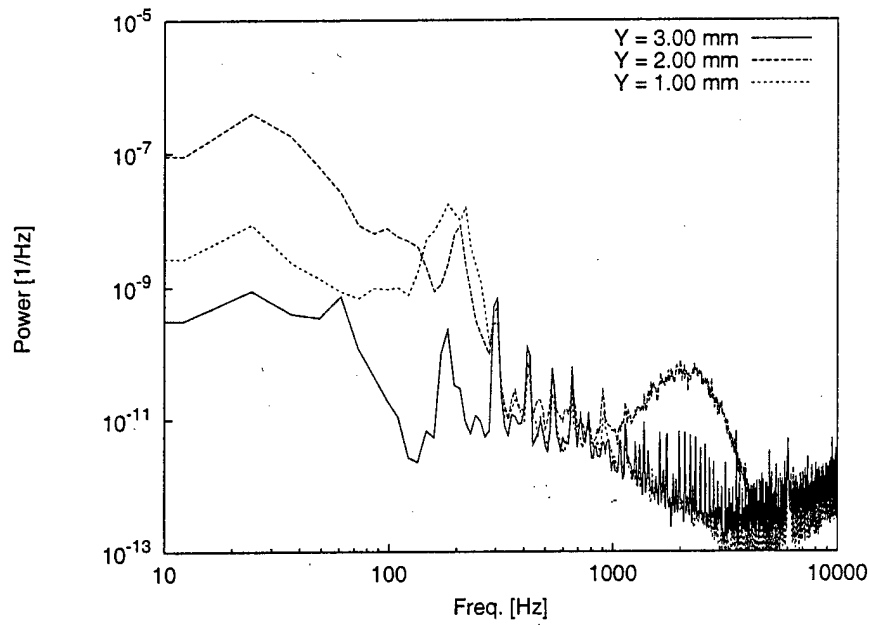


Figure 130: Fluctuating-velocity spectra,  $Re_c = 2.0 \times 10^6$ , [54|12] roughness,  $x/c = 0.46$ ,  $z = 118.8$  mm.

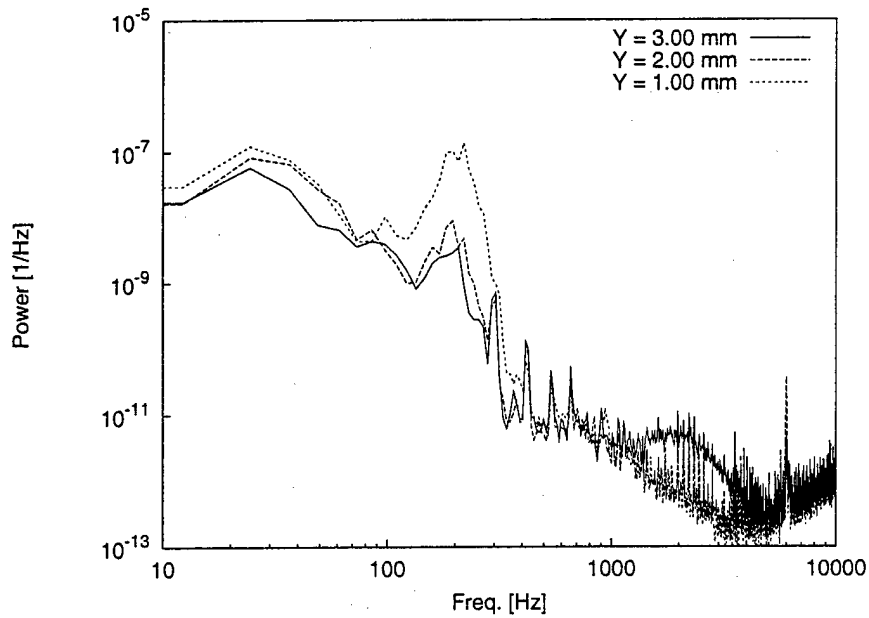


Figure 131: Fluctuating-velocity spectra,  $Re_c = 2.0 \times 10^6$ , [54|12] roughness,  $x/c = 0.46$ ,  $z = 121.2$  mm.

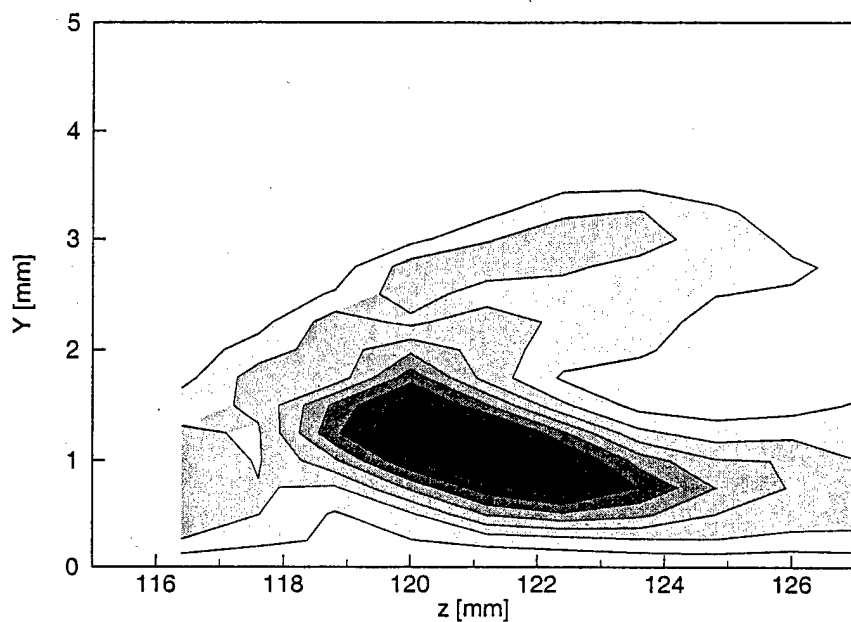


Figure 132: 200-Hz velocity-fluctuation rms distribution,  $Re_c = 2.0 \times 10^6$ , [54|12] roughness,  $x/c = 0.46$ , 100–300-Hz bandpass. Lines are 10% contours of the maximum in this band.

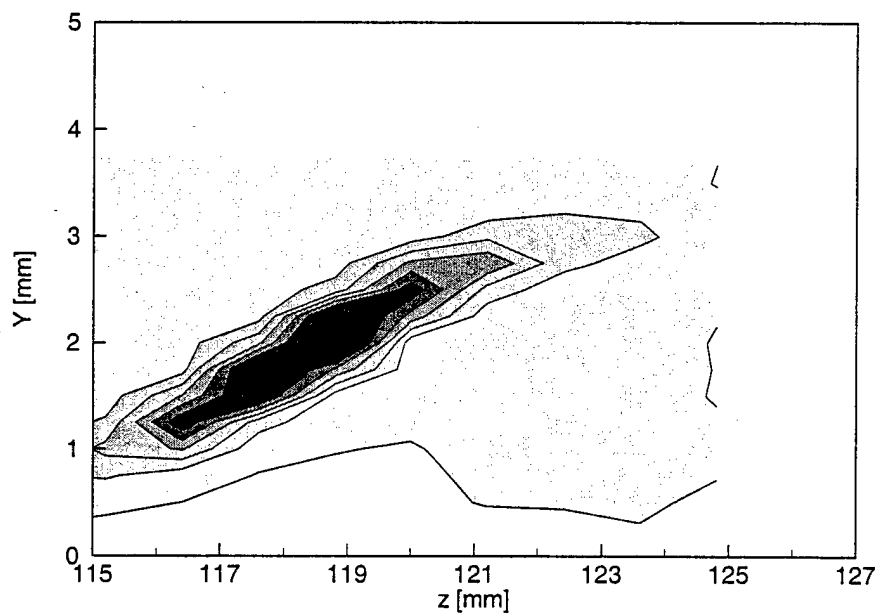


Figure 133: 2.4-kHz velocity-fluctuation rms distribution,  $Re_c = 2.0 \times 10^6$ , [54|12] roughness,  $x/c = 0.46$ , 2.3–2.5-kHz bandpass. Lines are 10% contours of the maximum in this band.

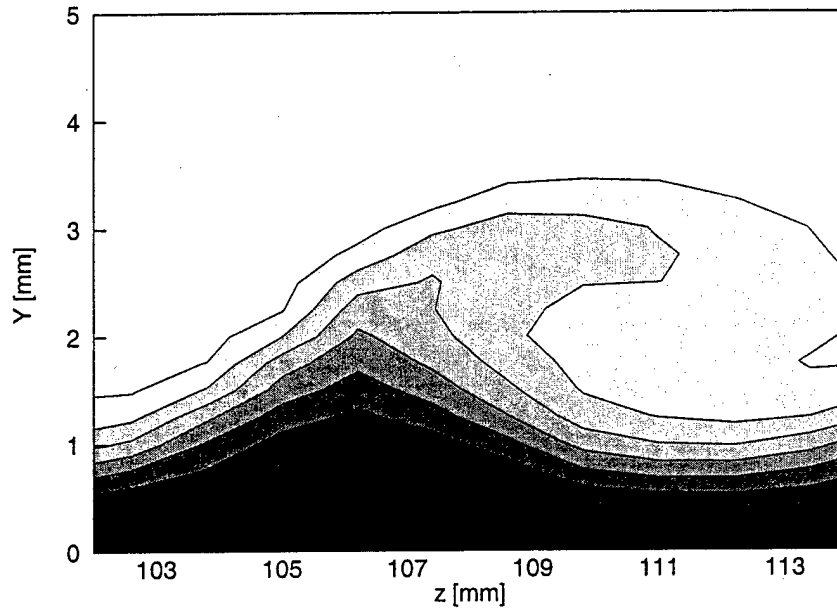


Figure 134: Mean-flow velocity contours,  $Re_c = 2.0 \times 10^6$ , [54|12] roughness,  $x/c = 0.50$ , contour lines at  $U/U_{\text{edge}} = 0.10, 0.20, \dots, 0.90$ .

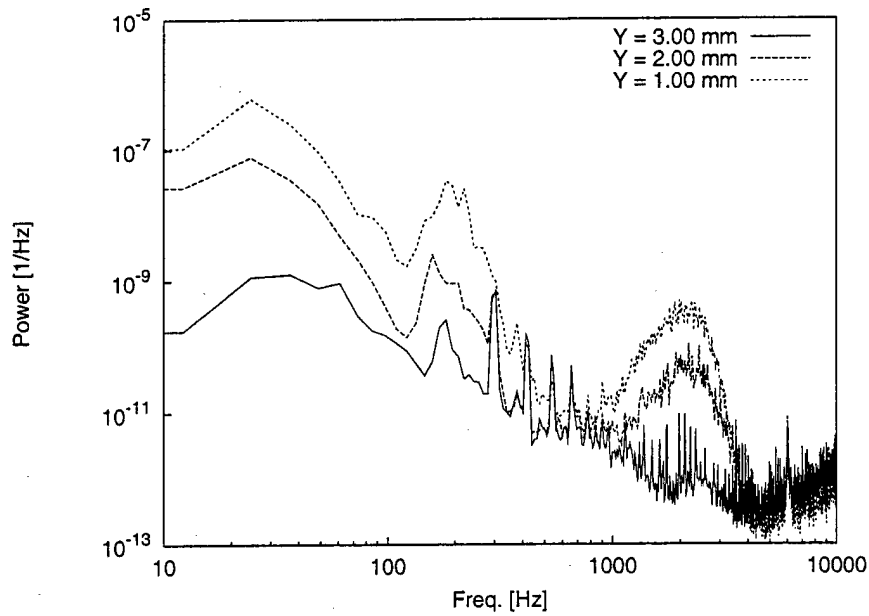


Figure 135: Fluctuating-velocity spectra,  $Re_c = 2.0 \times 10^6$ , [54|12] roughness,  $x/c = 0.50$ ,  $z = 103.8$  mm.

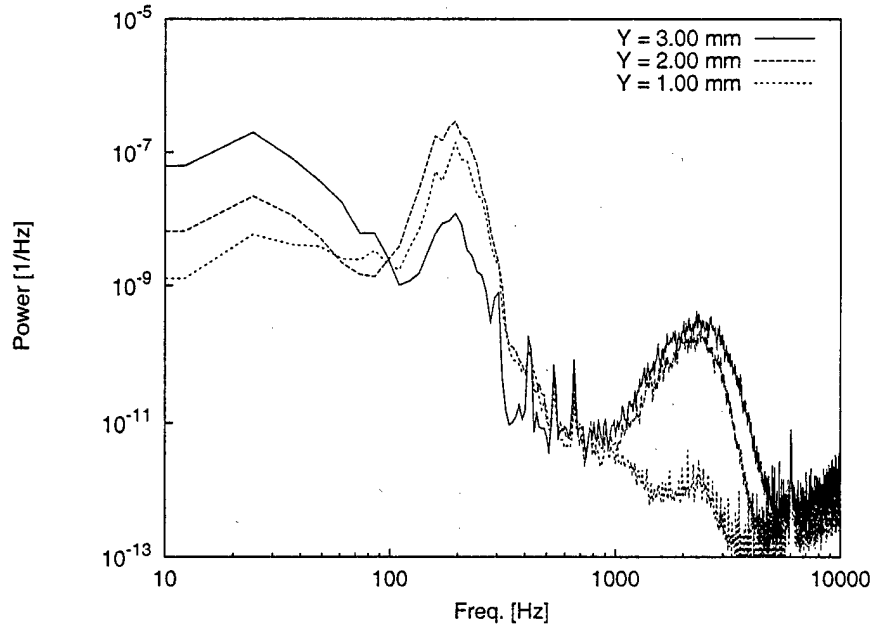


Figure 136: Fluctuating-velocity spectra,  $Re_c = 2.0 \times 10^6$ , [54|12] roughness,  $x/c = 0.50$ ,  $z = 106.2$  mm.

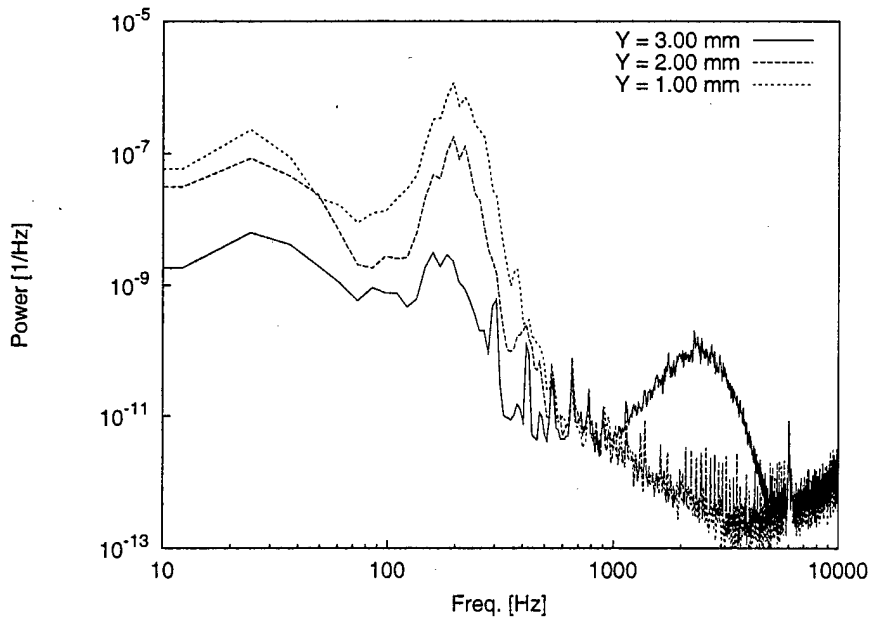


Figure 137: Fluctuating-velocity spectra,  $Re_c = 2.0 \times 10^6$ , [54|12] roughness,  $x/c = 0.50$ ,  $z = 108.6$  mm.

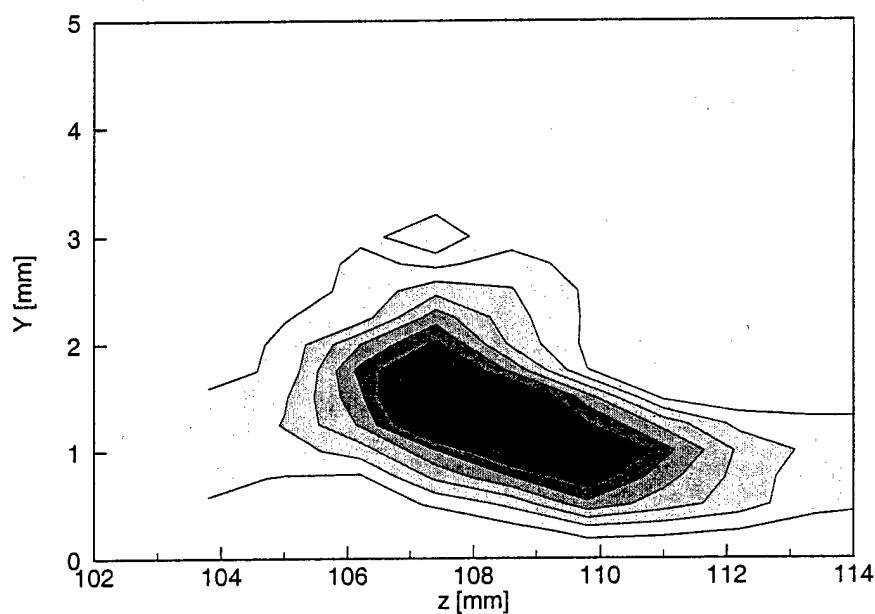


Figure 138: 200-Hz velocity-fluctuation rms distribution,  $Re_c = 2.0 \times 10^6$ , [54|12] roughness,  $x/c = 0.50$ , 100-300-Hz bandpass. Lines are 10% contours of the maximum in this band.

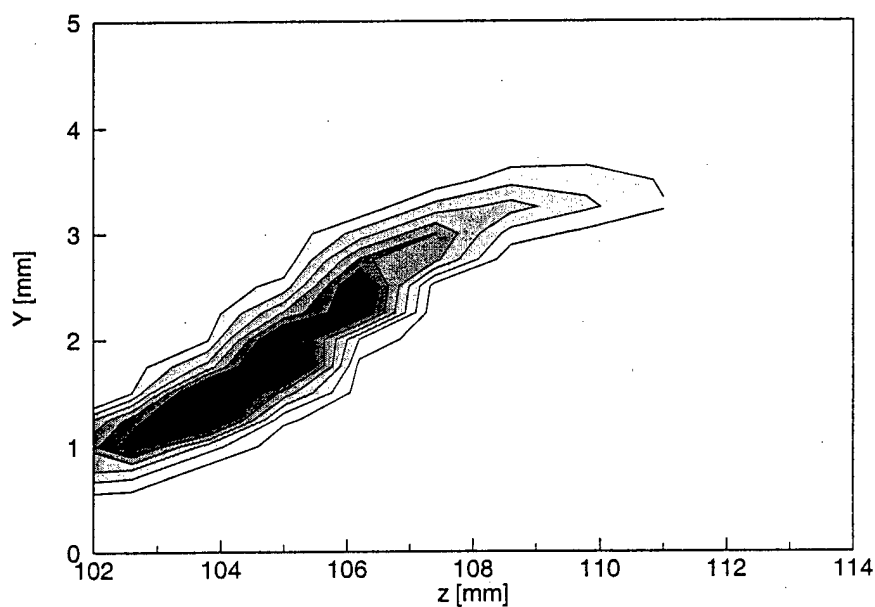


Figure 139: 2.4-kHz velocity-fluctuation rms distribution,  $Re_c = 2.0 \times 10^6$ , [54|12] roughness,  $x/c = 0.50$ , 2.3-2.5-kHz bandpass. Lines are 10% contours of the maximum in this band.

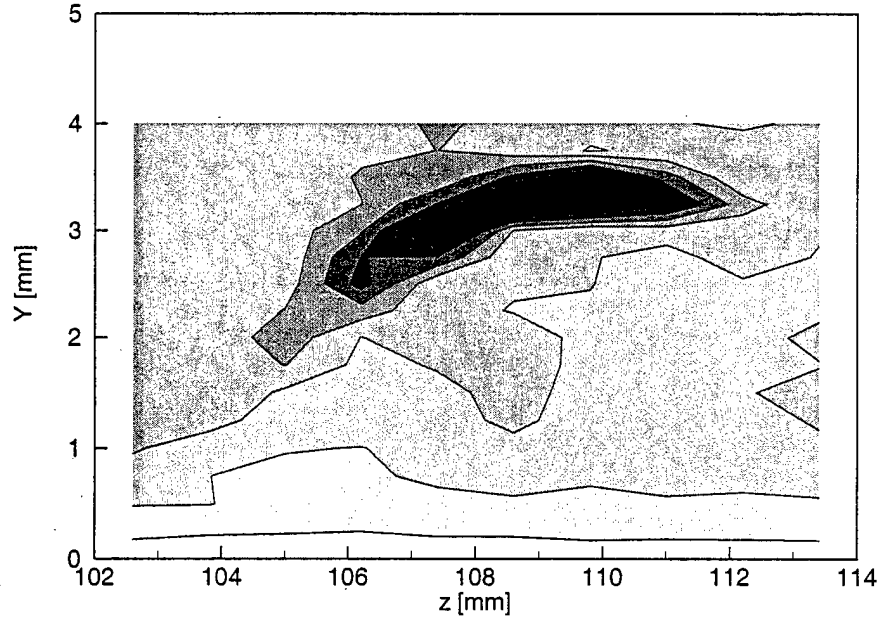


Figure 140: 4.9-kHz velocity-fluctuation rms distribution,  $Re_c = 2.0 \times 10^6$ , [54|12] roughness,  $x/c = 0.50$ , 4.8–5.0-kHz bandpass. Lines are 10% contours of the maximum in this band.

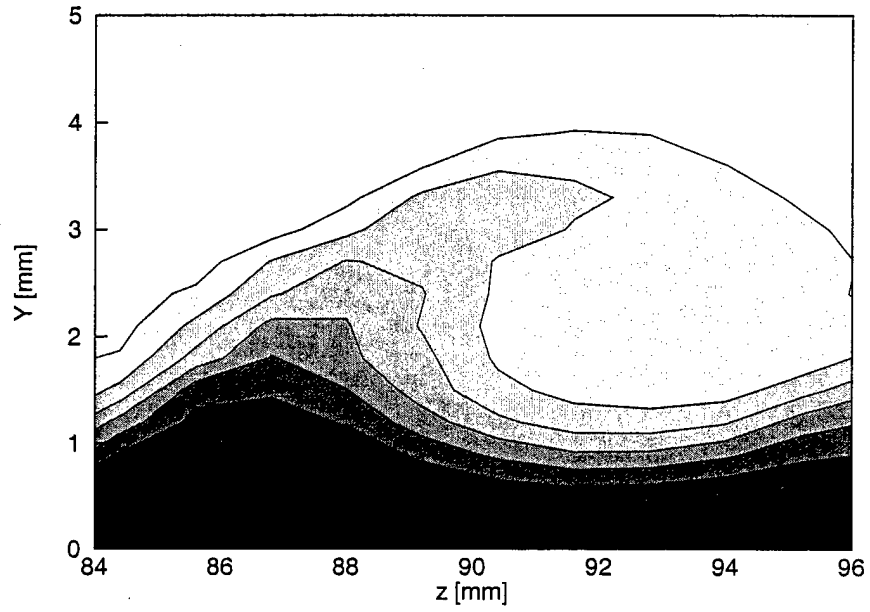


Figure 141: Mean-flow velocity contours,  $Re_c = 2.0 \times 10^6$ , [54|12] roughness,  $x/c = 0.55$ , contour lines at  $U/U_{\text{edge}} = 0.10, 0.20, \dots, 0.90$ .



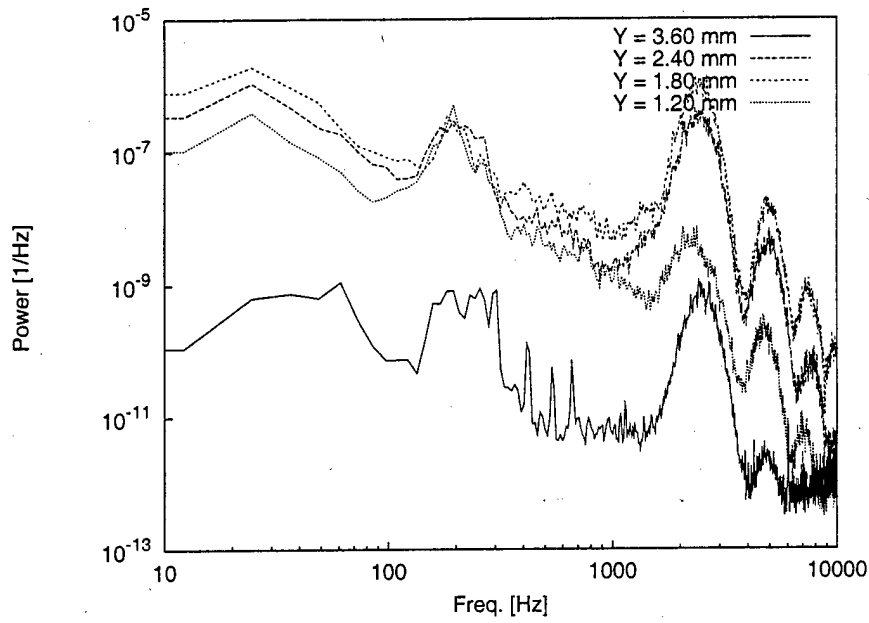


Figure 142: Fluctuating-velocity spectra,  $Re_c = 2.0 \times 10^6$ , [54|12] roughness,  $x/c = 0.55$ ,  $z = 85.6$  mm.

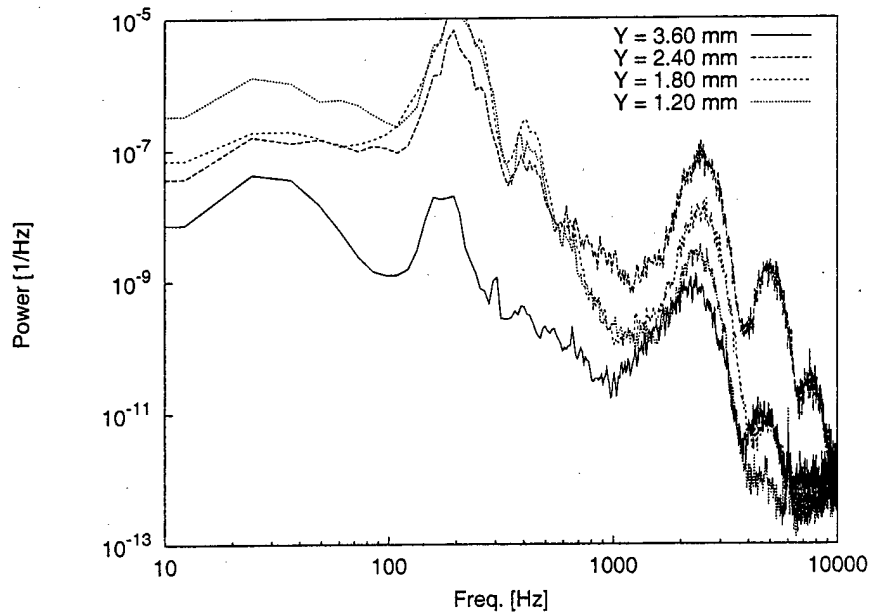


Figure 143: Fluctuating-velocity spectra,  $Re_c = 2.0 \times 10^6$ , [54|12] roughness,  $x/c = 0.55$ ,  $z = 88.0$  mm.

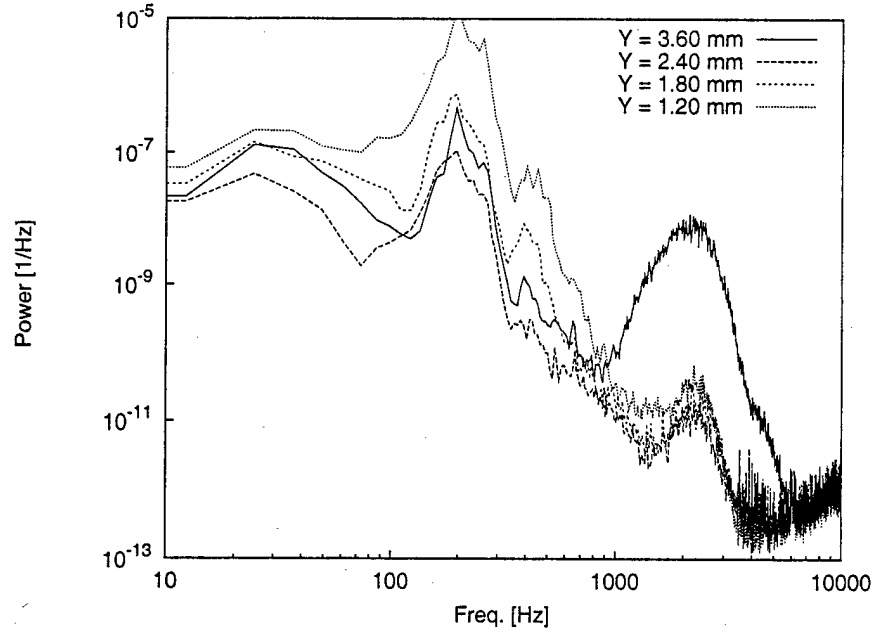


Figure 144: Fluctuating-velocity spectra,  $Re_c = 2.0 \times 10^6$ , [54|12] roughness,  $x/c = 0.55$ ,  $z = 90.4$  mm.

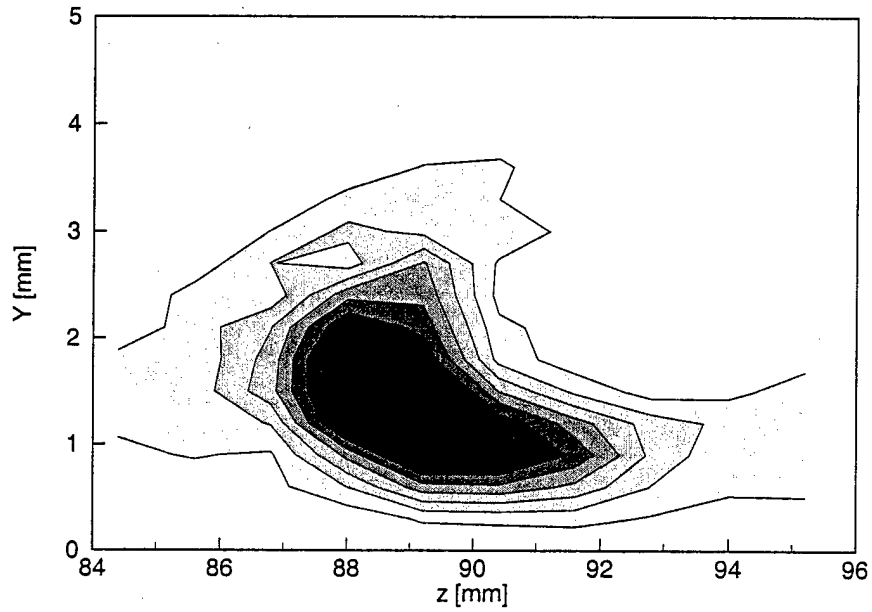


Figure 145: 200-Hz velocity-fluctuation rms distribution,  $Re_c = 2.0 \times 10^6$ , [54|12] roughness,  $x/c = 0.55$ , 100–300-Hz bandpass. Lines are 10% contours of the maximum in this band.

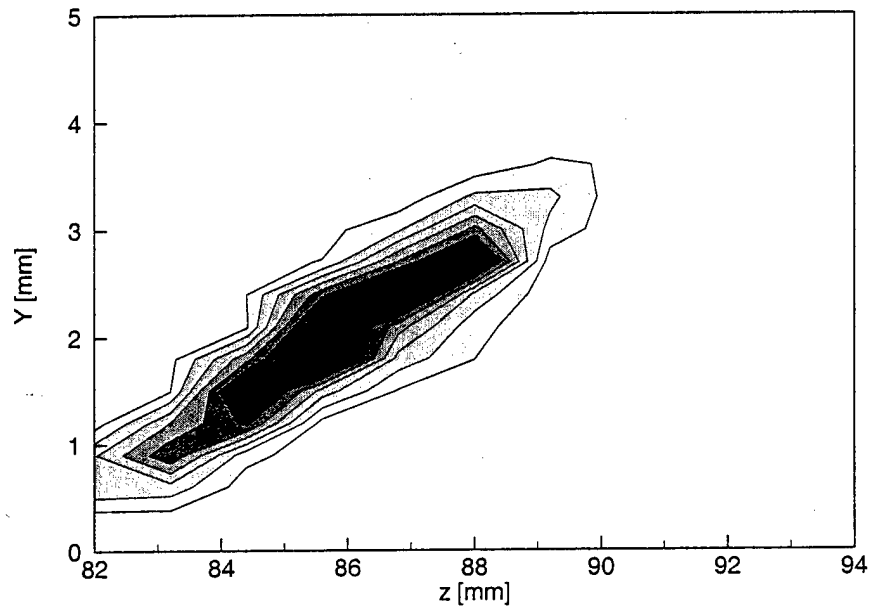


Figure 146: 2.4-kHz velocity-fluctuation rms distribution,  $Re_c = 2.0 \times 10^6$ , [54|12] roughness,  $x/c = 0.55$ , 2.3–2.5-kHz bandpass. Lines are 10% contours of the maximum in this band.

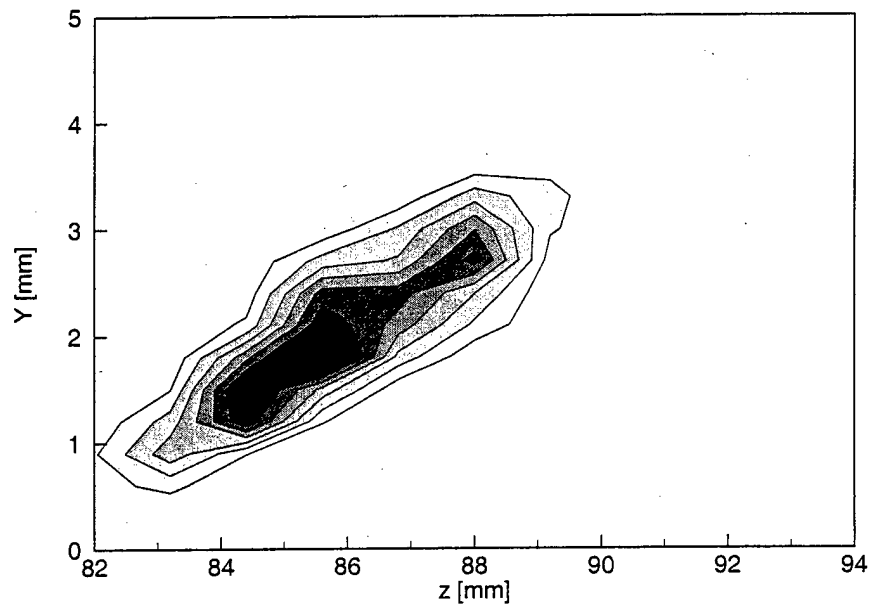


Figure 147: 4.9-kHz velocity-fluctuation rms distribution,  $Re_c = 2.0 \times 10^6$ , [54|12] roughness,  $x/c = 0.55$ , 4.8–5.0-kHz bandpass. Lines are 10% contours of the maximum in this band.

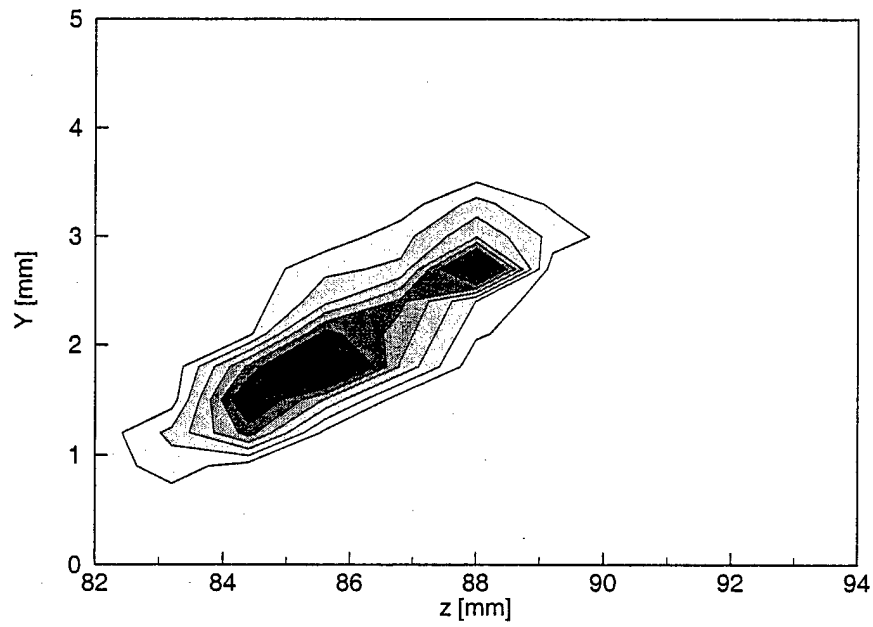


Figure 148: 7.5-kHz velocity-fluctuation rms distribution,  $Re_c = 2.0 \times 10^6$ , [54|12] roughness,  $x/c = 0.55$ , 7.4–7.6-kHz bandpass. Lines are 10% contours of the maximum in this band.

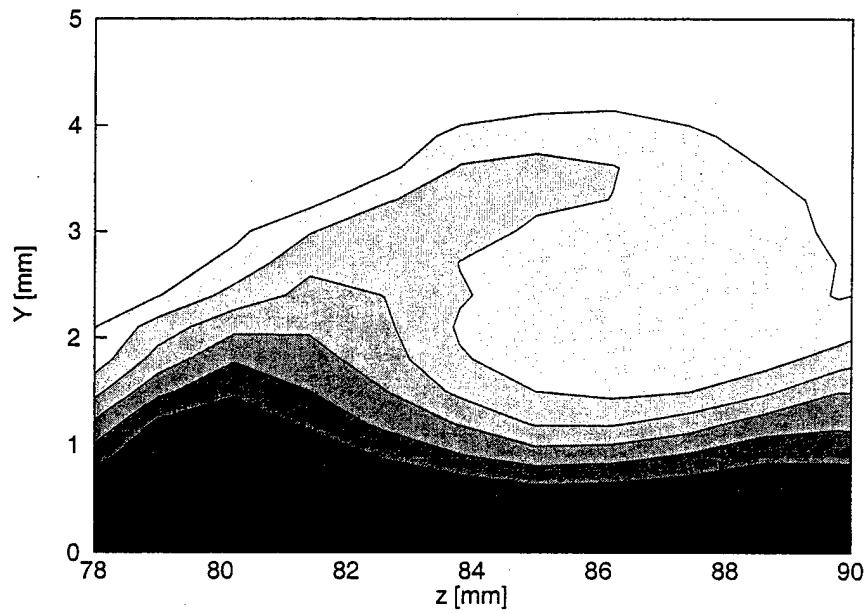


Figure 149: Mean-flow velocity contours,  $Re_c = 2.0 \times 10^6$ , [54|12] roughness,  $x/c = 0.57$ , contour lines at  $U/U_{\text{edge}} = 0.10, 0.20, \dots, 0.90$ .

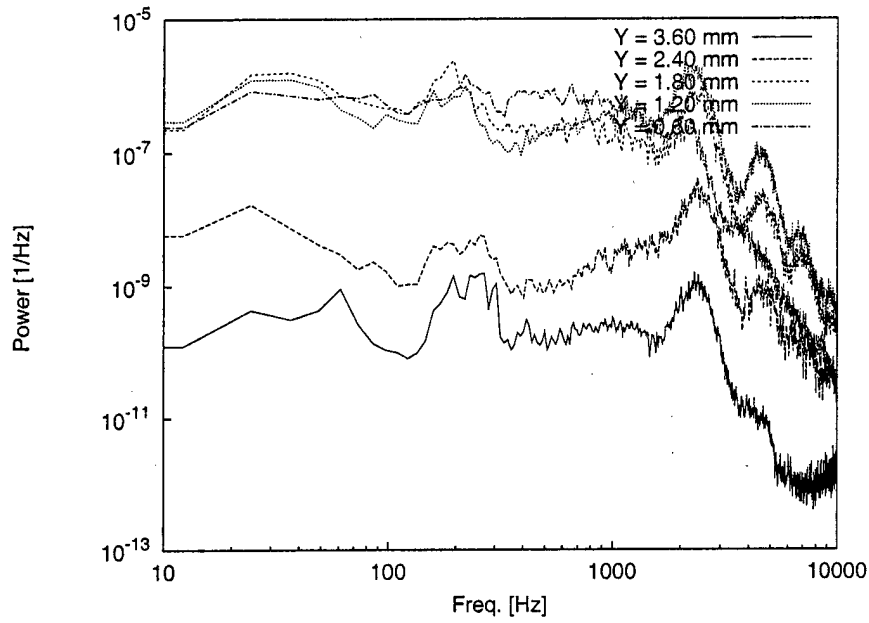


Figure 150: Fluctuating-velocity spectra,  $Re_c = 2.0 \times 10^6$ , [54|12] roughness,  $x/c = 0.57$ ,  $z = 77.8$  mm.

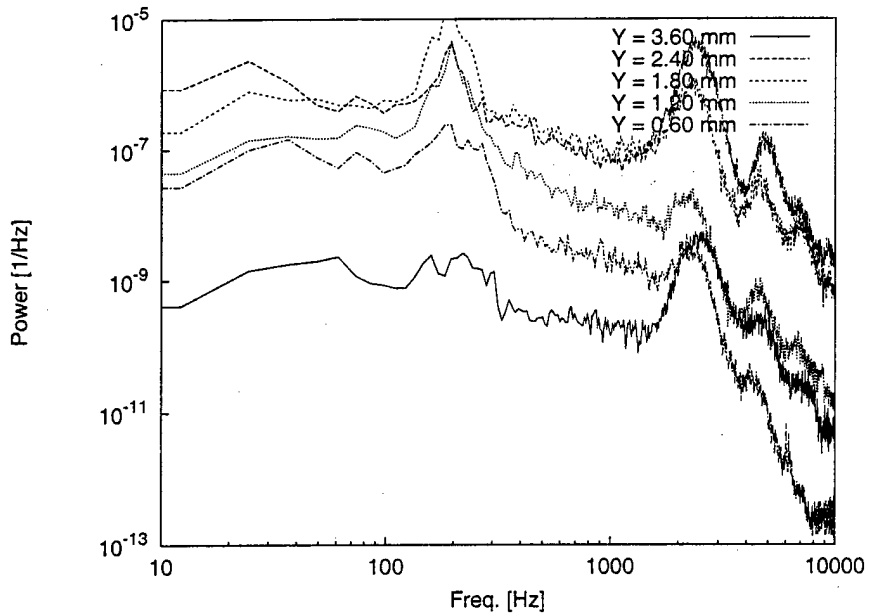


Figure 151: Fluctuating-velocity spectra,  $Re_c = 2.0 \times 10^6$ , [54|12] roughness,  $x/c = 0.57$ ,  $z = 80.2$  mm.

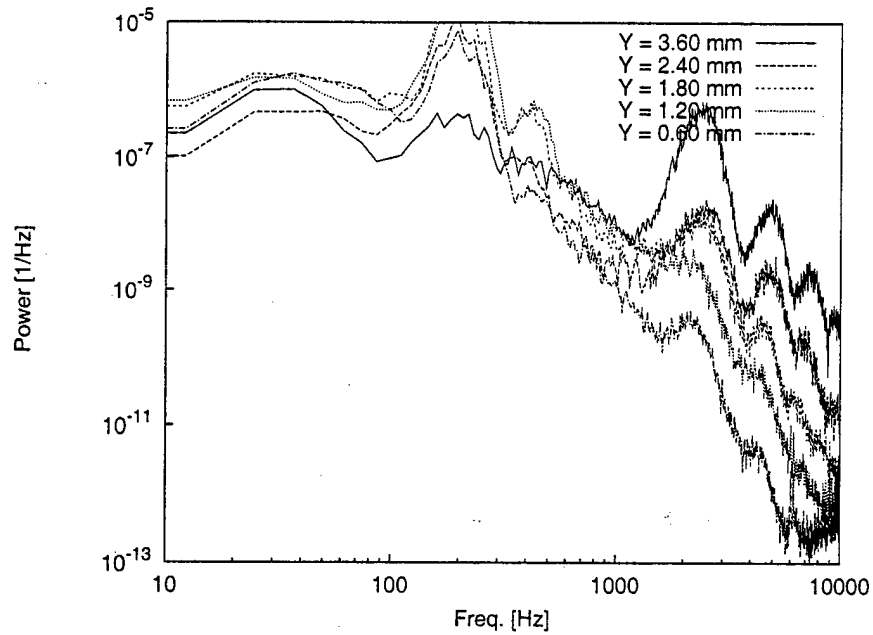


Figure 152: Fluctuating-velocity spectra,  $Re_c = 2.0 \times 10^6$ , [54|12] roughness,  $x/c = 0.57$ ,  $z = 82.6$  mm.

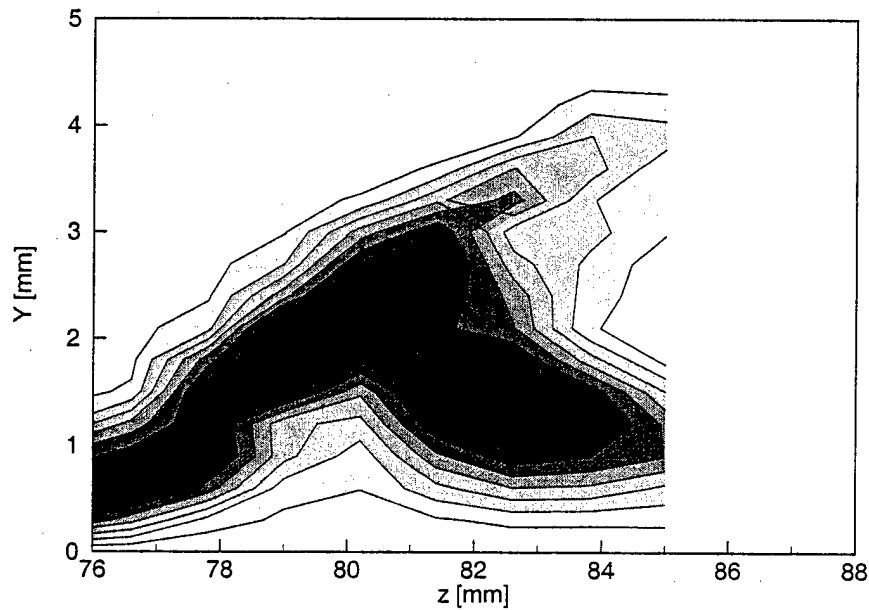


Figure 153: Total velocity-fluctuation rms distribution,  $Re_c = 2.0 \times 10^6$ , [54|12] roughness,  $x/c = 0.57$ , 20-Hz-12.0-kHz bandpass. Lines are 10% contours of the maximum rms fluctuations.

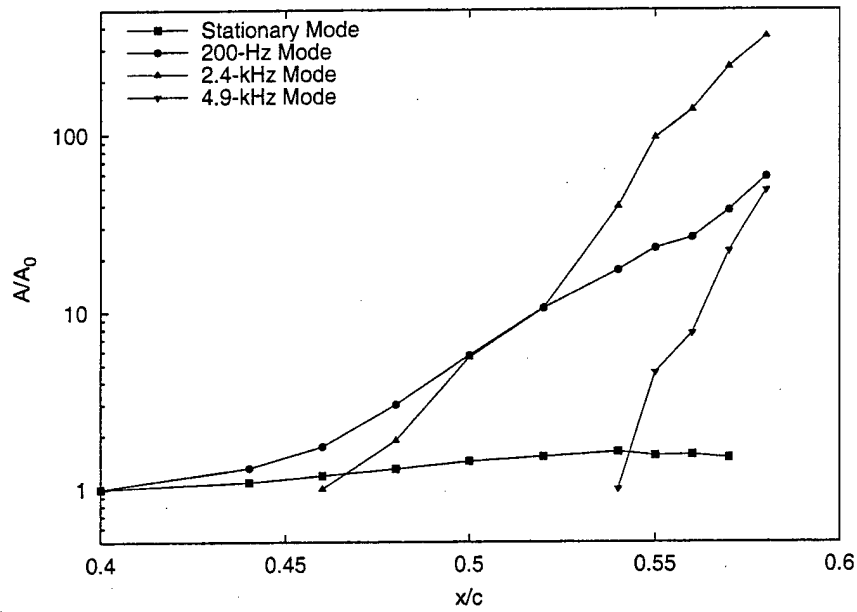


Figure 154: Velocity-fluctuation rms growth,  $Re_c = 2.0 \times 10^6$ , [54|12] roughness.

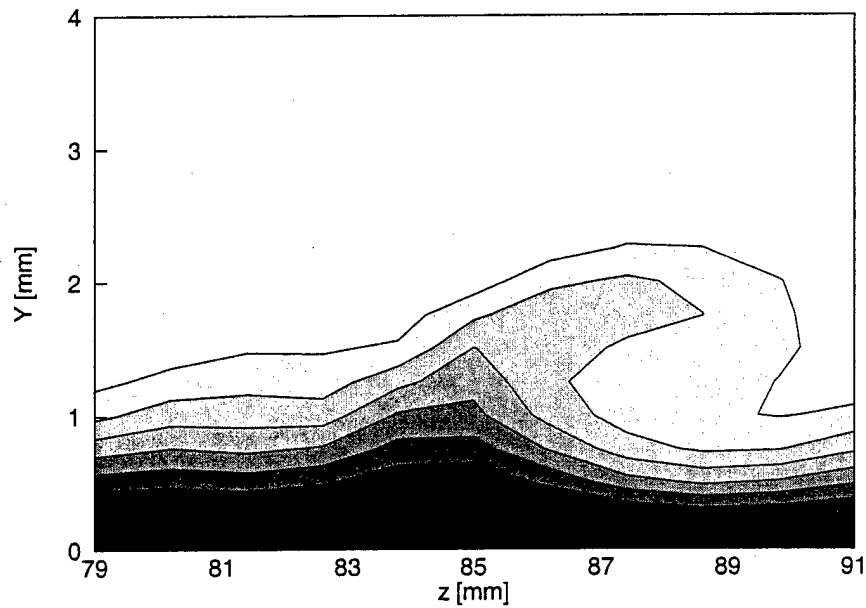


Figure 155: Mean-flow velocity contours,  $Re_c = 2.8 \times 10^6$ , [54|12] roughness,  $x/c = 0.30$ , contour lines at  $U/U_{\text{edge}} = 0.10, 0.20, \dots, 0.90$ .

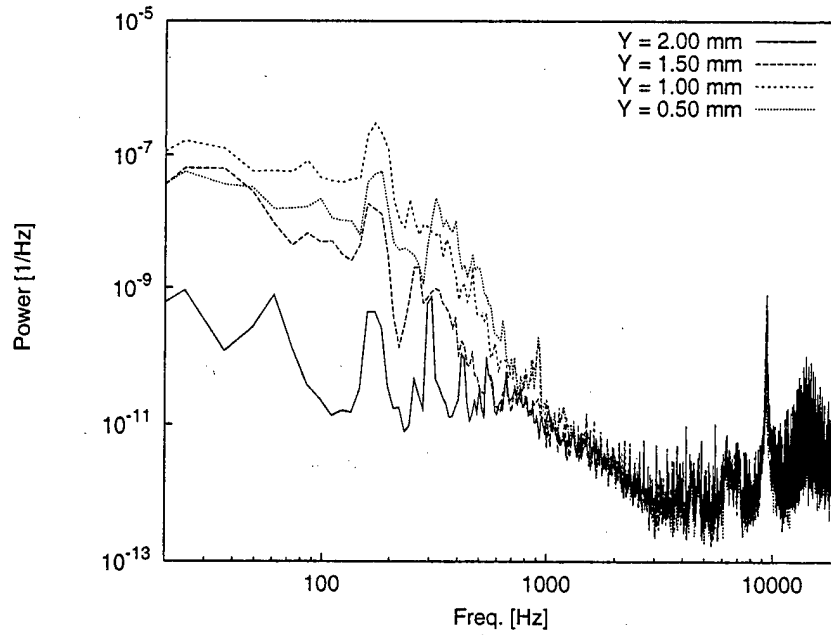


Figure 156: Fluctuating-velocity spectra,  $Re_c = 2.8 \times 10^6$ , [54|12] roughness,  $x/c = 0.30$ ,  $z = 80.2$  mm.

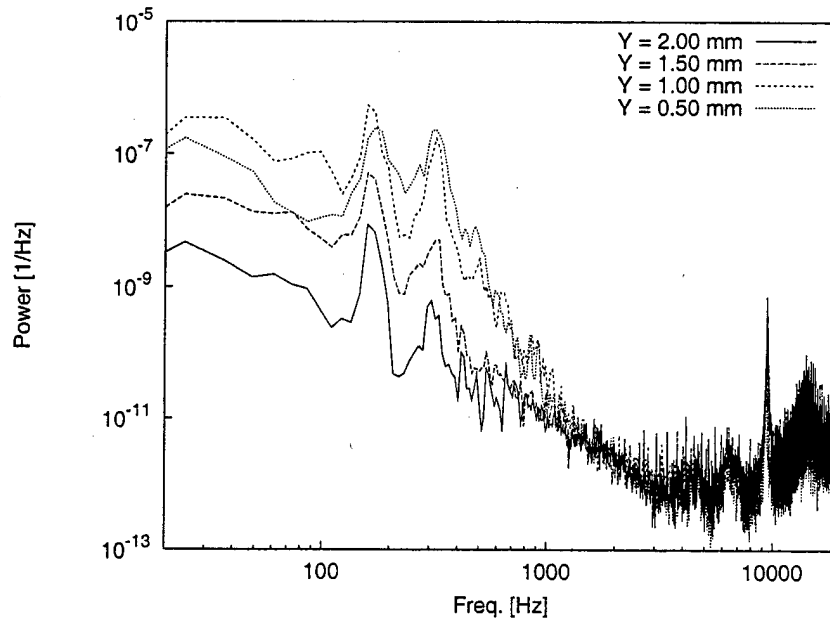


Figure 157: Fluctuating-velocity spectra,  $Re_c = 2.8 \times 10^6$ , [54|12] roughness,  $x/c = 0.30$ ,  $z = 82.6$  mm.



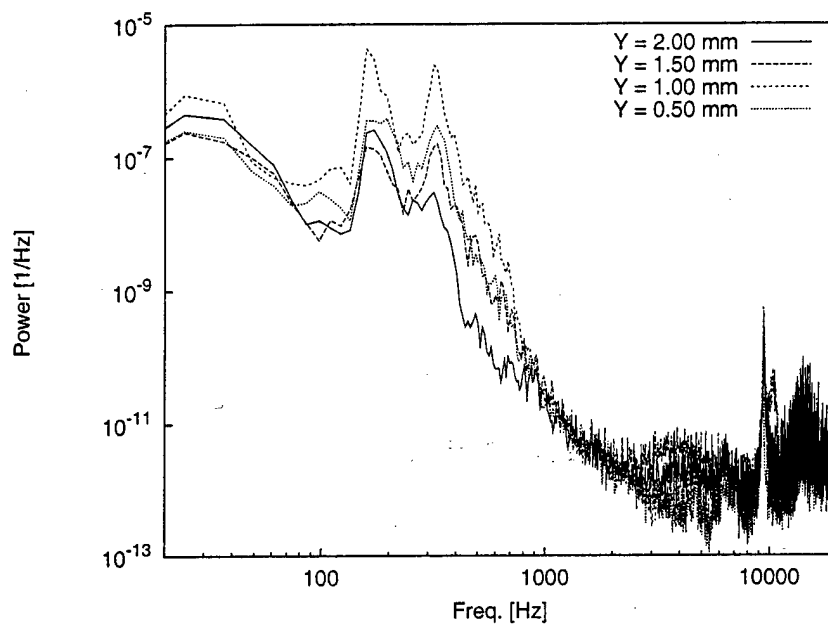


Figure 158: Fluctuating-velocity spectra,  $Re_c = 2.8 \times 10^6$ , [54|12] roughness,  $x/c = 0.30$ ,  $z = 85.0$  mm.

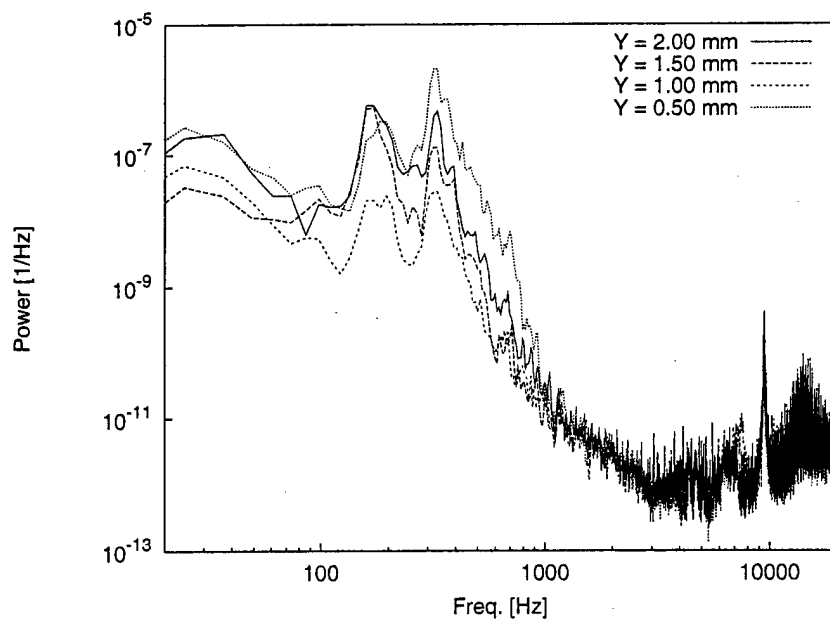


Figure 159: Fluctuating-velocity spectra,  $Re_c = 2.8 \times 10^6$ , [54|12] roughness,  $x/c = 0.30$ ,  $z = 87.4$  mm.

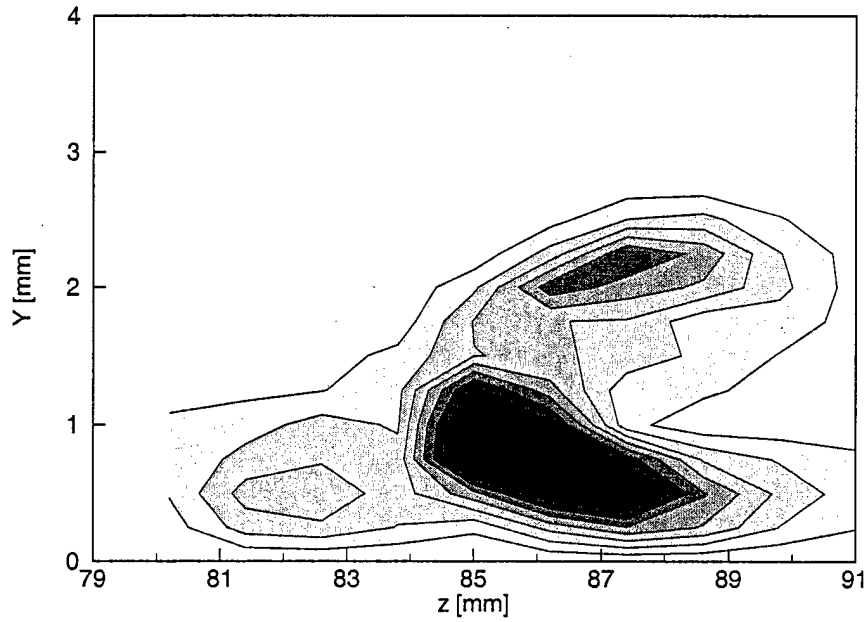


Figure 160: 300-Hz velocity-fluctuation rms distribution,  $Re_c = 2.8 \times 10^6$ , [54|12] roughness,  $x/c = 0.30$ , 200–400-Hz bandpass. Lines are 10% contours of the maximum in this band.

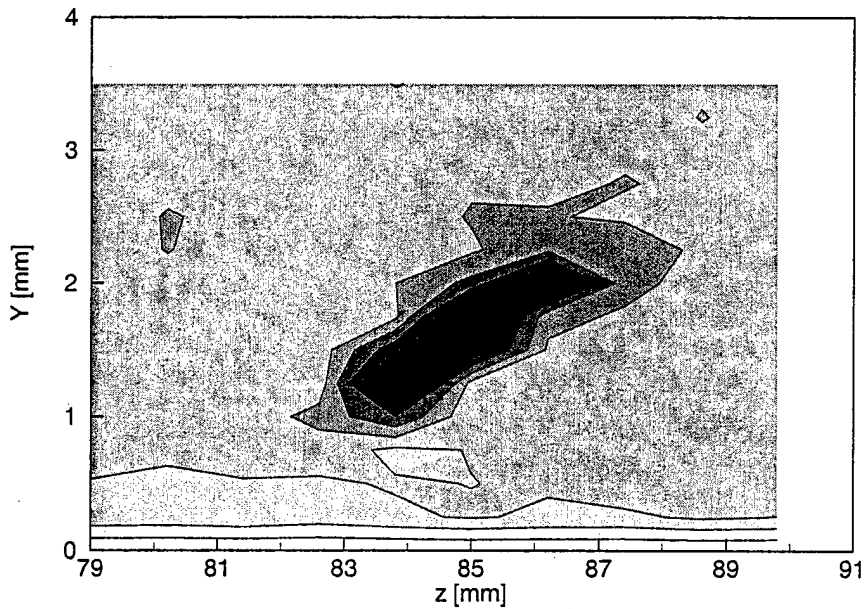


Figure 161: 3.6-kHz velocity-fluctuation rms distribution,  $Re_c = 2.8 \times 10^6$ , [54|12] roughness,  $x/c = 0.30$ , 3.5–3.7-kHz bandpass. Lines are 10% contours of the maximum in this band.

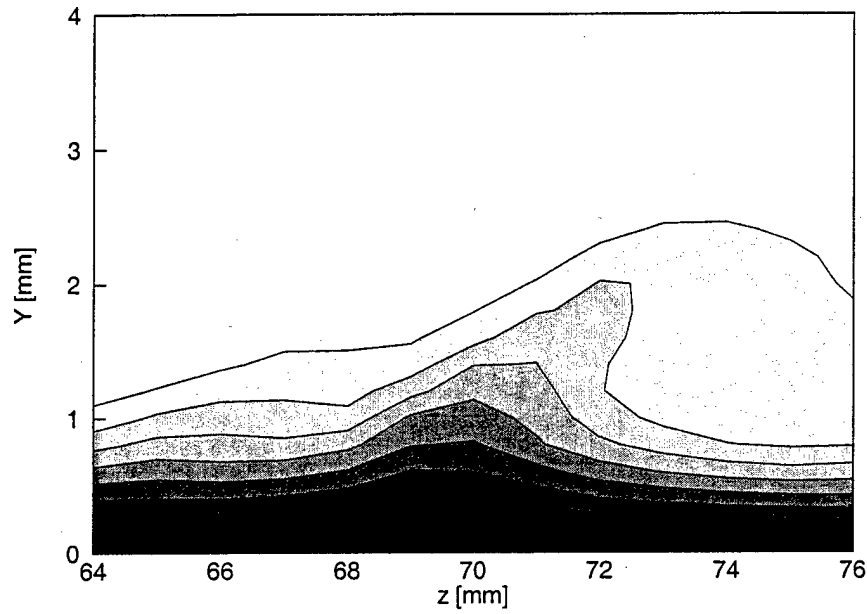


Figure 162: Mean-flow velocity contours,  $Re_c = 2.8 \times 10^6$ , [54|12] roughness,  $x/c = 0.35$ , contour lines at  $U/U_{\text{edge}} = 0.10, 0.20, \dots, 0.90$ .

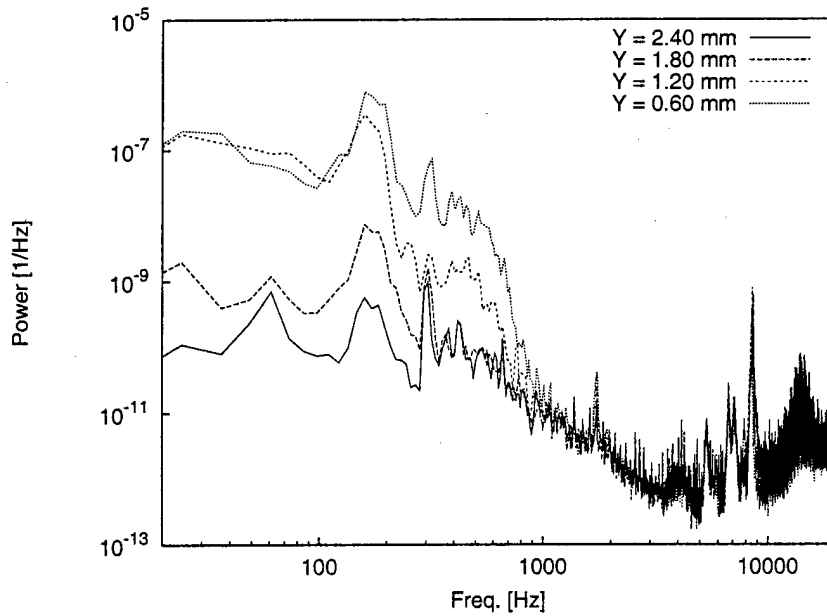


Figure 163: Fluctuating-velocity spectra,  $Re_c = 2.8 \times 10^6$ , [54|12] roughness,  $x/c = 0.35$ ,  $z = 66$  mm.

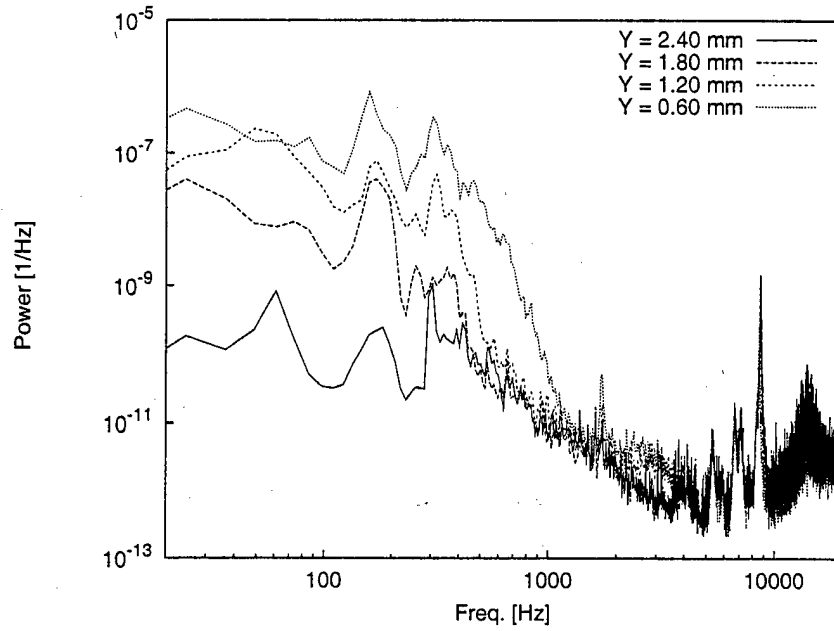


Figure 164: Fluctuating-velocity spectra,  $Re_c = 2.8 \times 10^6$ , [54|12] roughness,  $x/c = 0.35$ ,  $z = 68$  mm.

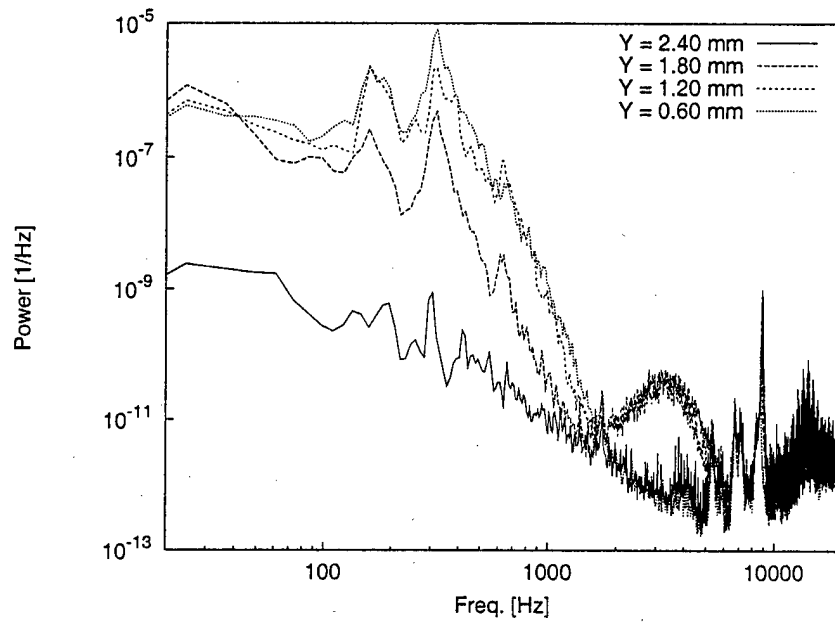


Figure 165: Fluctuating-velocity spectra,  $Re_c = 2.8 \times 10^6$ , [54|12] roughness,  $x/c = 0.35$ ,  $z = 70$  mm.

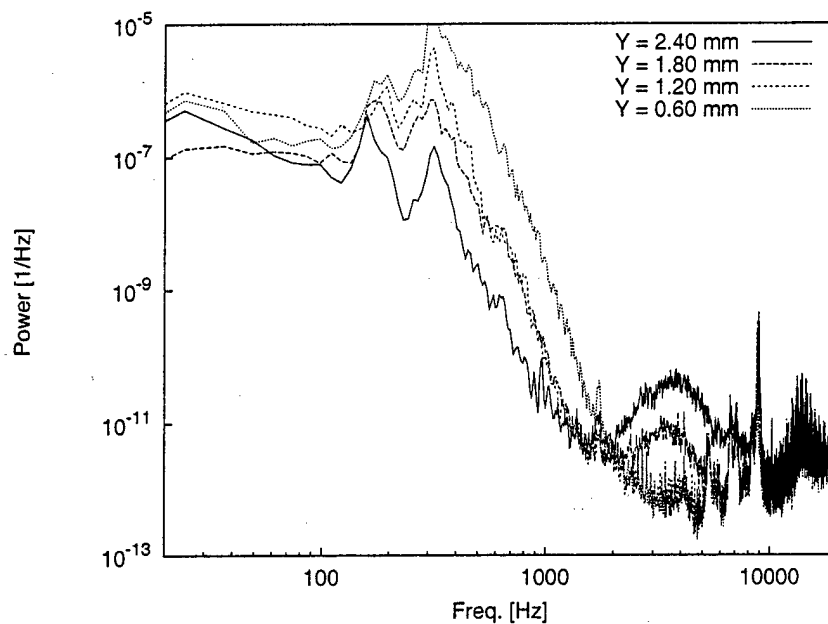


Figure 166: Fluctuating-velocity spectra,  $Re_c = 2.8 \times 10^6$ , [54|12] roughness,  $x/c = 0.35$ ,  $z = 72$  mm.

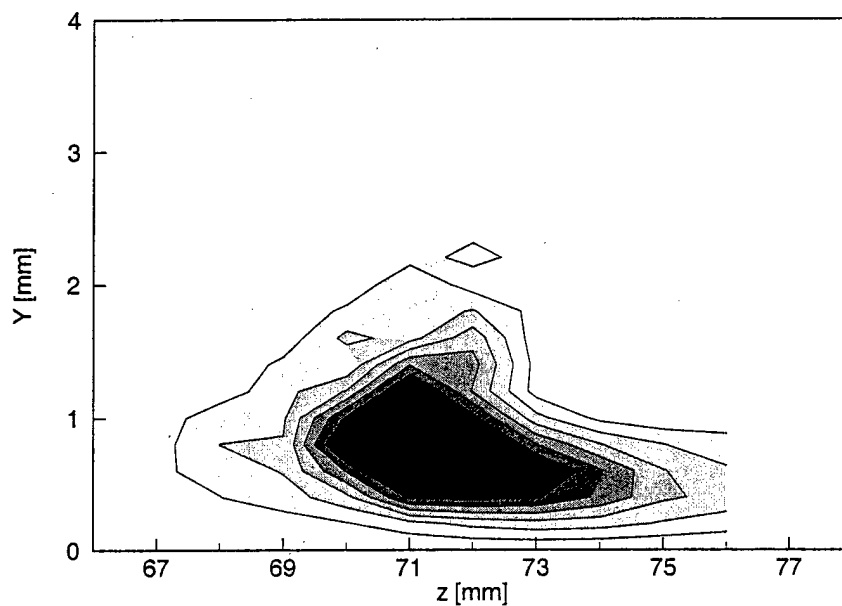


Figure 167: 300-Hz velocity-fluctuation rms distribution,  $Re_c = 2.8 \times 10^6$ , [54|12] roughness,  $x/c = 0.35$ , 200-400-Hz bandpass. Lines are 10% contours of the maximum in this band.

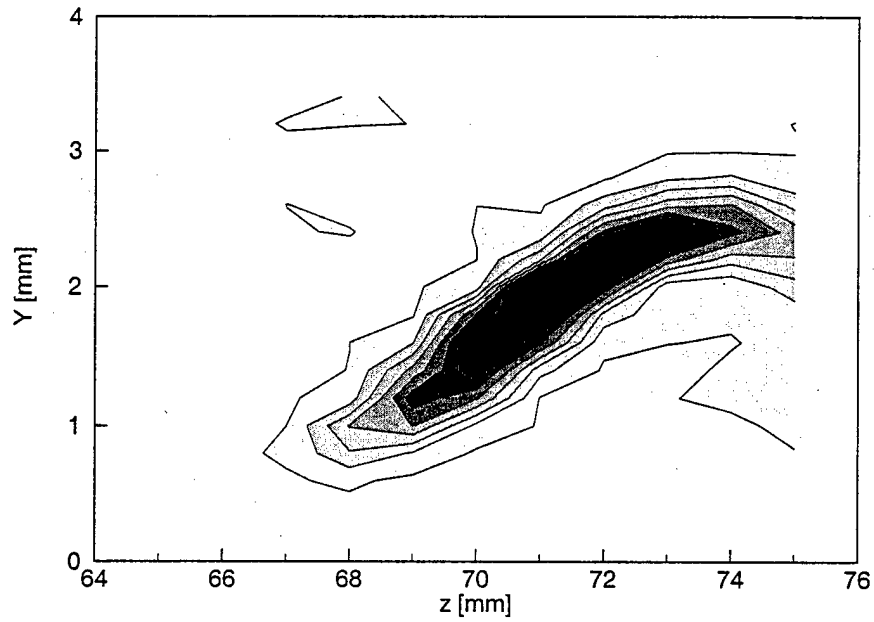


Figure 168: 3.6-kHz velocity-fluctuation rms distribution,  $Re_c = 2.8 \times 10^6$ , [54|12] roughness,  $x/c = 0.35$ , 3.5–3.7-kHz bandpass. Lines are 10% contours of the maximum in this band.

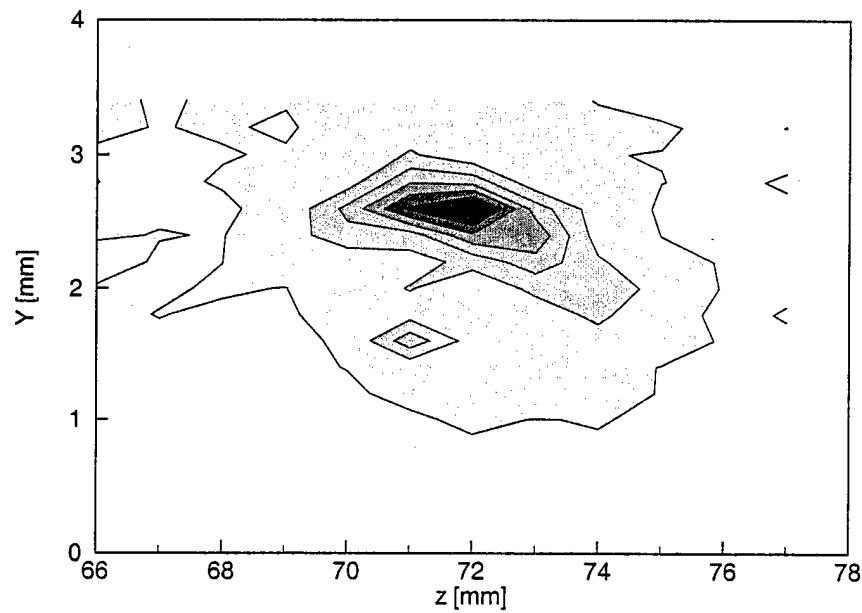


Figure 169: 6.5-kHz velocity-fluctuation rms distribution,  $Re_c = 2.8 \times 10^6$ , [54|12] roughness,  $x/c = 0.35$ , 6.4–6.6 kHz bandpass. Lines are 10% contours of the maximum in this band.

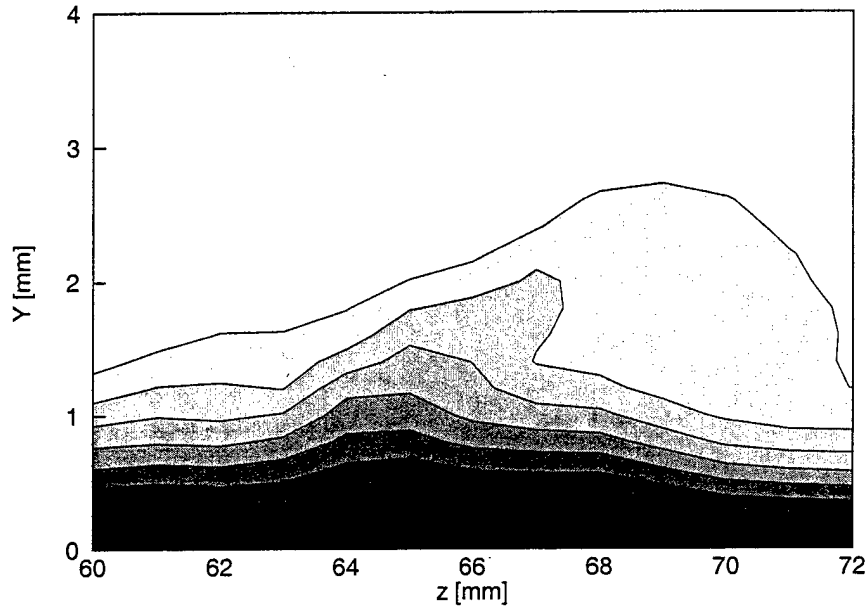


Figure 170: Mean-flow velocity contours,  $Re_c = 2.8 \times 10^6$ , [54|12] roughness,  $x/c = 0.37$ , contour lines at  $U/U_{\text{edge}} = 0.10, 0.20, \dots, 0.90$ .

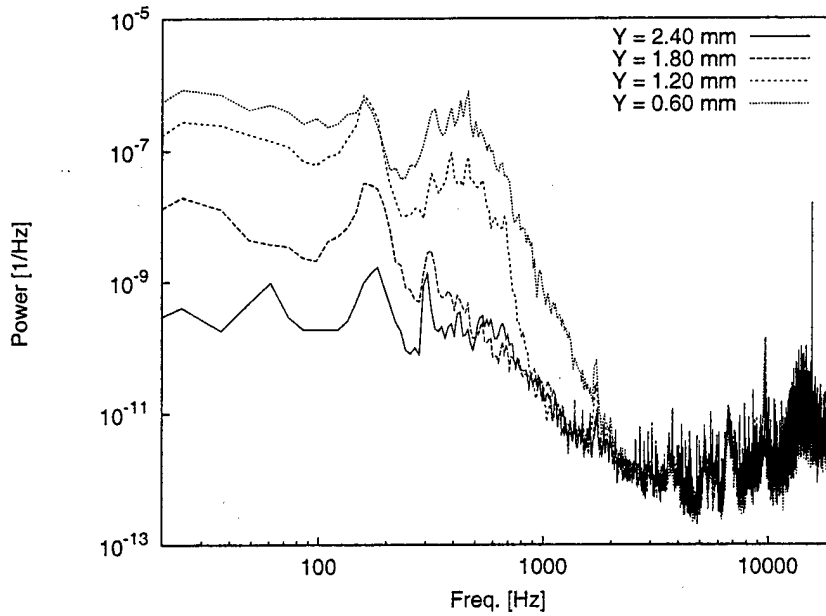


Figure 171: Fluctuating-velocity spectra,  $Re_c = 2.8 \times 10^6$ , [54|12] roughness,  $x/c = 0.37$ ,  $z = 61$  mm.

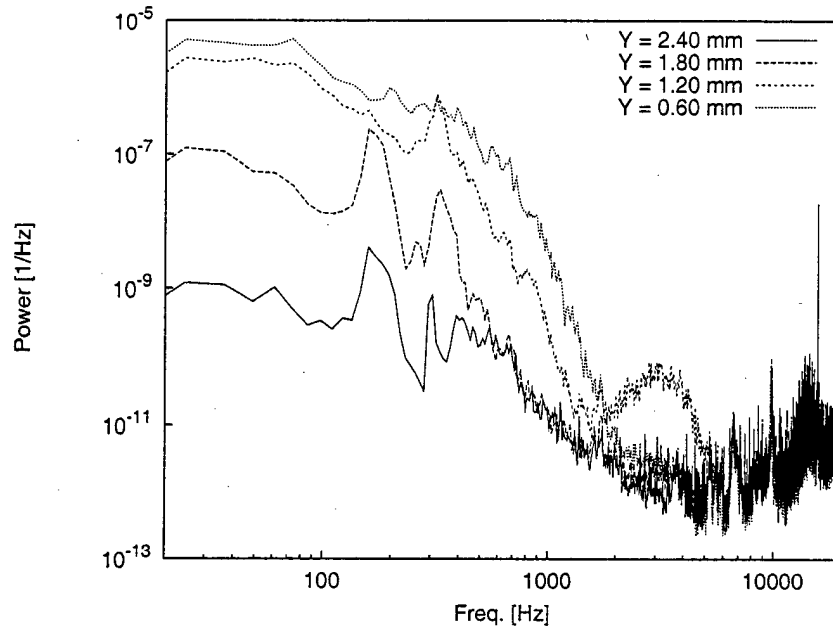


Figure 172: Fluctuating-velocity spectra,  $Re_c = 2.8 \times 10^6$ , [54|12] roughness,  $x/c = 0.37$ ,  $z = 63$  mm.

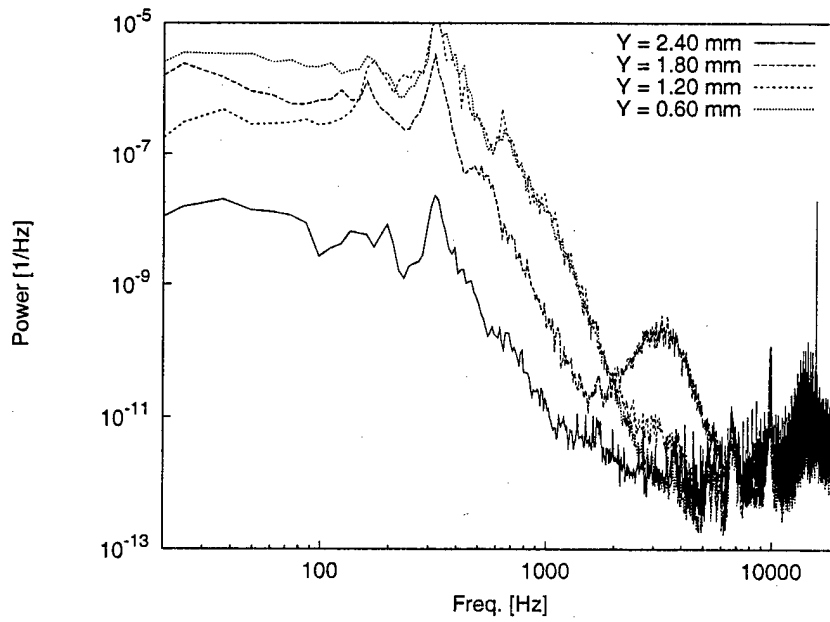


Figure 173: Fluctuating-velocity spectra,  $Re_c = 2.8 \times 10^6$ , [54|12] roughness,  $x/c = 0.37$ ,  $z = 65$  mm.



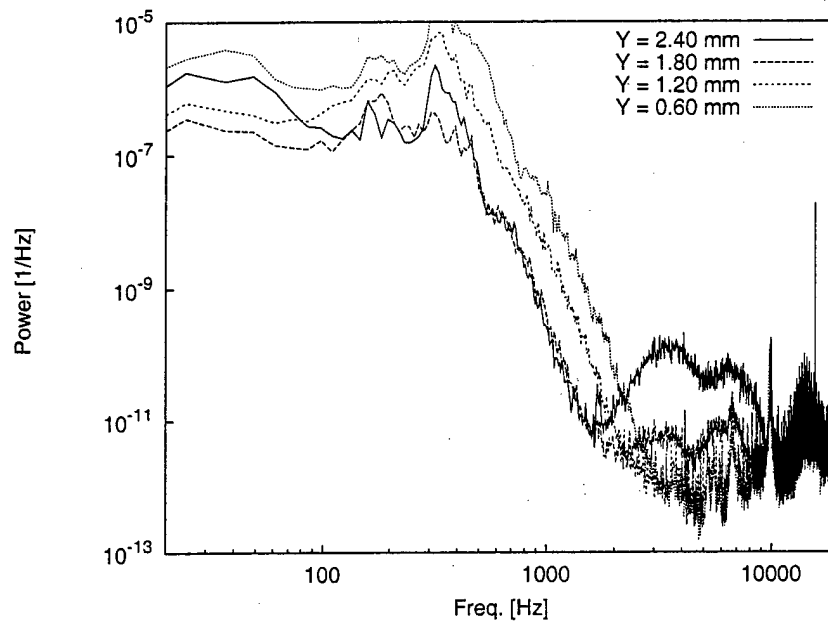


Figure 174: Fluctuating-velocity spectra,  $Re_c = 2.8 \times 10^6$ , [54|12] roughness,  $x/c = 0.37$ ,  $z = 67$  mm.

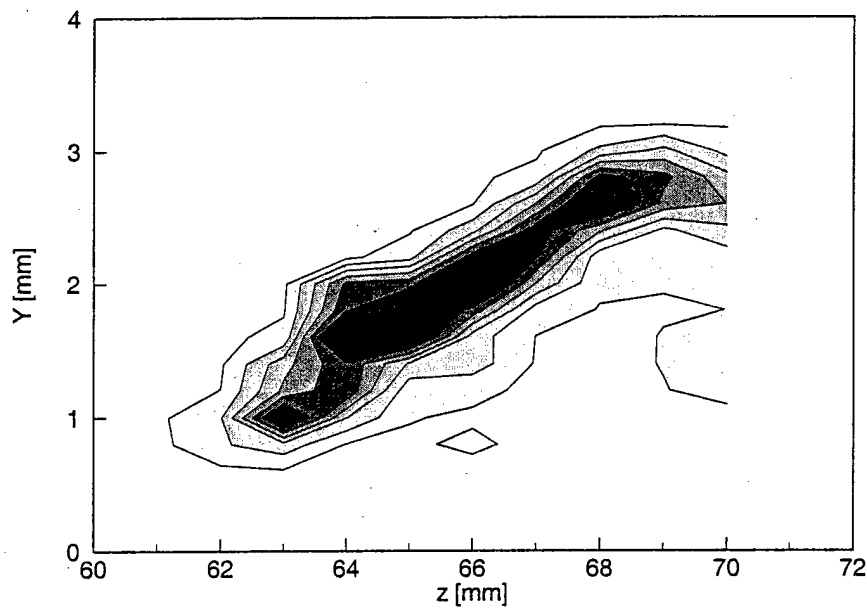


Figure 175: 3.6-kHz velocity-fluctuation rms distribution,  $Re_c = 2.8 \times 10^6$ , [54|12] roughness,  $x/c = 0.37$ , 3.5 kHz–3.7-kHz bandpass. Lines are 10% contours of the maximum in this band.

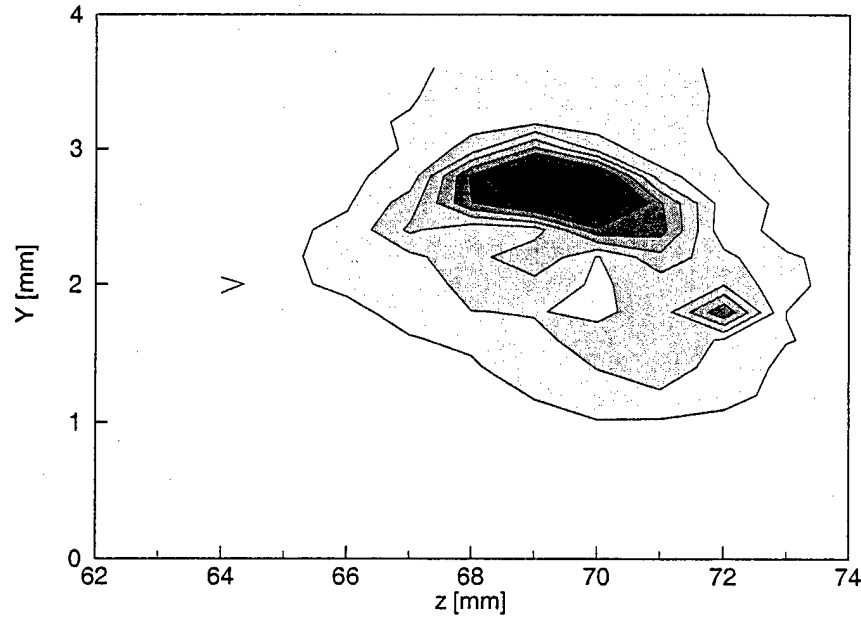


Figure 176: 6.5-kHz velocity-fluctuation rms distribution,  $Re_c = 2.8 \times 10^6$ , [54|12] roughness,  $x/c = 0.37$ , 6.4 kHz–6.6 kHz bandpass. Lines are 10% contours of the maximum in this band.

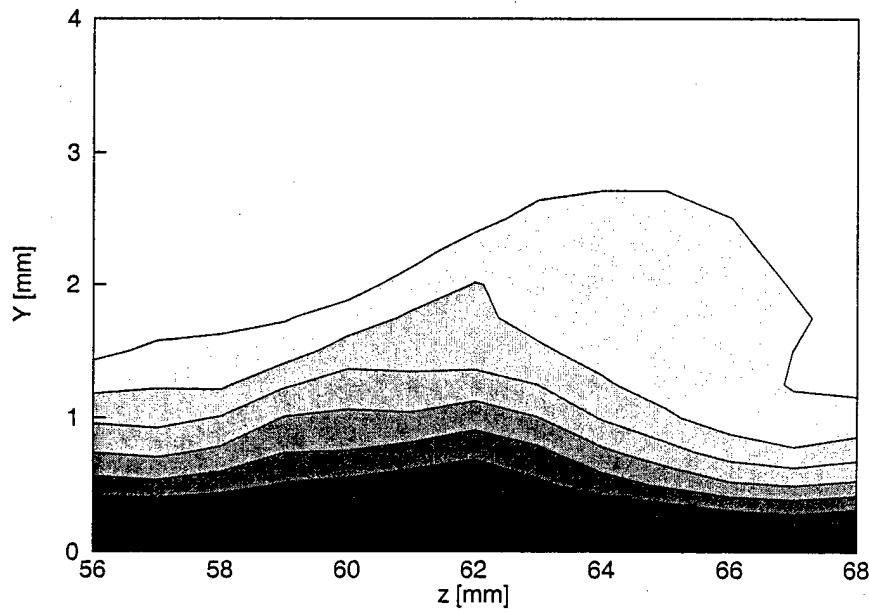


Figure 177: Mean-flow velocity contours,  $Re_c = 2.8 \times 10^6$ , [54|12] roughness,  $x/c = 0.38$ , contour lines at  $U/U_{\text{edge}} = 0.10, 0.20, \dots, 0.90$ .

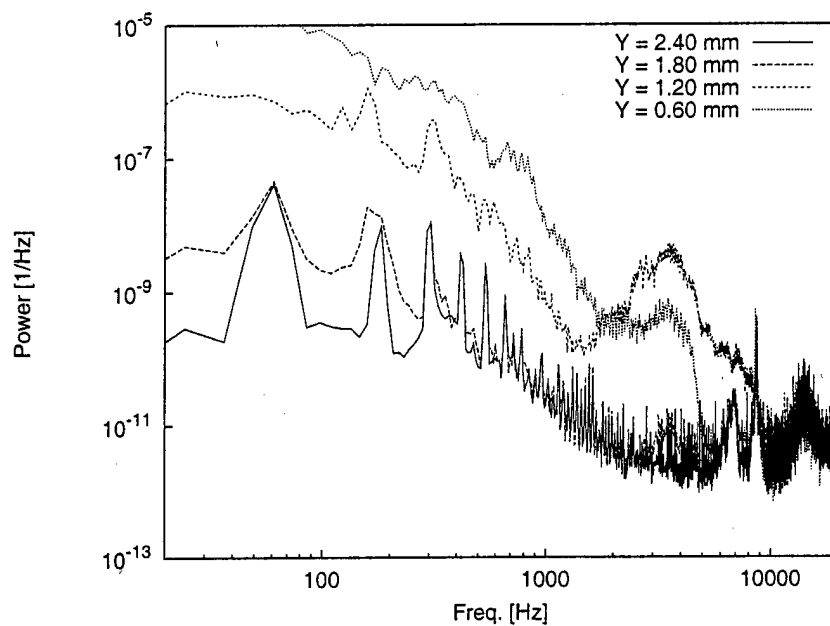


Figure 178: Fluctuating-velocity spectra,  $Re_c = 2.8 \times 10^6$ , [54|12] roughness,  $x/c = 0.385$ ,  $z = 58$  mm.

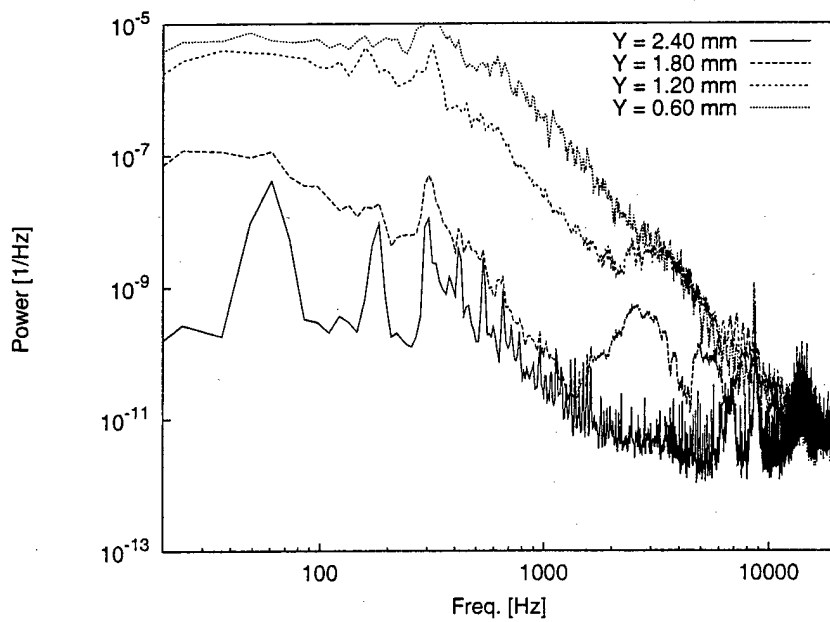


Figure 179: Fluctuating-velocity spectra,  $Re_c = 2.8 \times 10^6$ , [54|12] roughness,  $x/c = 0.385$ ,  $z = 60$  mm.

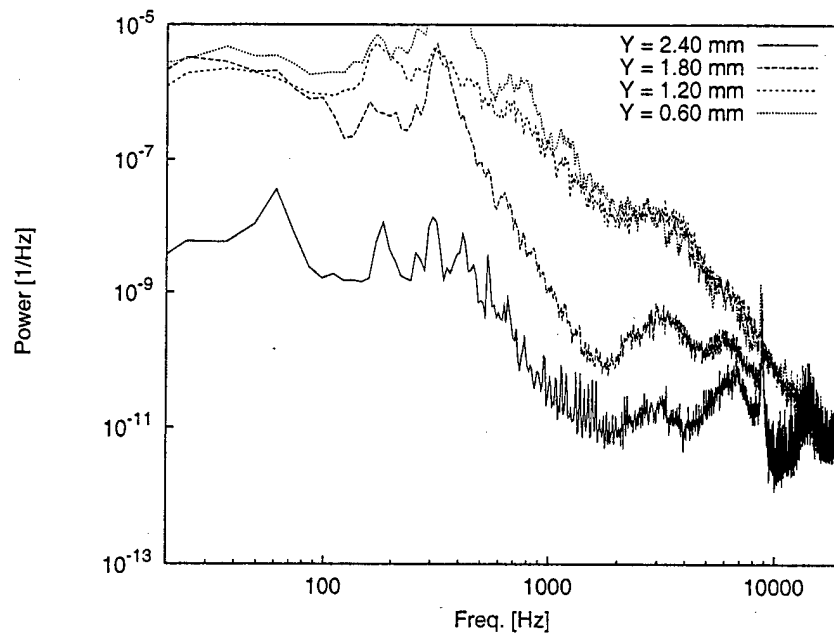


Figure 180: Fluctuating-velocity spectra,  $Re_c = 2.8 \times 10^6$ , [54|12] roughness,  $x/c = 0.385$ ,  $z = 62$  mm.

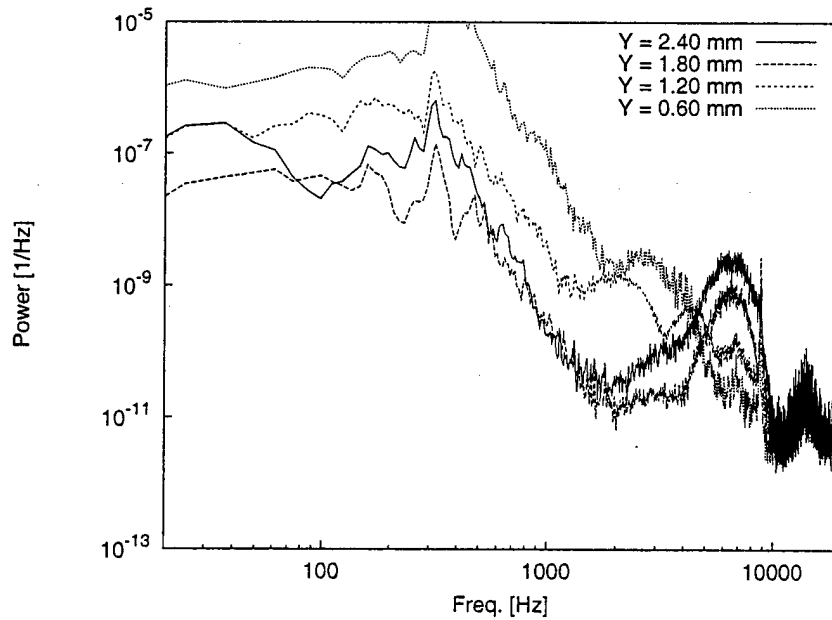


Figure 181: Fluctuating-velocity spectra,  $Re_c = 2.8 \times 10^6$ , [54|12] roughness,  $x/c = 0.385$ ,  $z = 64$  mm.

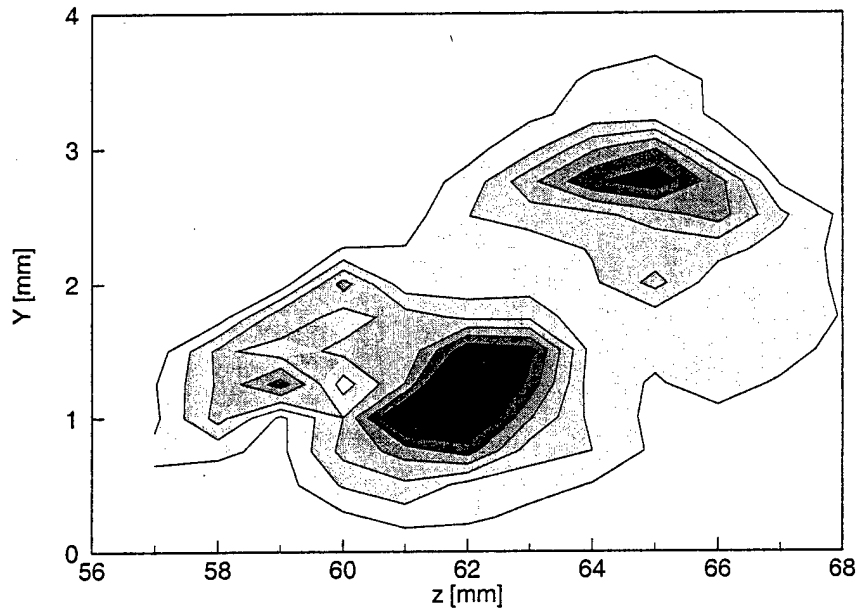


Figure 182: Total velocity-fluctuation rms distribution,  $Re_c = 2.8 \times 10^6$ , [54|12] roughness,  $x/c = 0.385$ , 20-Hz–12.0-kHz bandpass. Lines are 10% contours of the maximum rms fluctuations.

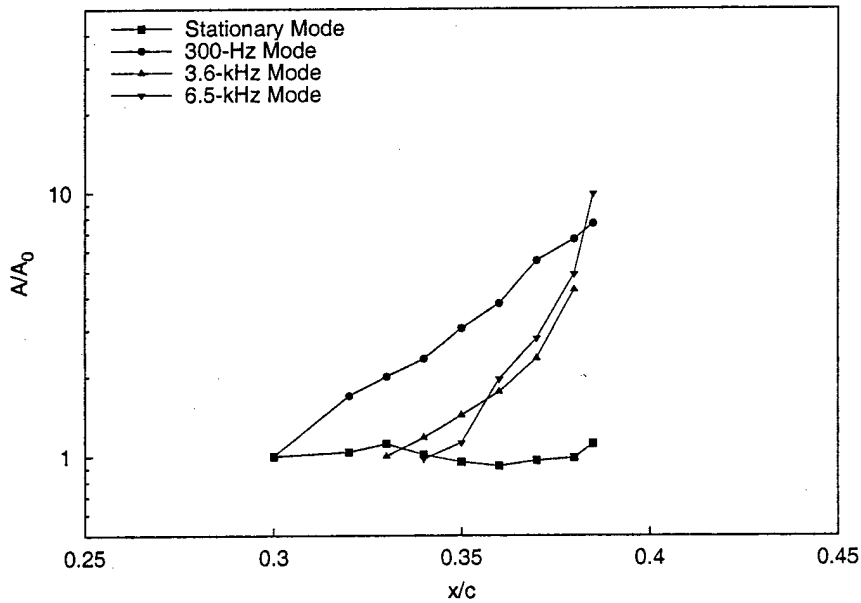


Figure 183: Velocity-fluctuation rms growth,  $Re_c = 2.8 \times 10^6$ , [54|12] roughness.

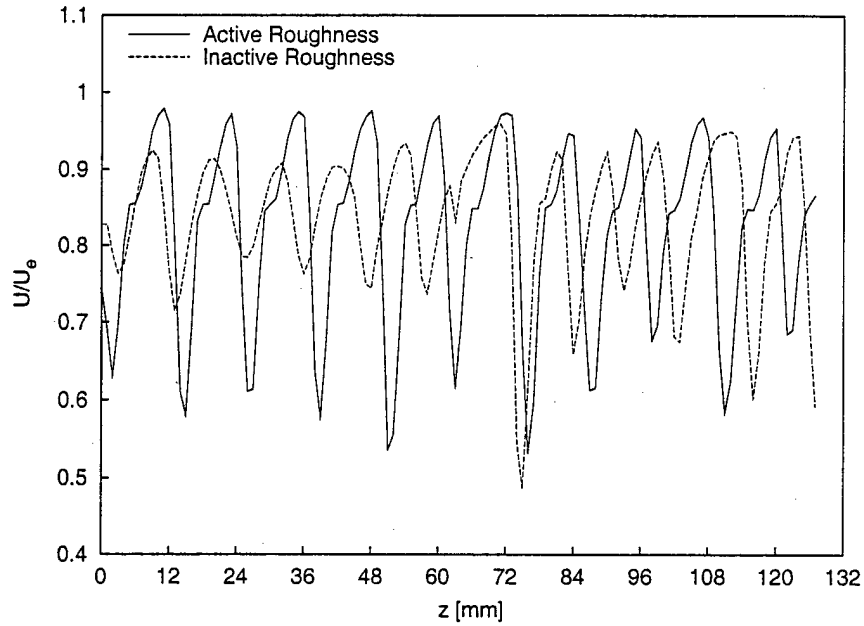


Figure 184: Spanwise mean-flow hotwire scan with and without activated 12-mm-spaced artificial roughness,  $Re_c = 2.4 \times 10^6$ ,  $x/c = 0.40$ ,  $Y = 1.5$  mm.

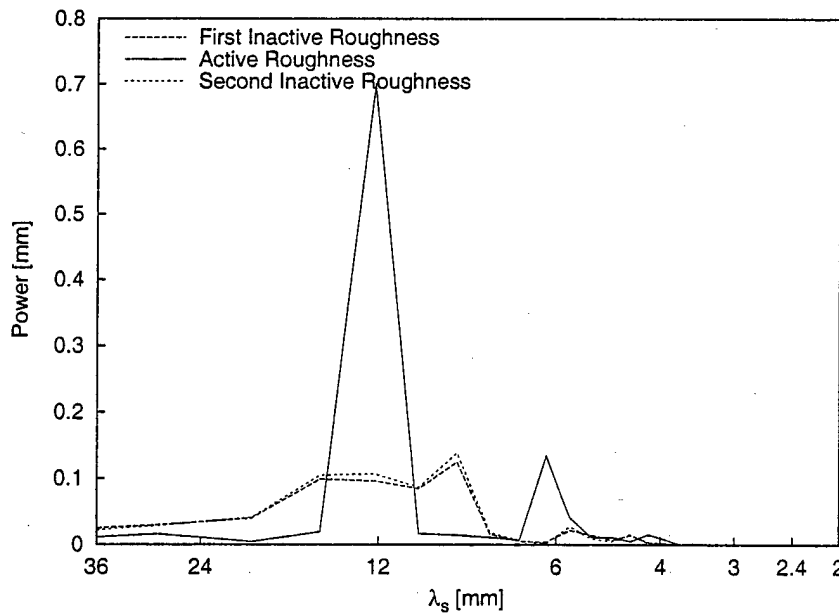


Figure 185: Power spectral density of the spanwise mean-flow hotwire scan with and without activated 12-mm-spaced artificial roughness,  $Re_c = 2.4 \times 10^6$ ,  $x/c = 0.40$ ,  $Y = 1.5$  mm.

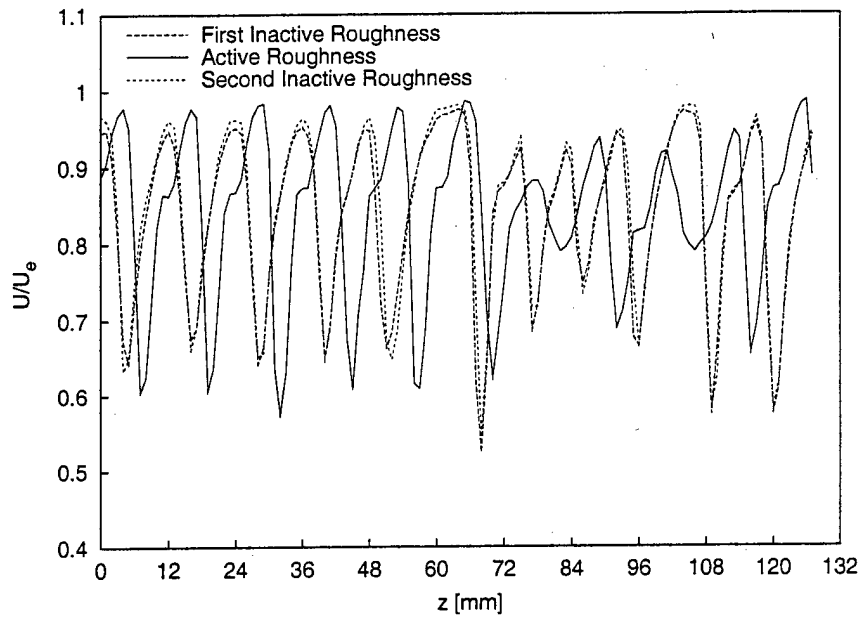


Figure 186: Spanwise mean-flow hotwire scan with and without activated 12-mm-spaced artificial roughness,  $Re_c = 2.4 \times 10^6$ ,  $x/c = 0.43$ ,  $Y = 2.0$  mm.

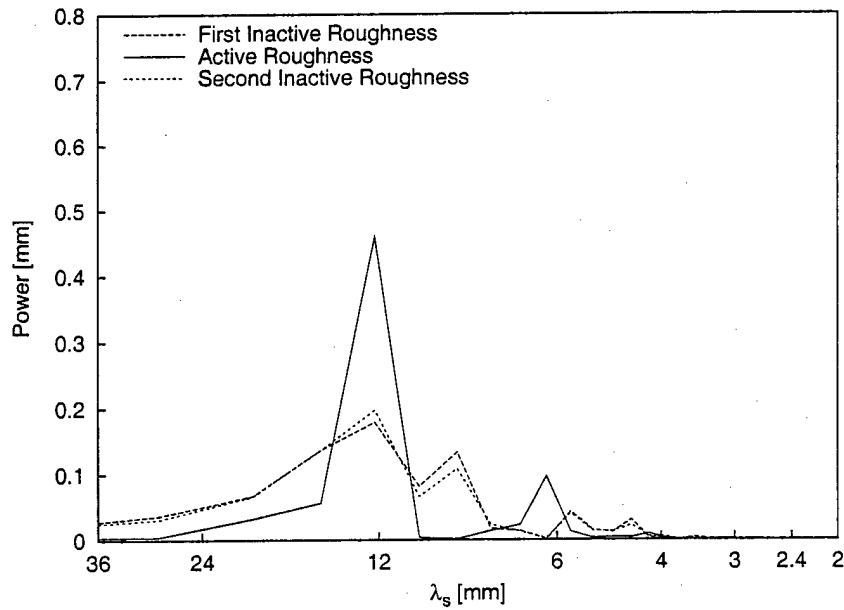


Figure 187: Power spectral density of the spanwise mean-flow hotwire scan with and without activated 12-mm-spaced artificial roughness,  $Re_c = 2.4 \times 10^6$ ,  $x/c = 0.43$ ,  $Y = 2.0$  mm.

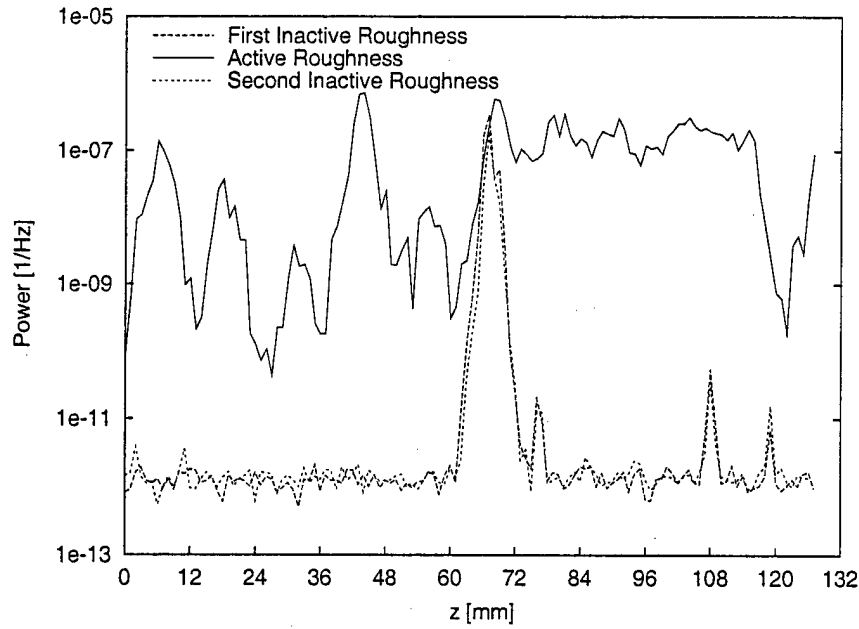


Figure 188: Spanwise distribution of velocity-fluctuation power spectral density at 3.0 kHz with and without activated 12-mm-spaced artificial roughness,  $Re_c = 2.4 \times 10^6$ ,  $x/c = 0.43$ ,  $Y = 2.0$  mm.

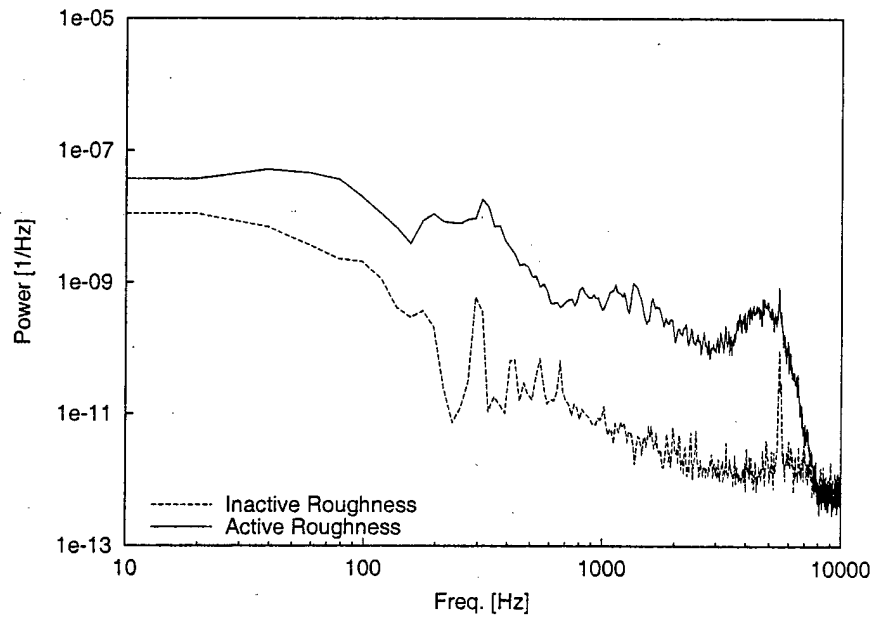


Figure 189: Fluctuating-velocity spectral density with and without activated 12-mm-spaced artificial roughness,  $Re_c = 2.4 \times 10^6$ ,  $x/c = 0.43$ ,  $Y = 2.0$  mm,  $z = 24$  mm.



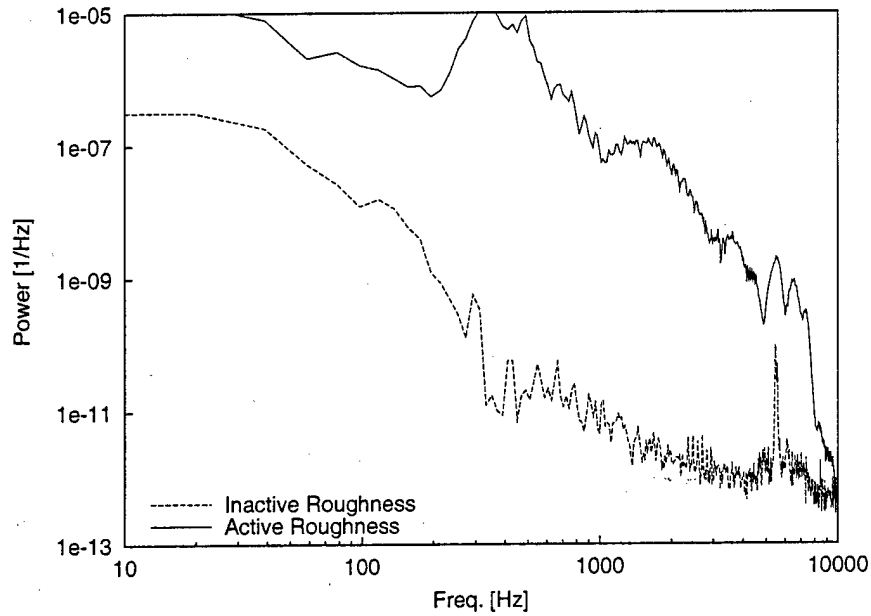


Figure 190: Fluctuating-velocity spectral density with and without activated 12-mm-spaced artificial roughness,  $Re_c = 2.4 \times 10^6$ ,  $x/c = 0.43$ ,  $Y = 2.0$  mm,  $z = 31$  mm.

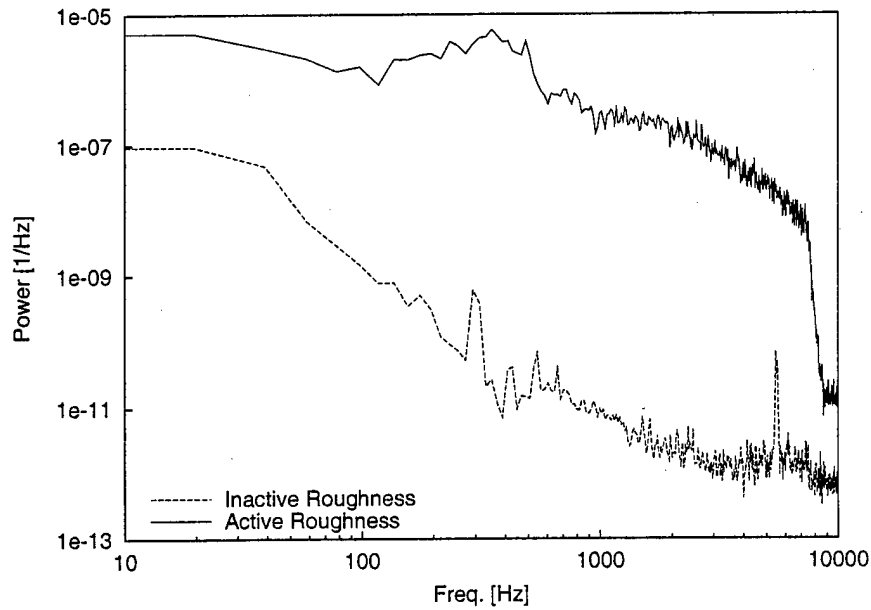


Figure 191: Fluctuating-velocity spectral density with and without activated 12-mm-spaced artificial roughness,  $Re_c = 2.4 \times 10^6$ ,  $x/c = 0.43$ ,  $Y = 2.0$  mm,  $z = 46$  mm.

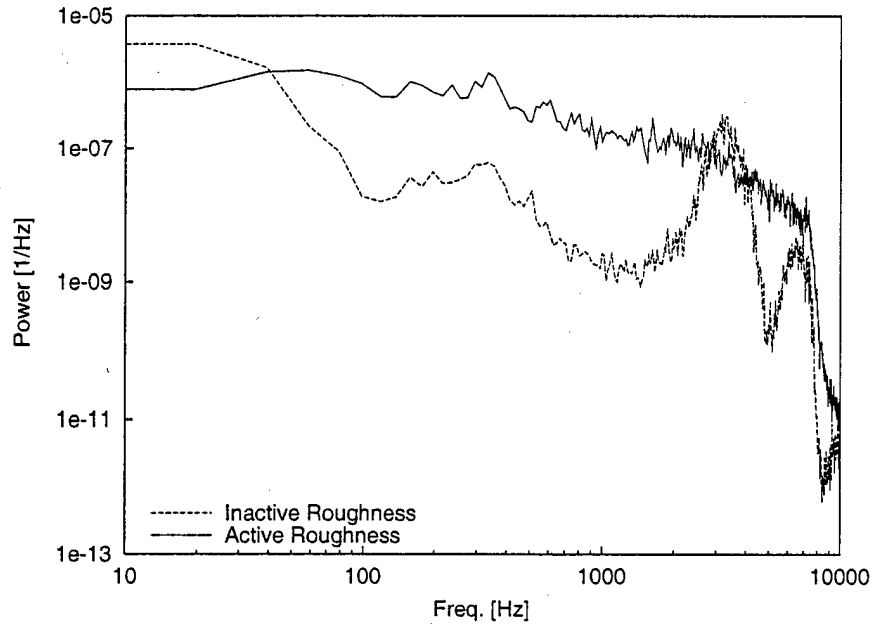


Figure 192: Fluctuating-velocity spectral density with and without activated 12-mm-spaced artificial roughness,  $Re_c = 2.4 \times 10^6$ ,  $x/c = 0.43$ ,  $Y = 2.0$  mm,  $z = 66$  mm.

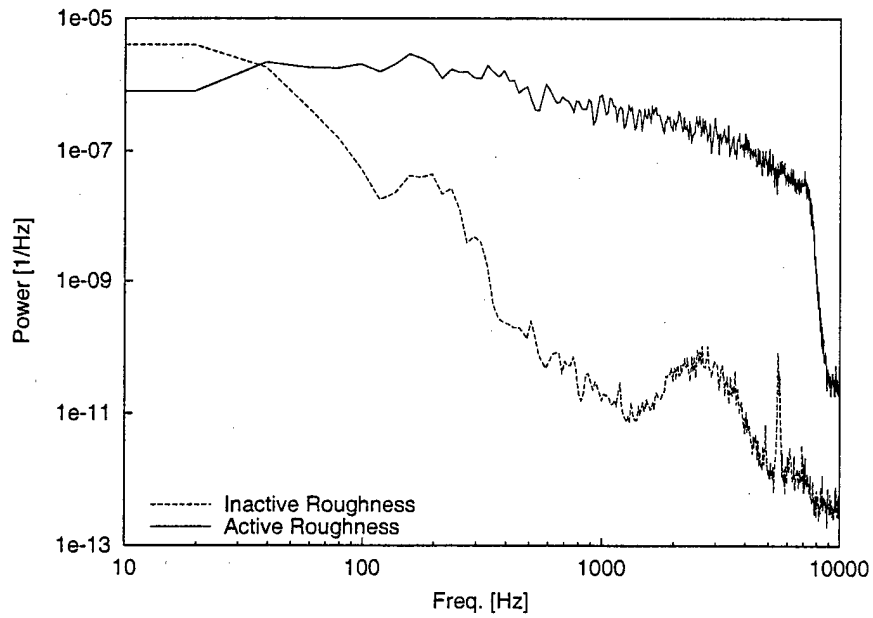


Figure 193: Fluctuating-velocity spectral density with and without activated 12-mm-spaced artificial roughness,  $Re_c = 2.4 \times 10^6$ ,  $x/c = 0.43$ ,  $Y = 2.0$  mm,  $z = 108$  mm.

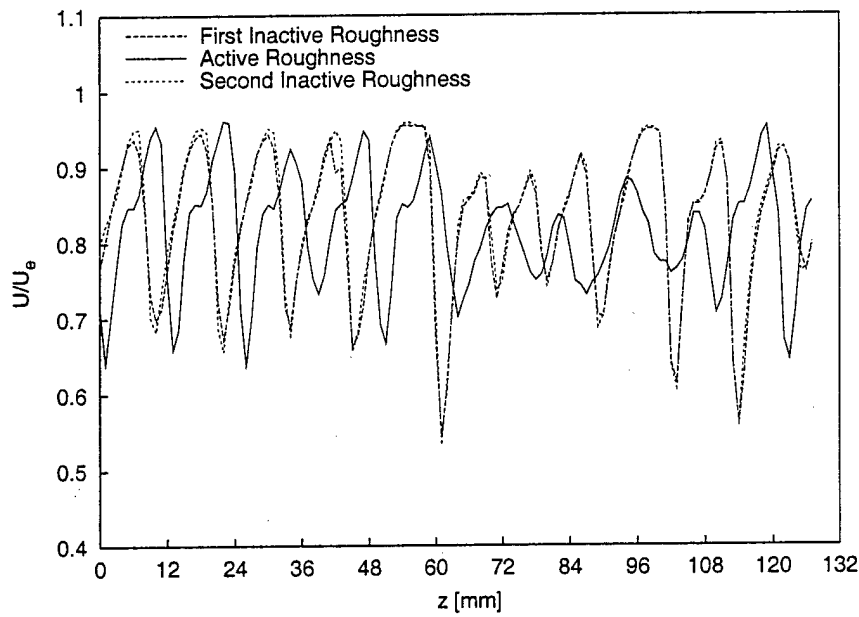


Figure 194: Spanwise mean-flow hotwire scan with and without activated 12-mm-spaced artificial roughness,  $Re_c = 2.4 \times 10^6$ ,  $x/c = 0.45$ ,  $Y = 2.0$  mm.

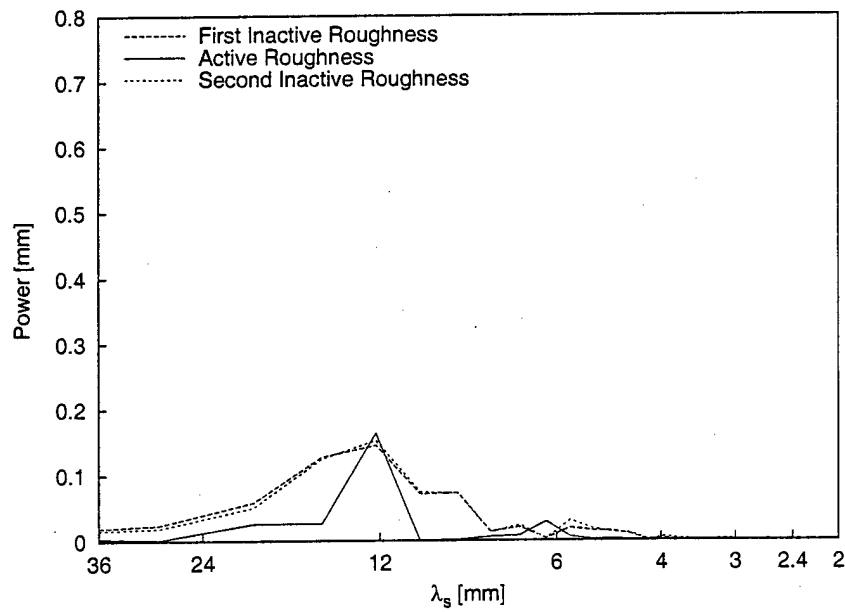


Figure 195: Power spectral density of the spanwise mean-flow hotwire scan with and without activated 12-mm-spaced artificial roughness,  $Re_c = 2.4 \times 10^6$ ,  $x/c = 0.45$ ,  $Y = 2.0$  mm.

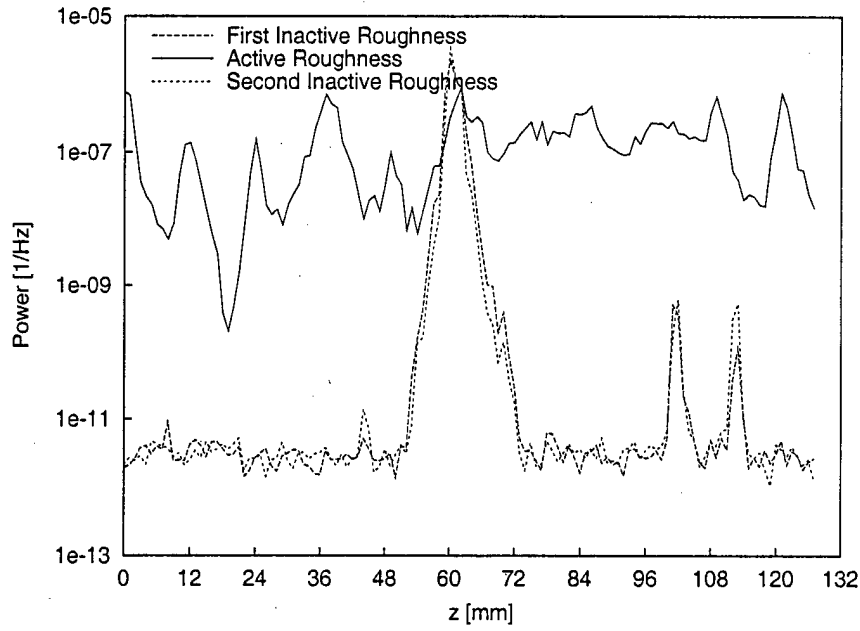


Figure 196: Spanwise distribution of velocity-fluctuation power spectral density at 3.0 kHz with and without activated 12-mm-spaced artificial roughness,  $Re_c = 2.4 \times 10^6$ ,  $x/c = 0.45$ ,  $Y = 2.0$  mm.

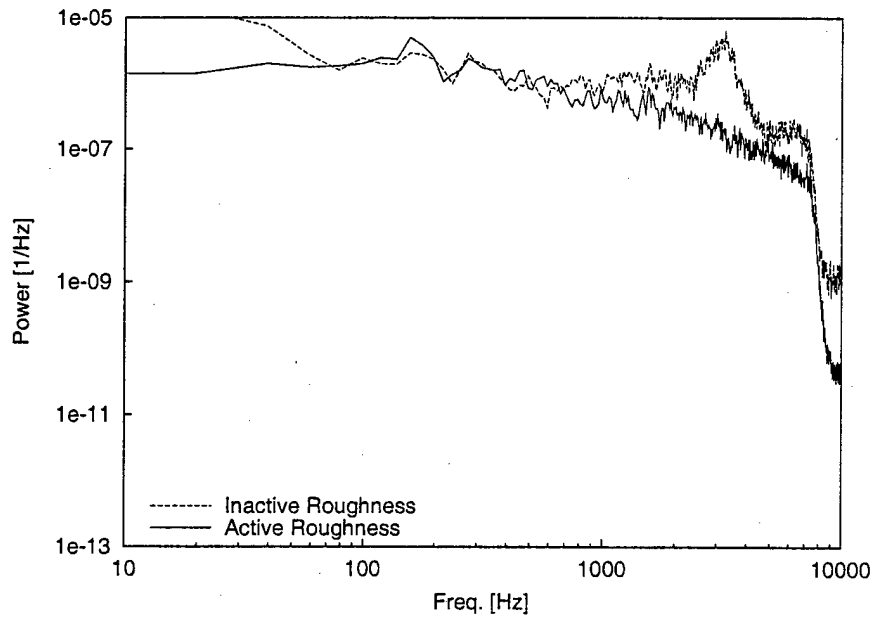


Figure 197: Fluctuating-velocity spectral density with and without activated 12-mm-spaced artificial roughness,  $Re_c = 2.4 \times 10^6$ ,  $x/c = 0.45$ ,  $Y = 2.0$  mm,  $z = 60$  mm.

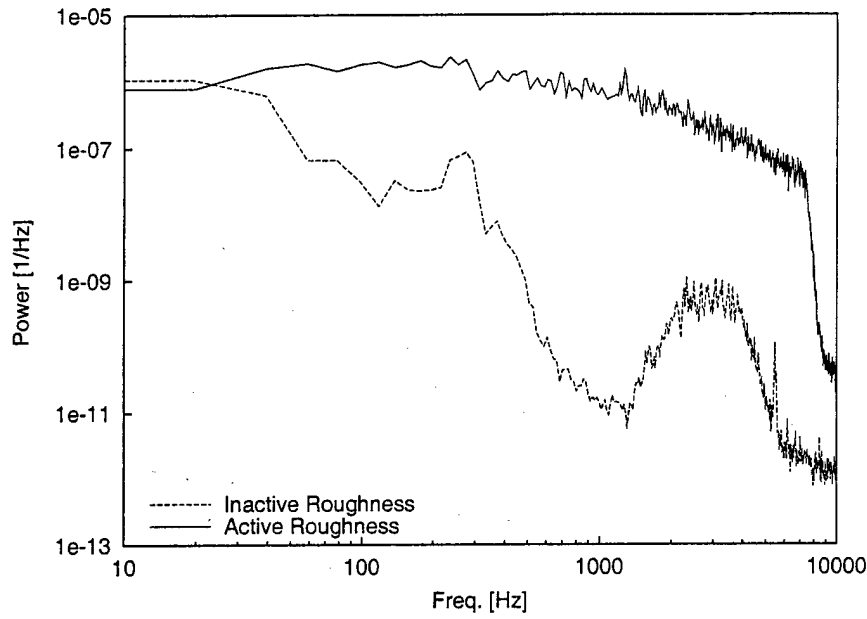


Figure 198: Fluctuating-velocity spectral density with and without activated 12-mm-spaced artificial roughness,  $Re_c = 2.4 \times 10^6$ ,  $x/c = 0.45$ ,  $Y = 2.0$  mm,  $z = 60$  mm.

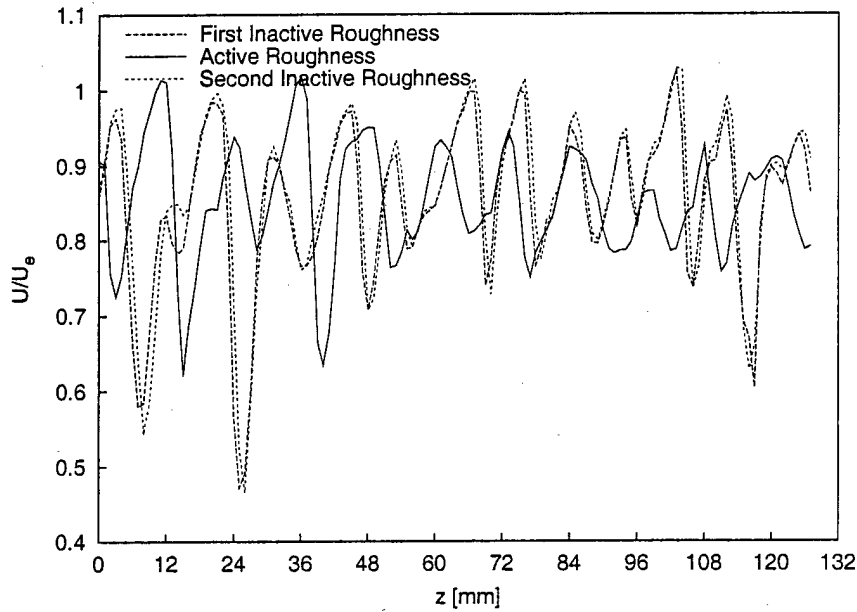


Figure 199: Spanwise mean-flow hotwire scan with and without activated 12-mm-spaced artificial roughness,  $Re_c = 2.8 \times 10^6$ ,  $x/c = 0.38$ ,  $Y = 1.2$  mm.

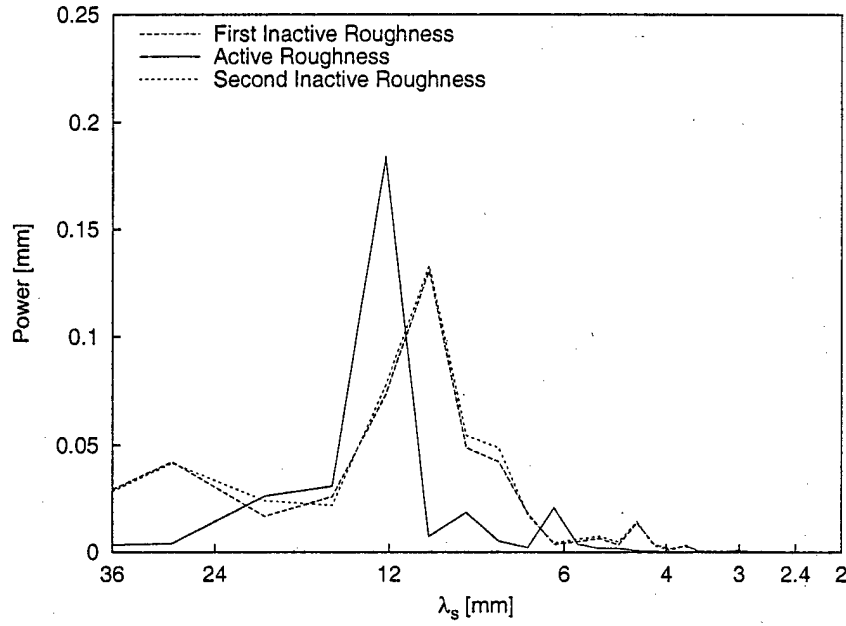


Figure 200: Power spectral density of the spanwise mean-flow hotwire scan with and without activated 12-mm-spaced artificial roughness,  $Re_c = 2.8 \times 10^6$ ,  $x/c = 0.38$ ,  $Y = 1.2$  mm.

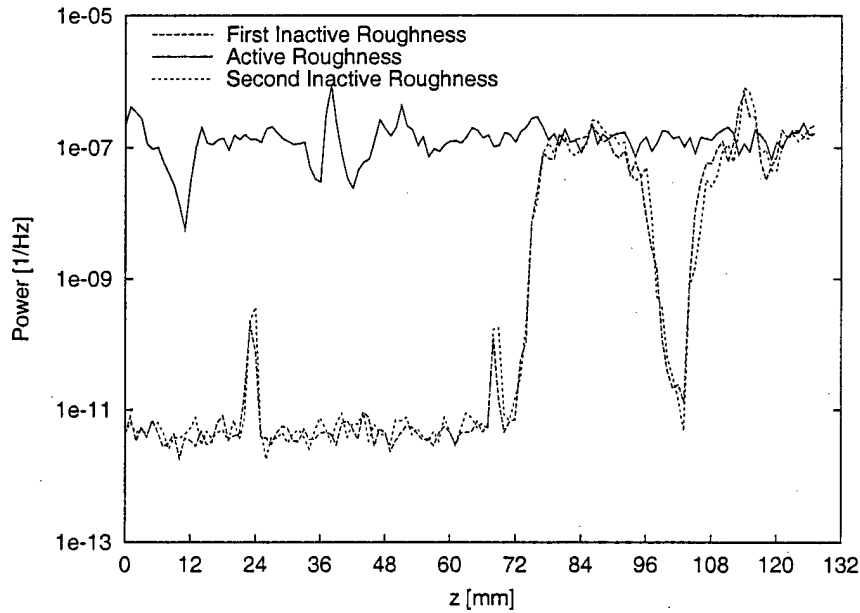


Figure 201: Spanwise distribution of velocity-fluctuation power spectral density at 4.0 kHz with and without activated 12-mm-spaced artificial roughness,  $Re_c = 2.8 \times 10^6$ ,  $x/c = 0.38$ ,  $Y = 1.2$  mm.

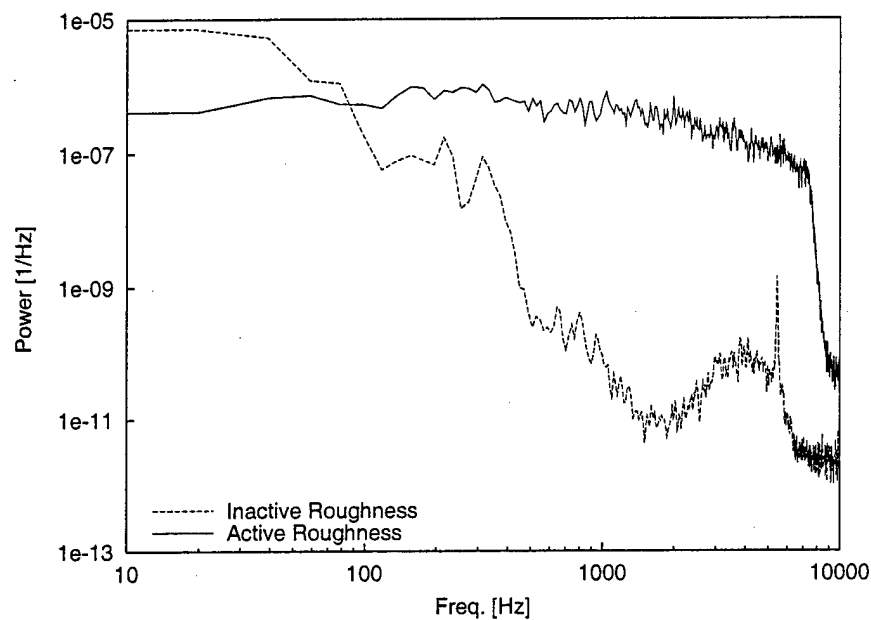


Figure 202: Fluctuating-velocity spectral density with and without activated 12-mm-spaced artificial roughness,  $Re_c = 2.8 \times 10^6$ ,  $x/c = 0.38$ ,  $Y = 1.2$  mm,  $z = 23$  mm.

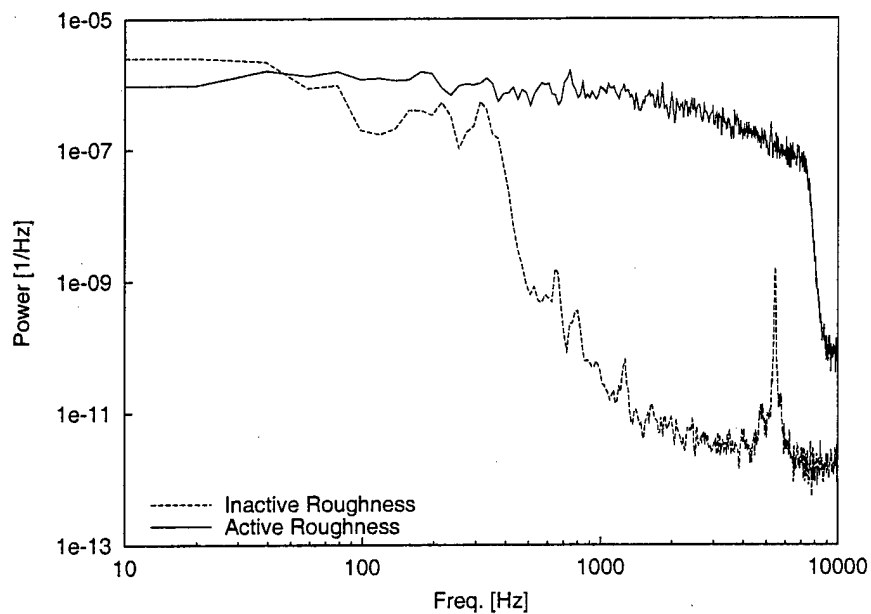


Figure 203: Fluctuating-velocity spectral density with and without activated 12-mm-spaced artificial roughness,  $Re_c = 2.8 \times 10^6$ ,  $x/c = 0.38$ ,  $Y = 1.2$  mm,  $z = 26$  mm.

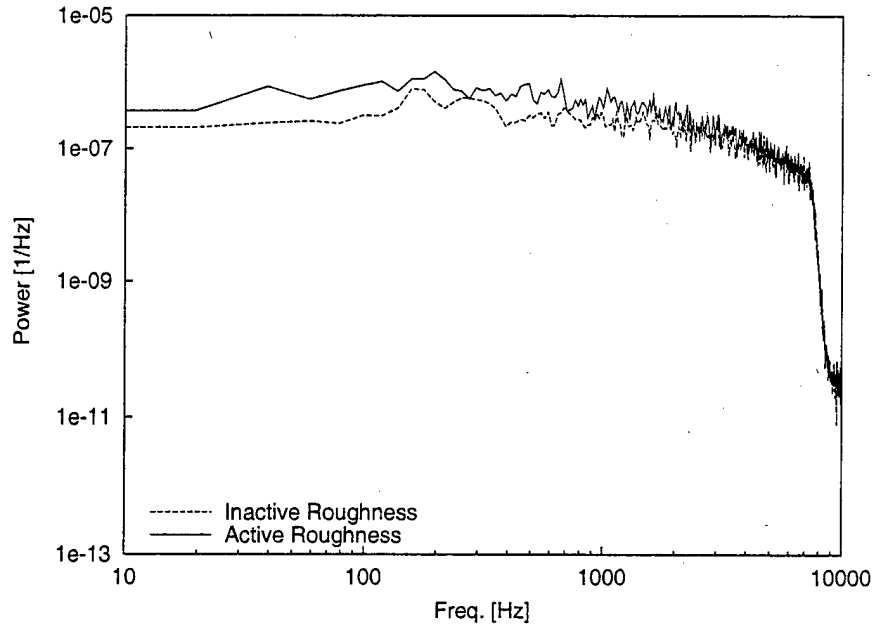


Figure 204: Fluctuating-velocity spectral density with and without activated 12-mm-spaced artificial roughness,  $Re_c = 2.8 \times 10^6$ ,  $x/c = 0.38$ ,  $Y = 1.2$  mm,  $z = 84$  mm.

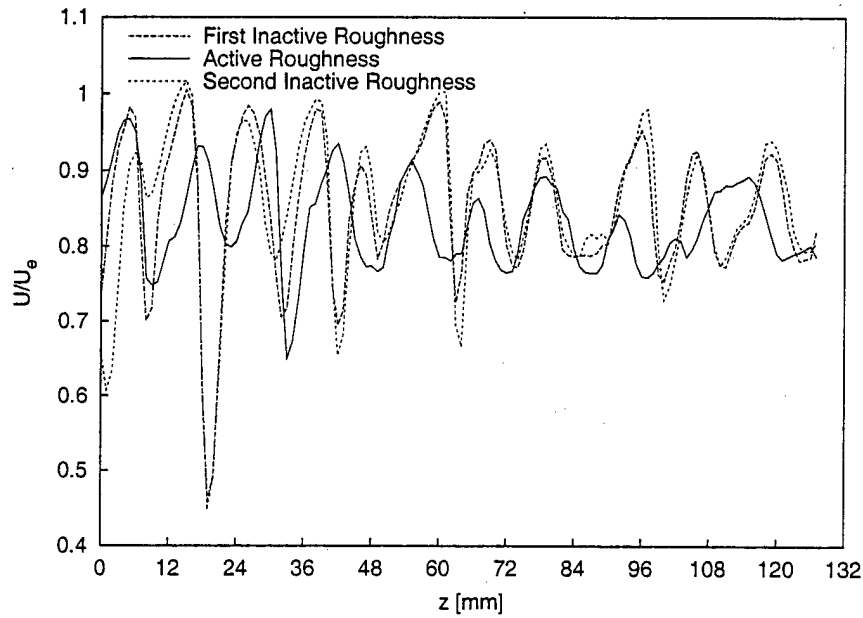


Figure 205: Spanwise mean-flow hotwire scan with and without activated 12-mm-spaced artificial roughness,  $Re_c = 2.8 \times 10^6$ ,  $x/c = 0.40$ ,  $Y = 1.2$  mm.



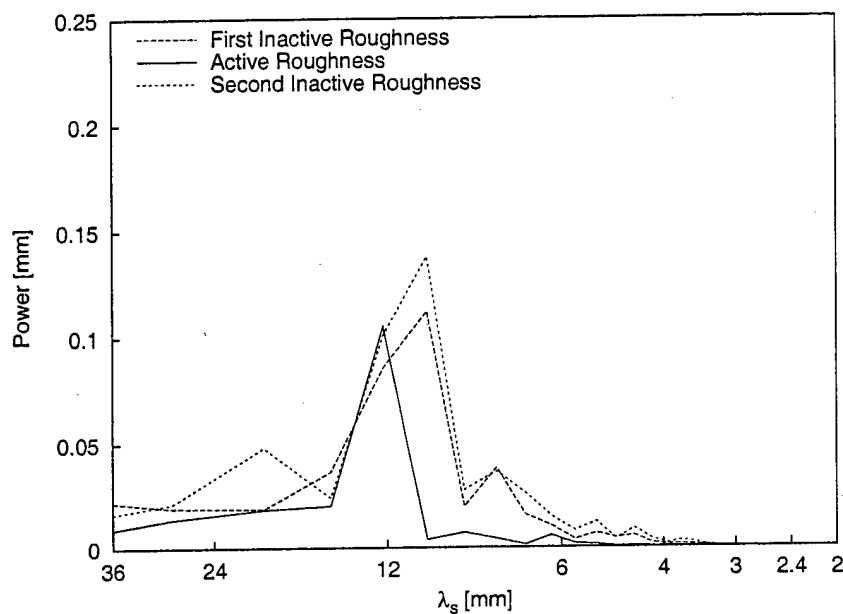


Figure 206: Power spectral density of the spanwise mean-flow hotwire scan with and without activated 12-mm-spaced artificial roughness,  $Re_c = 2.8 \times 10^6$ ,  $x/c = 0.40$ ,  $Y = 1.2$  mm.

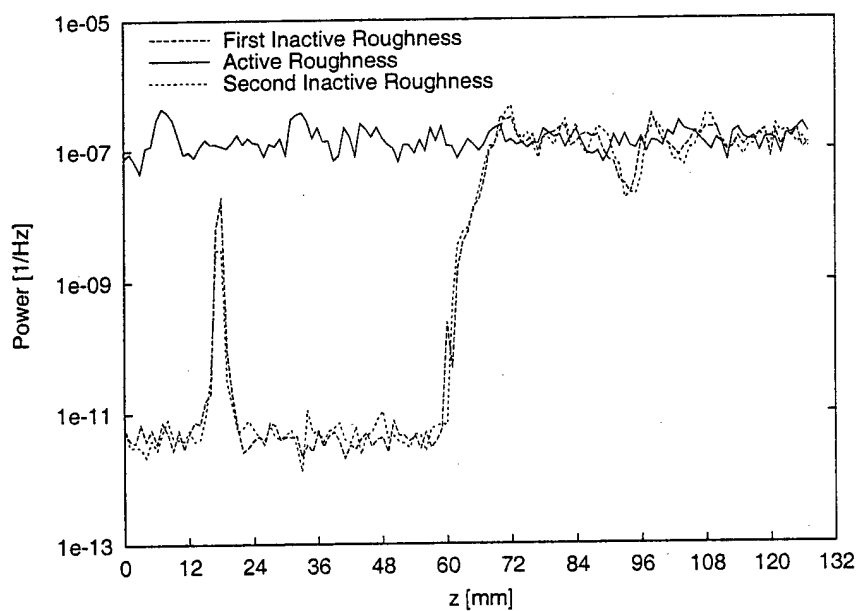


Figure 207: Spanwise distribution of velocity-fluctuation power spectral density at 4.0 kHz with and without activated 12-mm-spaced artificial roughness,  $Re_c = 2.8 \times 10^6$ ,  $x/c = 0.40$ ,  $Y = 1.2$  mm.

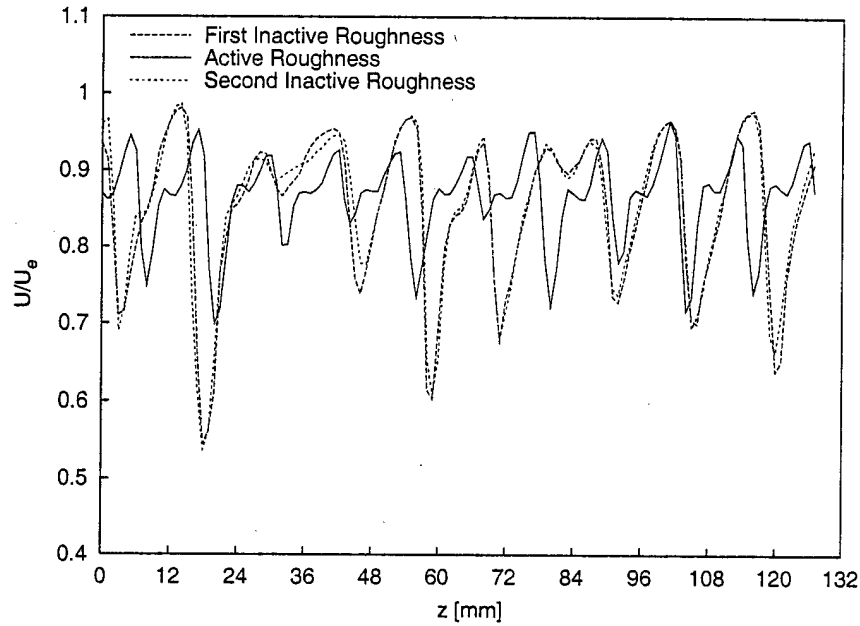


Figure 208: Spanwise mean-flow hotwire scan with and without activated 12-mm-spaced artificial roughness,  $Re_c = 2.0 \times 10^6$ ,  $x/c = 0.58$ ,  $Y = 2.0$  mm.

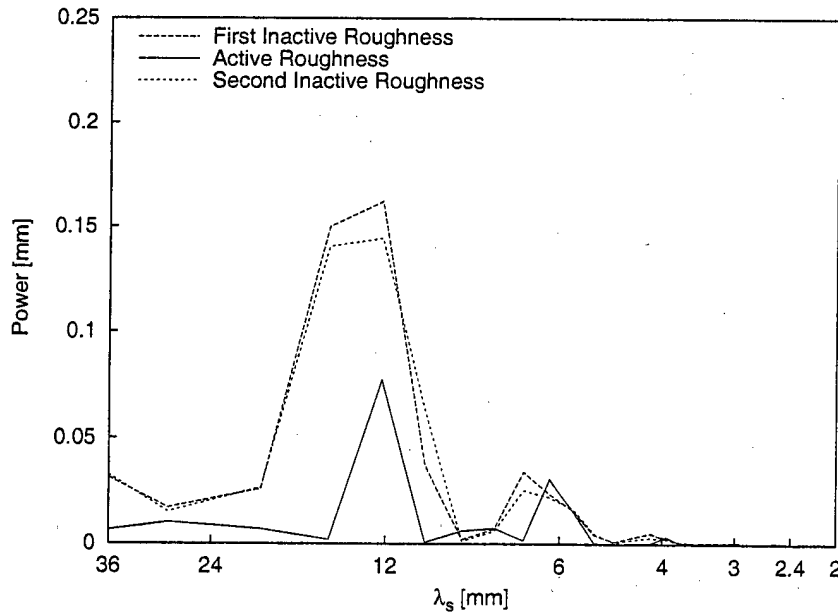


Figure 209: Power spectral density of the spanwise mean-flow hotwire scan with and without activated 12-mm-spaced artificial roughness,  $Re_c = 2.0 \times 10^6$ ,  $x/c = 0.58$ ,  $Y = 2.0$  mm.

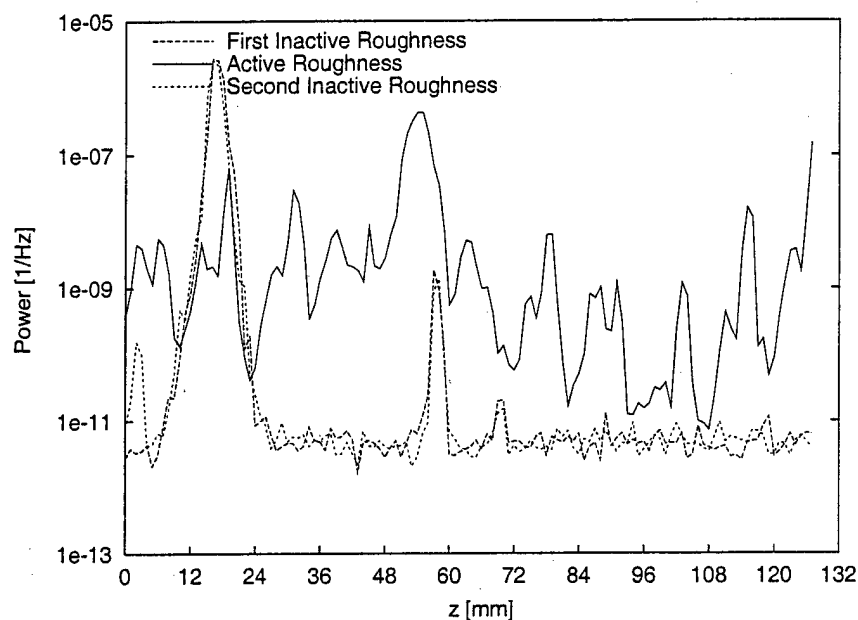


Figure 210: Spanwise distribution of velocity-fluctuation power spectral density at 2.0 kHz with and without activated 12-mm-spaced artificial roughness,  $Re_c = 2.0 \times 10^6$ ,  $x/c = 0.58$ ,  $Y = 2.0$  mm.

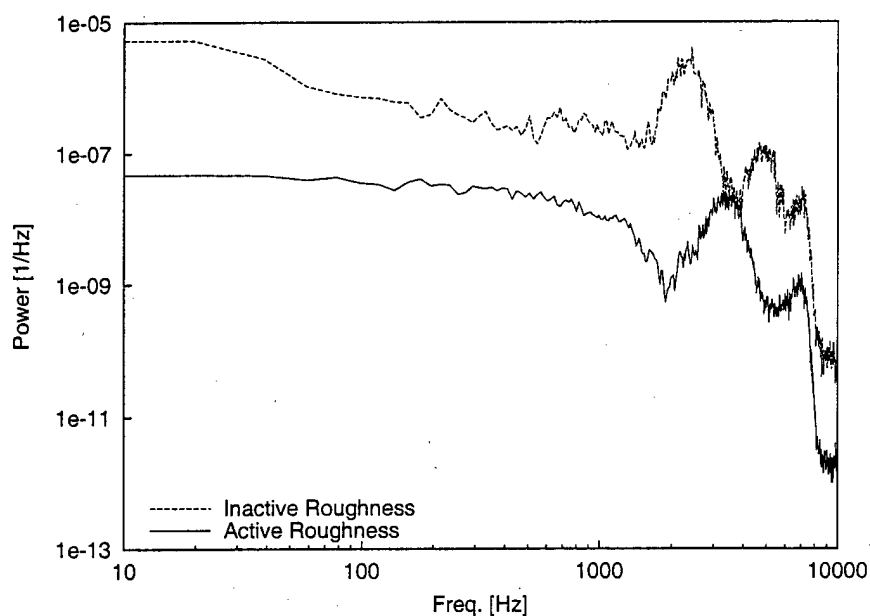


Figure 211: Fluctuating-velocity spectral density with and without activated 12-mm-spaced artificial roughness,  $Re_c = 2.0 \times 10^6$ ,  $x/c = 0.58$ ,  $Y = 2.0$  mm,  $z = 16$  mm.

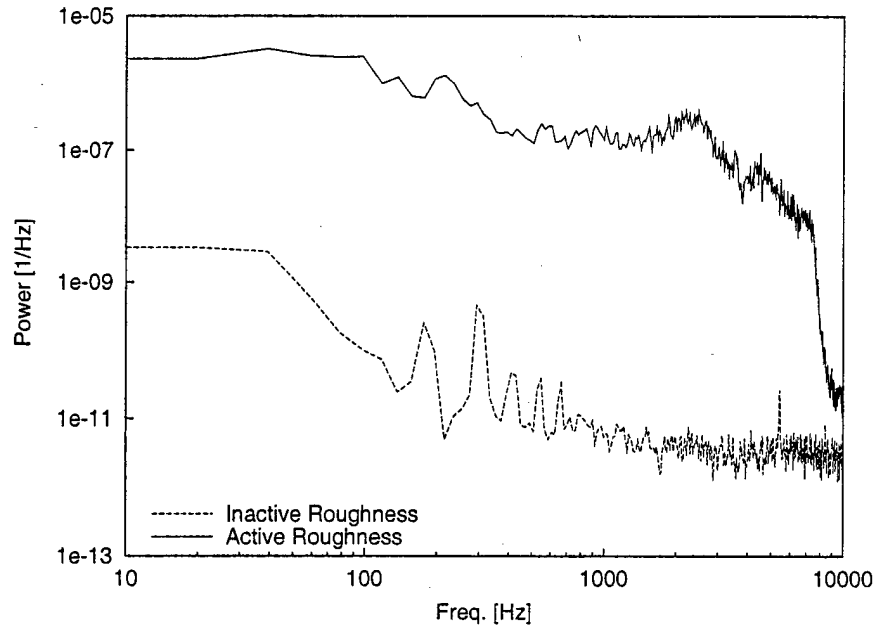


Figure 212: Fluctuating-velocity spectral density with and without activated 12-mm-spaced artificial roughness,  $Re_c = 2.0 \times 10^6$ ,  $x/c = 0.58$ ,  $Y = 2.0$  mm,  $z = 53$  mm.

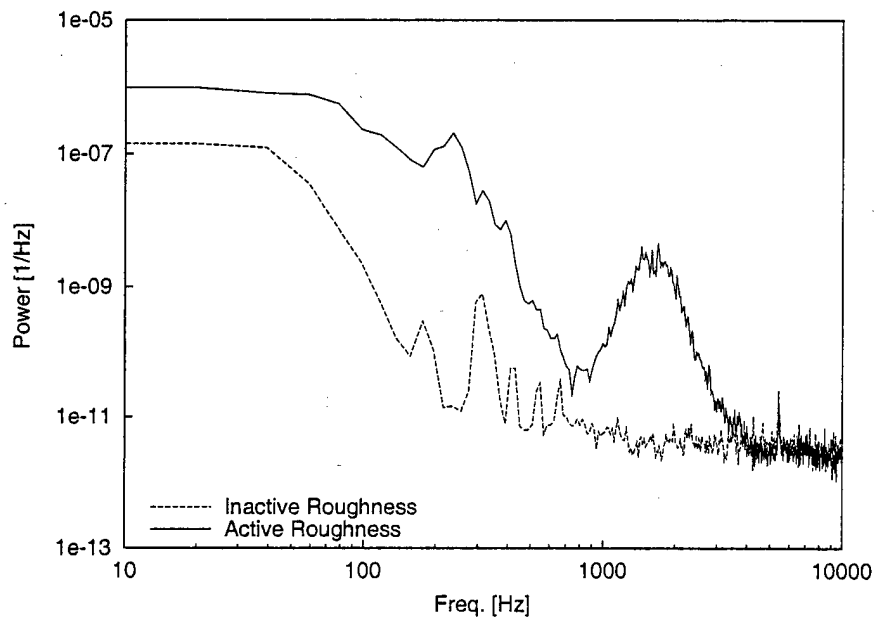


Figure 213: Fluctuating-velocity spectral density with and without activated 12-mm-spaced artificial roughness,  $Re_c = 2.0 \times 10^6$ ,  $x/c = 0.58$ ,  $Y = 2.0$  mm,  $z = 103$  mm.

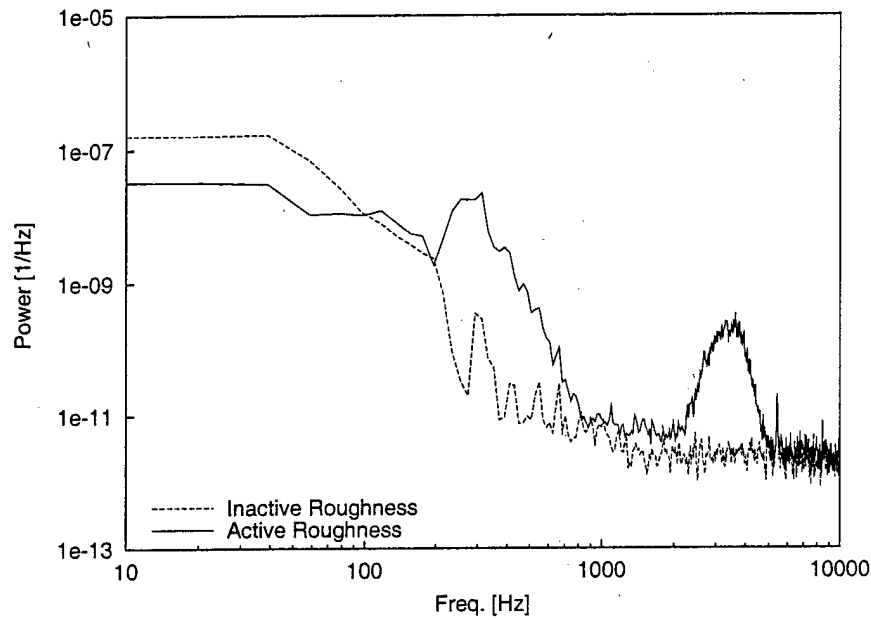


Figure 214: Fluctuating-velocity spectral density with and without activated 12-mm-spaced artificial roughness,  $Re_c = 2.0 \times 10^6$ ,  $x/c = 0.58$ ,  $Y = 2.0$  mm,  $z = 107$  mm.

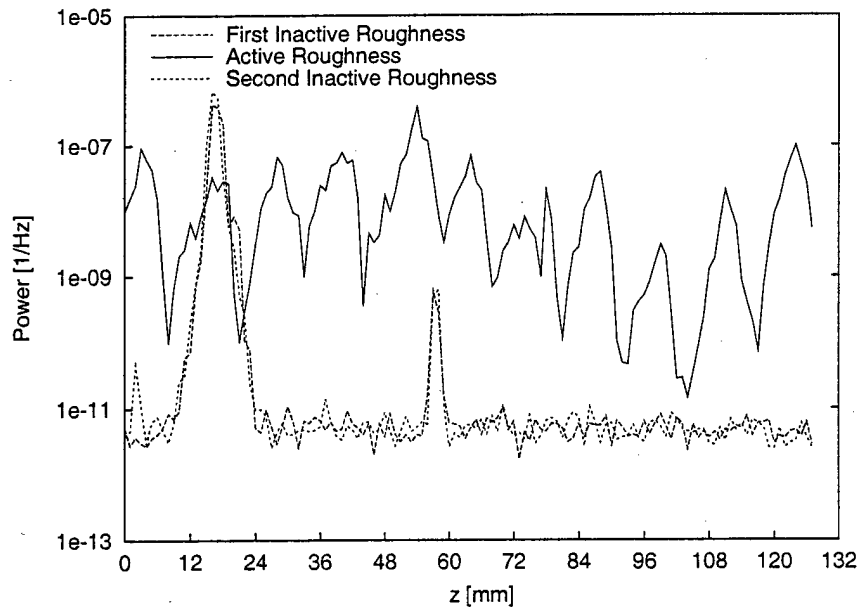


Figure 215: Spanwise distribution of velocity-fluctuation power spectral density at 3.0 kHz with and without activated 12-mm-spaced artificial roughness,  $Re_c = 2.0 \times 10^6$ ,  $x/c = 0.58$ ,  $Y = 2.0$  mm.

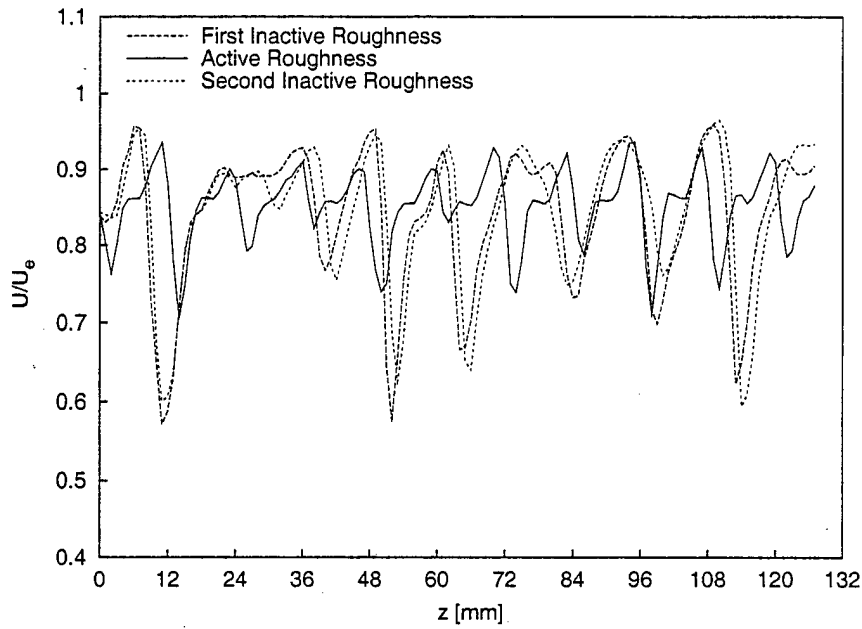


Figure 216: Spanwise mean-flow hotwire scan with and without activated 12-mm-spaced artificial roughness,  $Re_c = 2.0 \times 10^6$ ,  $x/c = 0.60$ ,  $Y = 2.0$  mm.

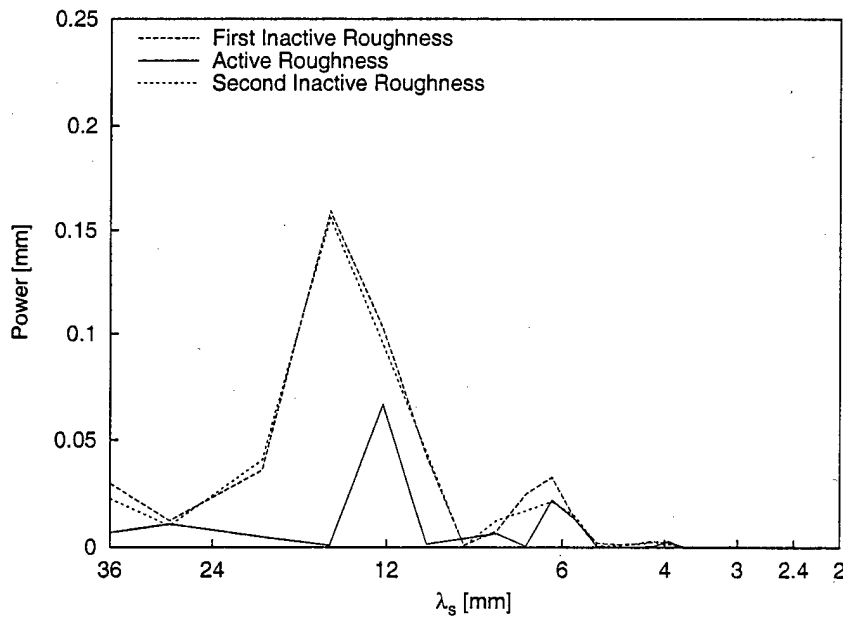


Figure 217: Power spectral density of the spanwise mean-flow hotwire scan with and without activated 12-mm-spaced artificial roughness,  $Re_c = 2.0 \times 10^6$ ,  $x/c = 0.60$ ,  $Y = 2.0$  mm.

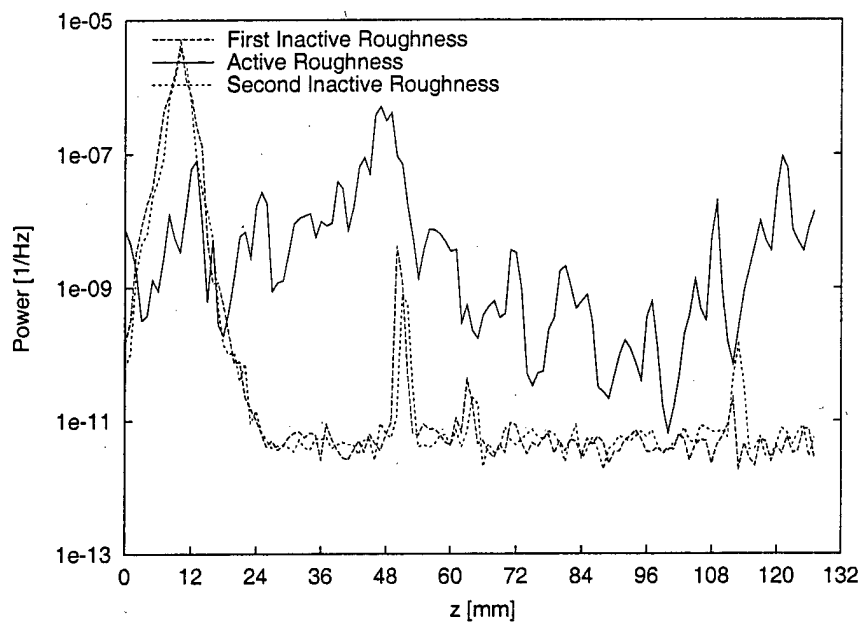


Figure 218: Spanwise distribution of velocity-fluctuation power spectral density at 2.0 kHz with and without activated 12-mm-spaced artificial roughness,  $Re_c = 2.0 \times 10^6$ ,  $x/c = 0.60$ ,  $Y = 2.0$  mm.

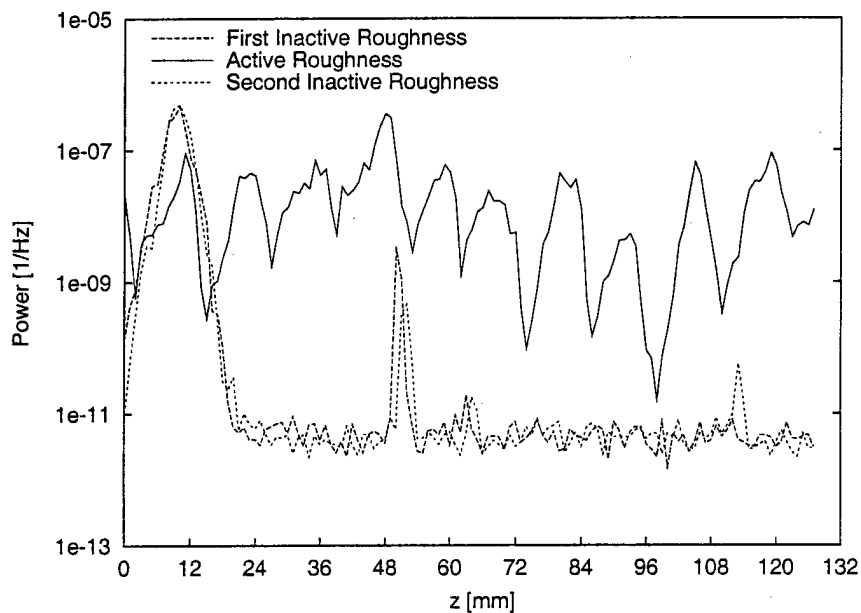


Figure 219: Spanwise distribution of velocity-fluctuation power spectral density at 3.0 kHz with and without activated 12-mm-spaced artificial roughness,  $Re_c = 2.0 \times 10^6$ ,  $x/c = 0.60$ ,  $Y = 2.0$  mm.